Electronic Supporting Information

Metal-metal cooperative bond activation by heterobimetallic alkyl, aryl, and acetylide Pt^{II}/Cu^{I} complexes

Shubham Deolka,[a] Orestes Rivada-Wheelaghan,*[a]† Sandra L. Aristizábal,[a] Robert R. Fayzullin,[b] Shrinwantu Pal,[c] Kyoko Nozaki,[c] Eugene Khaskin[a] and Julia R. Khusnutdinova*[a]

[a]Coordination Chemistry and Catalysis Unit Okinawa Institute of Science and Technology Graduate University, 1919-1 Tancha, Onna-son, 904-0495, Okinawa, Japan.

[b]Arbuzov Institute of Organic and Physical Chemistry, FRC Kazan Scientific Center, Russian Academy of Sciences, 8 Arbuzov Street, Kazan, 420088, Russian Federation.

[c]Department of Chemistry and Biotechnology, Graduate School of Engineering, The University of Tokyo, 7-3-1 Hongo, Bunkyo-ku, Tokyo 113-8656, Japan.

† Current address: Université de Paris, Laboratoire d'Electrochimie Moléculaire, UMR 7591 CNRS, 15 rue Jean-Antoine de Baïf, F-75205 Paris Cedex 13, France

Table of Contents

Experimental procedures

General specifications

All reactions were performed using standard Schlenk or glovebox techniques under a dry nitrogen or argon atmosphere if not indicated otherwise. All chemicals unless noted otherwise were purchased from major commercial suppliers (TCI, Sigma-Aldrich and Nacalai Tesque) and used without purification. Anhydrous solvents were dispensed from an MBRAUN solvent purification system and degassed prior to use. Anhydrous deuterated solvents were purchased from Eurisotop and stored over 4 Å molecular sieves. $[Cu(MeCN)_4][B(Ar^F)_4]$ (copper tetrakis[3,5-bis(trifluoromethyl)phenyl]borate),[1] dimethyl (norbornadiene) platinum(II)[2] and trimethyl platinum(IV) iodide[3] were prepared according to the literature procedures. The ligand precursor $\mathbf{L_0}$ was previously reported in the literature and was prepared according to the published procedures.[1] All the metal complexes were prepared under a nitrogen atmosphere in a glovebox.
Instrumentation: NMR spectra were measured on JEOL ECZ600R 600MHz and JEOL ECZ400S 400 MHz spectrometers. The following abbreviations are used for describing NMR spectra: s (singlet), d (doublet), t (triplet), td (triplet of doublets), ddd (doublet of doublets of doublets), vd (virtual doublet), vt (virtual triplet), br (broad); Pt satellites are marked with stars in the figures showing NMR spectra. For the NOE experiment the mixing time and relaxation delay are determined by double pulse experiments. Electrospray Ionization Mass Spectrometry (ESI-MS) measurements were performed on a Thermo Scientific ETD apparatus. Elemental analyses were performed using an Exeter Analytical CE440 instrument. FT-IR spectra were measured using an Agilent Cary 630 with an ATR module in an argon-filled glovebox. The following abbreviations are used for describing FT-IR spectra: s (strong), m (medium), w (weak), br (broad). Absorbance UV/vis spectra were collected using an Agilent Cary 60 instrument.

Synthesis of ligand L

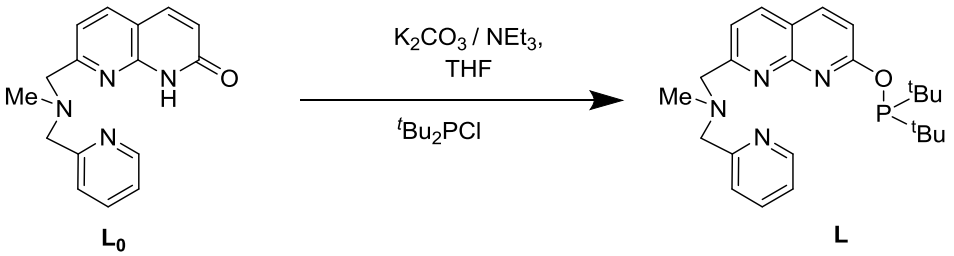

Scheme S1. Synthesis of **L**.

In a 20 ml vial $\mathbf{L_0}$ (100.3 mg, 0.3567 mmol) was dissolved in THF at room temperature (RT) in the presence of excess amount of K_2CO_3 (123.2 mg, 0.8917 mmol) and triethylamine (124 µL, 0.891 mmol) The solution was stirred for 30 minutes at room temperature. Then di-*tert*-butylchlorophosphine (74 µL, 0.39 mmol) was added to the reaction mixture and stirred for 1 hour. After that, the excess solid of K_2CO_3 was removed via filtration and the solvent was removed under vacuum. The white oil was further dissolved in a minimum amount of THF and hexane was then added to precipitate the white powder which was dried under vacuum to yield **L** as a white solid, 120.1 mg, 0.2830 mmol, 79% yield.
^{1}H NMR (600 MHz,THF-d_8, 22 °C) δ: 8.46 (d, $^3J_{HH}$ = 4.4 Hz, 1H, CH_{Py}), 8.14 (d, $^3J_{HH}$ = 3.1 Hz, 1H, CH_{Naph}), 8.13 (d, $^3J_{HH}$ = 3.1 Hz, 1H, CH_{Naph}), 7.71 (d, $^3J_{HH}$ = 8.4 Hz, 1H, CH_{Naph}), 7.67 (td, $^3J_{HH}$ = 7.7 Hz, $^4J_{HH}$ = 1.5 Hz, 1H, CH_{Py}), 7.59 (d, $^3J_{HH}$ = 7.7 Hz, 1H, CH_{Py}), 7.15 – 7.12 (br m, 1H, CH_{Py}), 7.11 (d, $^3J_{HH}$ = 8.4 Hz, 1H, CH_{Naph}), 3.89 (s, 2H, CH_2), 3.76 (s, 2H, CH_2), 2.29 (s, 3H, N-CH_3), 1.23 (d, $^3J_{PH}$ = 11.2 Hz, 18H, C(CH_3)$_3$).

$^{13}C\{^{1}H\}$ NMR (151 MHz, THF-d_8, 22 °C) δ: 165.85 (d, $^{2}J_{PC}$ = 7.8 Hz, $C_{q,Naph}$), 164.46 ($C_{q,Naph}$), 160.55 ($C_{q,Py}$), 155.79 ($C_{q,Naph}$), 149.61 ($C_{H,Py}$), 140.12 ($C_{H,Naph}$), 136.97 ($C_{H,Naph}$), 136.51 ($C_{H,Py}$), 123.17 ($C_{H,Py}$), 122.32 ($C_{H,Py}$), 119.90 ($C_{H,Naph}$), 119.36 ($C_{q,Naph}$), 114.50 ($C_{H,Naph}$), 64.98 (CH_2), 64.47 (CH_2), 42.87 (N-CH_3), 35.89 (d, $^{1}J_{PC}$ = 30.2 Hz, ***C***$(CH_3)_3$), 27.84 (d, $^{2}J_{PC}$ =16.4 Hz, C(***C***$H_3)_3$).
$^{31}P\{^{1}H\}$ NMR (242 MHz, THF-d_8, 22 °C) δ: 154.0.
ESI-HRMS (m/z pos): Found (Calcd): $C_{24}H_{33}ON_4P \cdot H^+$: 424.2454 (424.2465).
FT-IR (ATR, solid): 2871 (br, w), 2859 (br, w), 1605 (br, s), 1498 (br, s), 1431 (br, s), 1307 (s), 1252 (s), 1066 (br, s), 907 (s), 806 (m) cm^{-1}.
UV-vis (THF), λ, nm (ε, $M^{-1} \cdot cm^{-1}$) : 320 (7722), 314 (7341), 238 (7250).

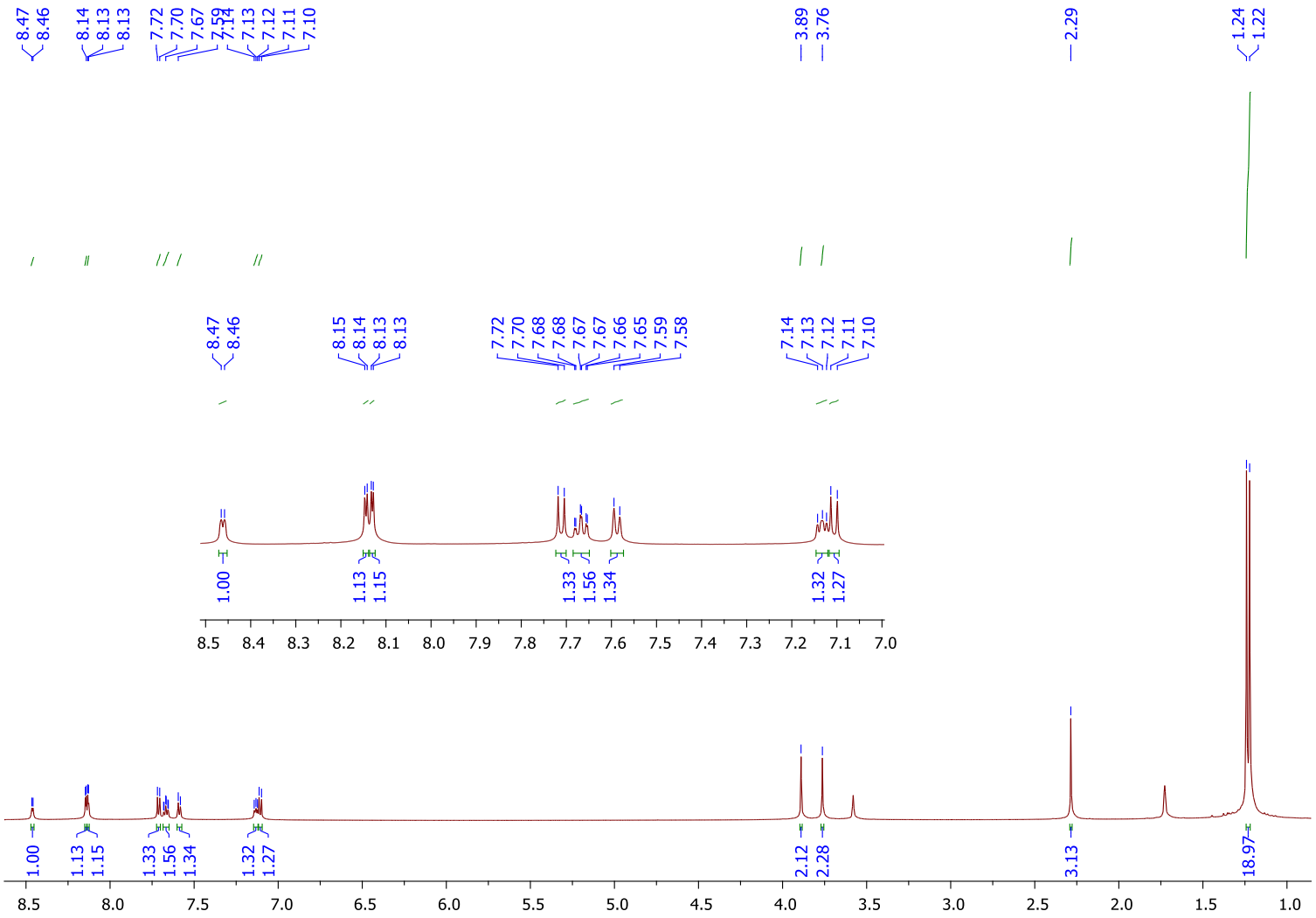

Figure S1. ^{1}H NMR spectrum of **L** in THF-d_8 at 22 °C.

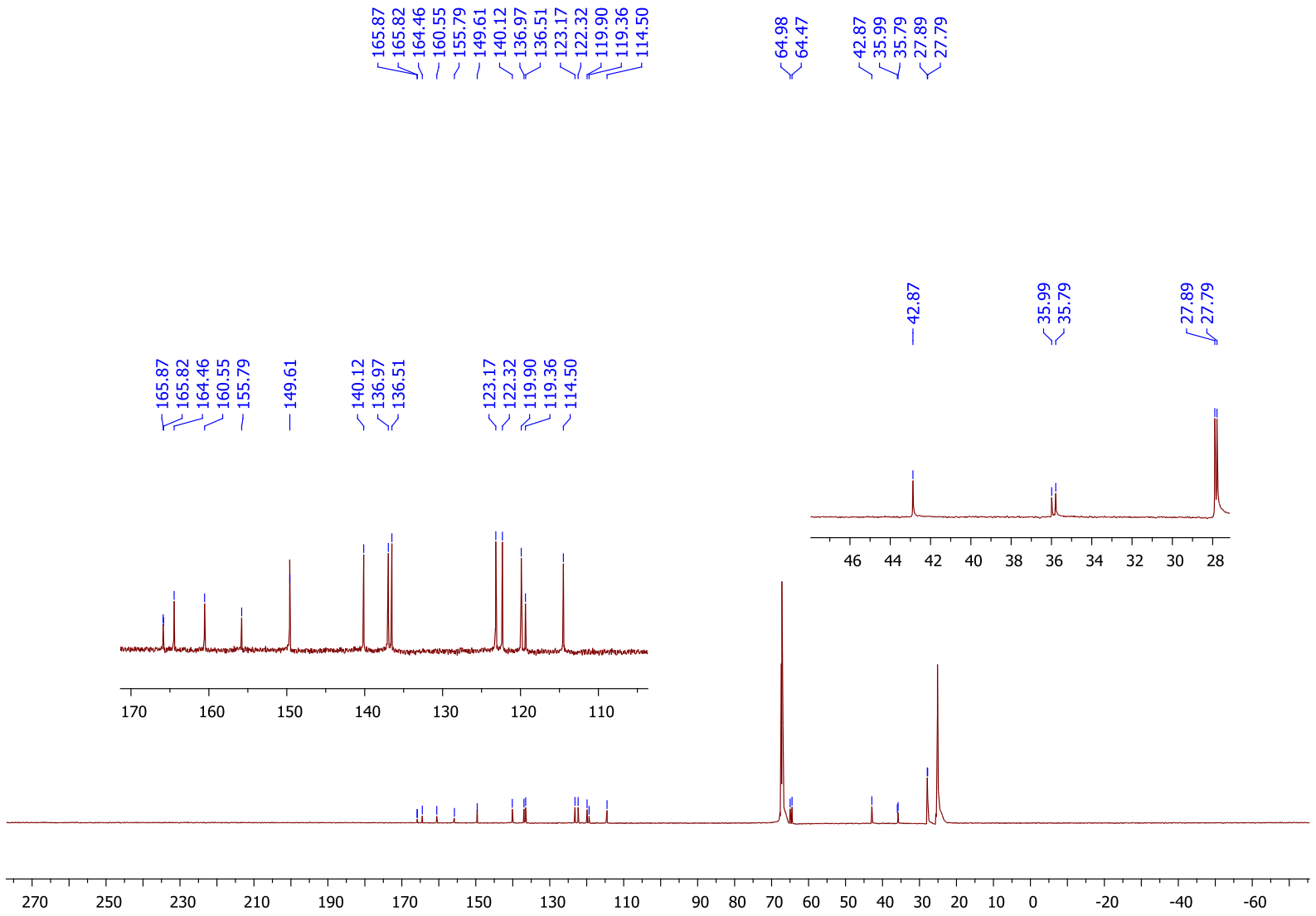

Figure S2. $^{13}C\{^{1}H\}$ NMR spectrum of **L** in THF-d_8 at 22 °C.

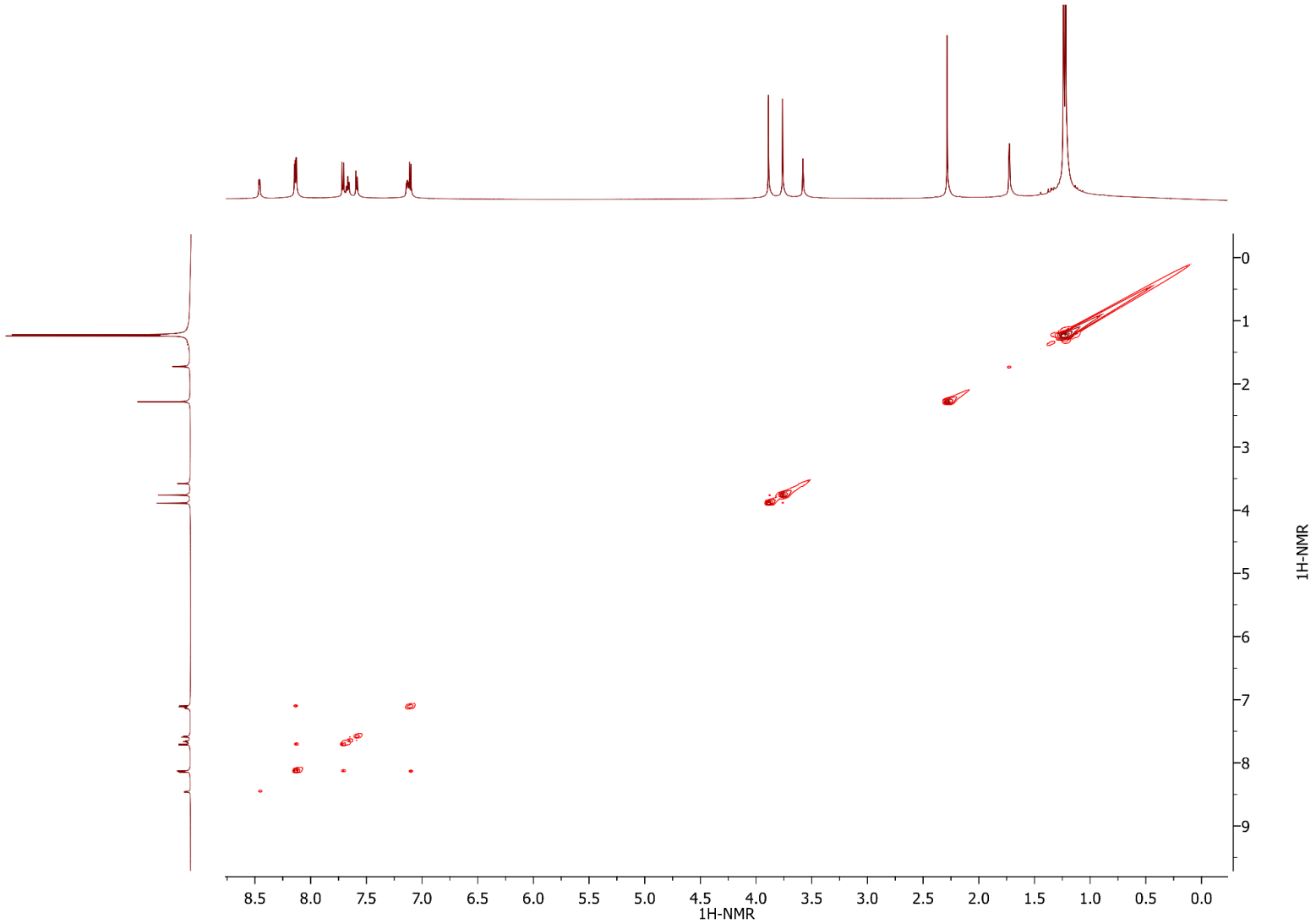

Figure S3. ^{1}H-^{1}H COSY spectrum of **L** in THF-d_8 at 22 °C.

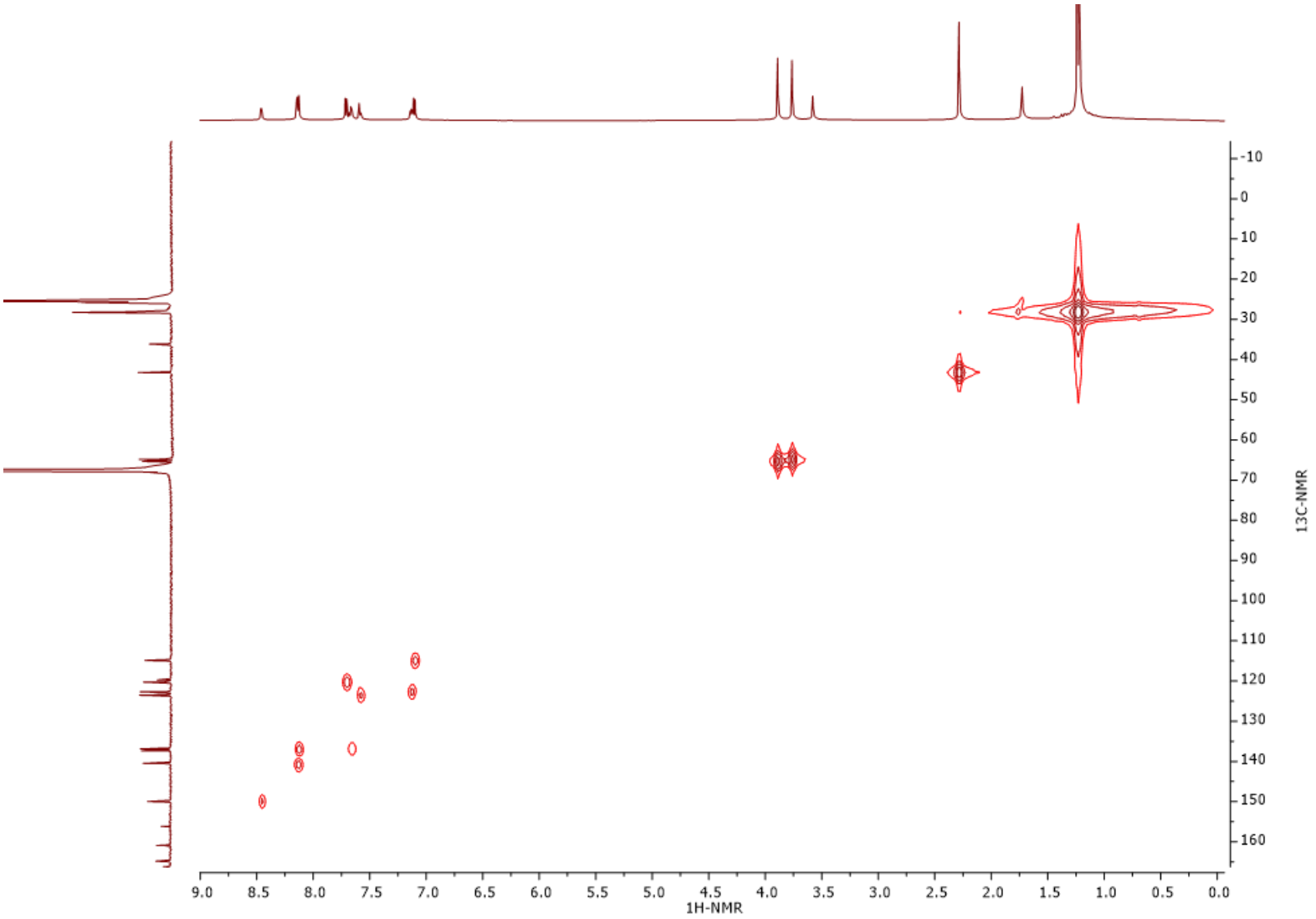

Figure S4. ^{1}H-^{13}C HMQC spectrum of **L1** in THF-d_8 at 22 °C.

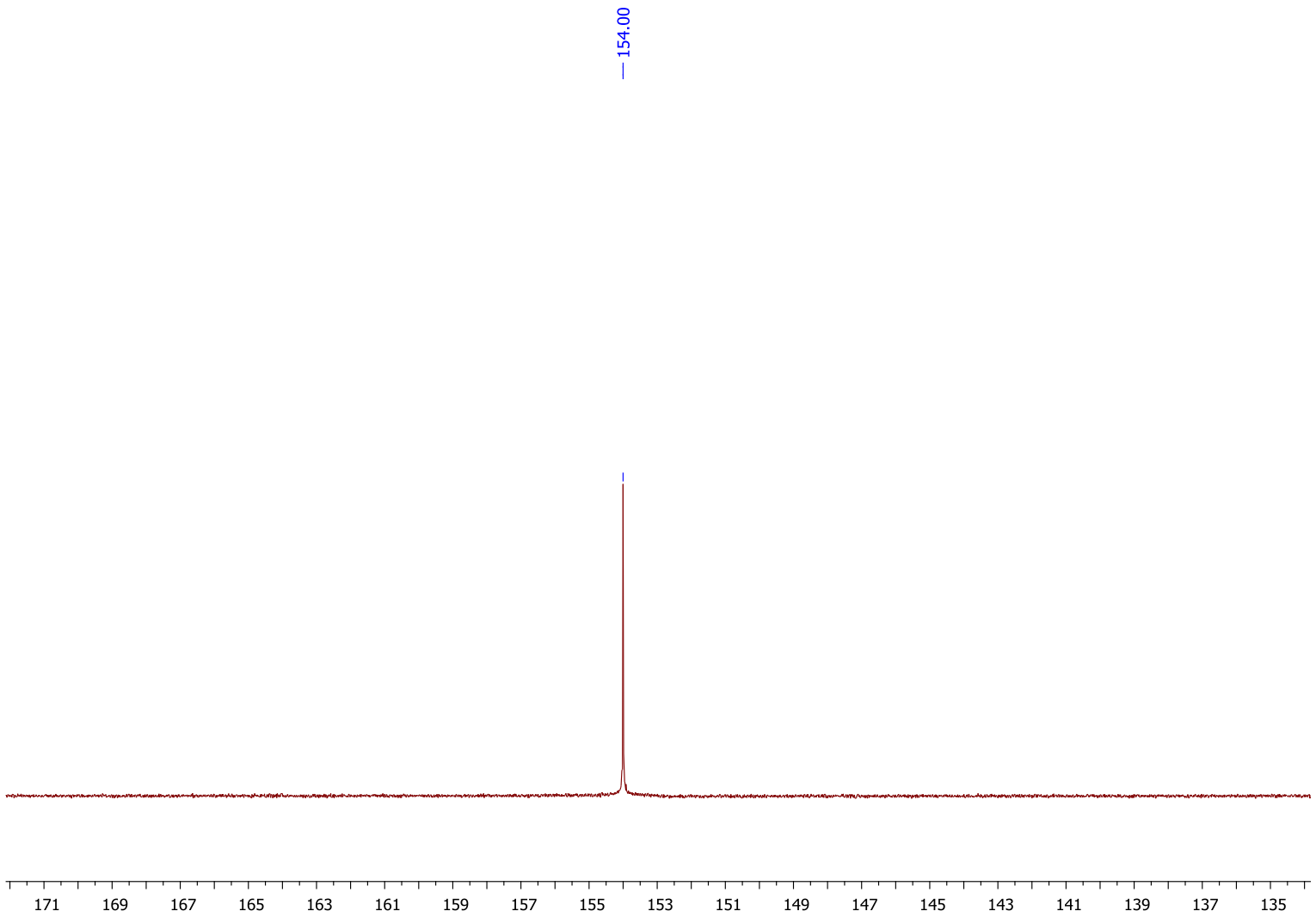

Figure S5. $^{31}P\{^{1}H\}$ NMR spectrum of **L** in THF-d_8 at 22 °C.

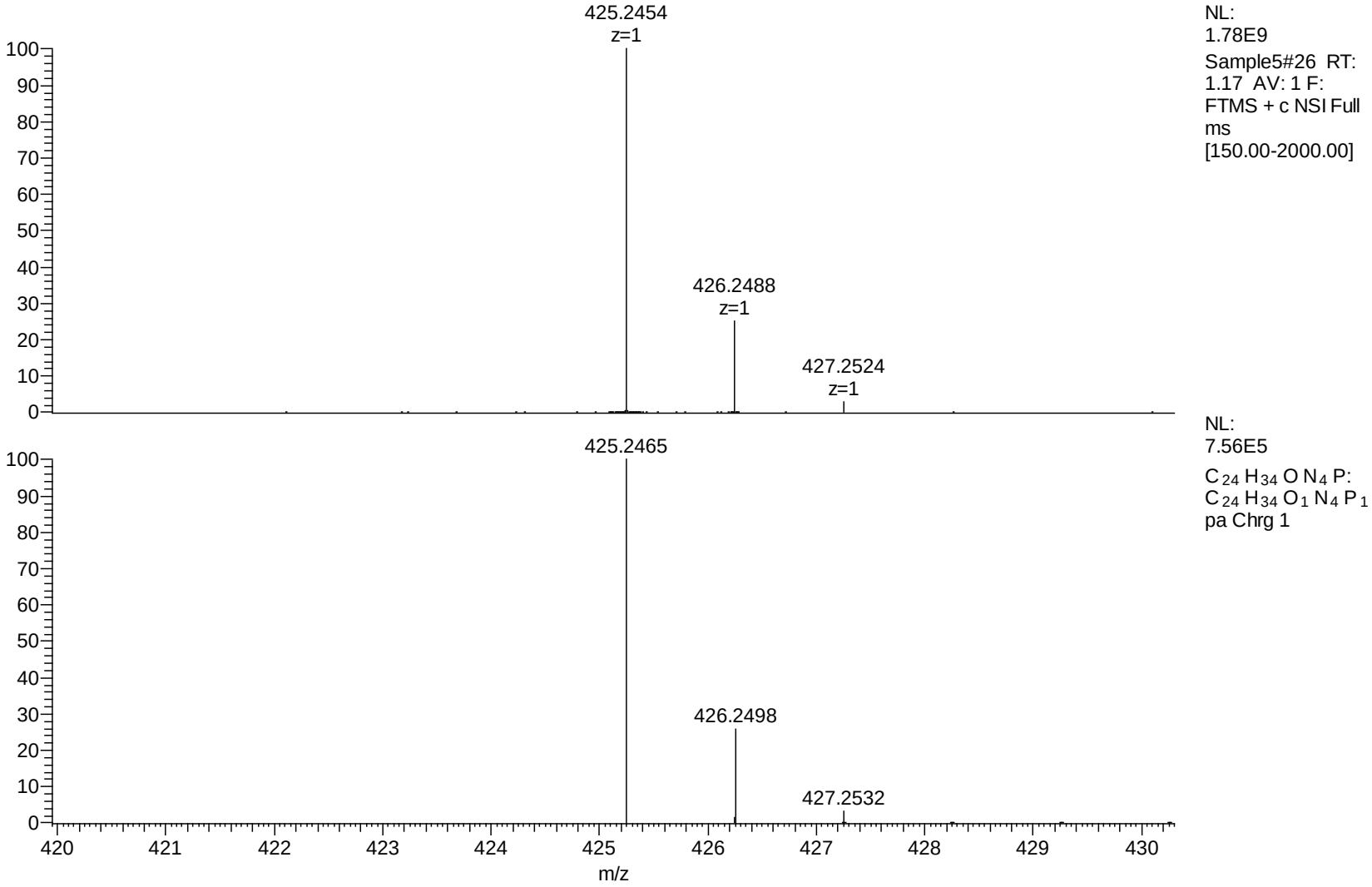

Figure S6. ESI-(HR)MS spectrum of THF solution of **L** (top) and simulated spectrum of $C_{24}H_{33}ON_4P{\cdot}H^+$: (bottom).

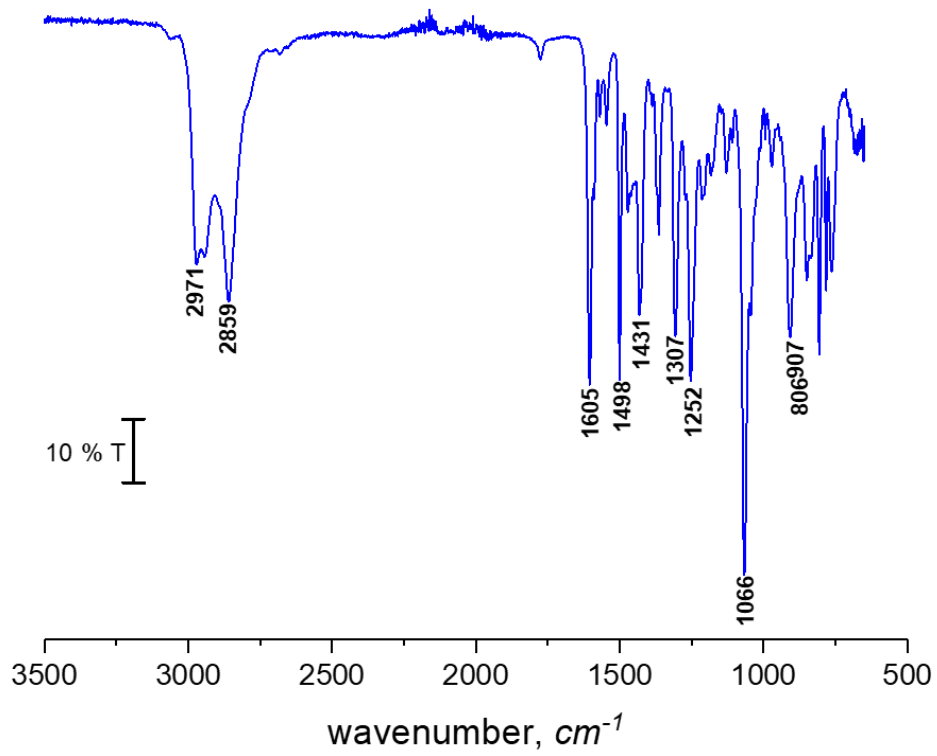

Figure S7. ATR FT-IR transmittance spectrum of **L**.

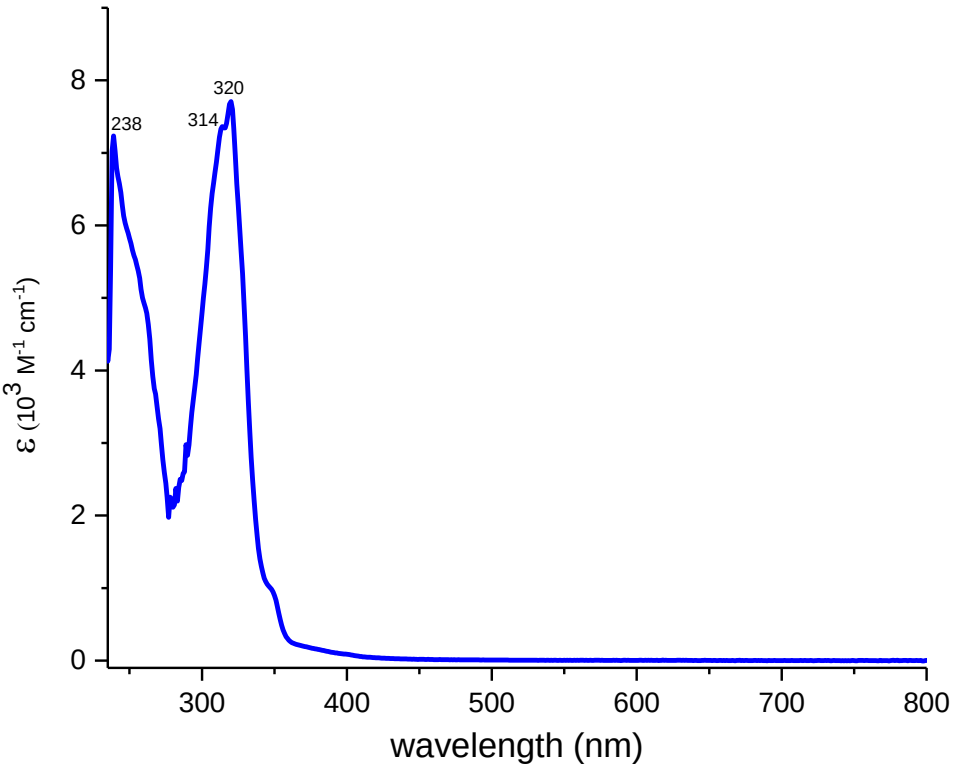

Figure S8. UV-vis absorbance spectrum of **L** in THF.

Synthesis of (L)PtMe$_2$, 1

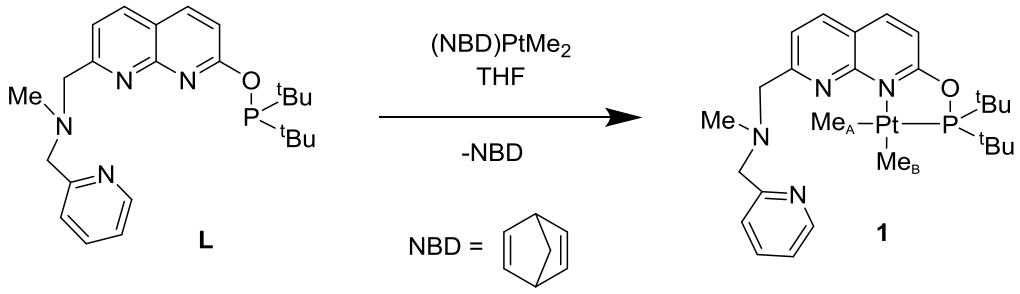

Scheme S2. Synthesis of **1**.

To a 20 mL vial containing dimethyl(norbornadiene)platinum(II), (NBD)PtMe$_2$, (74.7 mg, 0.23 mmol) and **L** (100 mg, 0.23 mmol), THF (4 mL) was added to give a yellow solution. The reaction was left to stir for 1 hour. Later the solvent was removed under vacuum and the desired complex was re-dissolved in THF (1 mL), then precipitated with hexane (5 x 2 mL) to crash out the yellow powder. Solvent removal yields complex **1** as a yellow solid, 115.8 mg, 0.17 mmol, 75% yield.

NMR characterization was performed in several solvents to allow comparison of NMR chemical shifts with heterobimetallic complexes.
Here and further on, in figures containing ^{1}H NMR spectra of Pt complexes, only central peak is integrated (≈66% of total integration) and satellites are not integrated (remaining 34% of total integration based on natural abundance of ^{195}Pt isotope).
NMR Characterization in CD_3CN:
^{1}H NMR (400 MHz, CD_3CN, 23 °C) δ: 8.50 (d, $^3J_{HH}$ = 4.3 Hz, 1H, CH_{Py}), 8.41 (d, $^3J_{HH}$ = 8.7 Hz, 1H, CH_{Naph}), 8.28 (d, $^3J_{HH}$ = 8.2 Hz, 1H, CH_{Naph}), 7.78 (d, $^3J_{HH}$ = 8.2 Hz, 1H, CH_{Naph}), 7.73 (td, $^3J_{HH}$ = 7.7 Hz, $^4J_{HH}$ = 1.8 Hz, 1H, CH_{Py}), 7.58 (d, $^3J_{HH}$ = 7.8 Hz, 1H, CH_{Py}), 7.33 (d, $^3J_{HH}$ = 8.7 Hz, 1H, CH_{Naph}), 7.21 (t, $^3J_{HH}$ = 6.3 Hz, 1H, CH_{Py}), 3.91 (s, 2H, CH_2), 3.75 (s, 2H, CH_2), 2.28 (s, 3H, N-CH_3), 1.34 (d, $^3J_{PH}$ = 13.5 Hz, 18H, C(CH_3)$_3$), 0.91 (d, $^3J_{PH}$ = 6.4 Hz, $^2J_{PtH}$ = 94.6 Hz, 3H, Pt-Me_B), 0.81 (d, $^3J_{PH}$ = 8.1 Hz, $^2J_{PtH}$ = 66.9 Hz, 3H, Pt-Me_A).
^{13}C{^{1}H} NMR (101 MHz, CD_3CN, 23 °C) δ: 168.57 ($C_{q,Naph}$), 164.60 ($C_{q,Naph}$), 160.39 ($C_{q,Py}$), 154.46 ($C_{q,Naph}$), 149.8 9($C_{H,Py}$), 142.42 ($C_{H,Naph}$), 138.41 ($C_{H,Py}$), 137.3 7 ($C_{H,Naph}$), 123.90 ($C_{H,Py}$), 123.90 ($C_{H,Py}$), 121.43 ($C_{H,Naph}$), 120.36 ($C_{q,Naph}$), 113.37 ($C_{H,Naph}$), 64.60 (CH_2), 64.07 (CH_2), 43.30 (N-CH_3), 40.62 (d, $^1J_{PC}$ = 7.9 Hz, ***C***(CH_3)$_3$), 27.67 (d, $^2J_{PC}$ = 6.6 Hz, C(***C***H_3)$_3$), 15.27 (d, $^2J_{PC}$ = 116.3 Hz, $^1J_{PtC}$ = 659.4 Hz, Pt-Me_A), -22.13 (d, $^2J_{PC}$ = 2.7 Hz, $^1J_{PtC}$ = 790.8 Hz, Pt-Me_B).
^{31}P{^{1}H} NMR (162 MHz, CD_3CN, 23 °C) δ:183.6 ($^1J_{PtP}$ = 2043 Hz).
^{195}Pt{^{1}H} NMR (129 MHz, CD_3CN, 23 °C) δ: -3914.8 (d, $^1J_{PtP}$ = 2043 Hz).

NMR Characterization in THF-d_8:
^{1}H NMR (400 MHz, THF-d_8, 23 °C) δ: 8.47 (d, $^3J_{HH}$ = 4.5 Hz, 1H, CH_{Py}), 8.42 (d, $^3J_{HH}$ = 8.6 Hz, 1H, CH_{Naph}), 8.25 (d, $^3J_{HH}$ = 8.1 Hz, 1H, CH_{Naph}), 7.83 (d, $^3J_{HH}$ = 8.1 Hz, 1H, CH_{Naph}), 7.67 (td, $^3J_{HH}$ = 7.6 Hz, $^4J_{HH}$ = 1.8 Hz, 1H, CH_{Py}), 7.60 (d, $^3J_{HH}$ = 8.1 Hz, 1H, CH_{Py}), 7.31 (d, $^3J_{HH}$ = 8.6 Hz, 1H, CH_{Naph}), 7.13 (t, $^3J_{HH}$ = 6.1 Hz, 1H, CH_{Py}), 3.98 (s, 2H, CH_2), 3.78 (s, 2H, CH_2), 2.31 (s, 3H, N-CH_3), 1.37 (d, $^3J_{PH}$ = 13.3 Hz, 18H, C(CH_3)$_3$), 0.96 (d, $^3J_{PH}$ = 6.7 Hz, $^2J_{PtH}$ = 94.5 Hz, 3H, Pt-Me_B), 0.93 (d, $^3J_{PH}$ = 8.3 Hz, $^2J_{PtH}$ = 66.1 Hz, 3H, Pt-Me_A).
^{13}C{^{1}H} NMR (101 MHz, THF-d_8, 23 °C) δ: 168.19 ($C_{q,Naph}$), 164.65 ($C_{q,Naph}$), 160.46 ($C_{q,Py}$), 154.65 ($C_{q,Naph}$), 149.67 ($C_{H,Py}$), 141.56 ($C_{H,Naph}$), 137.53 ($C_{H,Naph}$), 136.53 ($C_{H,Py}$), 123.21 ($C_{H,Py}$), 122.34 ($C_{H,Naph}$), 120.83 ($C_{H,Py}$), 120.10 ($C_{q,Naph}$), 112.59 ($C_{H,Naph}$), 64.52 (CH_2), 63.84 (CH_2), 43.03 (N-CH_3), 40.54 (d, $^1J_{PC}$ = 5.6 Hz, $^2J_{PtP}$ = 43.8 Hz ***C***(CH_3)$_3$), 27.59 (d, $^2J_{PC}$ = 6.8 Hz, C(***C***H_3)$_3$), 15.74 (d, $^2J_{PC}$ = 117.5 Hz, $^1J_{PtC}$ = 661.8 Hz, Pt-Me_A), -21.94 (d, $^2J_{PC}$ = 2.9 Hz, $^1J_{PtC}$ = 805.4 Hz, Pt-Me_B).
^{31}P{^{1}H} NMR (162 MHz, THF-d_8, 23 °C) δ: 182.9 ($^1J_{PtP}$ = 2006 Hz).
^{195}Pt{^{1}H} NMR (129 MHz, THF-d_8, 23 °C) δ: -3893.6 (d, $^1J_{PtP}$ = 2006 Hz).

NMR Characterization in C_6D_6:
^{1}H NMR (400 MHz, C_6D_6, 23 °C) δ: 8.51 (d, $^3J_{HH}$ = 4.8 Hz, 1H, CH_{Py}), 7.65 (d, $^3J_{HH}$ = 8.2 Hz, 1H, CH_{Naph}), 7.33 (d, $^3J_{HH}$ = 8.2 Hz, 1H, CH_{Naph}), 7.29 (d, $^3J_{HH}$ = 8.2 Hz, 1H, CH_{Naph}), 7.22 (d, $^3J_{HH}$ = 8.6 Hz, 1H, CH_{Py}), 6.64 (br m, 1H, CH_{Py}), 6.57 (d,$^3J_{HH}$ = 8.6 Hz, 1H, CH_{Naph}), 4.05 (s, 2H, CH_2), 3.73 (s, 2H, CH_2), 2.17 (s, 3H, N-CH_3), 2.00 (d, $^3J_{PH}$ = 8.2 Hz, 3H, $^2J_{PtH}$ = 65.8 Hz, Pt-Me_A), 1.82 (d, $^3J_{PH}$ = 6.6 Hz, $^2J_{PtH}$ = 96.4 Hz, 3H, Pt-Me_B), 1.28 (d, $^3J_{PH}$ = 13.4 Hz, 18H, C(CH_3)$_3$). One aromatic peak of pyridine overlaps with C_6D_6.
^{13}C{^{1}H} NMR (101 MHz, C_6D_6, 23 °C) δ: 167.48 ($C_{q,Naph}$), 164.68 ($C_{q,Naph}$), 160.01 ($C_{q,Py}$), 154.34 ($C_{q,Naph}$), 149.59 ($C_{H,Py}$), 140.10 ($C_{H,Py}$), 136.43 ($C_{H,Naph}$), 135.82 ($C_{H,Py}$), 123 ($C_{H,Naph}$), 121.82 ($C_{H,Naph}$), 120.43 ($C_{H,Naph}$), 119.10 ($C_{q,Naph}$), 111.54 ($C_{H,Py}$), 63.99 (CH_2), 63.56 (CH_2), 42.90 (N-CH_3), 40.08 (d, $^1J_{PC}$ = 5.1 Hz, $^2J_{PtP}$ = 46.6 Hz ***C***(CH_3)$_3$), 27.54 (d,$^2J_{PC}$ = 6.7 Hz, C(***C***H_3)$_3$), 16.60 (d, $^2J_{PC}$ = 117.4 Hz, $^1J_{PtC}$ = 660.8 Hz, Pt-Me_A), -20.77 (d, $^2J_{PC}$ = 2.6 Hz, $^1J_{PtC}$ = 802.4 Hz, Pt-Me_B).
^{31}P{^{1}H} NMR (162 MHz, C_6D_6, 23 °C) δ: 183.9 ($^1J_{PtP}$ = 2000 Hz).

^{195}Pt{^{1}H} NMR (129 MHz, C_6D_6, 23 °C) δ: -3889.4 (d, $^1J_{PtP}$ = 2000 Hz).

Elemental Analysis: Expt (Calc) for $C_{26}H_{39}N_4OPPt$: C 47.59 (48.07), H 5.86 (6.05), N 8.34 (8.62).

ESI-HRMS (m/z pos): Found (Calcd): $C_{25}H_{36}ON_4P^{195}Pt^+$ (M-CH_3) : 634.2288 (634.2269).

FT-IR (ATR, solid): 2868 (br, w), 2930 (br, w), 1601 (s), 1502 (s), 1428 (s), 1314 (m), 1254 (s), 1043 (s), 801 (m) cm^{-1}.

UV-vis (MeCN), λ, nm (ε, $M^{-1}\cdot cm^{-1}$) : 327 (2600), 317 (2400), 255 (4000), 216 (10500).

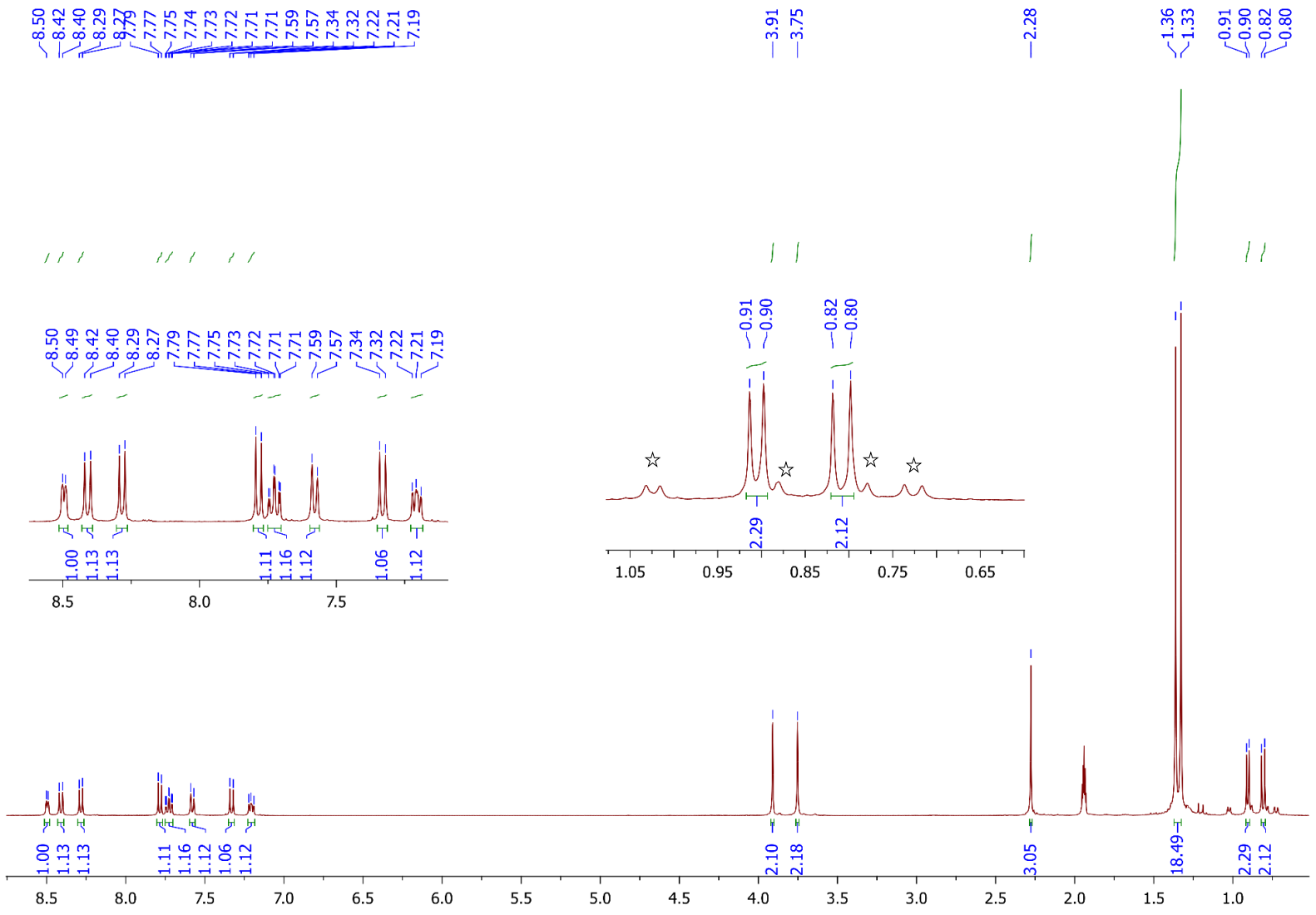

Figure S9. ^{1}H NMR spectrum of **1** in CD_3CN at 23 °C. Pt satellites are marked with stars.

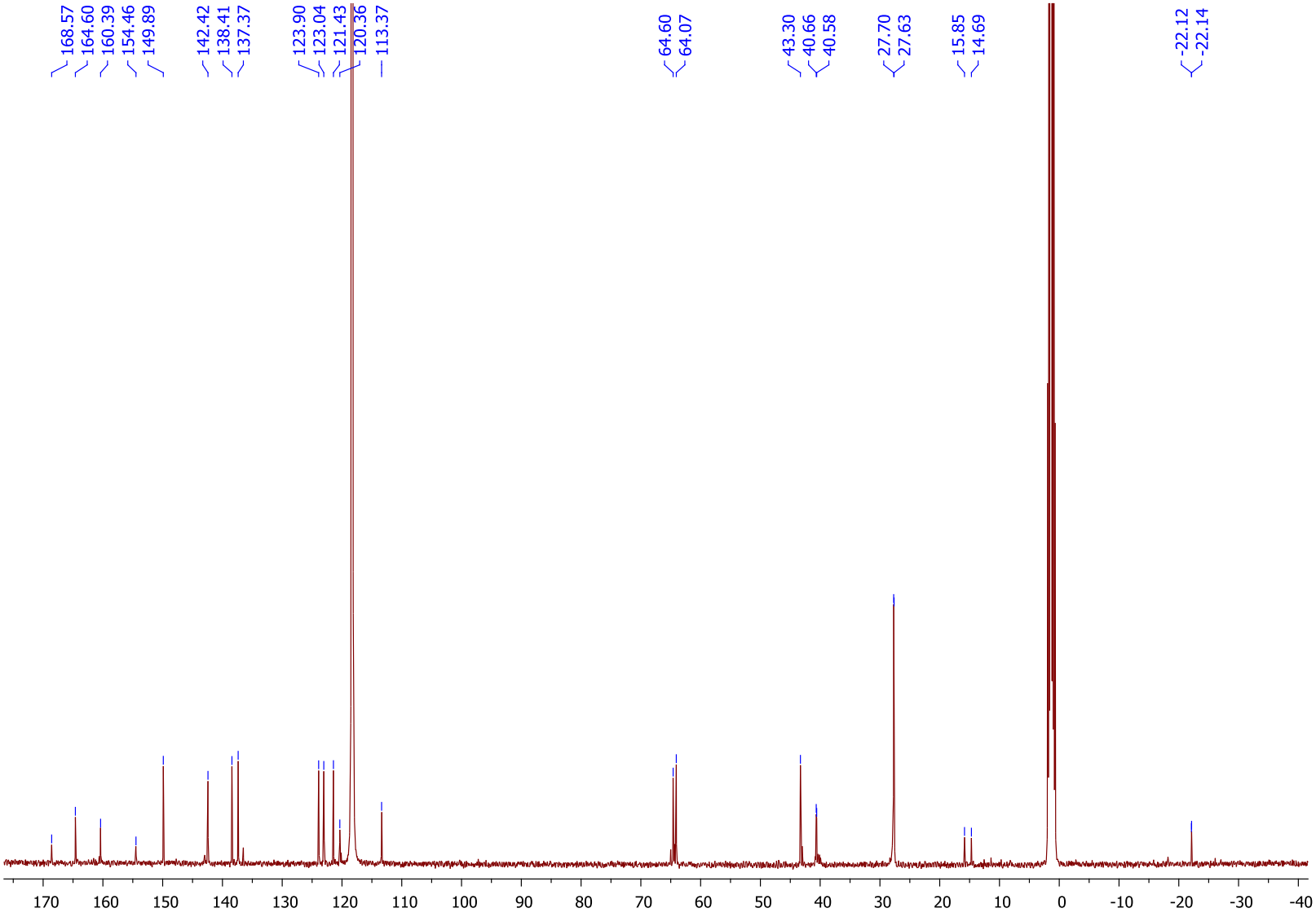

Figure S10. $^{13}C\{^{1}H\}$ NMR spectrum of **1** in CD_3CN at 23 °C.

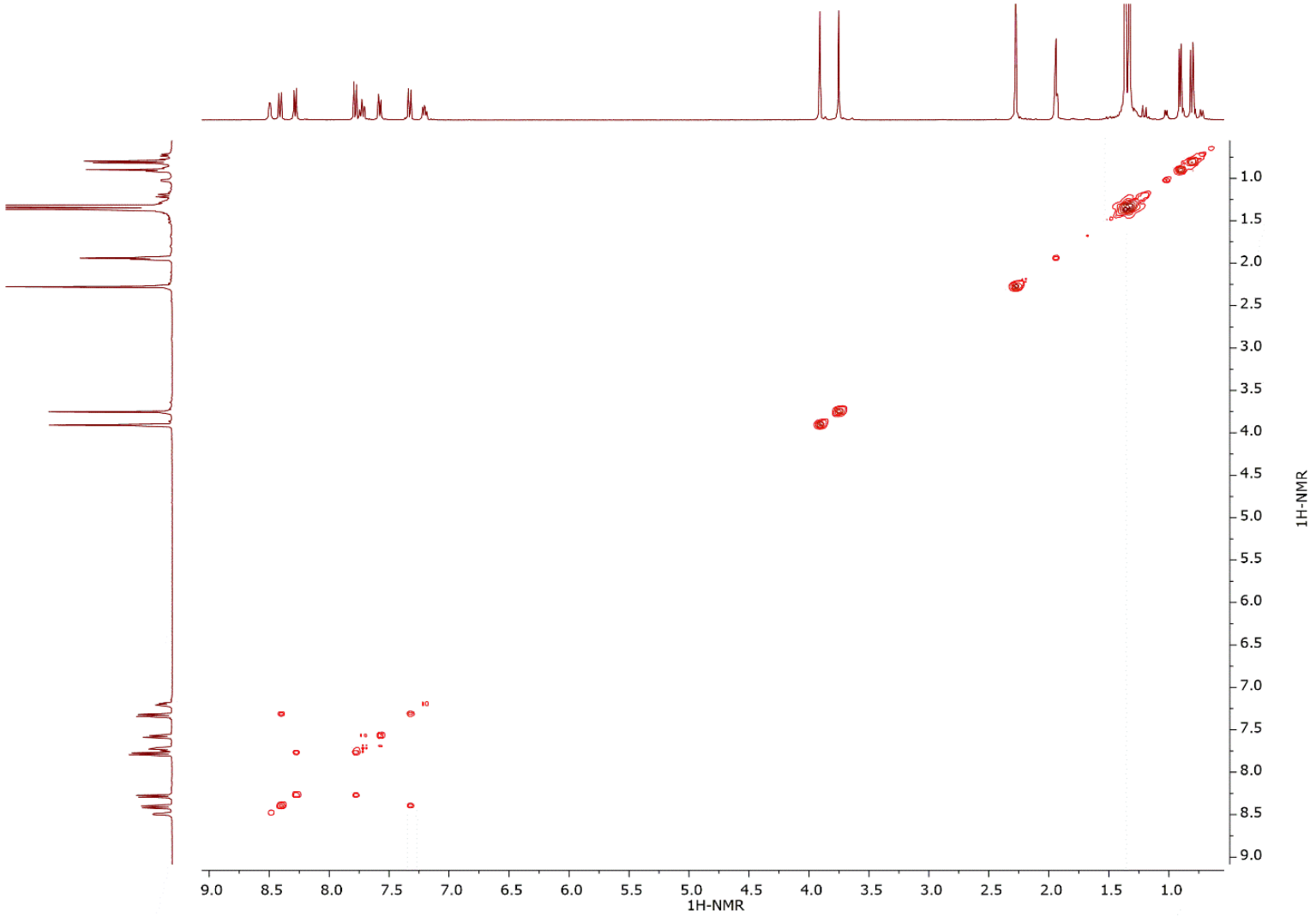

Figure S11 . ^{1}H-^{1}H COSY spectrum of **1** in CD_3CN at 23 °C.

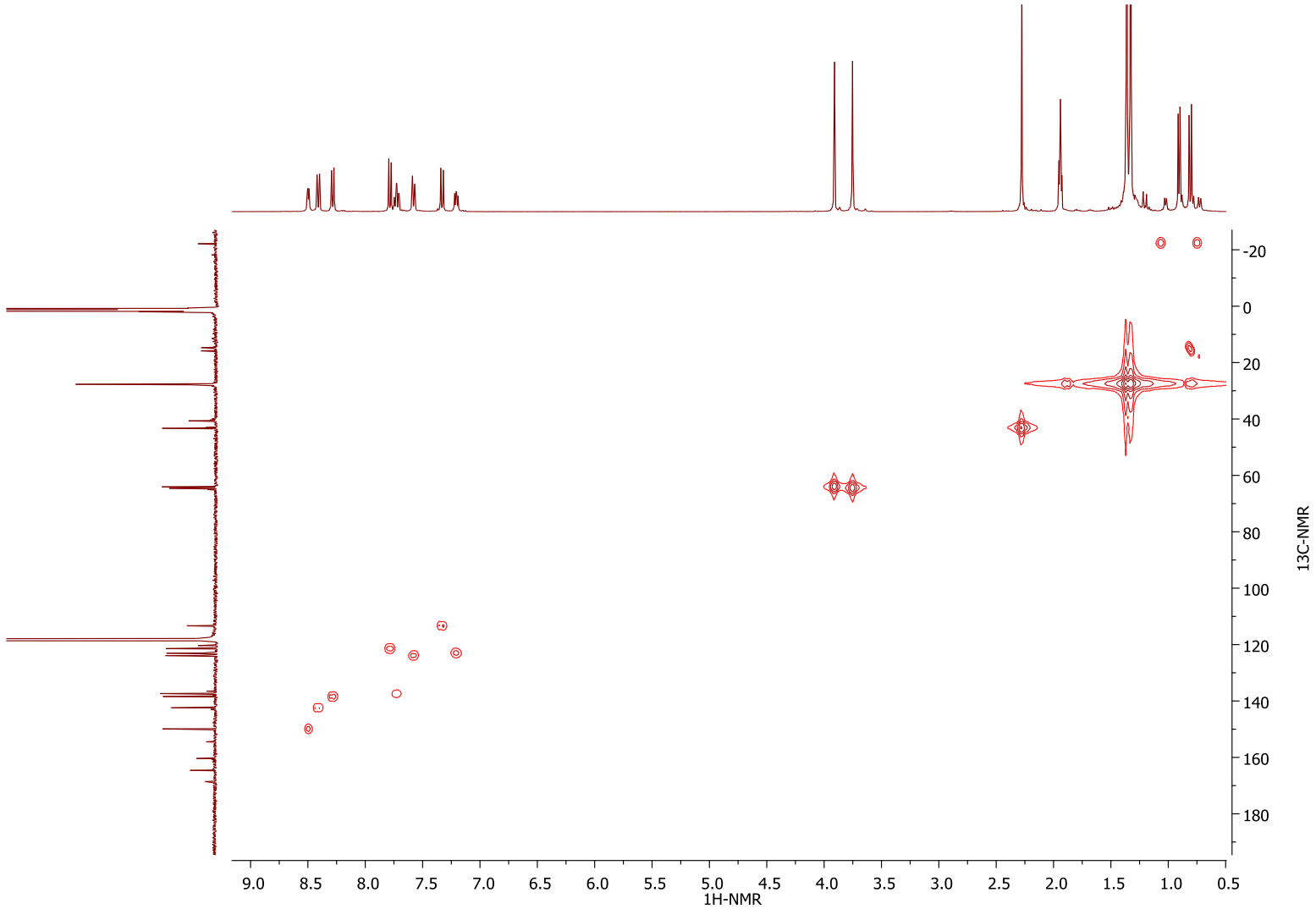

Figure S12. ^{1}H-^{13}C HMQC spectrum of **1** in CD_3CN at 23 °C.

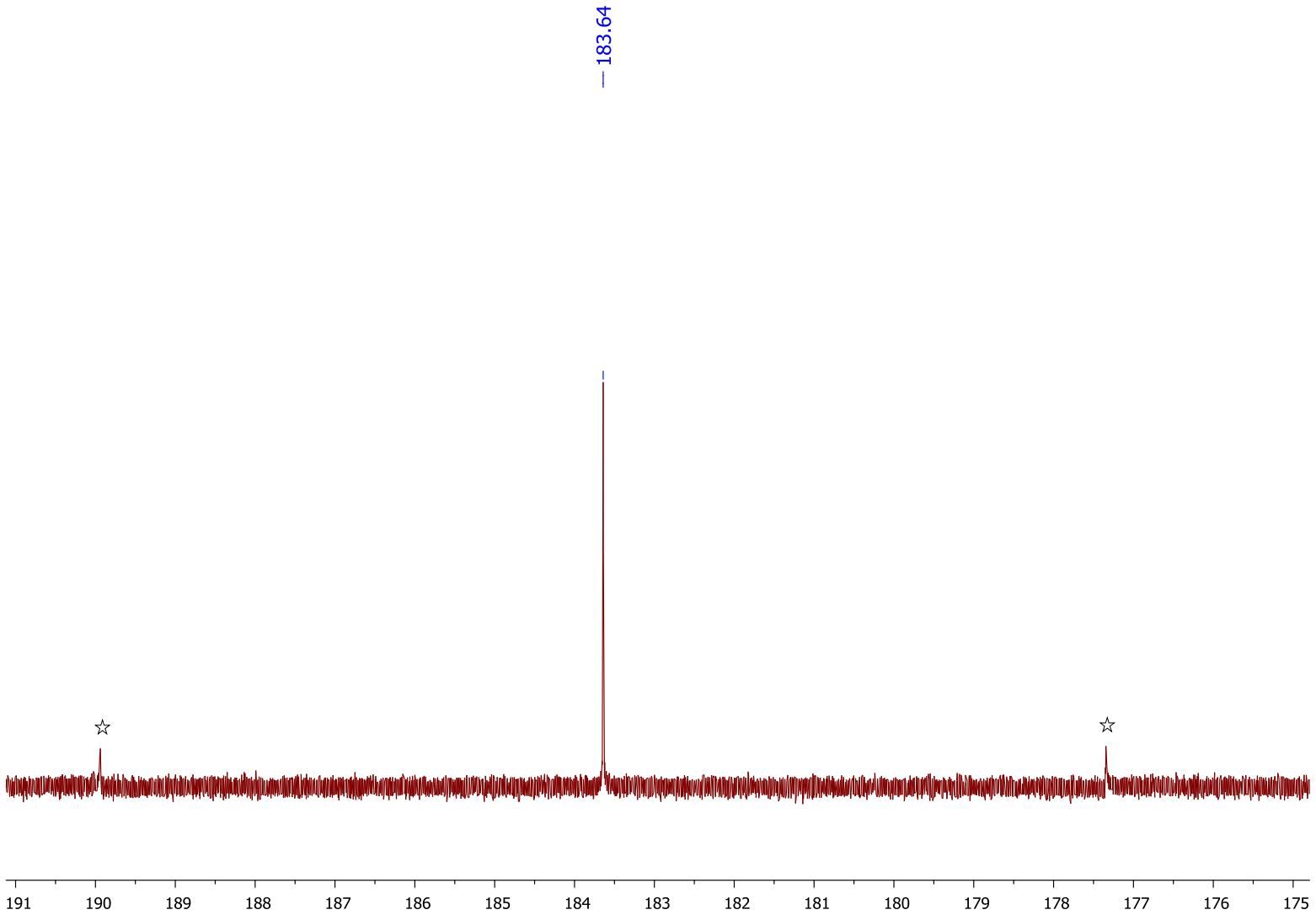

Figure S13. $^{31}P\{^{1}H\}$ NMR spectrum **1** in CD_3CN at 23 °C. Pt satellites are marked with stars.

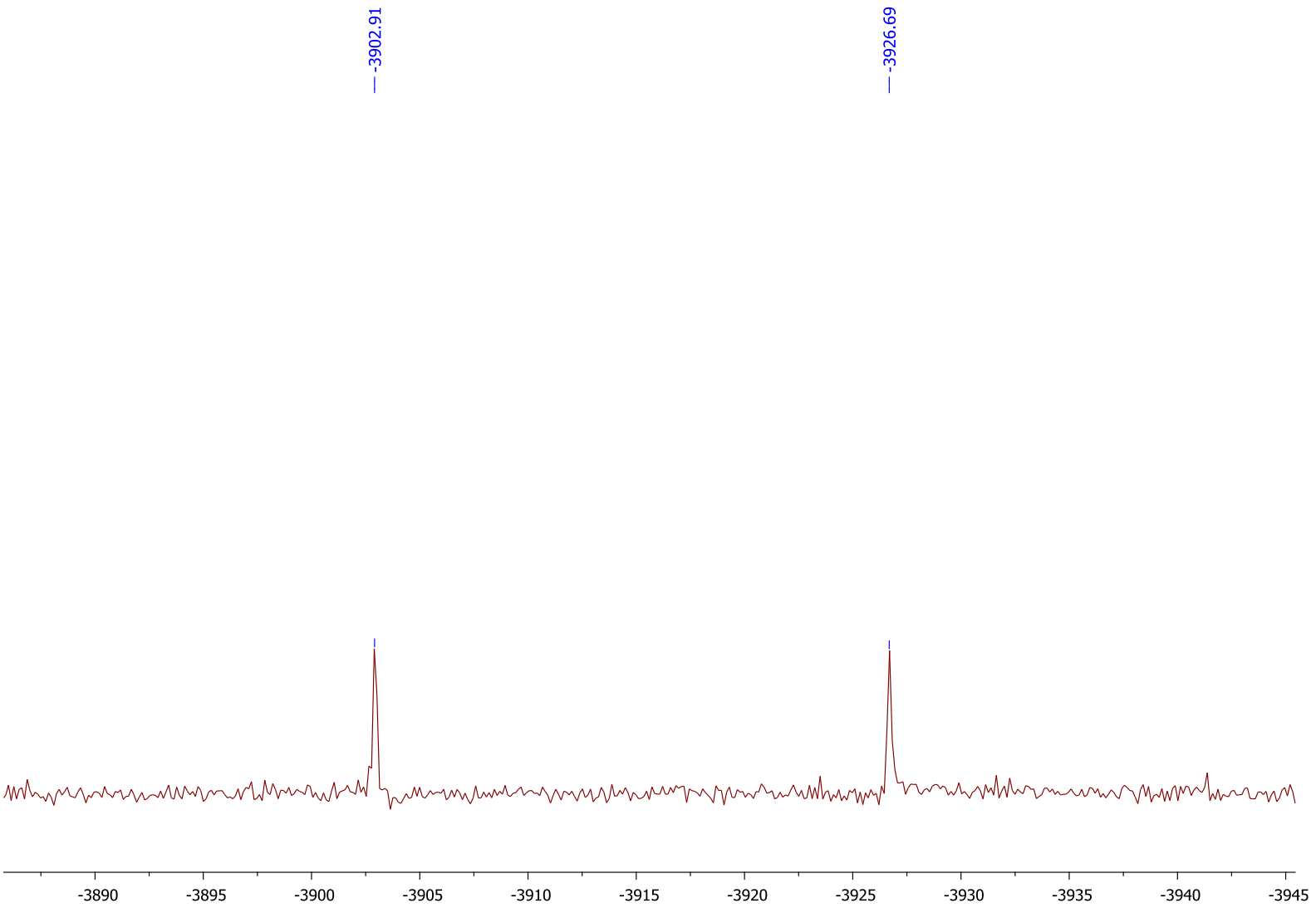

Figure S14. $^{195}Pt\{^{1}H\}$ NMR spectrum **1** in CD_3CN at 23 °C.

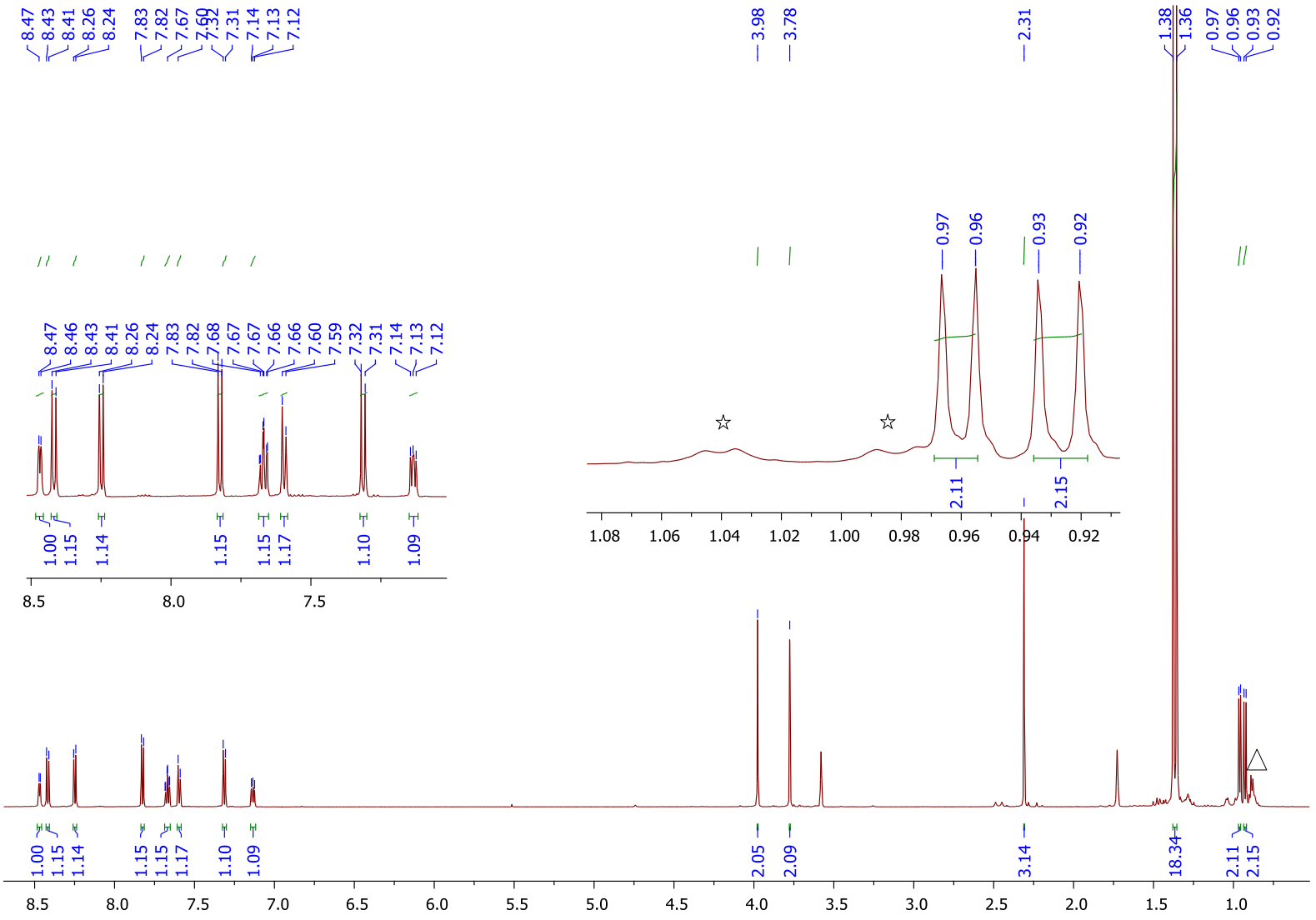

Figure S15. ^{1}H NMR spectrum of **1** in THF-d_8 at 23 °C. (Triangle symbol represents hexane). Pt satellites are marked with stars.

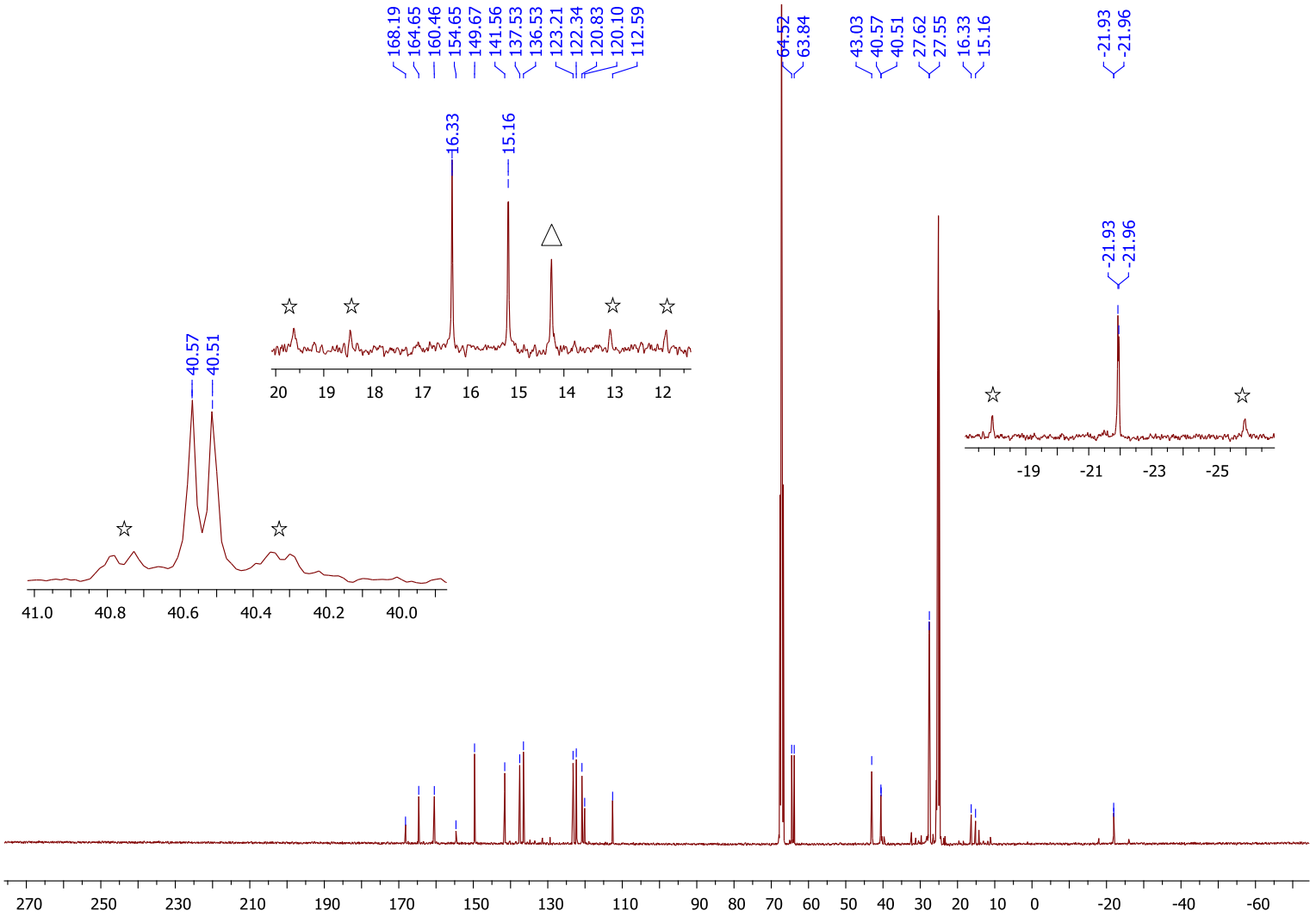

Figure S16. $^{13}C\{^{1}H\}$ NMR spectrum of **1** in THF-d_8 at 23 °C.(Triangle symbol represents hexane). Pt satellites are marked with stars.

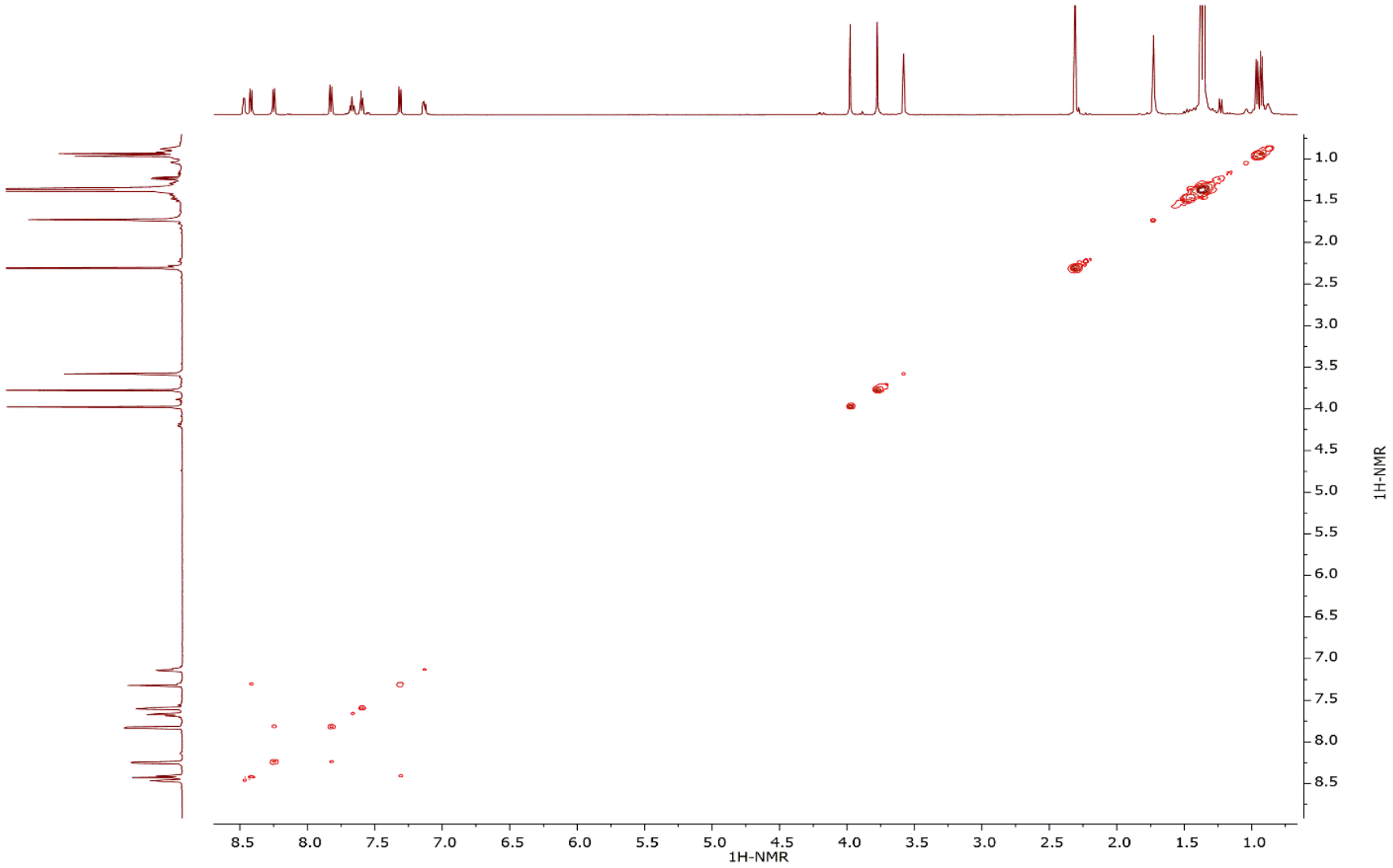

Figure S17. ^{1}H-^{1}H COSY spectrum **1** in THF-d_8 at 23 °C.

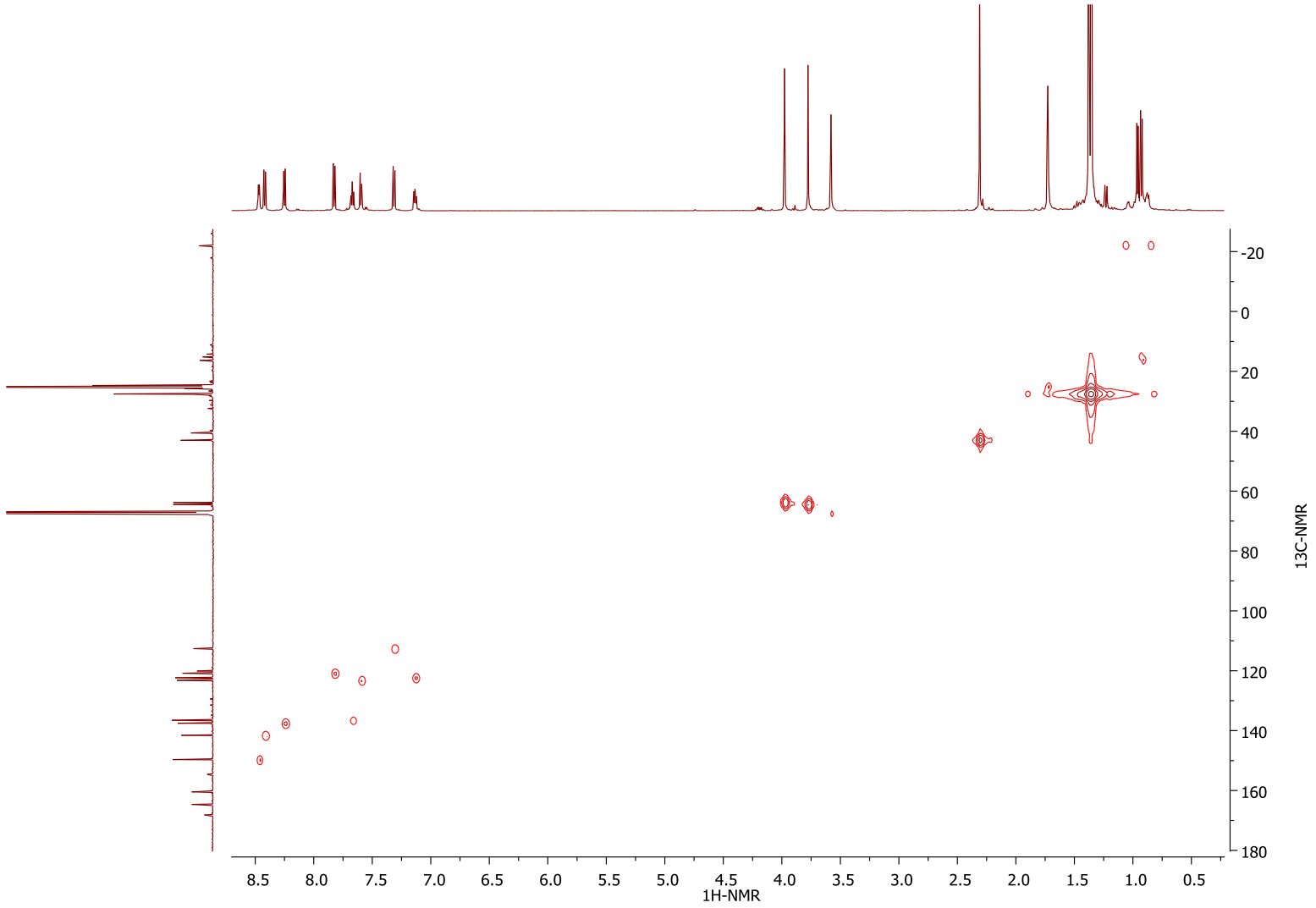

Figure S18 . ^{1}H-^{13}C HMQC spectrum **1** in THF-d_8 at 23 °C.

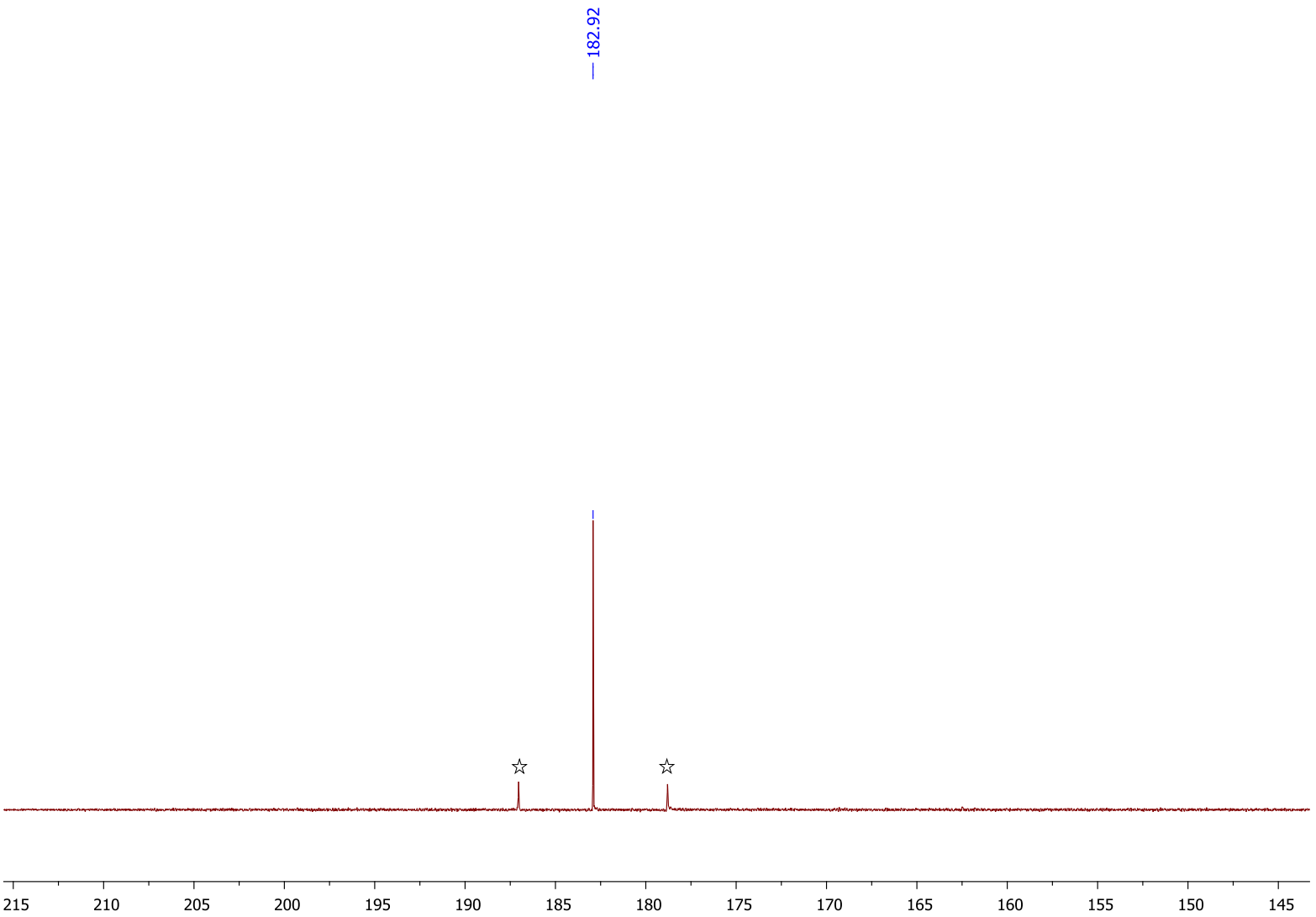

Figure S19 . ^{1}H-^{13}C HMQC spectrum **1** in THF-d_8 at 23 °C.

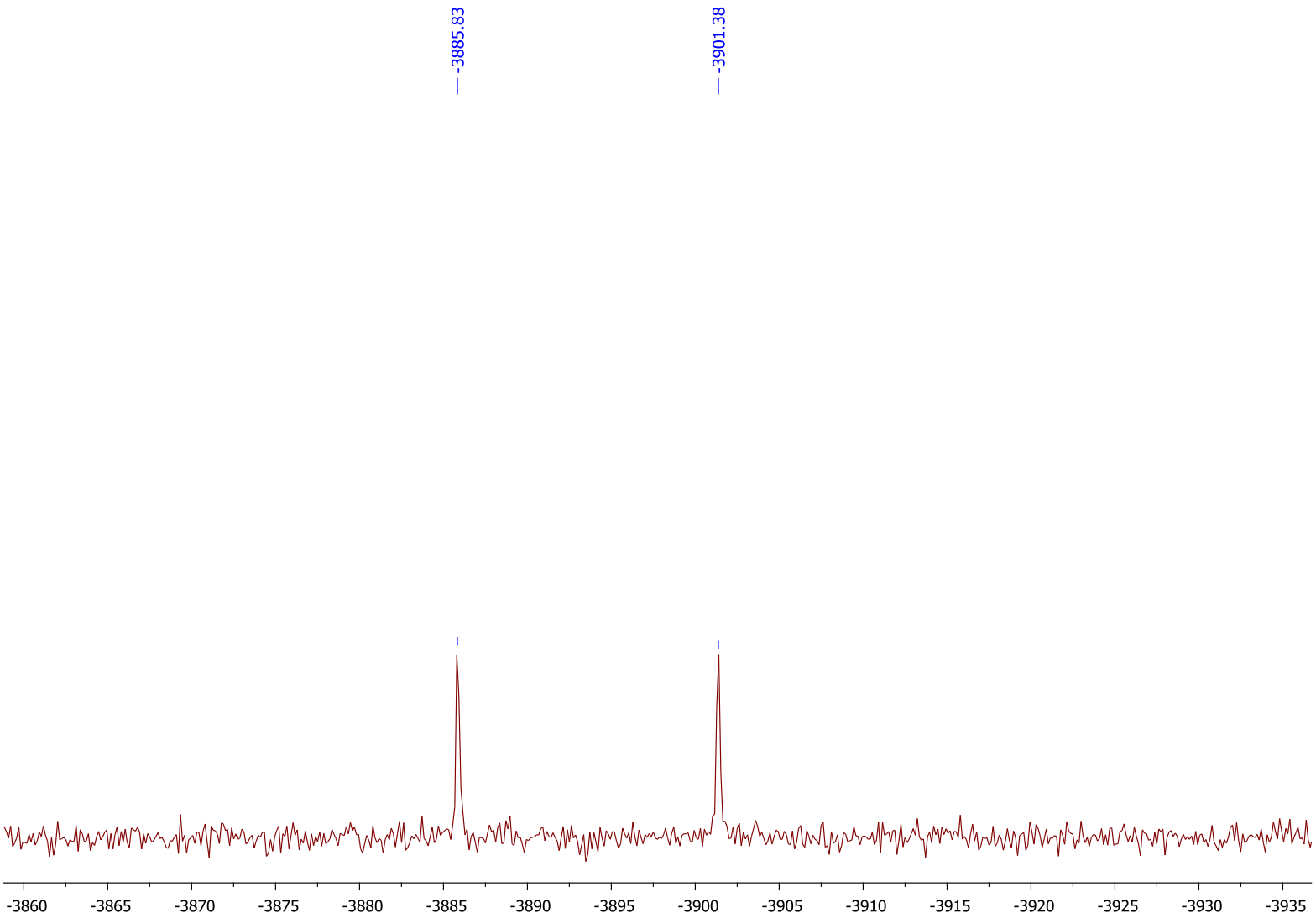

Figure S20. $^{195}Pt\{^{1}H\}$ NMR spectrum **1** in THF-d_8 at 23 °C.

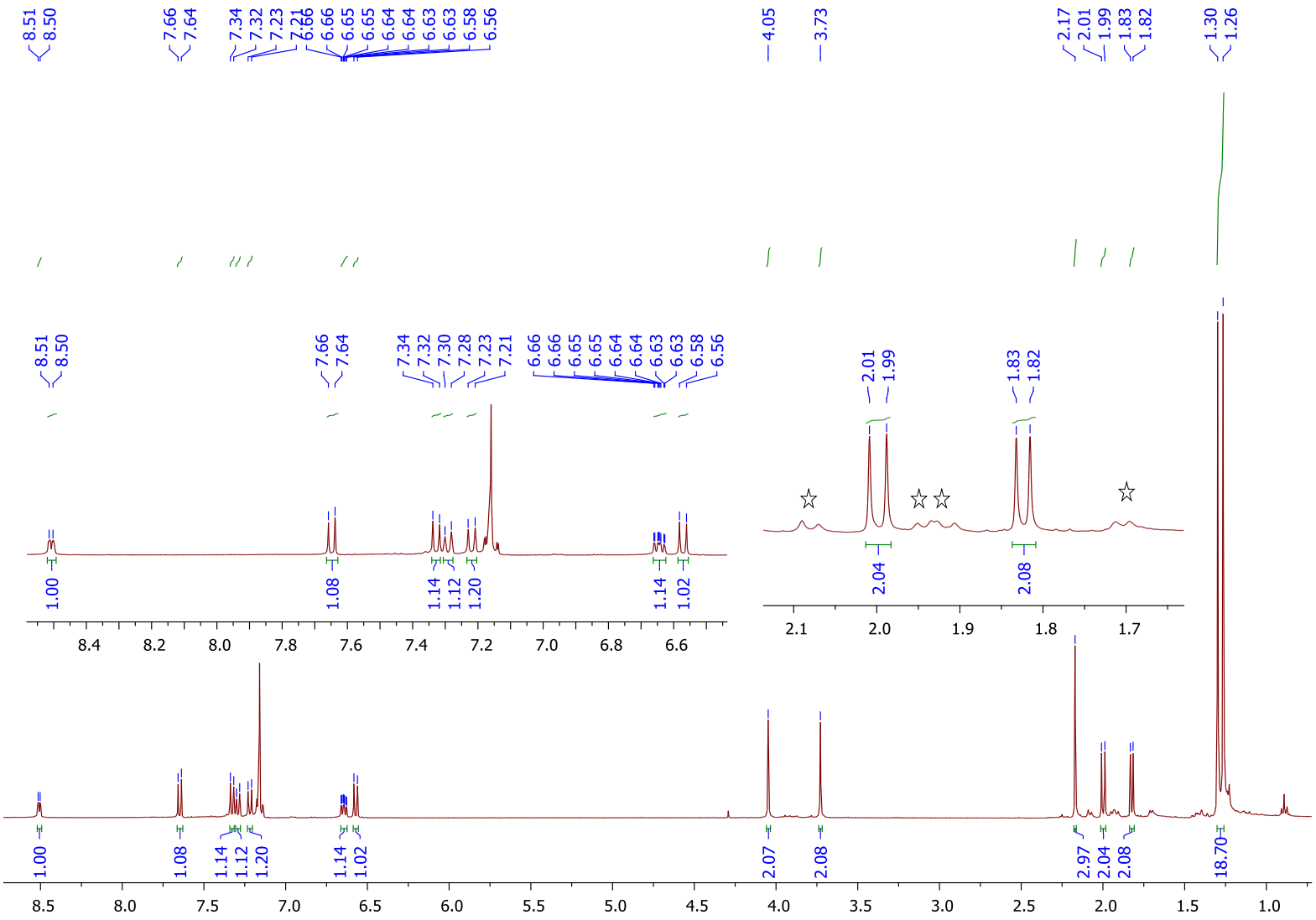

Figure S21. ^{1}H NMR spectrum of **1** in C_6D_6 at 23 °C. Pt satellites are marked with stars.

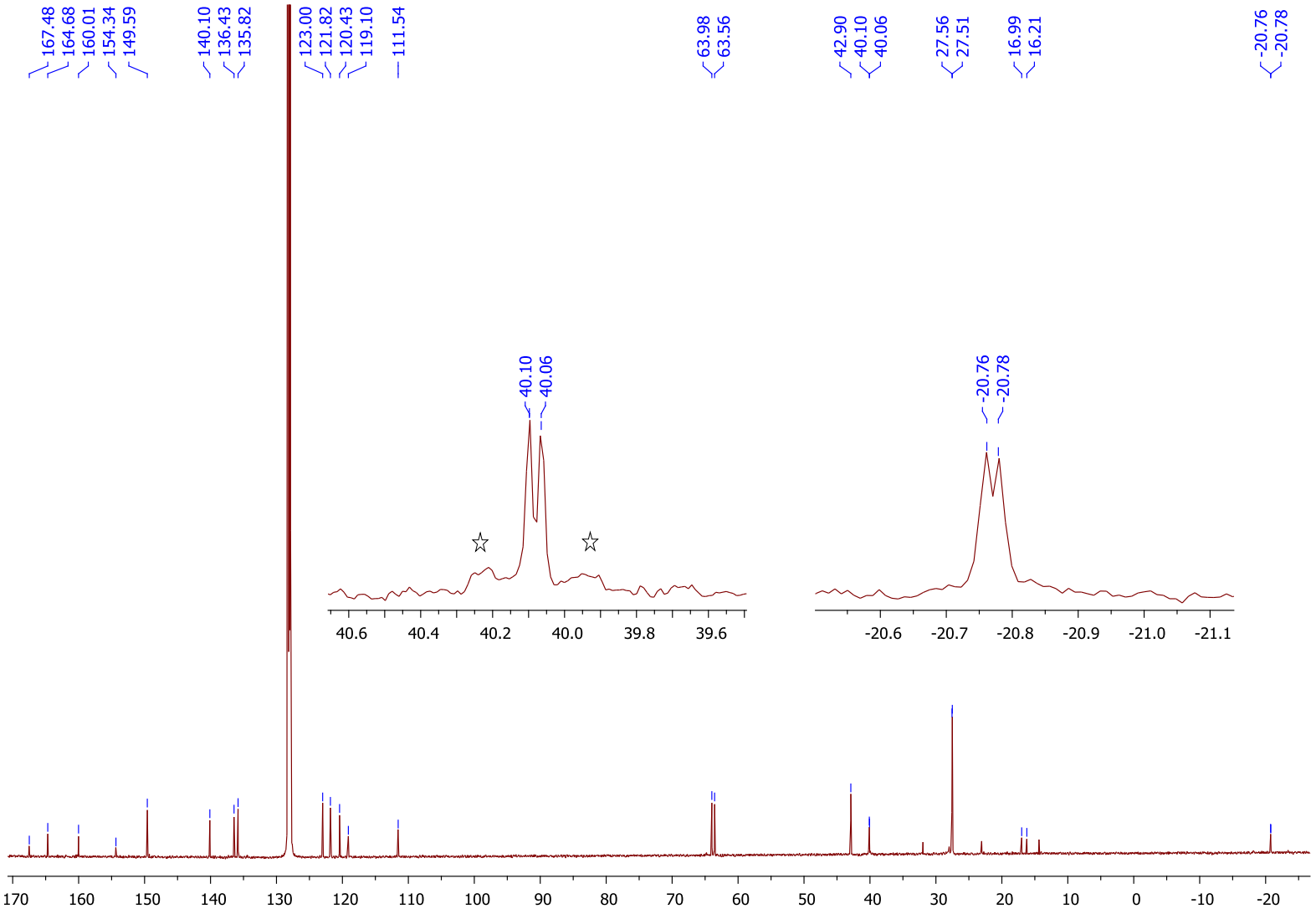

Figure S22. $^{13}C\{^{1}H\}$ NMR spectrum of **1** in C_6D_6 at 23 °C. Pt satellites are marked with stars.

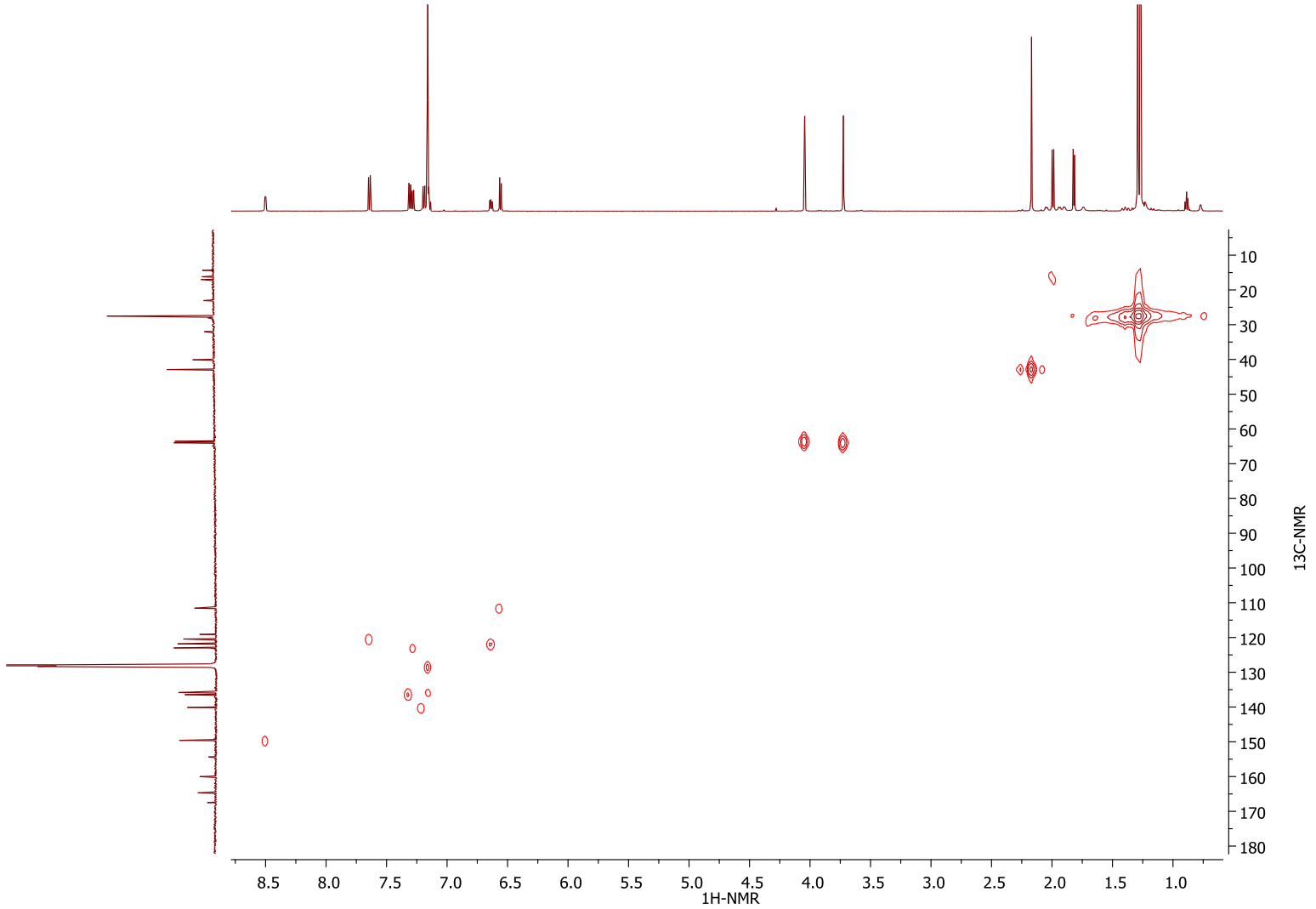

Figure S23. ^{1}H-^{13}C HMQC spectrum **1** in C_6D_6 at 23 °C.

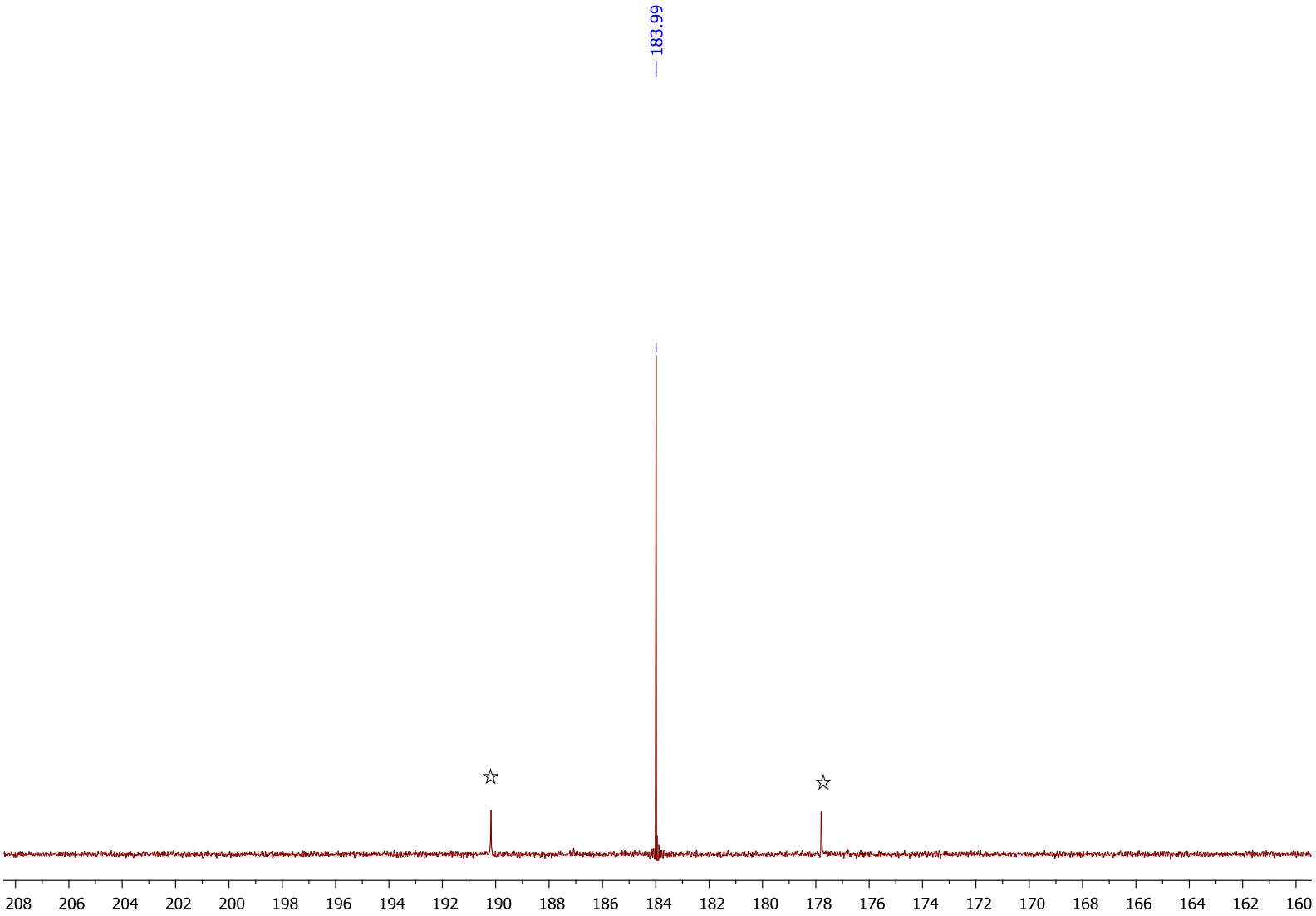

Figure S24. $^{31}P\{^{1}H\}$ NMR spectrum **1** in THF-d_8 at 23 °C. Pt satellites are marked with stars.

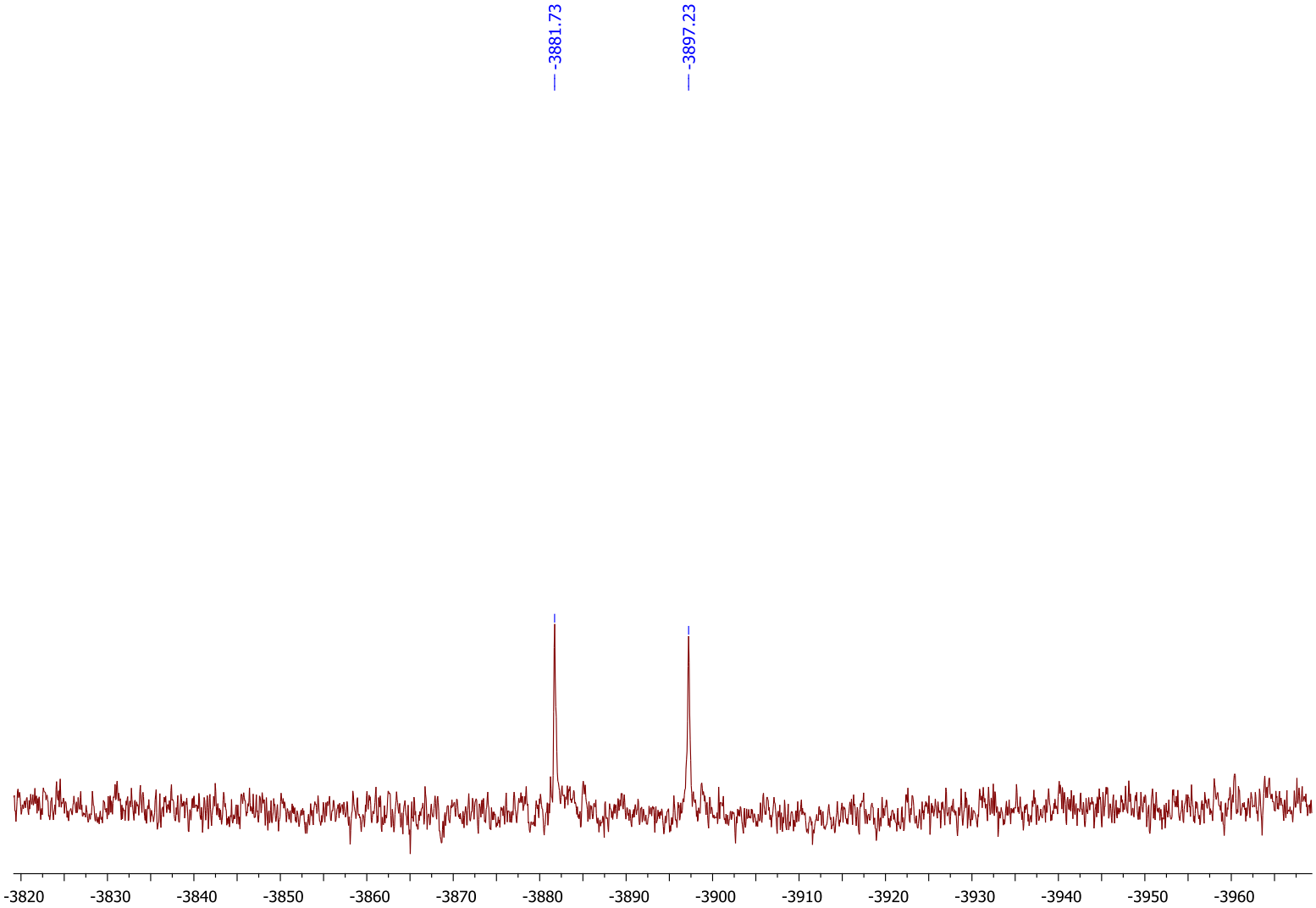

Figure S25. $^{195}Pt\{^{1}H\}$ NMR spectrum of **1** in C_6D_6 at 23 °C.

Selective 1D-difference NOE experiments of 1 in THF-d_8:

All experiments were performed using a mixing time of 1.1 s and a relaxation delay time of 7 s (if not otherwise indicated). The orientation of the methyl group relative to the *tert*-butyl group was determined by difference NOE 1D experiments. Irradiation of a resonance at 1.37 ppm ($C(CH_3)_3$) group induced enhancement (positive NOE) of a methyl group at 0.96 ppm.

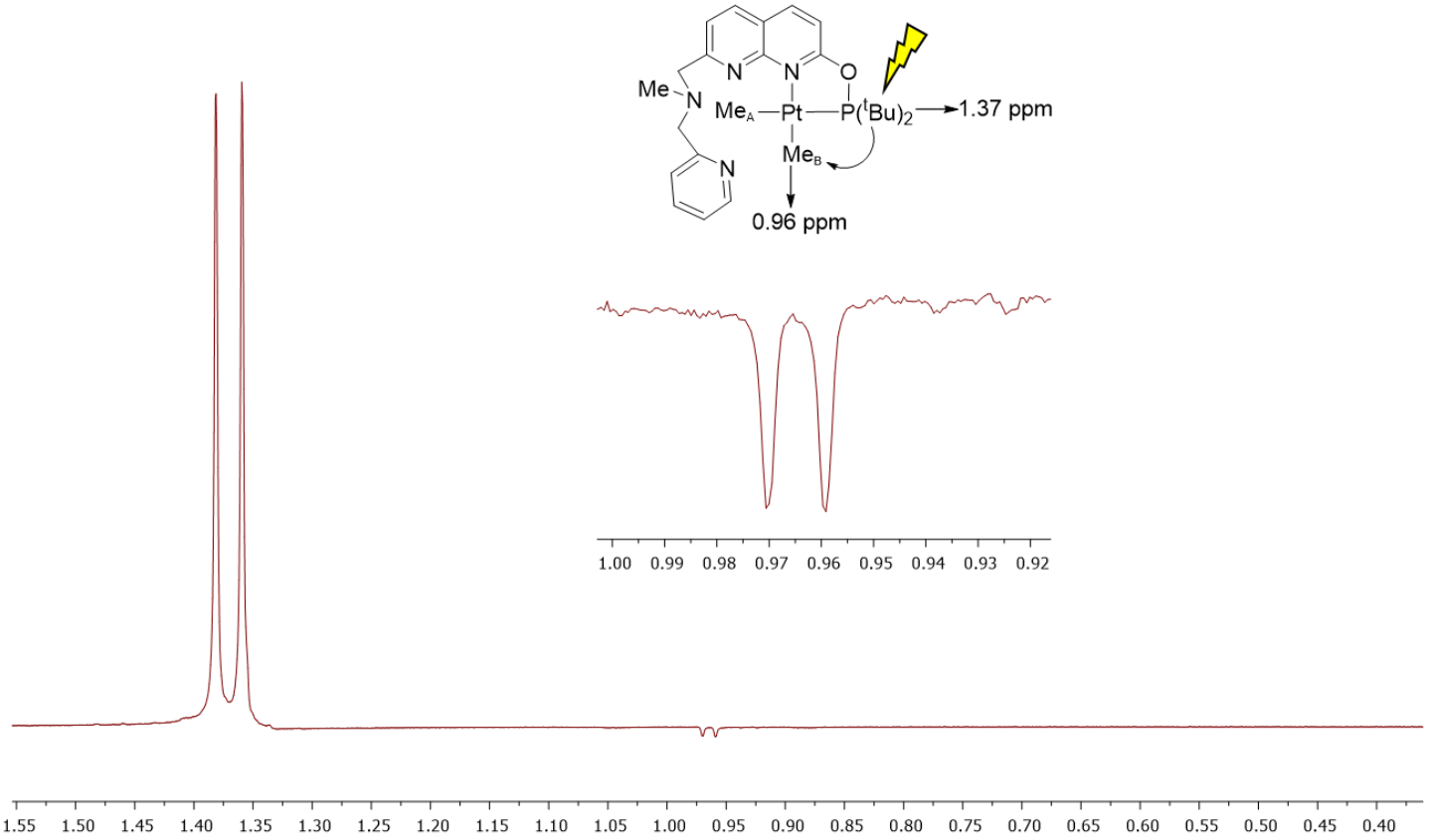

Figure S26. 1D-NOE NMR spectrum of **1** in THF-d_8 at 23 °C.

Selective 1D-difference NOE experiments of 1 in C_6D_6:

The orientation of the methyl group relative to the *tert*-butyl group was determined by difference NOE 1D experiments. Irradiation of a resonance at 1.82 ppm (Pt-methyl group) induced enhancement (positive NOE) of a ($C(CH_3)_3$) at 1.28 ppm and another methyl group at 2 ppm. In another experiment, irradiation of a resonance at 2 ppm methyl group induced enhancement (positive NOE) of on a methyl group at 1.82 ppm and no NOE to the ^{t}Bu group.

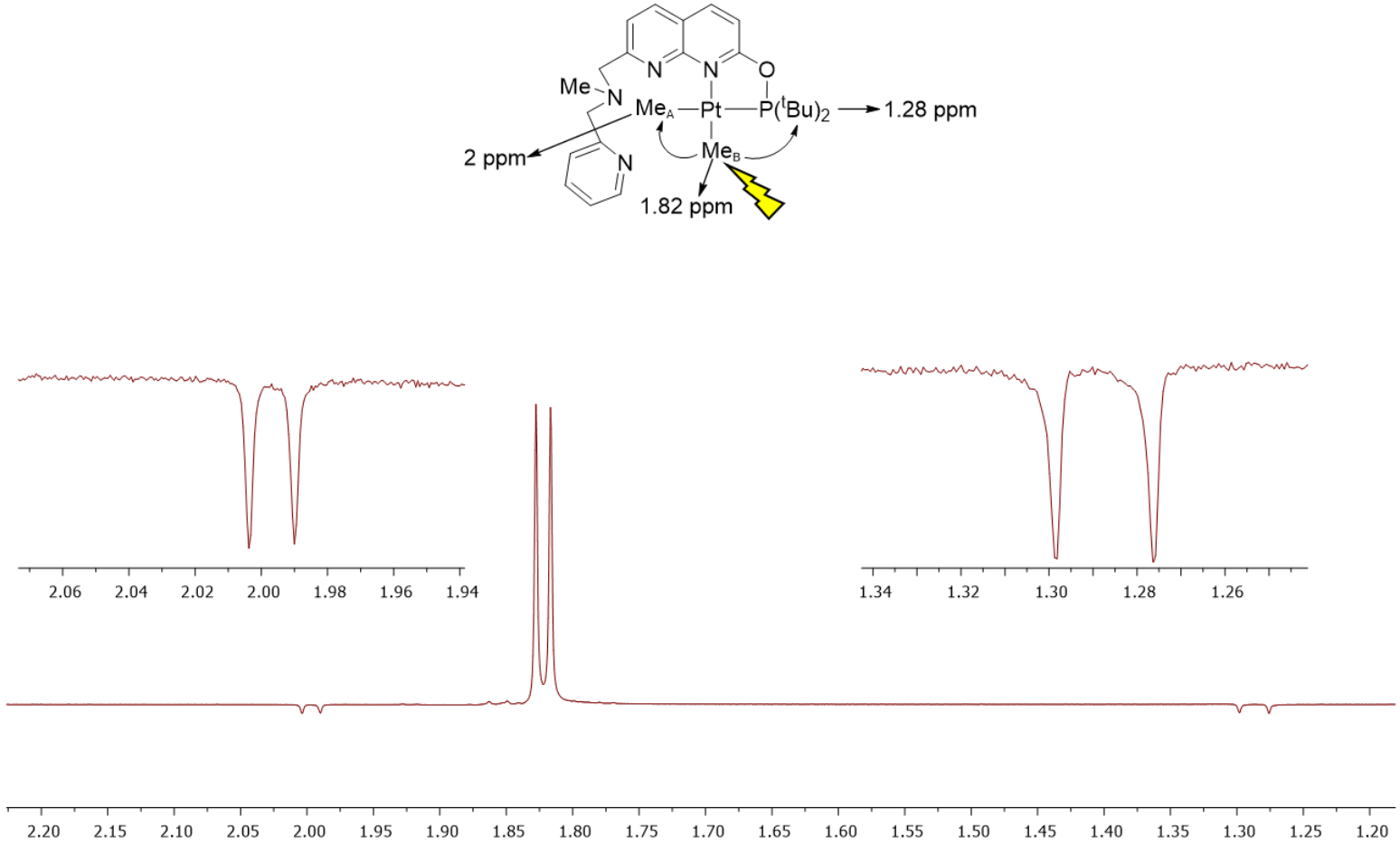

Figure S27. 1D-NOE NMR spectrum of **1** in C_6D_6 at 23 °C.

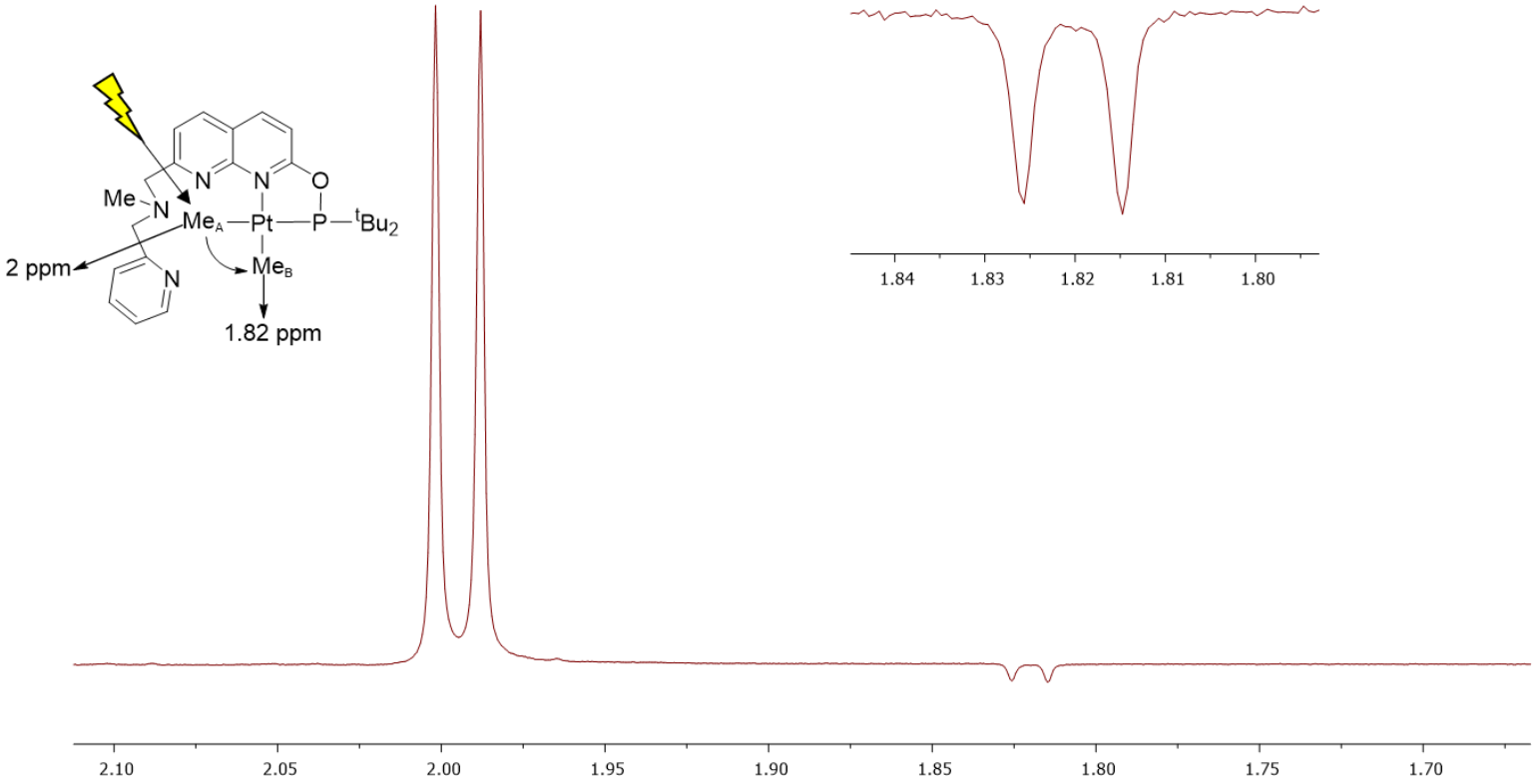

Figure S28. 1D-NOE NMR spectrum of **1** in C_6D_6 at 23 ℃.

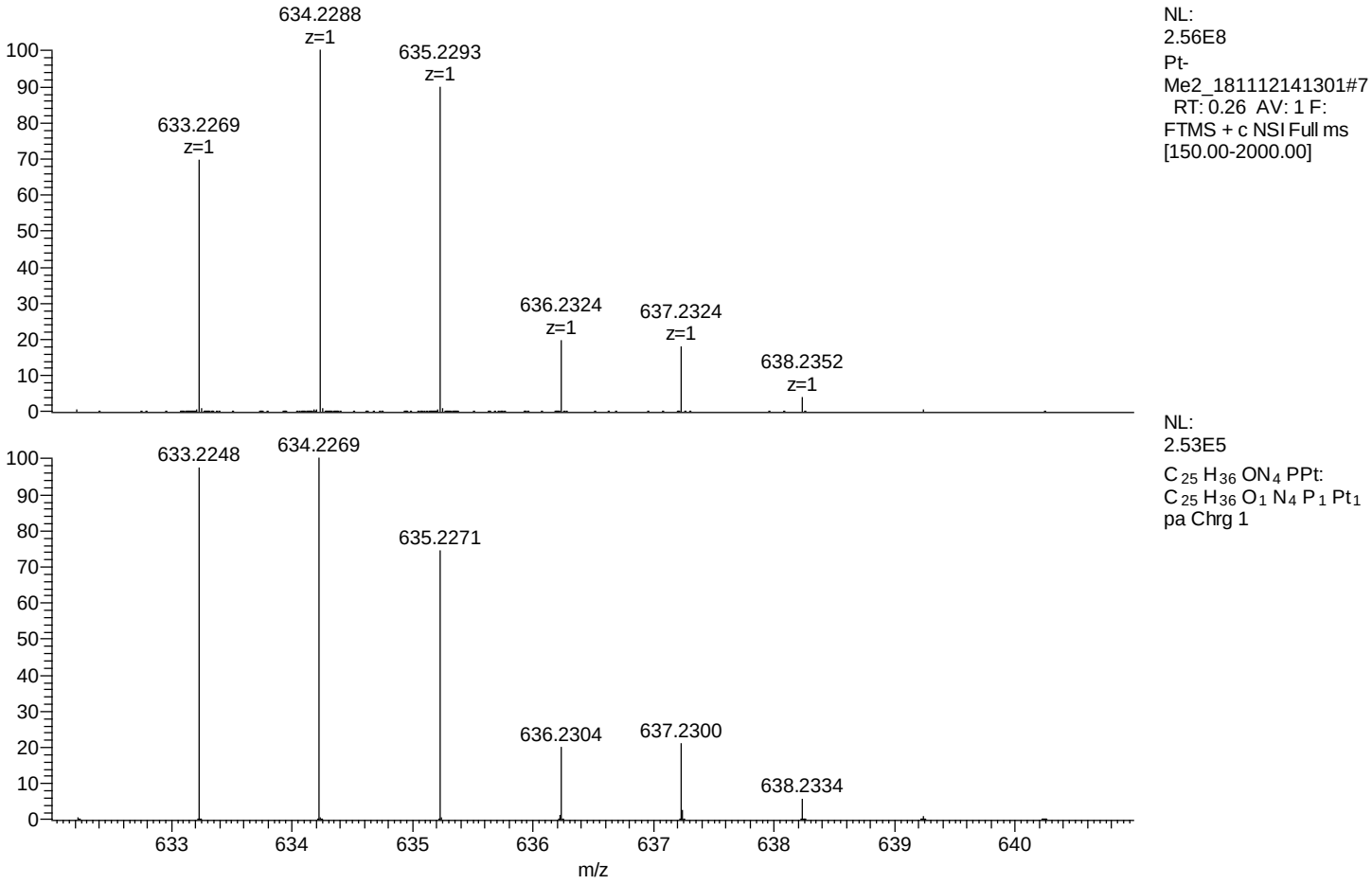

Figure S29. ESI-(HR)MS spectrum of a MeCN solution of **1** (top) and simulated spectrum for $C_{25}H_{36}ON_4PPt^+$ (bottom)

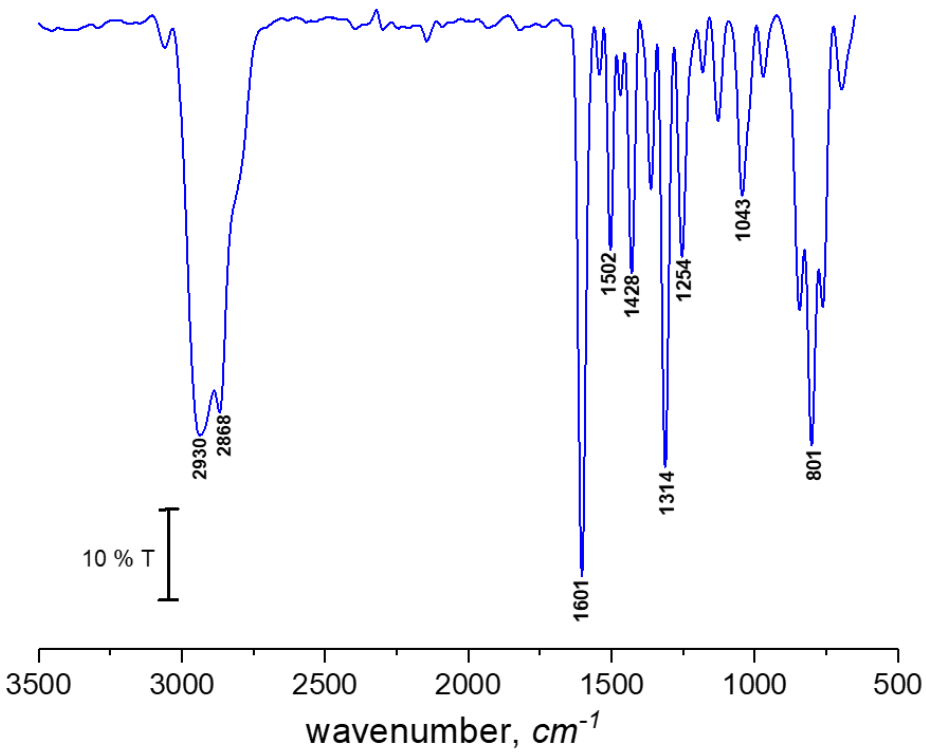

Figure S30. ATR FT-IR transmittance spectrum of **1**.

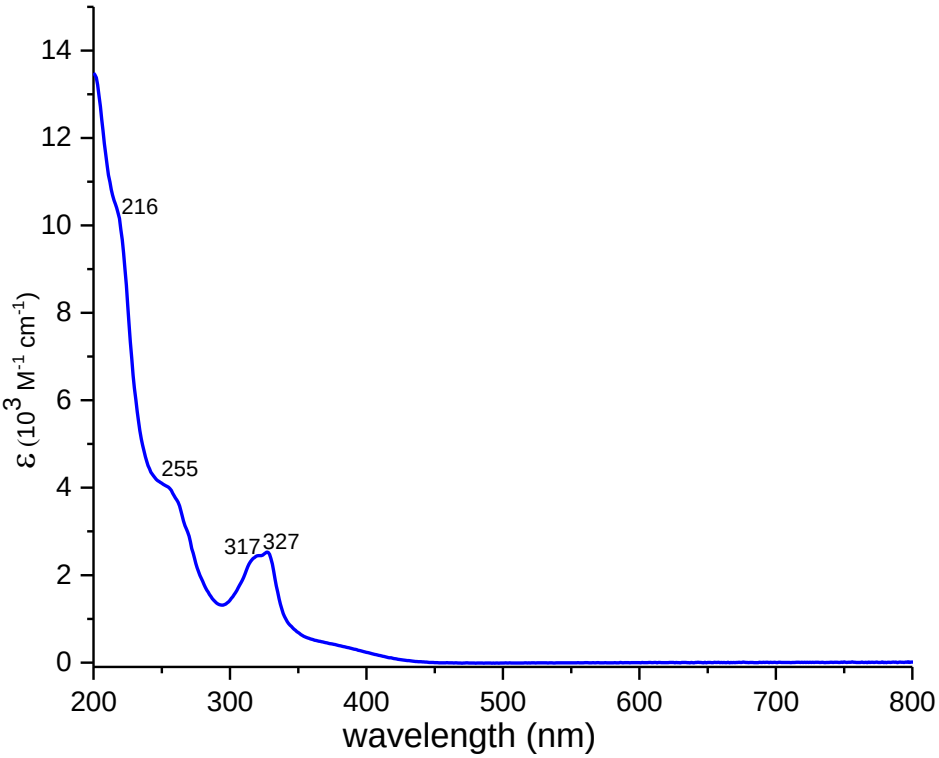

Figure S31. UV-vis absorbance spectrum for **1** in MeCN.

Synthesis of [(L)PtMe$_3$]I, 2

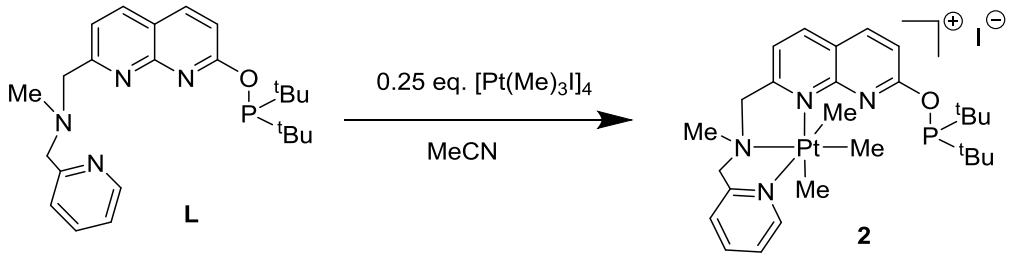

Scheme **S3.** Formation of **2**.

[PtMe$_3$I]$_4$ (86.9 mg, 0.059 mmol) and **L** (100.6 mg, 0.2369 mmol) were dissolved in acetonitrile (4 mL) in a 20 mL vial to give a yellow color solution. The reaction was stirred for 30 minutes. Then the solution was dried under vacuum and the yellow color oil was dissolved in the minimum amount of benzene (1 mL); hexane (5 mL) was added until the precipitate appears.The solution was then decanted and the solid was dried under vacuum to yield a yellow solid (110.4 mg, 0.1394 mmol, 58% yield). Crystals suitable for X-ray diffraction study were obtained at RT vapor diffusion of pentane into a benzene solution.

^{1}H NMR (400 MHz, CD_3CN, 23 °C) δ: 9 (br m, 1H, CH_{Py}), 8.45 (d, $^3J_{HH}$ = 8.2 Hz, 1H, CH_{Naph}), 8.30 (d, $^3J_{HH}$ = 8.8 Hz, 1H, CH_{Naph}), 7.92 (td, $^3J_{HH}$ = 7.8 Hz, $^4J_{HH}$ = 1.5 Hz, 1H, CH_{Py}), 7.61 (d, $^3J_{HH}$ = 8.2 Hz, 1H, CH_{Naph}), 7.56 (t, $^3J_{HH}$ = 6.2 Hz, 1H, CH_{Py}), 7.44 (d, $^3J_{HH}$ = 7.8 Hz, 1H, CH_{Py}), 7.24 (d, $^3J_{HH}$ = 8.8 Hz, 1H, CH_{Naph}), 4.85 (m, 2H, CH_2), 4.31 (m, 2H, CH_2), 2.89 (s, $^3J_{PtH}$ = 15.6 Hz, 3H, N-CH_3), 1.81 (s, $^2J_{PtH}$ = 70.5 Hz, 3H, Pt-Me), 1.26 (d, $^3J_{PH}$ = 11.8 Hz, 9H, $C(CH_3)_3$), 1.01 (d, $^3J_{PH}$ = 11.8 Hz, 9H, $C(CH_3)_3$), 0.71 (s, $^2J_{PtH}$ = 72.4 Hz, 3H, Pt-Me), 0.48 (s, $^2J_{PtH}$ = 68.8 Hz, 3H, Pt-Me).

^{13}C{^{1}H} NMR (101 MHz, CD_3CN, 23 °C) δ: 166.93 (d, 1C, $^2J_{PC}$ = 8.2 Hz, $C_{q,Naph}$), 163.21 ($C_{q,Naph}$), 161.07 ($C_{q,Py}$), 154.80 ($C_{q,Naph}$), 148.29 ($C_{H,Py}$), 141.80 ($C_{H,Naph}$), 141.55 ($C_{H,Naph}$), 139.96 ($C_{H,Py}$), 126.12 ($C_{H,Py}$), 123.80 ($C_{H,Py}$), 121.70 ($C_{q,Naph}$), 120.44 ($C_{H,Naph}$), 117.22 ($C_{H,Naph}$), 69.09 (CH_2), 67.39 (CH_2), 47.63 (N-CH_3), 36.54 (d, $^1J_{P-C}$ = 30 Hz, ***C***$(CH_3)_3$), 35.97 (d, $^1J_{PC}$ = 27.8 Hz, ***C***$(CH_3)_3$), 27.60 (d, $^2J_{PC}$ = 16.2 Hz, C(***C***$H_3)_3$), 27.36 (d, $^2J_{PC}$ = 16.6 Hz, C(***C***$H_3)_3$), -3.14 (s, $^1J_{PtC}$ = 705 Hz, Pt-Me), -6.97 (s, $^1J_{PtC}$ = 682 Hz, Pt-Me). One Pt-Me group overlaps with CD_3CN as confirmed by HMQC spectrum.

^{31}P{^{1}H} NMR (242 MHz, CD_3CN, 23 °C) δ: 153.4.

^{195}Pt{^{1}H} NMR (129 MHz, CD_3CN, 23 °C) δ: -2320.9.

Elemental Analysis: Expt (Calc): [$C_{27}H_{42}N_4OIPPt$]: C 41.07 (40.97), H 5.48 (5.35), N 7.05 (7.08).

ESI-HRMS (m/z pos): Found (Calcd): $C_{27}H_{42}ON_4P^{195}Pt^+$: 664.2743 (664.2738).

FT-IR (ATR, solid): 2982 (br, w), 2896 (br, w), 1671 (s), 1603 (s), 1437 (m), 1255 (m), 1061 (s), 861 (s), 763 (m) cm^{-1}.

UV-vis (MeCN), λ, nm (ε, $M^{-1}\cdot cm^{-1}$) : 330 (2750), 243 (6600), 207 (14600).

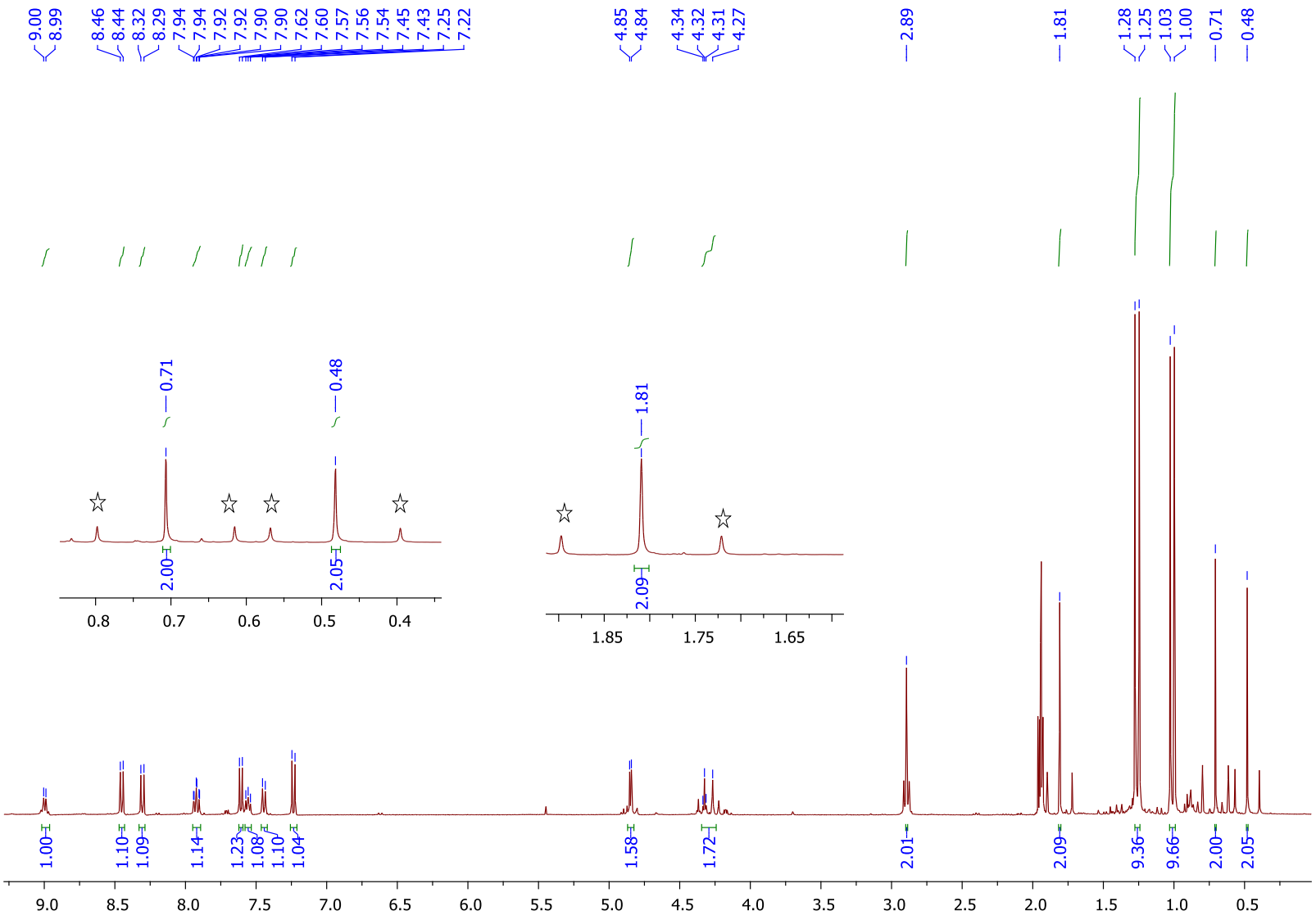

Figure S32. ^{1}H NMR spectrum of **2** in CD_3CN at 23 °C. Pt satellites are marked with stars.

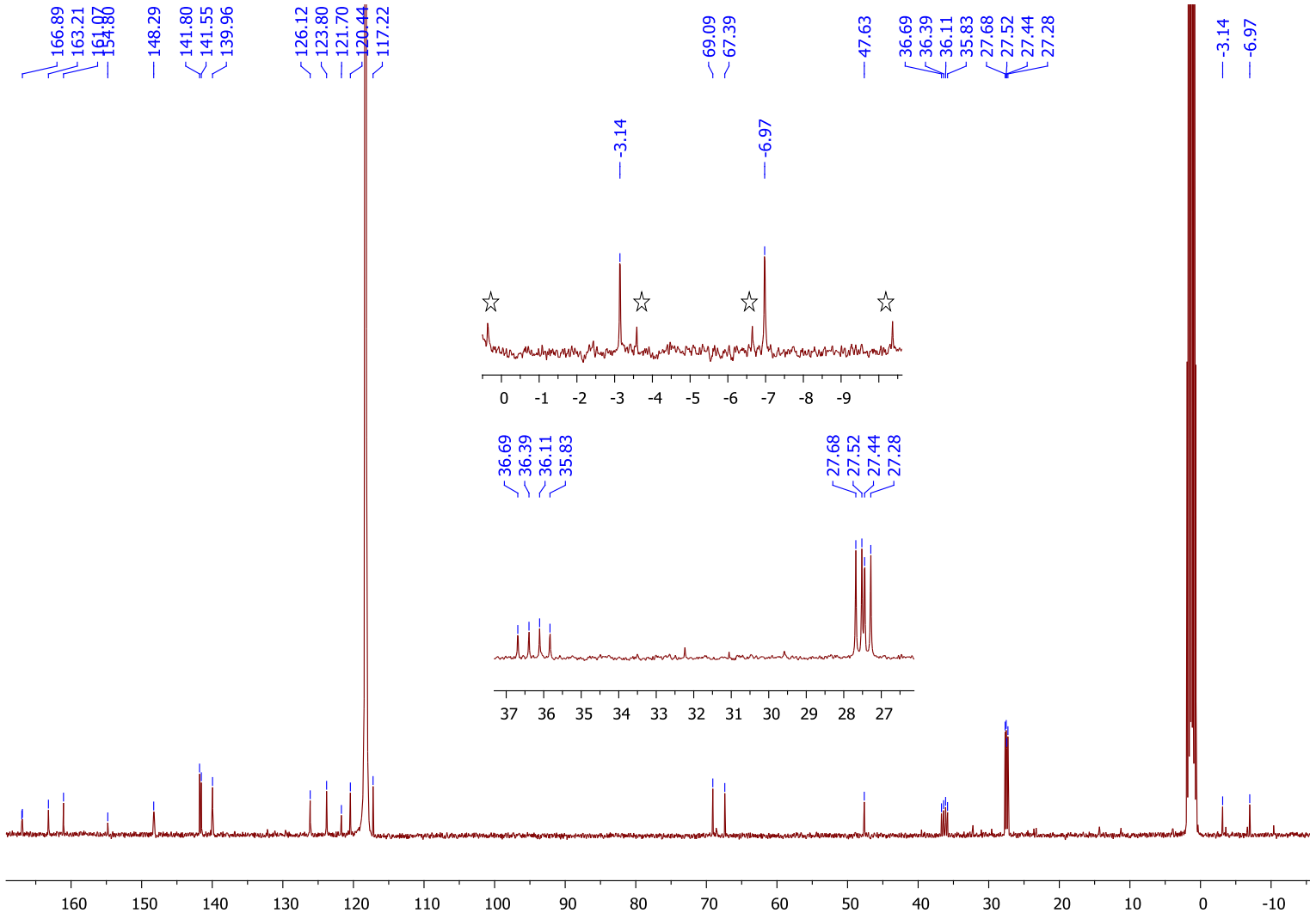

Figure S33. $^{13}C\{^{1}H\}$ NMR spectrum of **2** in CD_3CN at 23 °C. Pt satellites are marked with stars.

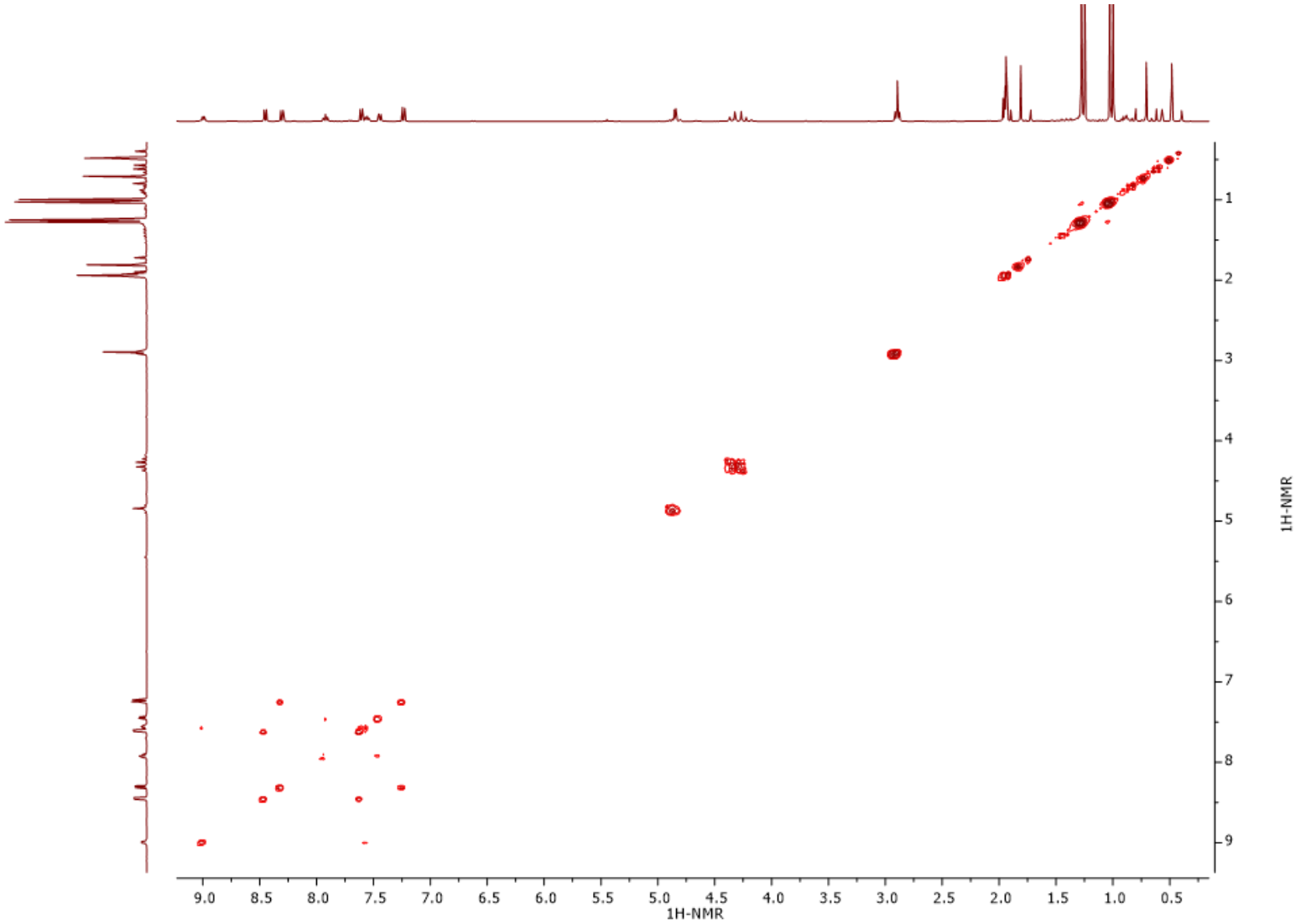

Figure S34. ^{1}H-^{1}H COSY spectrum of **2** in CD_3CN at 23 °C.

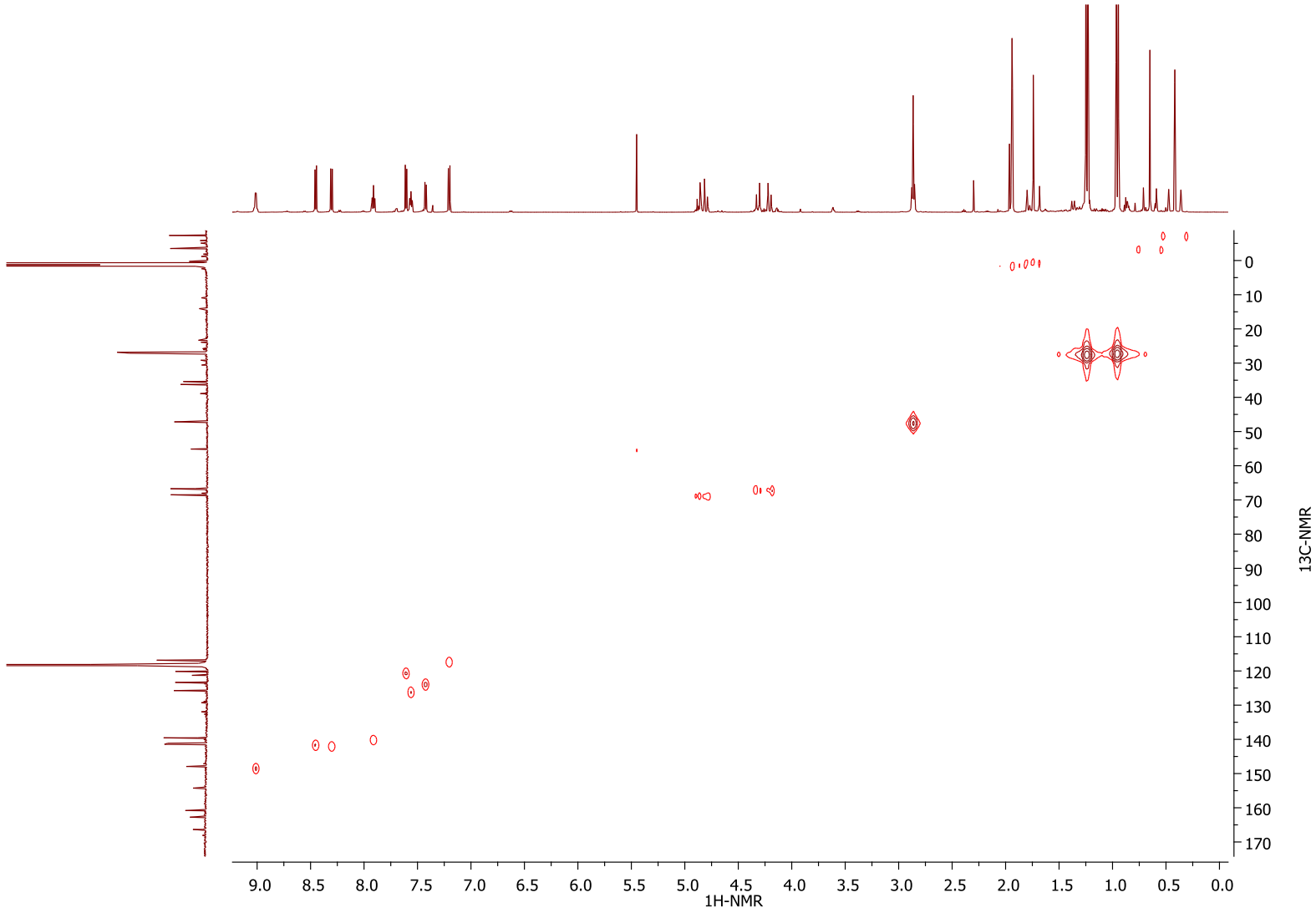

Figure S35. ^{1}H-^{13}C HMQC spectrum of **2** in CD_3CN at 23 °C.

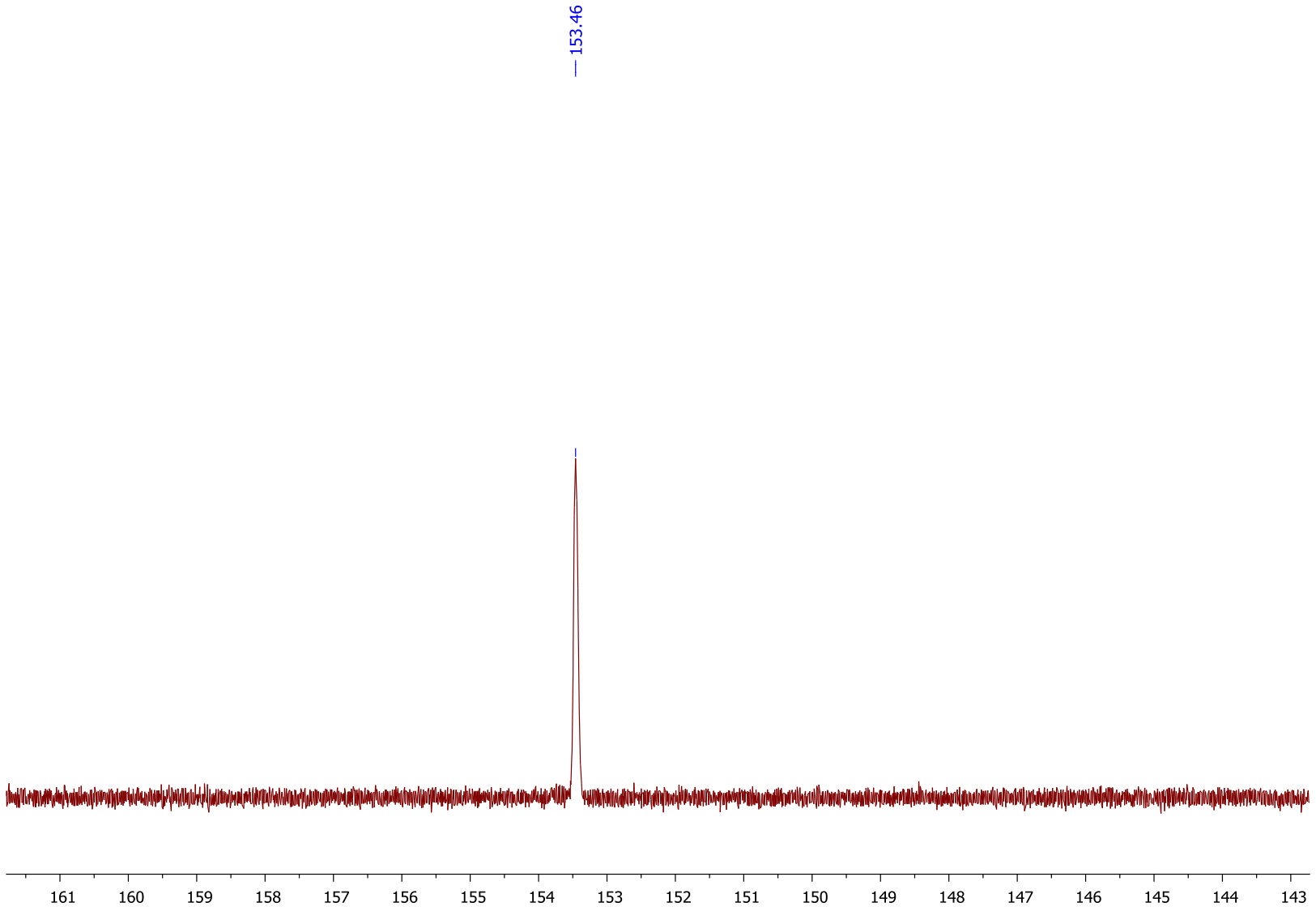

Figure S36. $^{31}P\{^{1}H\}$ NMR spectrum of **2** in CD_3CN at 23 °C.

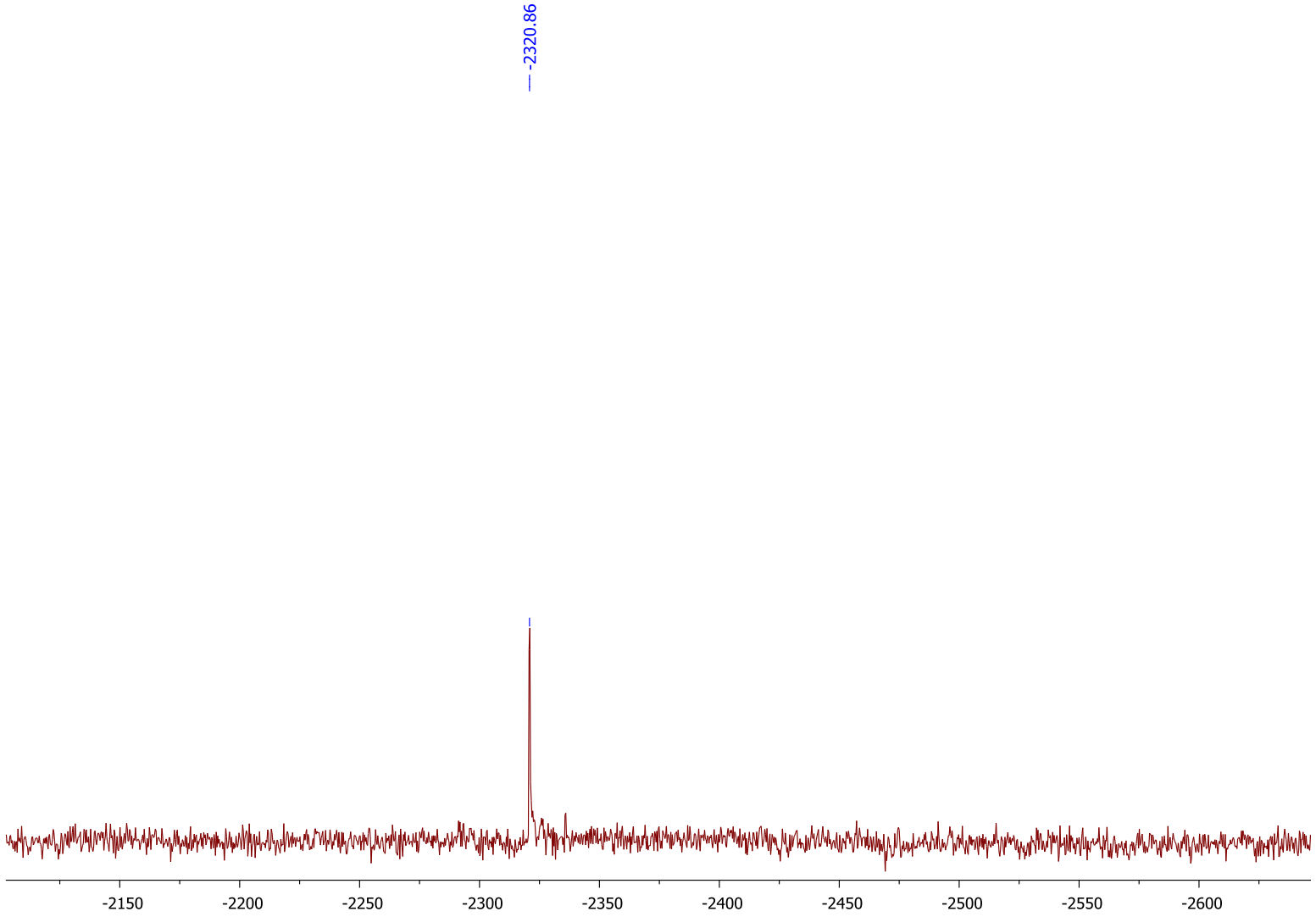

Figure S37. $^{195}Pt\{^{1}H\}$ NMR spectrum of **2** in CD_3CN at 23 °C.

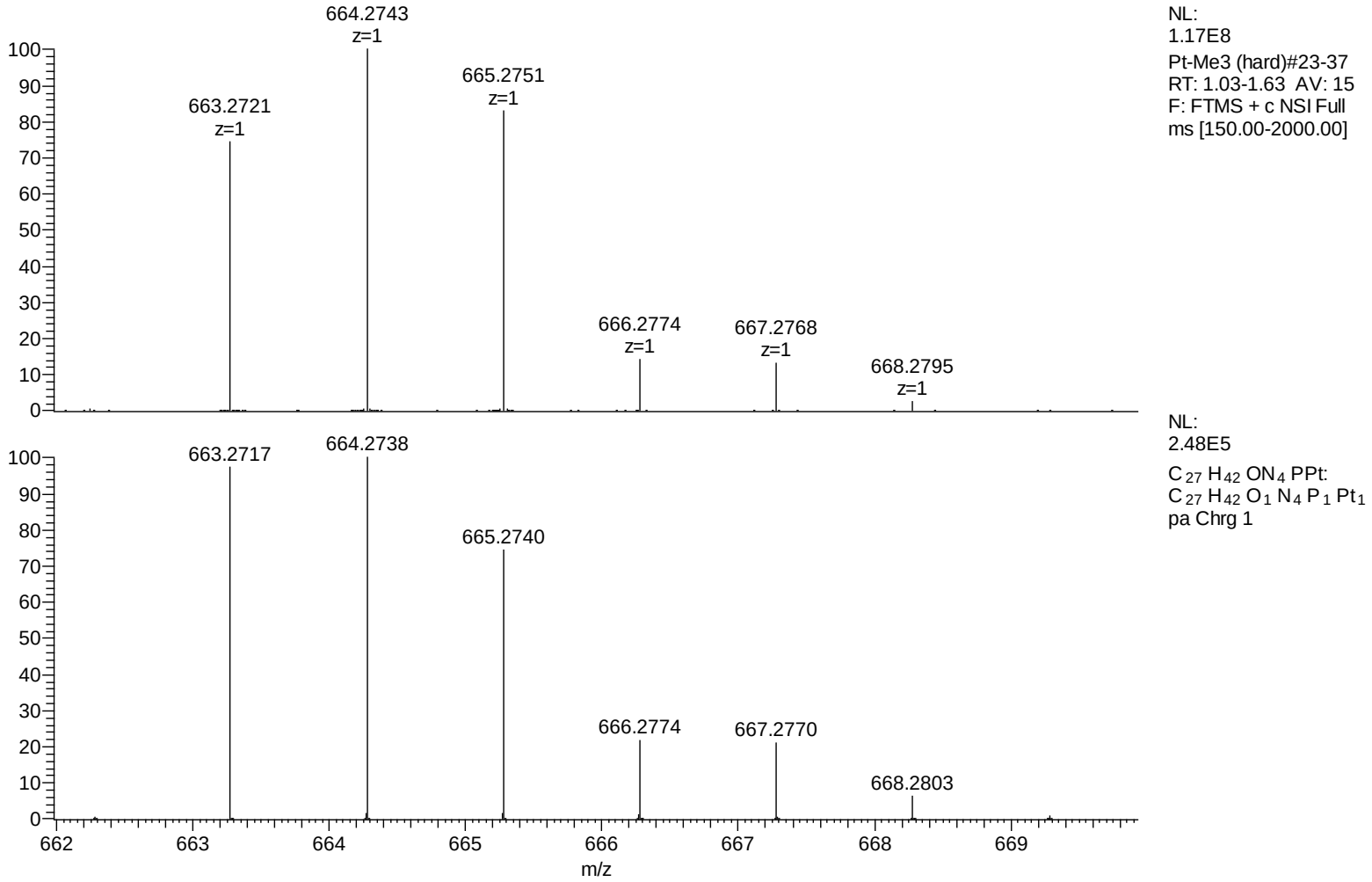

Figure S38. ESI-(HR)MS spectrum of a MeCN solution of **2** (top) and simulated spectrum for $C_{27}H_{42}ON_4PPt^+$ (bottom).

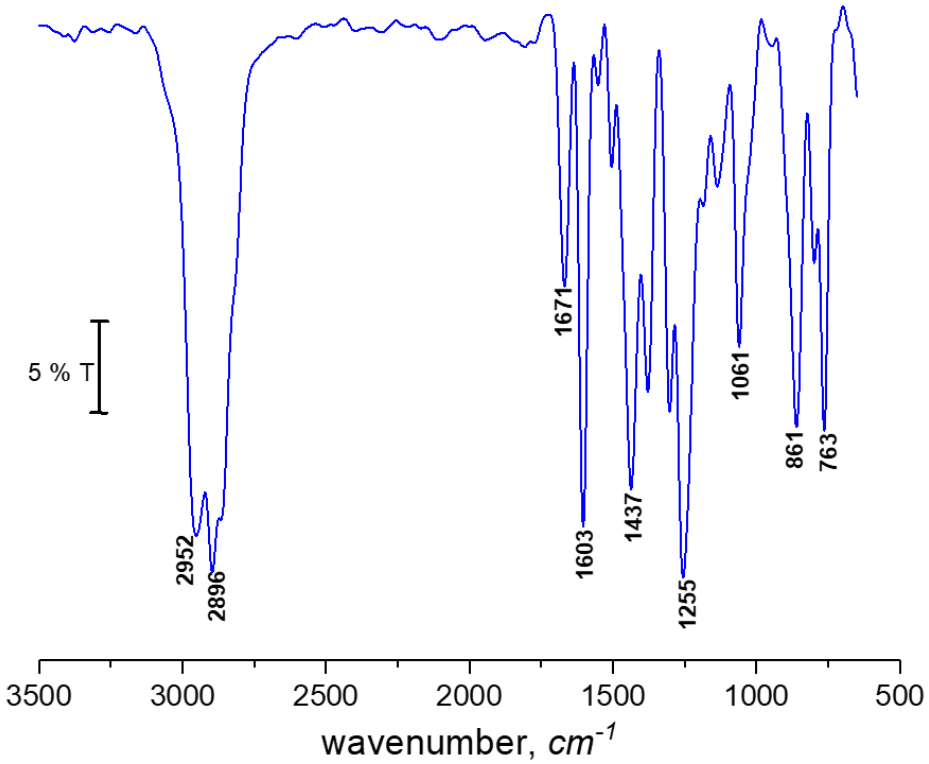

Figure S39. ATR FT-IR transmittance spectrum of **2**.

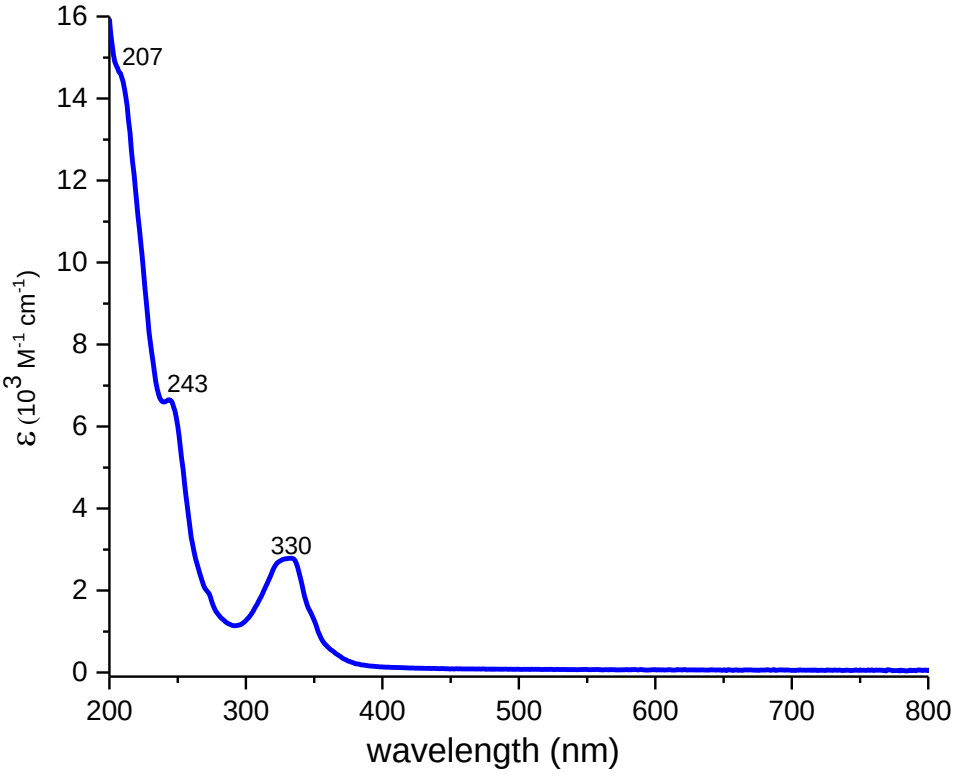

Figure S40. UV-vis absorbance spectrum for **2** in MeCN.

Reaction of 1 with methyl iodide to form 2.

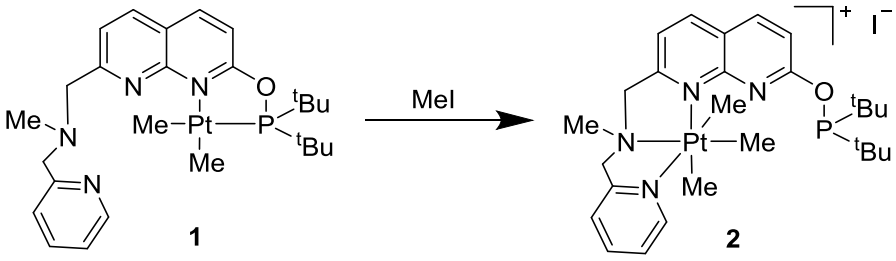

Scheme S4. Formation of **2** by reaction of **1** with MeI.

1 equiv of methyl iodide (1.0 μL, 0.016 mmol) was added to **1** (10.2 mg, 0.0157 mmol), in MeCN-d_3 (500 μL) in the presence of 1.1 equiv of mesitylene (2.1 μL) as an internal standard. The crude mixture was analyzed by ^{1}H NMR after 24 h. Formation of complex **2** is observed in solution (47% yield by NMR based in integration of methyl peak at 0.91 ppm for **1**, integration of new methyl group at 0.71 ppm for complex **2** vs. mesitylene peak of internal standard at 2.24 ppm). The $C(CH_3)_3$ group in complex **2** appears as two different doublets compared to **1** where $C(CH_3)_3$ group appears as one doublet. The methyl groups and ^{t}Bu groups in **2** are marked with an arrow in the figure below.

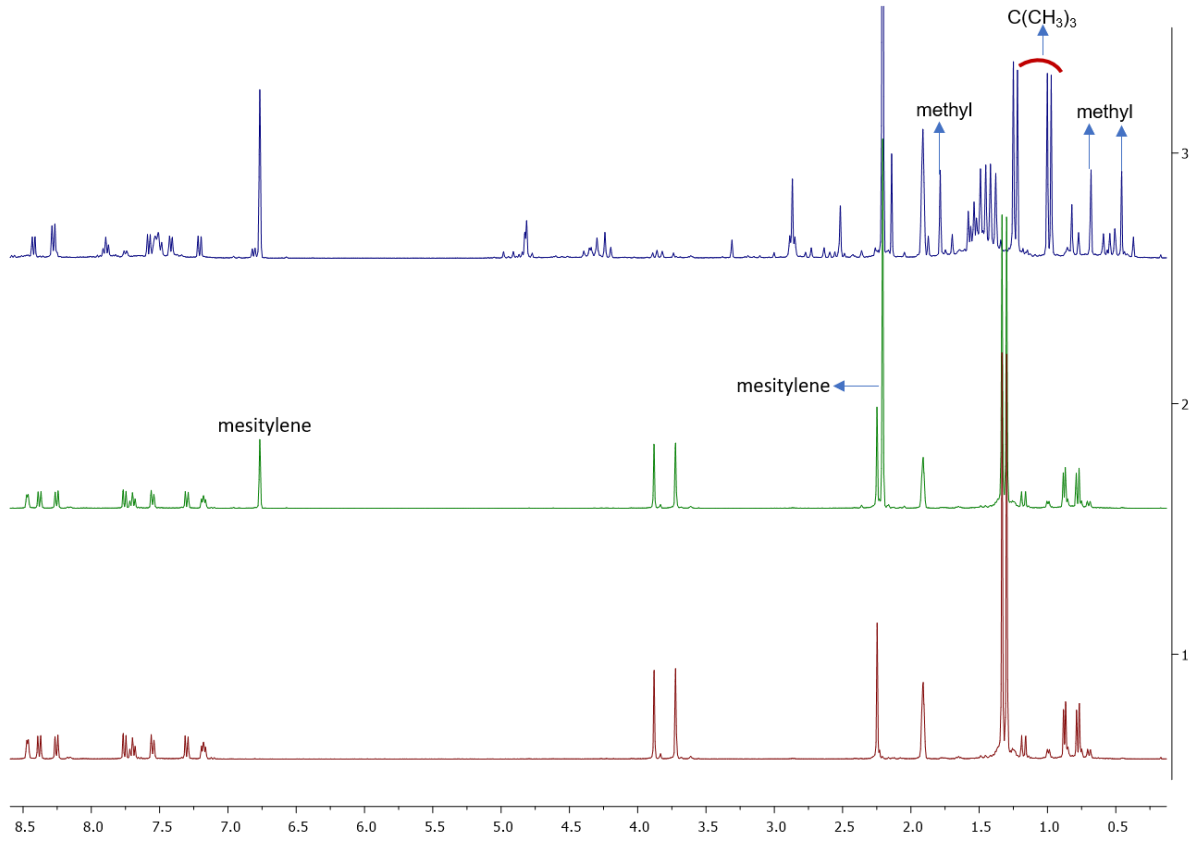

Figure S41. ^{1}H NMR spectra of **1** (red line, bottom), **1** in mesitylene (green line, middle) and **2** (blue line, top) performed in MeCN-d_3 at 20 °C.

Comparison of NMR spectra of isolated complex **2** prepared from $[PtMe_3I]_4$ prepared as described above, and complex **2** prepared by a reaction of complex **1** with methyl iodide.

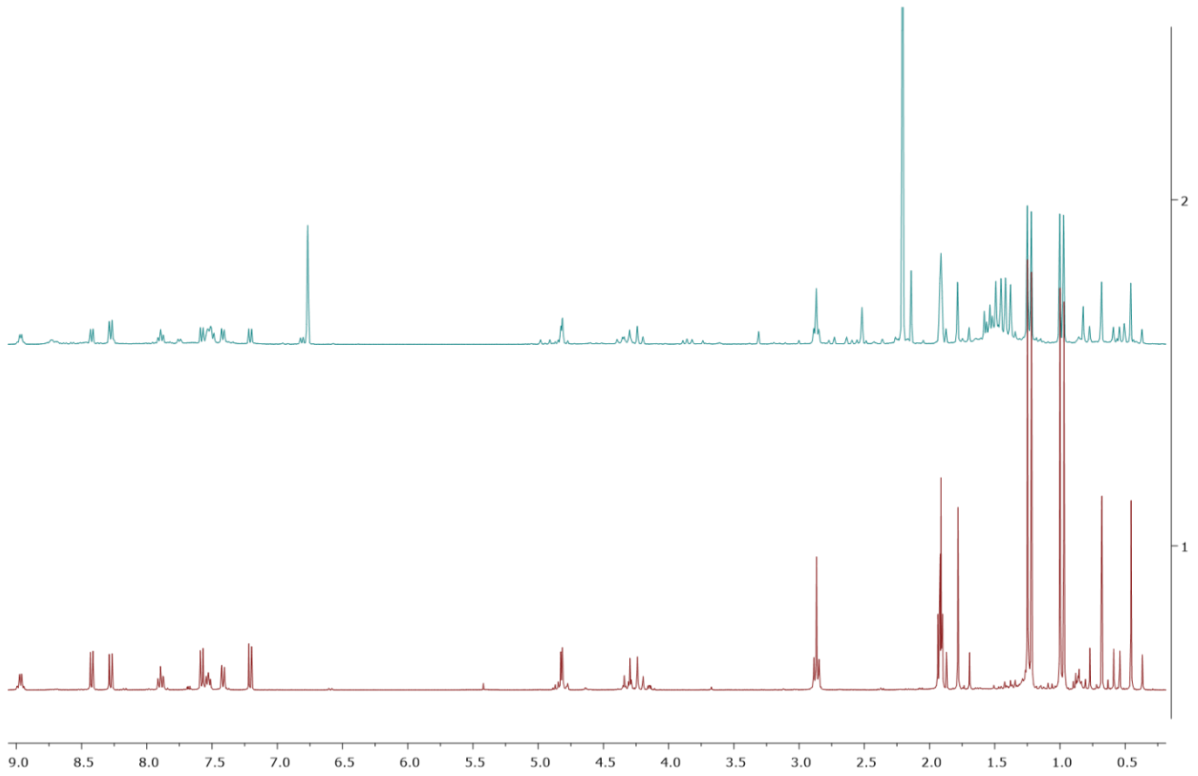

Figure S42. ^{1}H NMR spectra of isolated complex **2** (red line, bottom) and crude reaction mixture after reacting **1** with methyl iodide (blue line, top) in MeCN-d_3.

Synthesis of [(L)CuPtMe$_2$][CuCl$_2$], 3[CuCl$_2$]

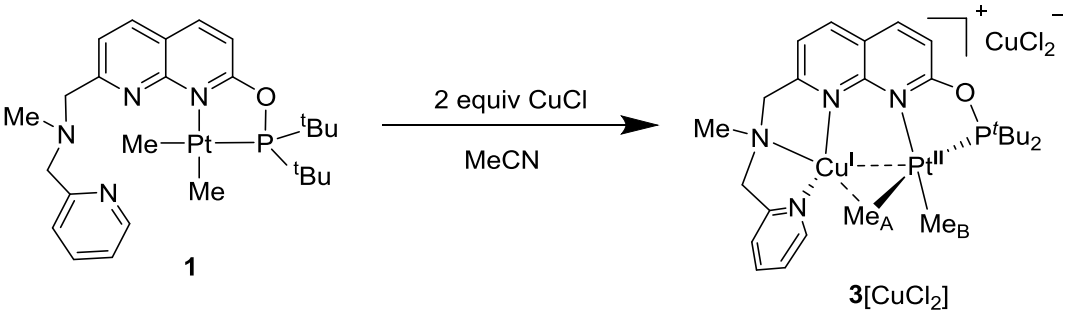

Scheme S5. Formation of **3**·[CuCl$_2$].

In a 20 mL vial CuCl (20.7 mg, 0.154 mmol) and **1** (50.2 mg, 0.077 mmol) were dissolved in MeCN (3 mL) giving a brown color solution which was stirred at RT for 5 min. Later, the solvent was removed under vacuum and the brown color viscous liquid was dissolved in a minimum amount of MeCN (1mL). The desired complex was precipitated with hexane (3 x 2 mL). The solvent removal under vacuum yields complex **3**[CuCl$_2$] as a brown solid (45.7 mg, 0.0539 mmol, 69%). Crystal suitable for X-ray diffraction study were grown by vapor diffusion in benzene/pentane solvent.

^{1}H NMR (600 MHz, CD$_3$CN, 0 °C) δ: 8.76 (d, $^3J_{HH}$ = 5.1 Hz, 1H, CH$_{Py}$), 8.58 (d, $^3J_{HH}$ = 8.8 Hz, 1H, CH$_{Naph}$), 8.48 (d, $^3J_{HH}$ = 8.2 Hz, 1H, CH$_{Naph}$), 7.88 (td, $^3J_{HH}$ = 7.8 Hz, $^4J_{HH}$ = 1.6 Hz, 1H, CH$_{Py}$), 7.54 (d, $^3J_{HH}$ = 8.2 Hz, 1H, CH$_{Naph}$), 7.50 (d, $^3J_{HH}$ = 8.8 Hz, 1H, CH$_{Naph}$), 7.46 (t, $^3J_{HH}$ = 6.4 Hz, 1H, CH$_{Py}$), 7.42 (d, $^3J_{HH}$ = 7.8 Hz, 1H, CH$_{Py}$), 4.17 (br s, 2H, CH$_2$), 3.67 (s, 2H, CH$_2$), 2.58 (s, 3H, N-CH$_3$), 1.52 (br m, 9H, C(CH$_3$)$_3$), 1.25 (br m, 9H, C(CH$_3$)$_3$), 1.14 (d, $^3J_{PH}$ = 5.2 Hz, $^2J_{PtH}$ = 85.2 Hz, 3H, Pt-Me$_B$), 0.97 (d, $^3J_{PH}$ = 4.1 Hz, $^2J_{PtH}$ = 46.2 Hz, 3H, Pt-Me$_A$).

^{13}C{^{1}H} NMR (151 MHz, CD$_3$CN, 0 °C) δ: 167.79 (C$_{q,Naph}$), 161.67 (C$_{q,Naph}$), 158.48 (C$_{q,Py}$), 150.86 (C$_{q,Naph}$), 150.65 (C$_{H,Py}$), 143.47 (C$_{H,Naph}$), 140.06 (C$_{H,Naph}$), 139.03 (C$_{H,Py}$), 125.35 (C$_{H,Py}$), 122.46 (C$_{H,Naph}$), 121.93 (C$_{q,Naph}$), 114.14 (C$_{H,Py}$), 114.12 (C$_{H,Naph}$), 62.15 (CH$_2$), 61.92 (CH$_2$), 44.04 (N-CH$_3$), 43.45 - 42.57 (br m, ***C***(CH$_3$)$_3$), 40.06 – 39.18 (br m, ***C***(CH$_3$)$_3$), 28.15 – 26.83 (br m, C(***C***H$_3$)$_3$), -5.95 (d, $^2J_{PC}$ = 98.9 Hz, $^1J_{PtC}$ = 489.9 Hz, Pt-Me$_A$), -21.57 (d, $^2J_{PC}$ = 3.2 Hz, $^1J_{PtC}$ = 710.8 Hz, Pt-Me$_B$).

^{31}P{^{1}H} NMR (242 MHz, CD$_3$CN, 0 °C) δ: 186.7 ($^1J_{PtP}$ = 2850 Hz).

^{195}Pt{^{1}H} NMR (129 MHz, CD$_3$CN, 0 °C) δ: -3978.4 ($^1J_{PtP}$ = 2850 Hz).

Elemental Analysis: Expt (Calc): [C$_{26}$H$_{39}$Cl$_2$Cu$_2$N$_4$OPPt]: C 36.73 (36.84), H 4.26 (4.64), N 6.45 (6.61).

ESI-HRMS (m/z pos): Found (Calcd): C$_{26}$H$_{39}$ON$_4$P^{195}Pt^{63}Cu$^+$: 712.1763 (712.1800).

FT-IR (ATR, solid): 2961 (br, w), 2887 (br, w), 22236 (w), 2089 (w), 1607 (s), 1351 (m), 1271 (s), 1119 (m), 888 (m), 759 (m), 673 (m) cm^{-1}.

UV-vis (MeCN), λ, nm (ε, M^{-1}·cm^{-1}) : 331 (3850), 286 (2700), 205 (18200).

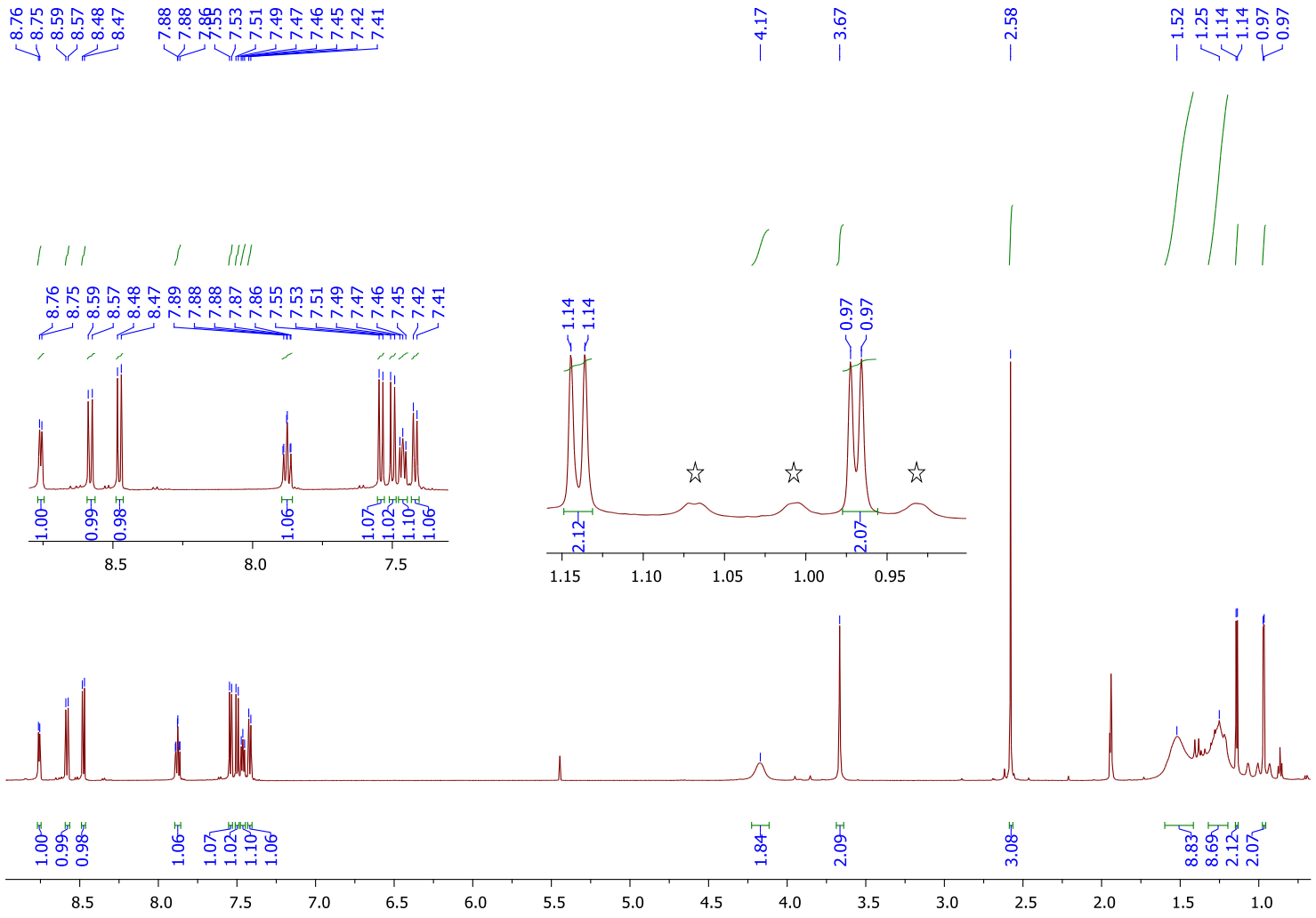

Figure S43. ^{1}H NMR spectrum of **3**[$CuCl_2$] in CD_3CN at 0 °C. Pt satellites are marked with stars.

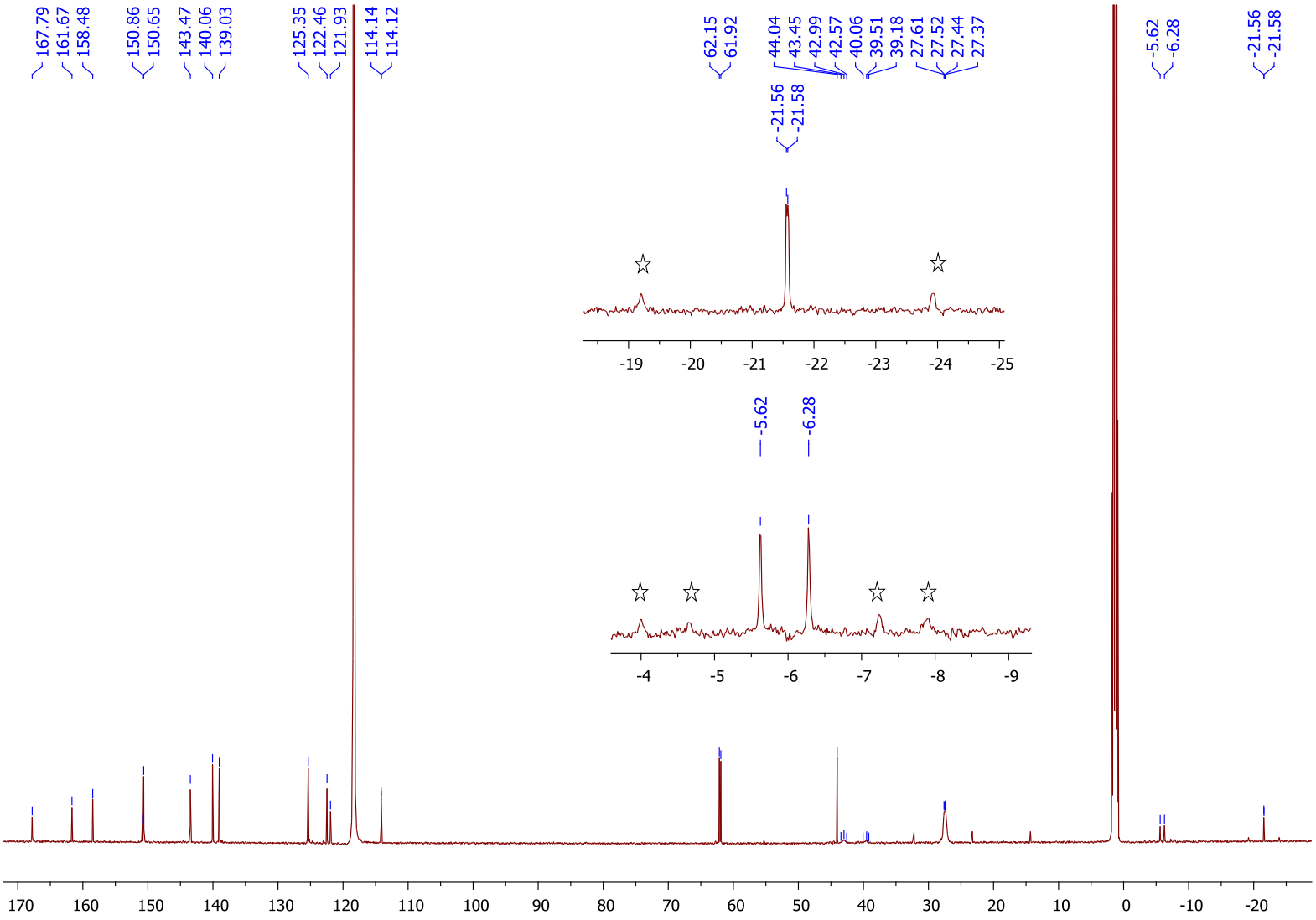

Figure S44. $^{13}C\{^{1}H\}$ NMR spectrum of **3**[$CuCl_2$] in CD_3CN at 0 °C. Pt satellites are marked with stars.

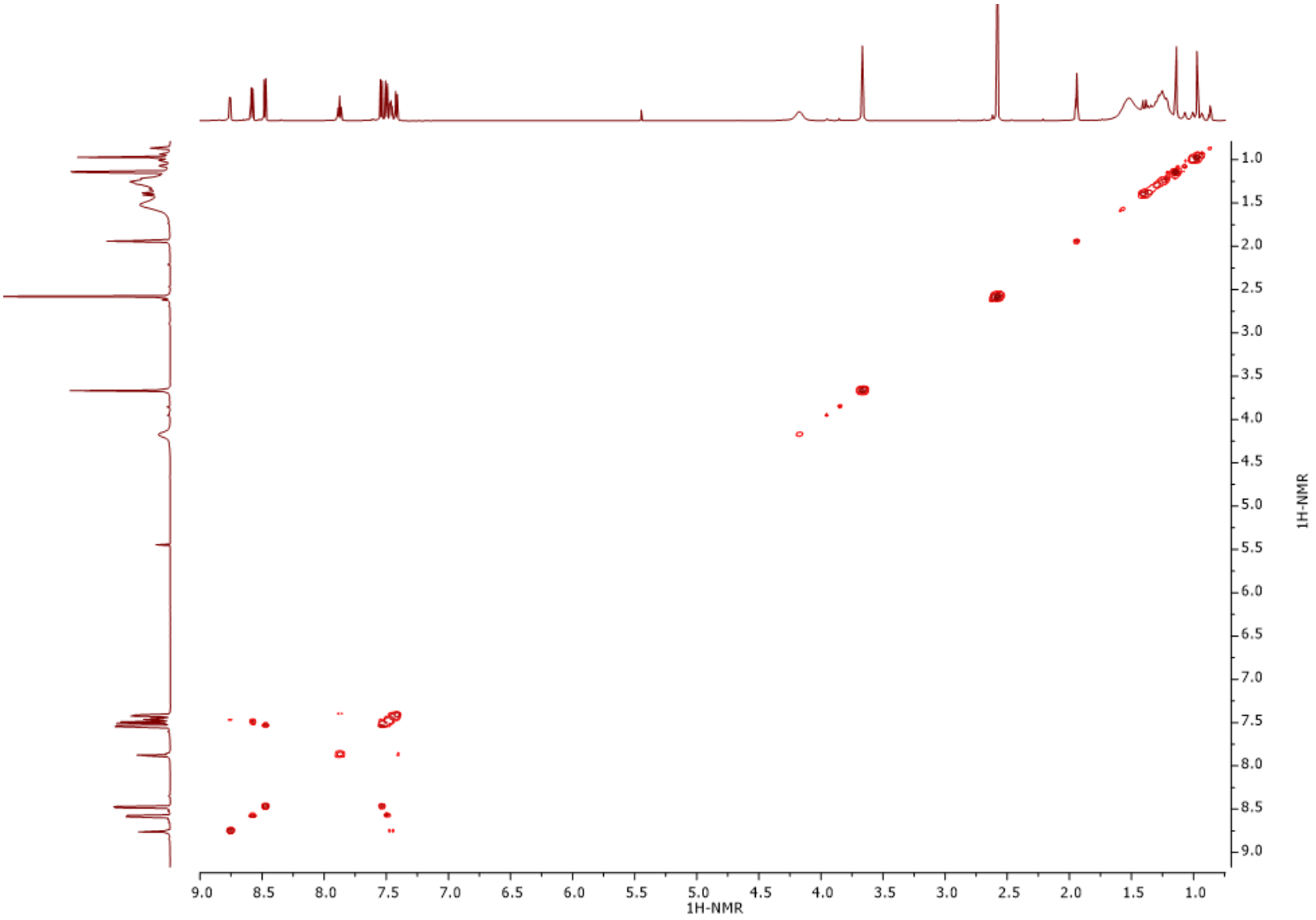

Figure S45. ^{1}H-^{1}H COSY spectrum of **3**[$CuCl_2$] in CD_3CN at 0 °C.

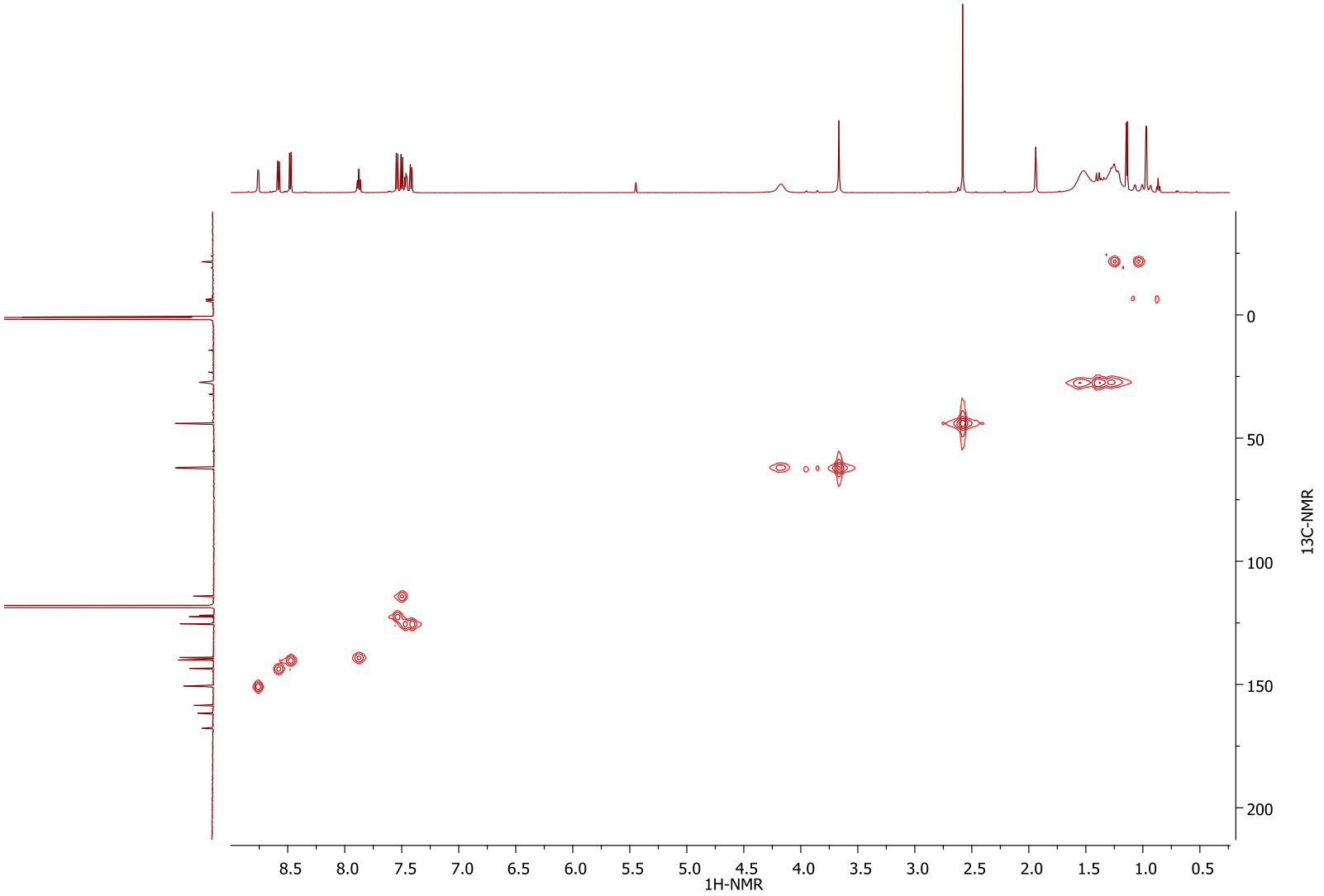

Figure S46. ^{1}H-^{13}C HMQC spectrum of **3**[$CuCl_2$] in CD_3CN at 0 °C.

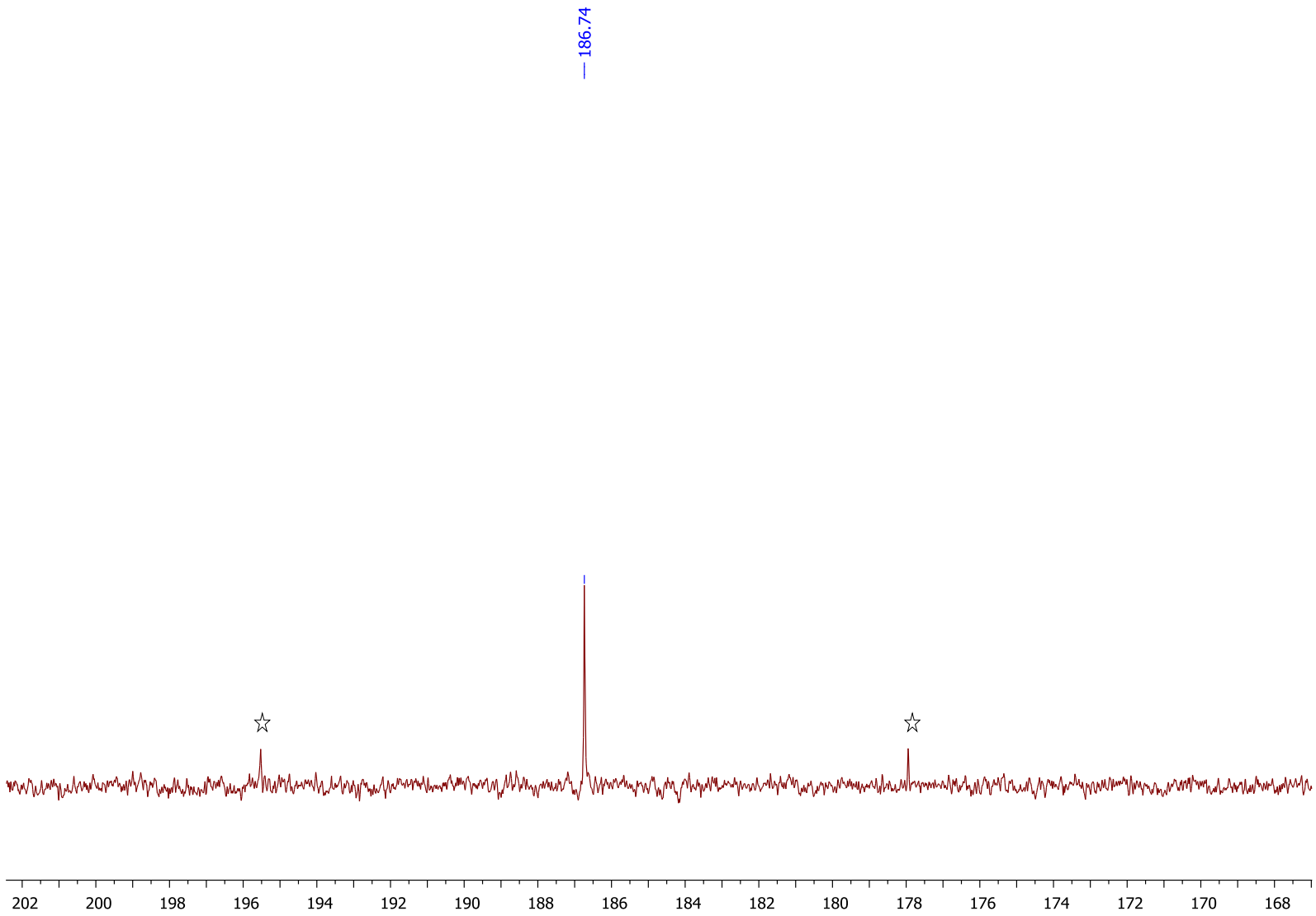

Figure S47. $^{31}P\{^{1}H\}$ NMR spectrum of **3**[$CuCl_2$] in CD_3CN at 0 °C. Pt satellites are marked with stars.

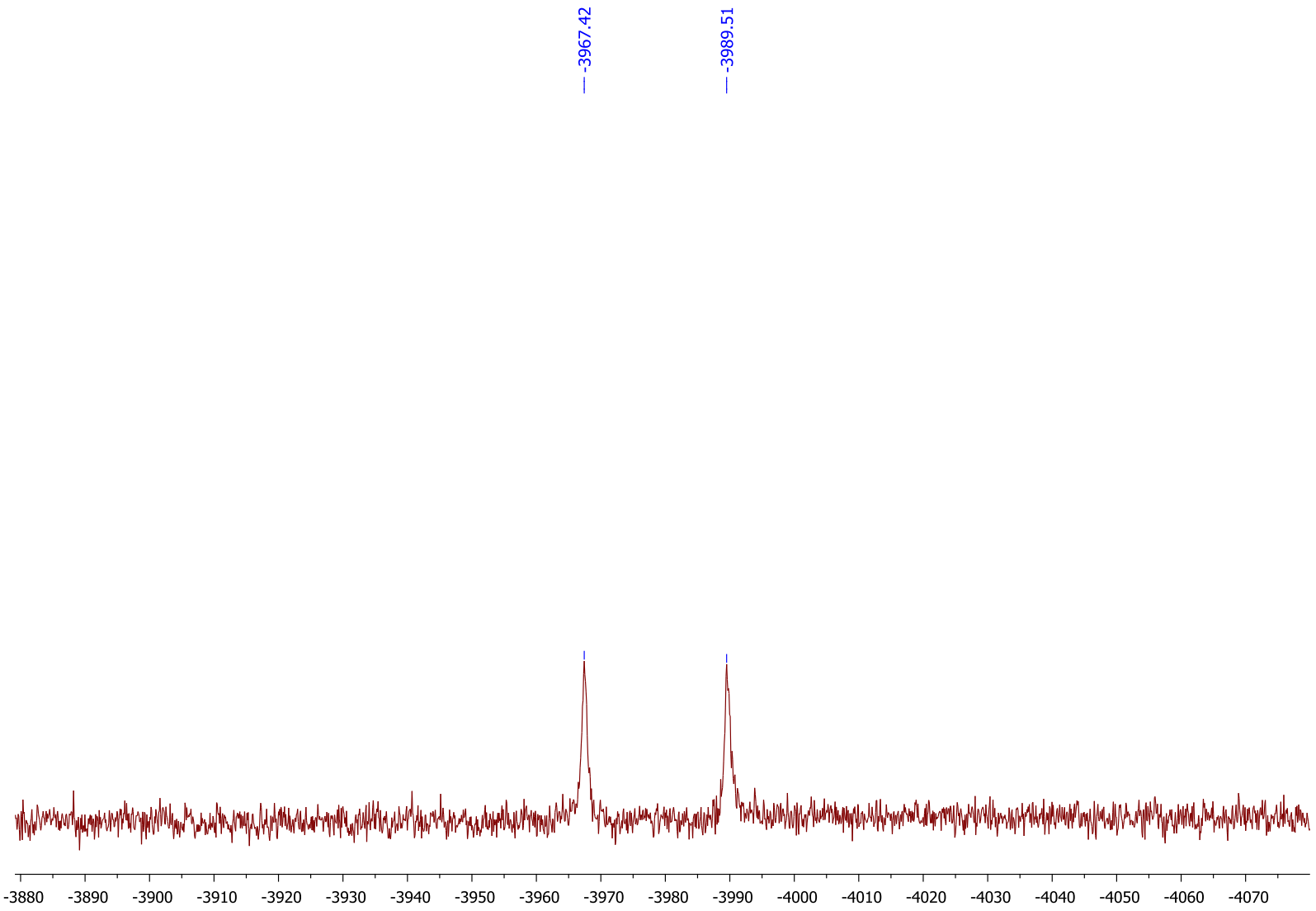

Figure S48. $^{195}Pt\{^{1}H\}$ NMR spectrum of **3**[$CuCl_2$] in CD_3CN at 0 °C.

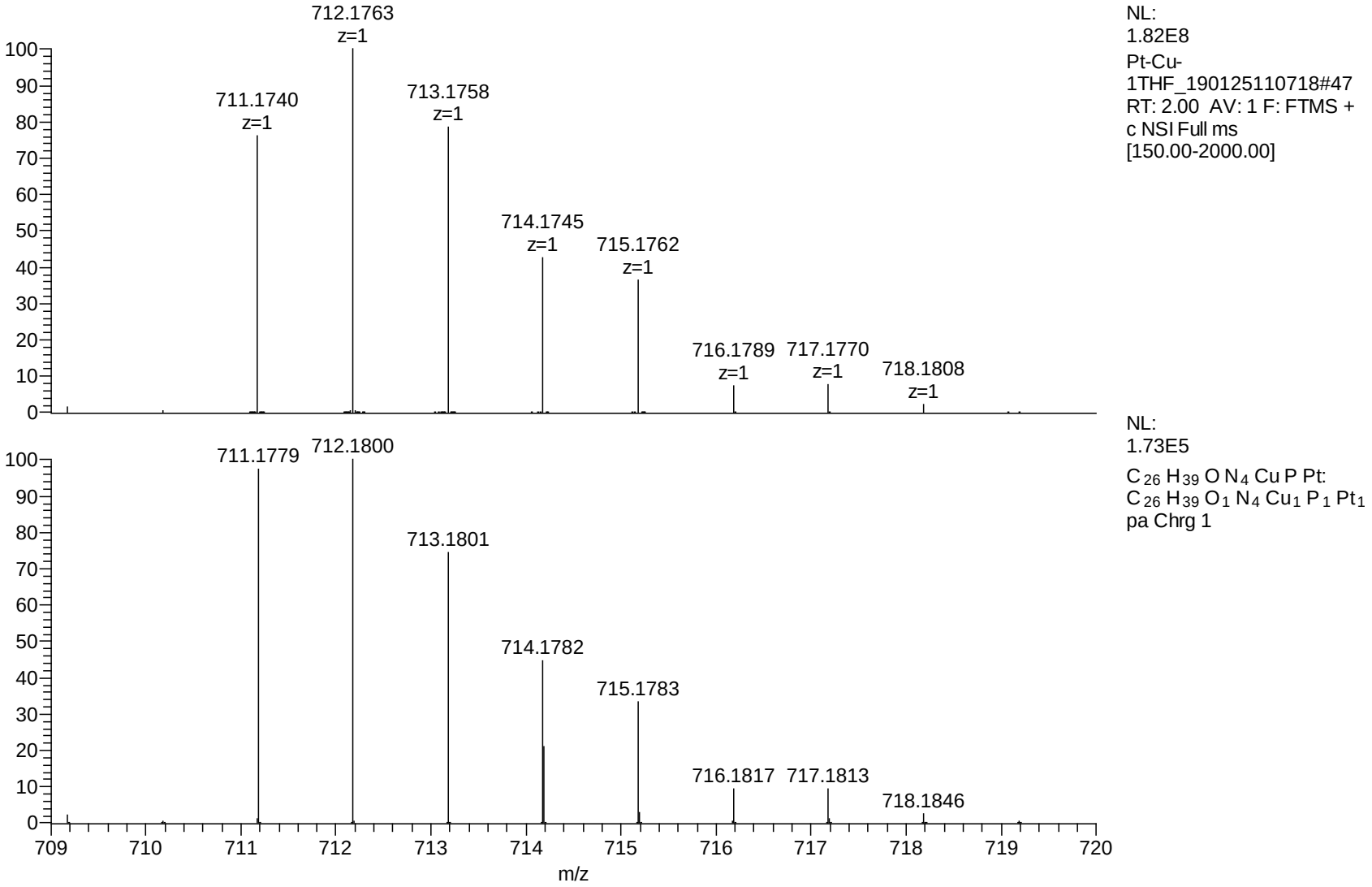

Figure S49. ESI-(HR)MS spectrum of a MeCN solution of **3**[$CuCl_2$] (top) and simulated spectrum for $C_{26}H_{39}ON_4PPtCu^+$ (bottom).

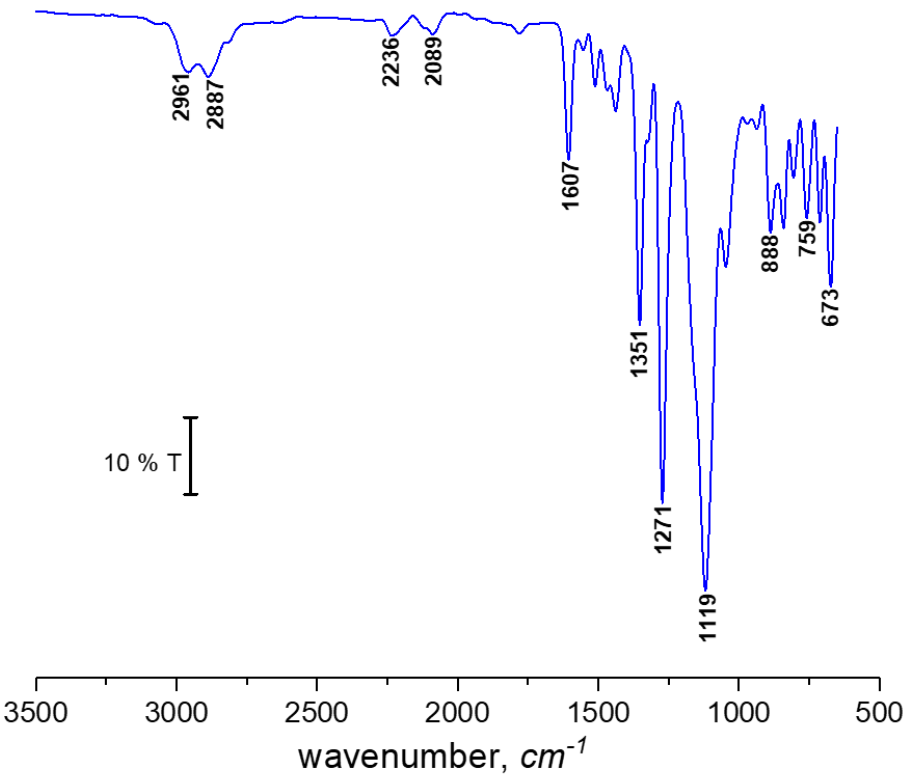

Figure S50. ATR FT-IR transmittance spectrum of **3**[$CuCl_2$].

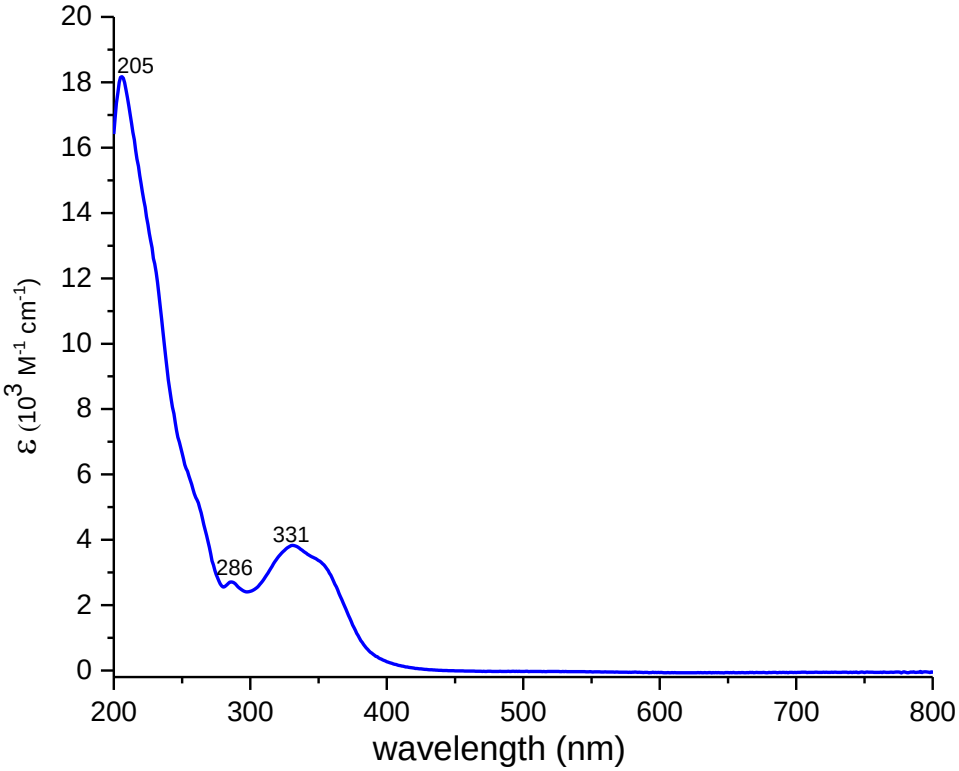

Figure S51. UV-vis absorbance spectrum for **3**[$CuCl_2$] in MeCN.

Reaction of 1 with 1 equivalent of CuCl

In a 20 mL vial CuCl (2.3 mg, 0.023 mmol) and **1** (15.2 mg, 0.023 mmol) were dissolved in MeCN (2 mL) giving a brown color solution which was stirred at RT for 5 min. The solvent was then removed under vacuum and the brown color viscous liquid was dissolved in a minimum amount of MeCN (1 mL). The desired complex was precipitated with hexane (4 mL). Drying under vacuum for 8h gave brown powder solid. NMR spectrum of the obtained product shows the presence of some unidentified product along with the major species, which has almost identical NMR spectrum to that of **3**[$CuCl_2$], indicating that the major product likely contains the same Pt/Cu core, although the nature of the counter anion remains unclear. These peaks were not observed when 2 equivalents of CuCl as precursor used in the formation of complex **3**[$CuCl_2$].

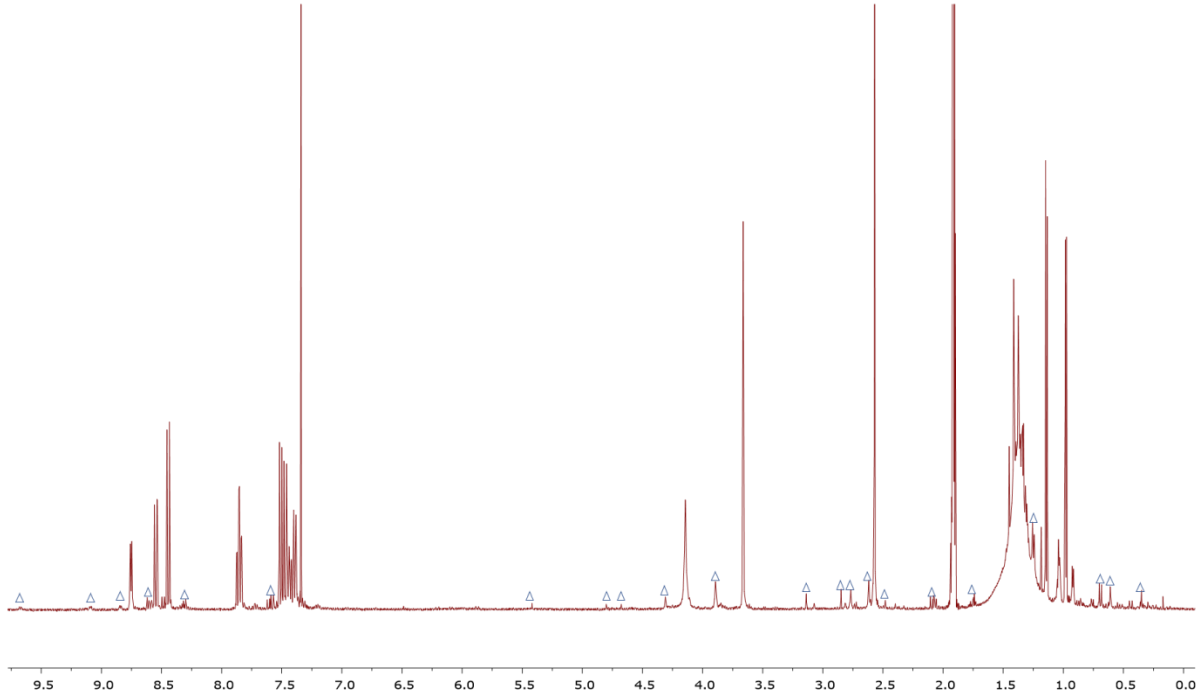

Figure S52. ^{1}H NMR spectrum of the product of reaction of **1** with 1 equiv of CuCl.

Synthesis of [(L)CuPtMe$_2$][B(Ar^F)$_4$], 3[B(Ar^F)$_4$]

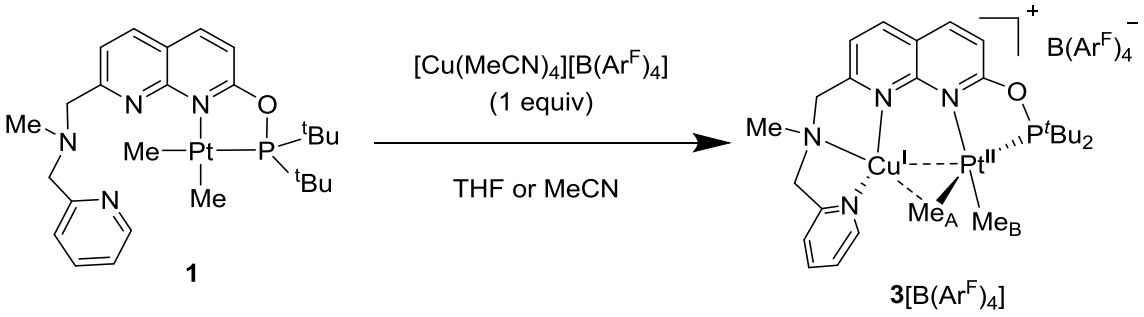

Scheme S6. Formation of **3**·[B(Ar^F)$_4$].

In a 20 mL vial, [Cu(MeCN)$_4$][B(Ar^F)$_4$] (170.3 mg, 0.1549 mmol) and **1** (100.7 mg, 0.1549 mmol) were dissolved in THF (5 mL) to give a brown solution which was stirred at room temperature for 30 min. Then the solvent was removed under vacuum and the brown oil was dissolved in a minimum amount of THF (1 mL) was and then precipitated with pentane (4 x 2 mL). The liquid was then decanted and the remaining solid was dried under vacuum to afford complex **3**[B(Ar^F)$_4$] (157.4 mg, 0.0998 mmol, 65%). Complex **3**[B(Ar^F)$_4$] is sparingly soluble in pentane; X-ray quality crystals of this complex were obtained by slow evaporation at – 30 °C.

^{1}H NMR (600 MHz, THF-d_8, 23 °C) δ: 8.84 (d, $^3J_{HH}$ = 4.9 Hz, 1H, CH_{Py}), 8.68 (d, $^3J_{HH}$ = 8.9 Hz, 1H, CH_{Naph}), 8.55 (d, $^3J_{HH}$ = 8.2 Hz, 1H, CH_{Naph}), 7.91 (td, $^3J_{HH}$ = 7.7 Hz, $^4J_{HH}$ = 1.7 Hz, 1H, CH_{Py}), 7.79 (s, 8H, *o*-CH_{BArF}), 7.62 (d, $^3J_{HH}$ = 6.2 Hz, 1H, CH_{Naph}), 7.61 (d, $^3J_{HH}$ = 6.2 Hz, 1H, CH_{Naph}), 7.57 (s, 4H, *p*-CH_{BArF}), 7.51-7.48 (m, 1H, CH_{Py}), 7.46 (d, $^3J_{HH}$ = 7.7 Hz, 1H, CH_{Py}), 4.33 (d, $^2J_{HH}$ = 16.9 Hz, 1H, CH_2), 4.27 (d, $^2J_{HH}$ = 16.9 Hz, 1H, CH_2), 3.77 (s, 2H, CH_2), 2.66 (s, 3H, N-CH_3), 1.59 (d, $^3J_{PH}$ = 14.6 Hz, 9H, $C(CH_3)_3$), 1.30 (d, $^3J_{PH}$ = 14.6 Hz, 9H, $C(CH_3)_3$), 1.23 (d, $^3J_{PH}$ = 5.3 Hz, $^2J_{PtH}$ = 86.4 Hz, 3H, Pt-Me_B), 1.10 (d, $^3J_{PH}$ = 3.6 Hz, $^2J_{PtH}$ = 44.2 Hz, 3H, Pt-Me_A).

^{13}C NMR (151 MHz, THF-d_8, -25 °C) δ: 167.81 ($C_{q,Naph}$), 162.65 ($C_{q,BArF}$), 162.04 ($C_{q,Naph}$), 158.58 ($C_{q,Py}$), 150.72 ($C_{q,Naph}$), 150.46 ($C_{H,Py}$), 143.55 ($C_{H,Naph}$), 140.02 ($C_{H,Naph}$), 139.02 ($C_{H,Py}$), 135.31 ($C_{H,BArF}$), 129.79 ($C_{q,BArF}$), 127.97 ($C_{q,BArF}$), 125.27 ($C_{H,Py}$), 125.22 ($C_{H,Py}$), 122.55 ($C_{q,Naph}$), 121.91 ($C_{H,Naph}$), 118.09 ($C_{H,BArF}$), 113.92 ($C_{H,Naph}$), 62.11 (CH_2), 61.79 (CH_2), 43.89 (N-CH_3), 43 (d, $^1J_{PC}$ = 4.1 Hz, $\boldsymbol{C}(CH_3)_3$), 39.74 (d, $^1J_{PC}$ = 18.4 Hz, $\boldsymbol{C}(CH_3)_3$), 27.51 (d,$^2J_{PC}$ = 4.2 Hz, C($\boldsymbol{C}H_3)_3$), 26.95 (d,$^2J_{PC}$ = 5.7 Hz, C($\boldsymbol{C}H_3)_3$), -5.95 (d, $^2J_{PC}$ = 98.9 Hz, $^1J_{PtC}$ = 491.4 Hz, Pt-Me_A), -21.34 (d, $^2J_{PC}$ = 3.1Hz, $^1J_{PtC}$ = 710.9 Hz, Pt-Me_B).

^{31}P{^{1}H} NMR (242 MHz, THF-d_8, -25 °C) δ: 186 ($^1J_{PtP}$ = 2877 Hz).

^{195}Pt{^{1}H} NMR (129 MHz, THF-d_8, -25 °C) δ: -3971.2 ($^1J_{PtP}$ = 2877 Hz).

^{1}H NMR (600 MHz, CD_3CN, -25 °C) δ: 8.74 (d, $^3J_{HH}$ = 5 Hz, 1H, CH_{Py}), 8.55 (d, $^3J_{HH}$ = 8.7 Hz, 1H, CH_{Naph}), 8.45 (d, $^3J_{HH}$ = 8.1 Hz, 1H, CH_{Naph}), 7.85 (td, $^3J_{HH}$ = 7.7 Hz, $^4J_{HH}$ = 1.4 Hz, 1H, CH_{Py}), 7.70 (s, 8H, *o*-CH_{BArF}), 7.67 (s, 4H, *p*-CH_{BArF}), 7.52 (d, $^3J_{HH}$ = 8.1 Hz, 1H, CH_{Naph}), 7.48 (d, $^3J_{HH}$ = 8.7 Hz, 1H, CH_{Naph}), 7.46-7.43 (m, 1H, CH_{Py}), 7.39 (d, $^3J_{HH}$ = 7.7 Hz, 1H, CH_{Py}), 4.21 (d, $^2J_{HH}$ = 16.8 Hz, 1H, CH_2), 4.10 (d, $^2J_{HH}$ = 16.8 Hz, 1H, CH_2), 3.62 (s, 2H, CH_2), 2.56 (s, 3H, N-CH_3), 1.51 (d, $^3J_{PH}$ = 14.6 Hz, 9H, $C(CH_3)_3$), 1.20 (d, $^3J_{PH}$ = 14.6 Hz, 9H, $C(CH_3)_3$), 1.12 (d, $^3J_{PH}$ = 5.1 Hz, $^2J_{PtH}$ = 86.8 Hz, 3H, Pt-Me_B), 0.94 (d, $^3J_{PH}$ = 4 Hz, $^2J_{PtH}$ = 44.7 Hz, 3H, Pt-Me_A).

^{13}C NMR (151 MHz, CD_3CN, -25 °C) δ: 167.42 ($C_{q,Naph}$), 162.15 ($C_{q,BArF}$), 161.26 ($C_{q,Naph}$), 158.13 ($C_{q,Py}$), 150.46 ($C_{q,Naph}$), 150.32 ($C_{H,Py}$), 143.12 ($C_{H,Naph}$), 139.72 ($C_{H,Naph}$), 138.71 ($C_{H,Py}$), 135.19 ($C_{H,BArF}$), 129.29 ($C_{q,BArF}$), 127.65 ($C_{q,BArF}$), 125.04 ($C_{H,Py}$), 124.04 ($C_{H,Py}$), 122.24 ($C_{q,Naph}$), 122.12 ($C_{H,Naph}$), 113.82 ($C_{H,Naph}$), 61.67 (CH_2), 61.44 (CH_2), 43.63 (N-CH_3), 42.71 (d, $^1J_{PC}$ = 5.2 Hz,

C$(CH_3)_3$), 39.15 (d, $^1J_{PC}$ = 18.6 Hz, ***C***$(CH_3)_3$), 27.29 (d,$^2J_{PC}$ = 3.1 Hz, C(***C***$H_3)_3$), 26.72 (d,$^2J_{PC}$ = 5.1 Hz, C(***C***$H_3)_3$), -6.41 (d, $^2J_{PC}$ = 99.6 Hz, Pt-Me_A), -21.88 (d, $^2J_{PC}$ = 3.6Hz, $^1J_{PtC}$ = 714.5 Hz, Pt-Me_B). One ($C_{H,BArF}$) peak of overlaps with CD_3CN confirmed by HMQC. Pt satellite for -6.41 ppm signal were not clearly seen due to low intensity.

ESI-HRMS (m/z pos): Found (Calcd): $C_{26}H_{39}ON_4P^{195}Pt^{63}Cu^+$: 712.1752 (712.1800).

FT-IR (ATR, solid): 2960 (br, w), 2886 (br, w), 1620 (m), 1355 (m), 1276 (s), 1125 (s), 891 (m), 674 (m) cm^{-1}.

UV-vis (MeCN), λ, nm (ε, $M^{-1}\cdot cm^{-1}$) : 463 (34), 326 (4000), 267 (5400), 209 (42400).

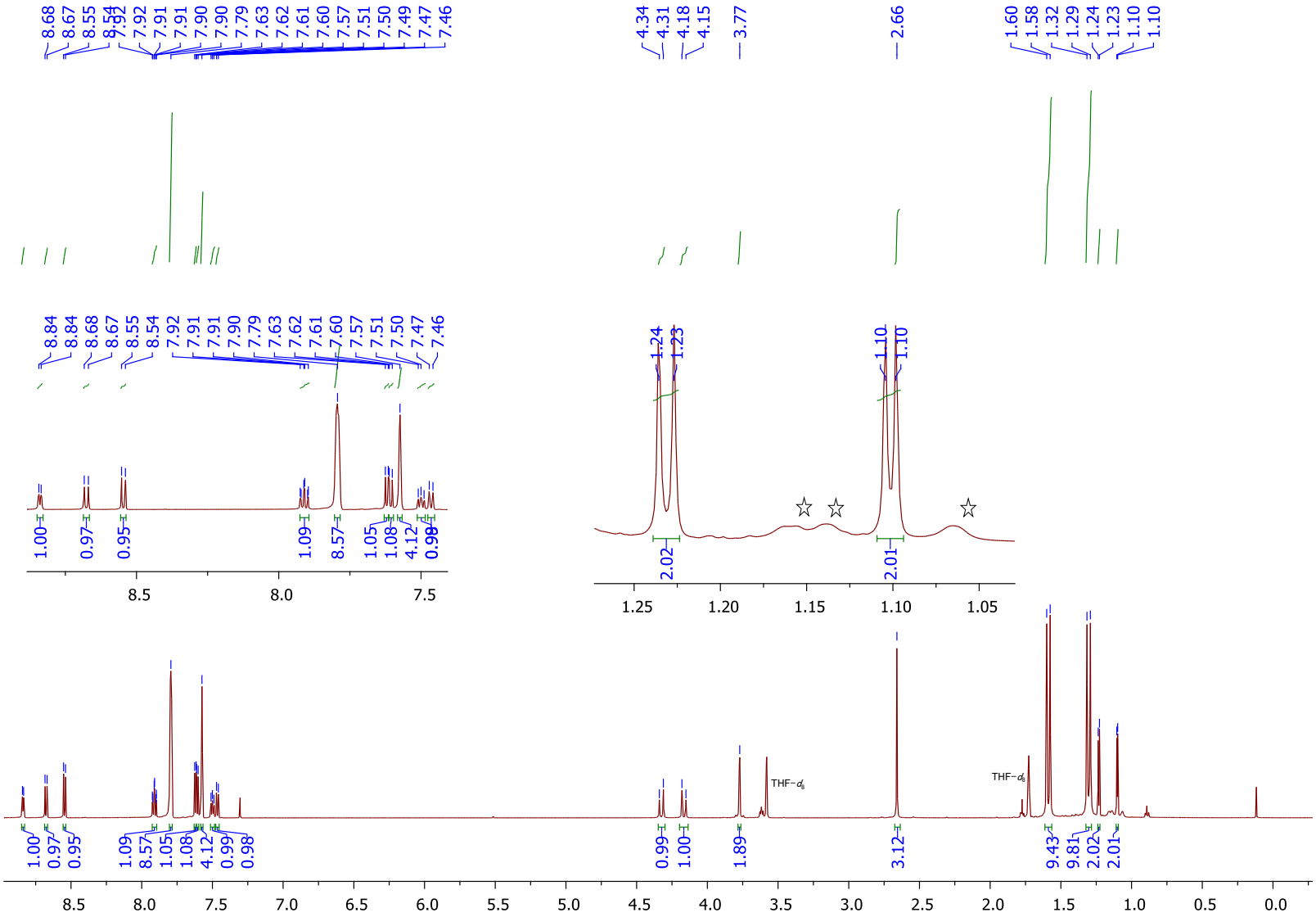

Figure S53. ^{1}H NMR spectrum of **3**[B(Ar^{F})$_4$] in THF-d_8 at 23 °C. Pt satellites are marked with stars.

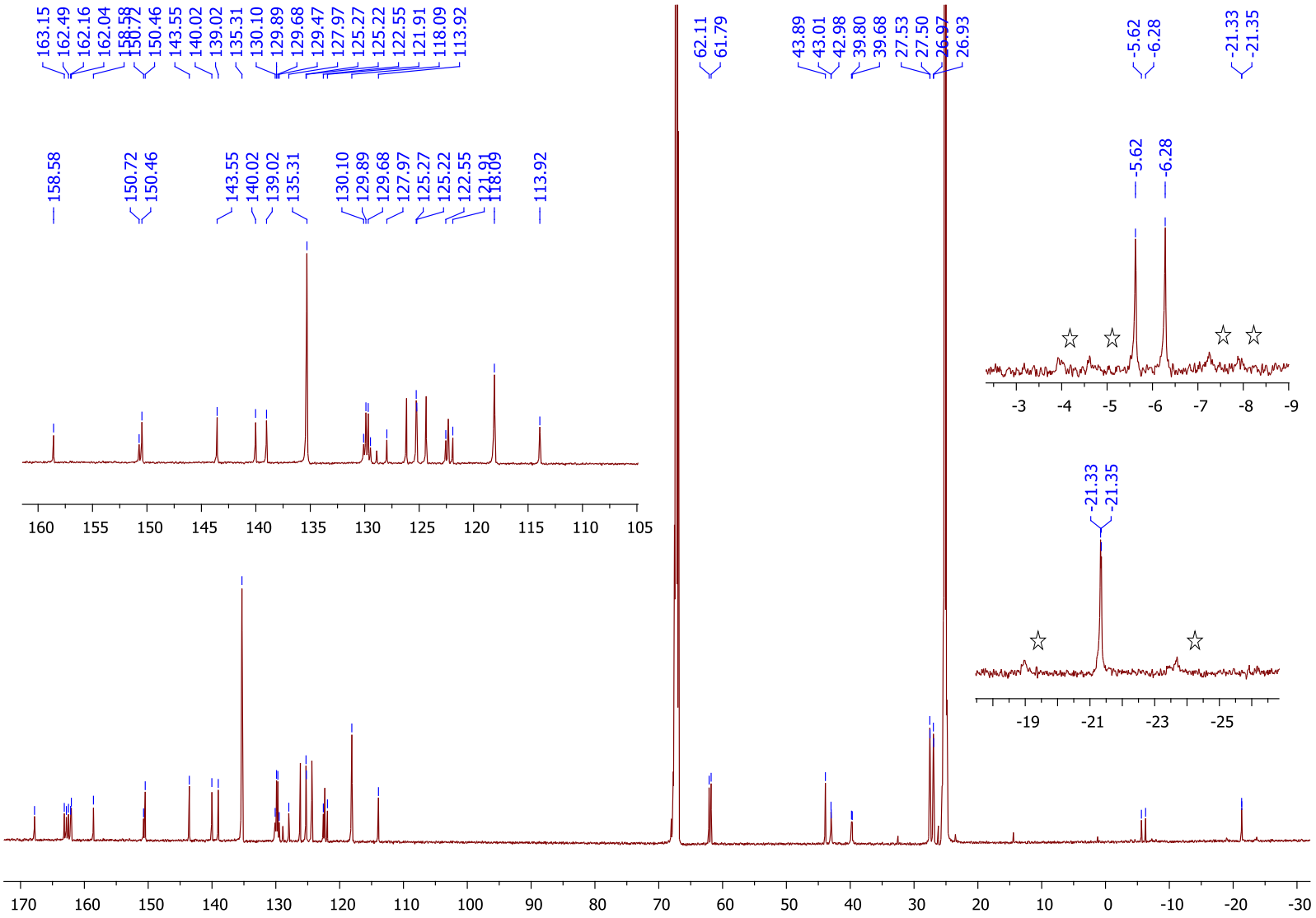

Figure S54. $^{13}C\{^{1}H\}$ NMR spectrum of **3**[B(Ar^{F})$_4$] in THF-d_8 at -25 °C. Pt satellites are marked with stars.

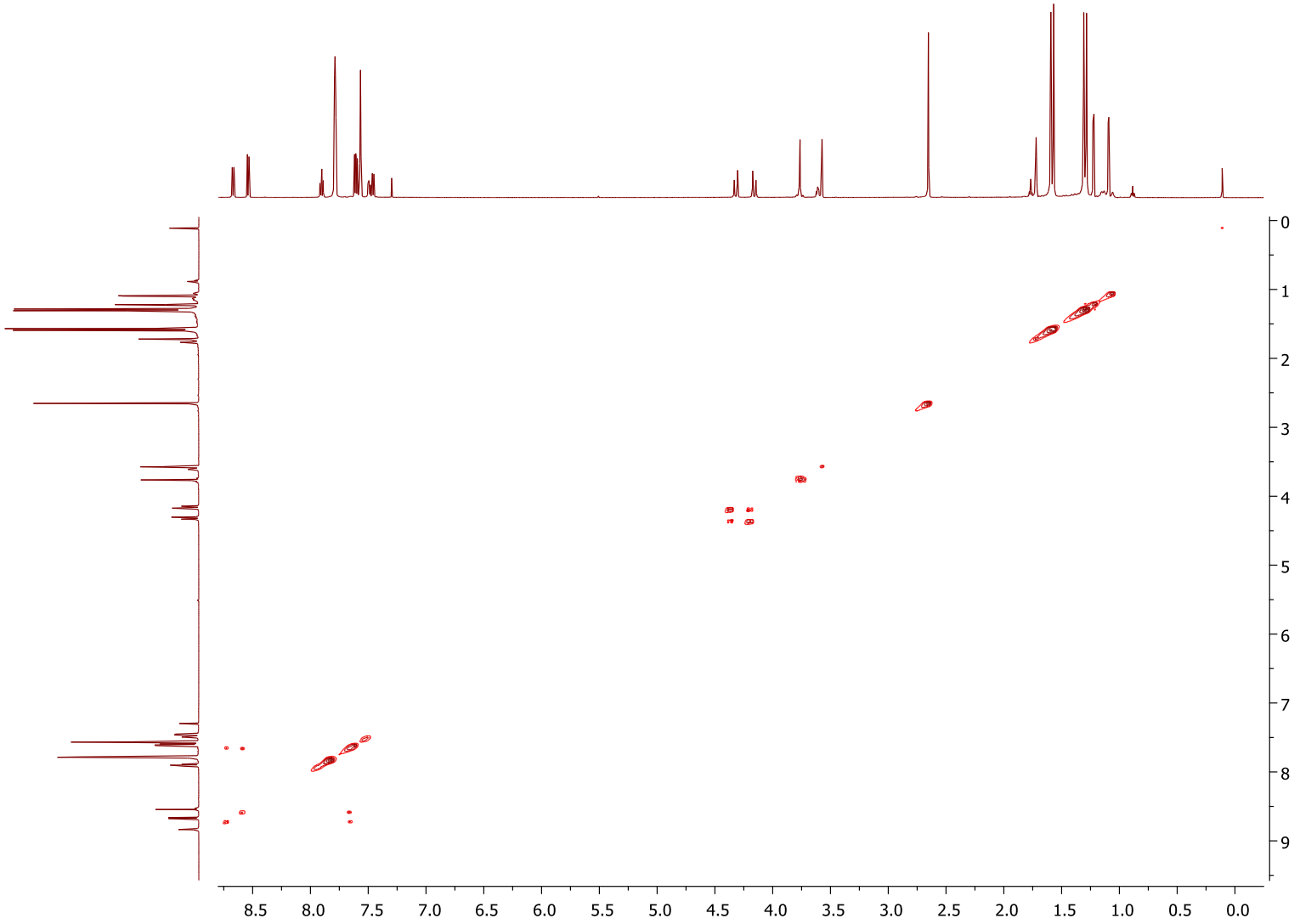

Figure S55. ^{1}H-^{1}H COSY spectrum of **3**[B(Ar^{F})$_4$] in THF-d_8 at -25 °C.

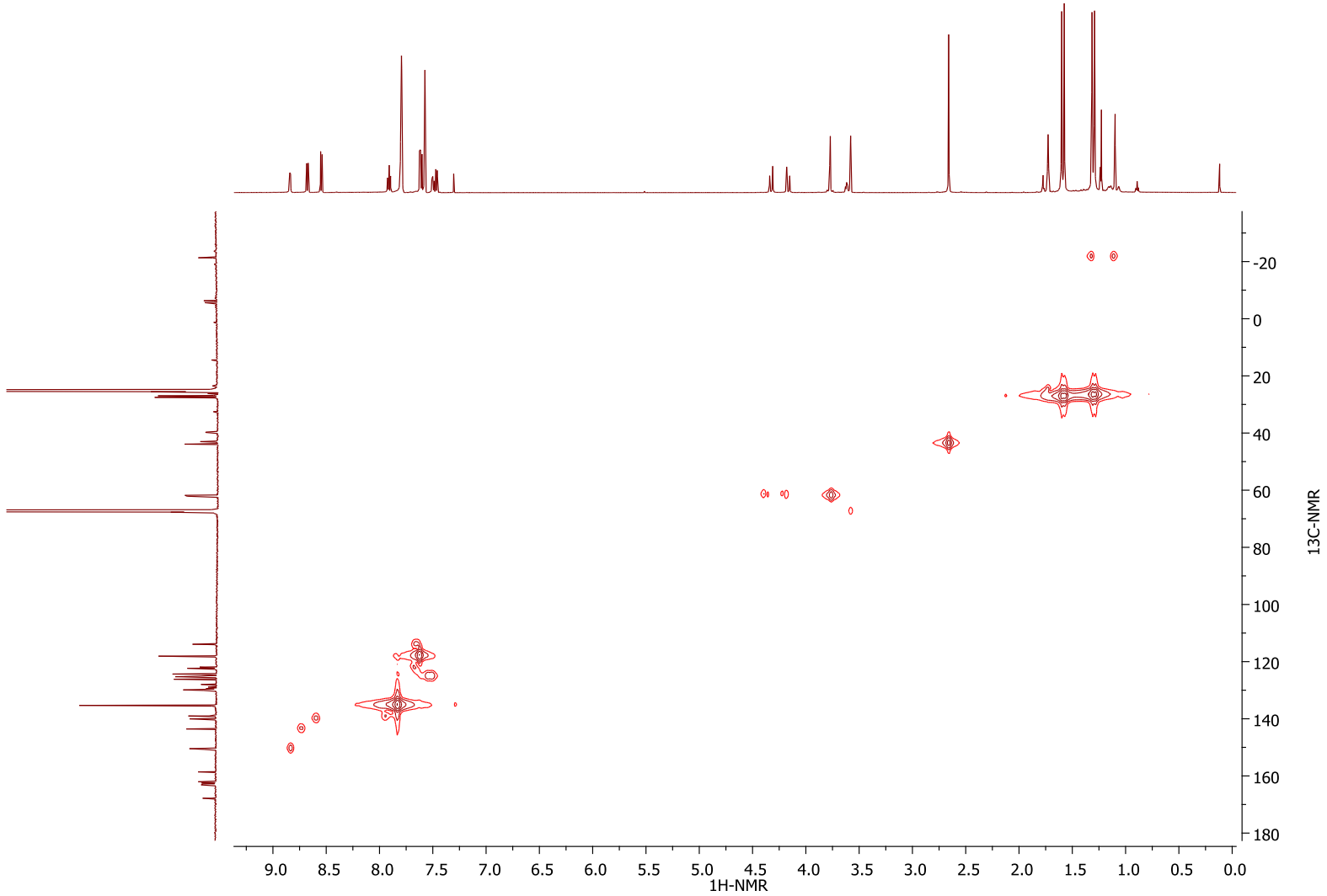

Figure S56. ^{1}H-^{13}C HMQC spectrum of **3**[B(Ar^{F})$_4$] in THF-d_8 at -25 °C.

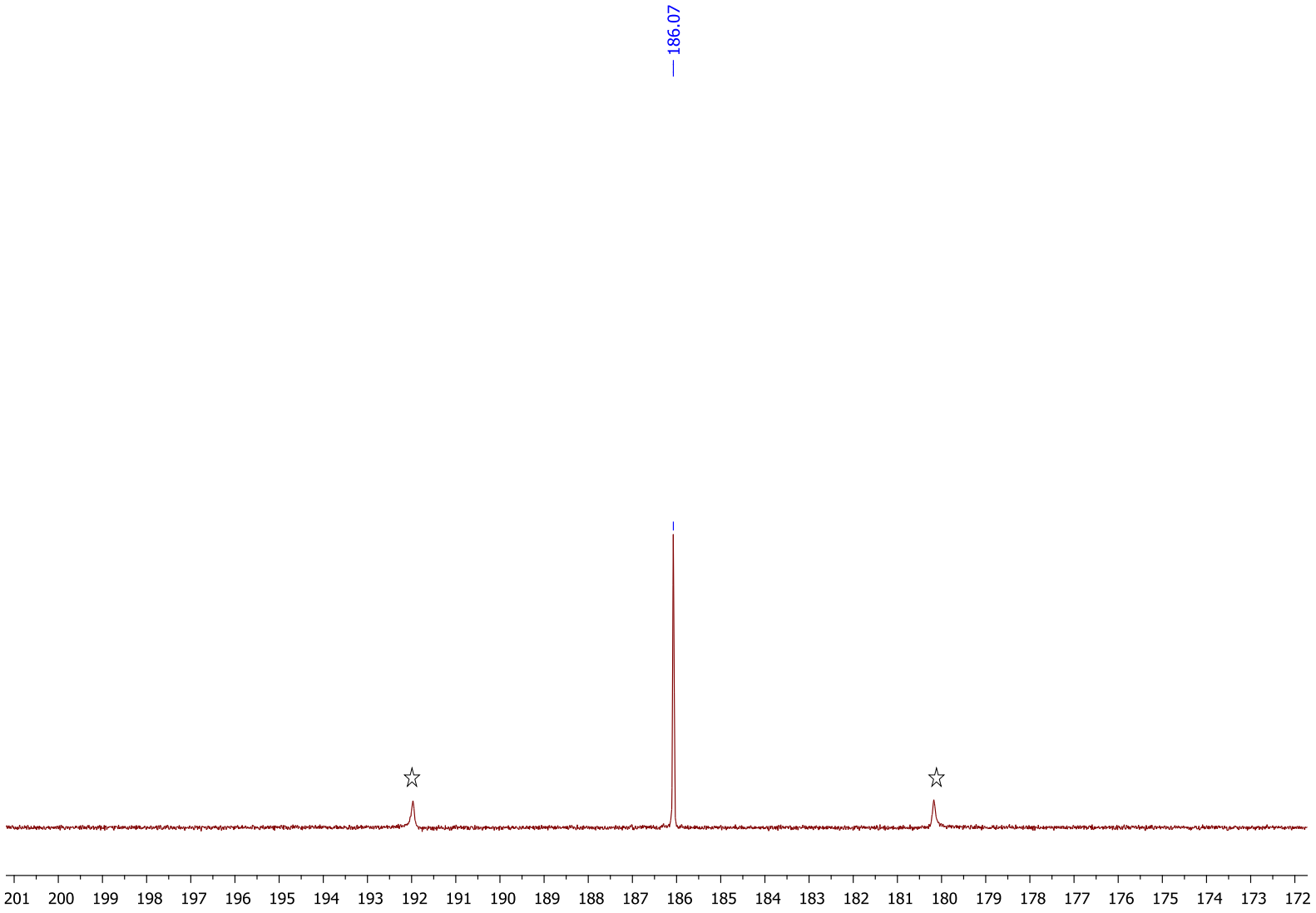

Figure S57. $^{31}P\{^{1}H\}$ NMR spectrum of **3**[$B(Ar^{F})_4$] in THF-d_8 at -25 °C.

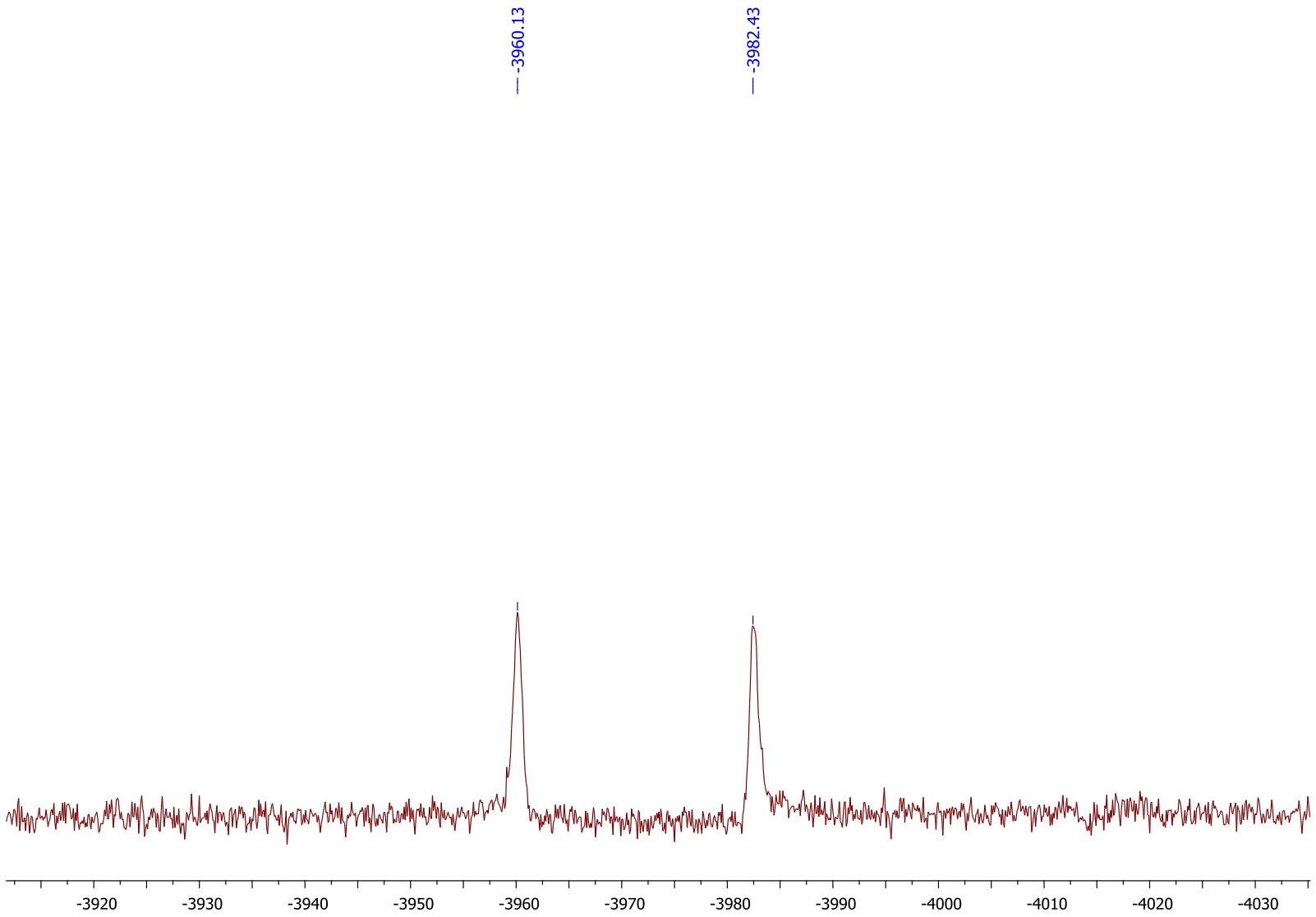

Figure S58. $^{195}Pt\{^{1}H\}$ NMR spectrum of **3**[$B(Ar^F)_4$] in THF-d_8 at -25 °C.

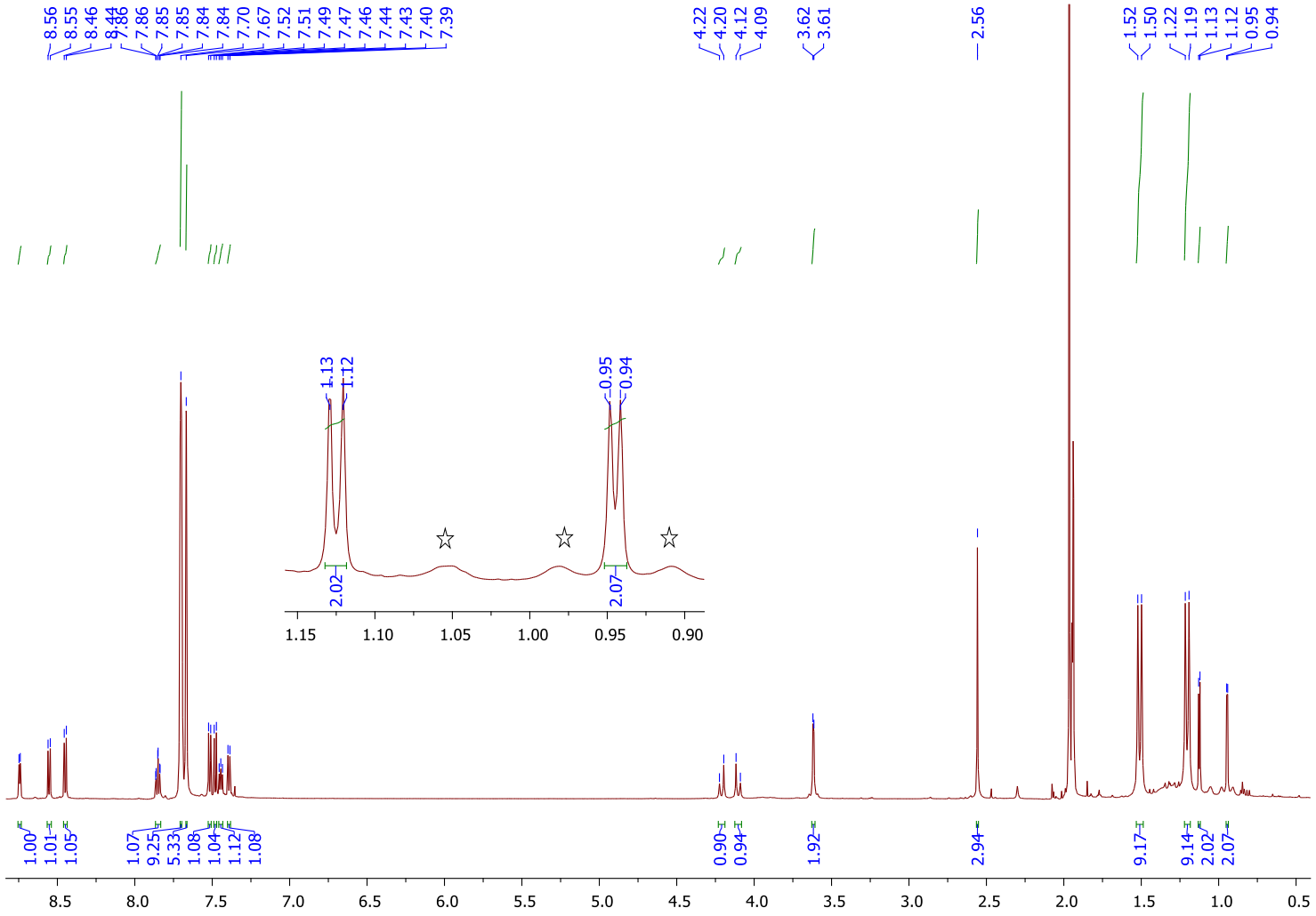

Figure S59. ^{1}H NMR spectrum of **3**[B(Ar^{F})$_4$] in CD_3CN at - 25 °C. Pt satellites are marked with stars.

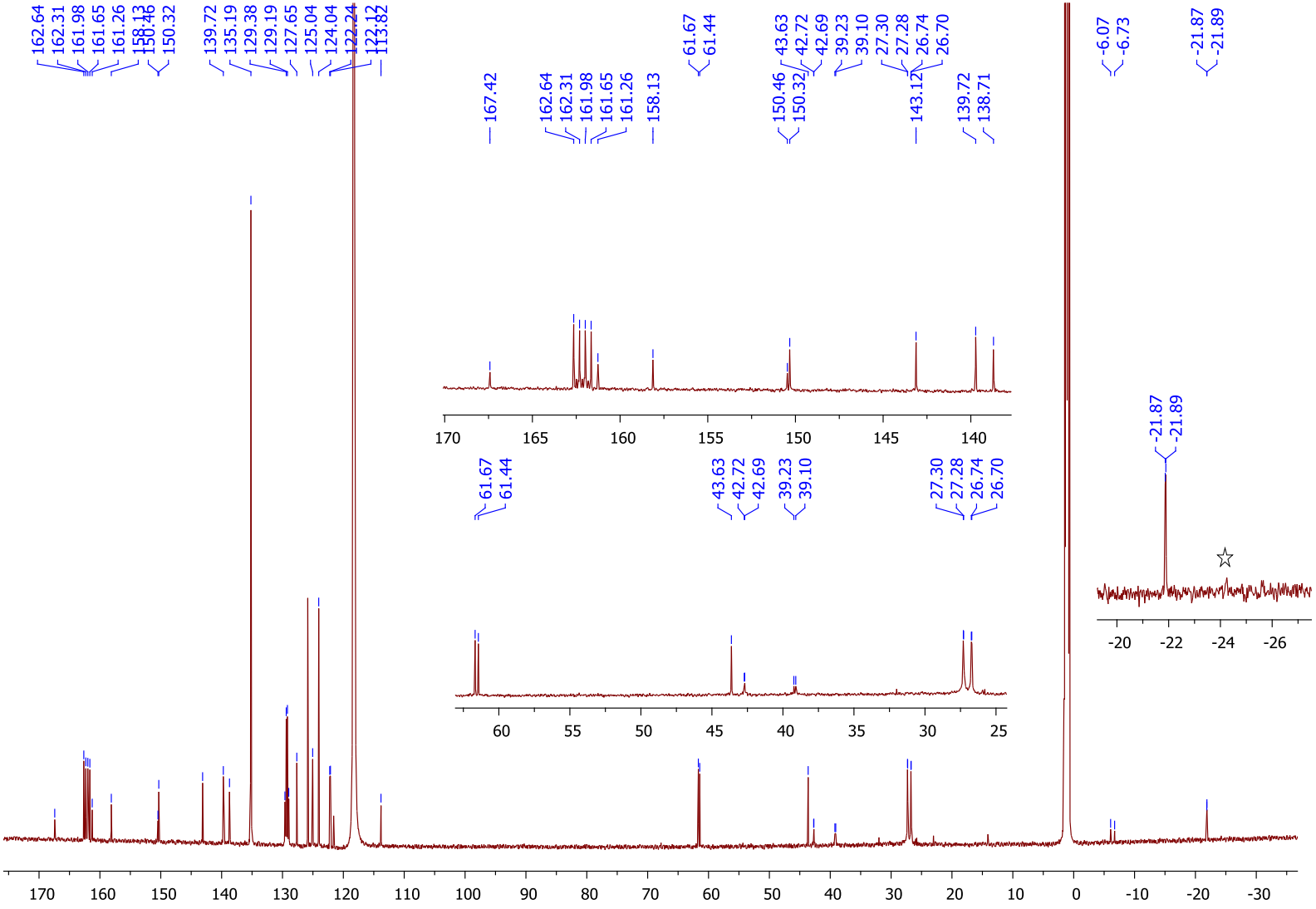

Figure S60. $^{13}C\{^{1}H\}$ NMR spectrum of **3**[$B(Ar^{F})_4$] in CD_3CN at -25 °C. Pt satellites are marked with stars.

Selective 1D-difference NOE experiments of 3[B(Ar^F)$_4$] in THF-d_8:

The orientation of the methyl group relative to the *tert*-butyl group was determined by difference NOE 1D experiments. Irradiation of a resonance at 1.59 ppm *tert*-butyl group induced enhancement (positive NOE) of another *tert*-butyl group at 1.30 ppm and a methyl group at 1.23 ppm.

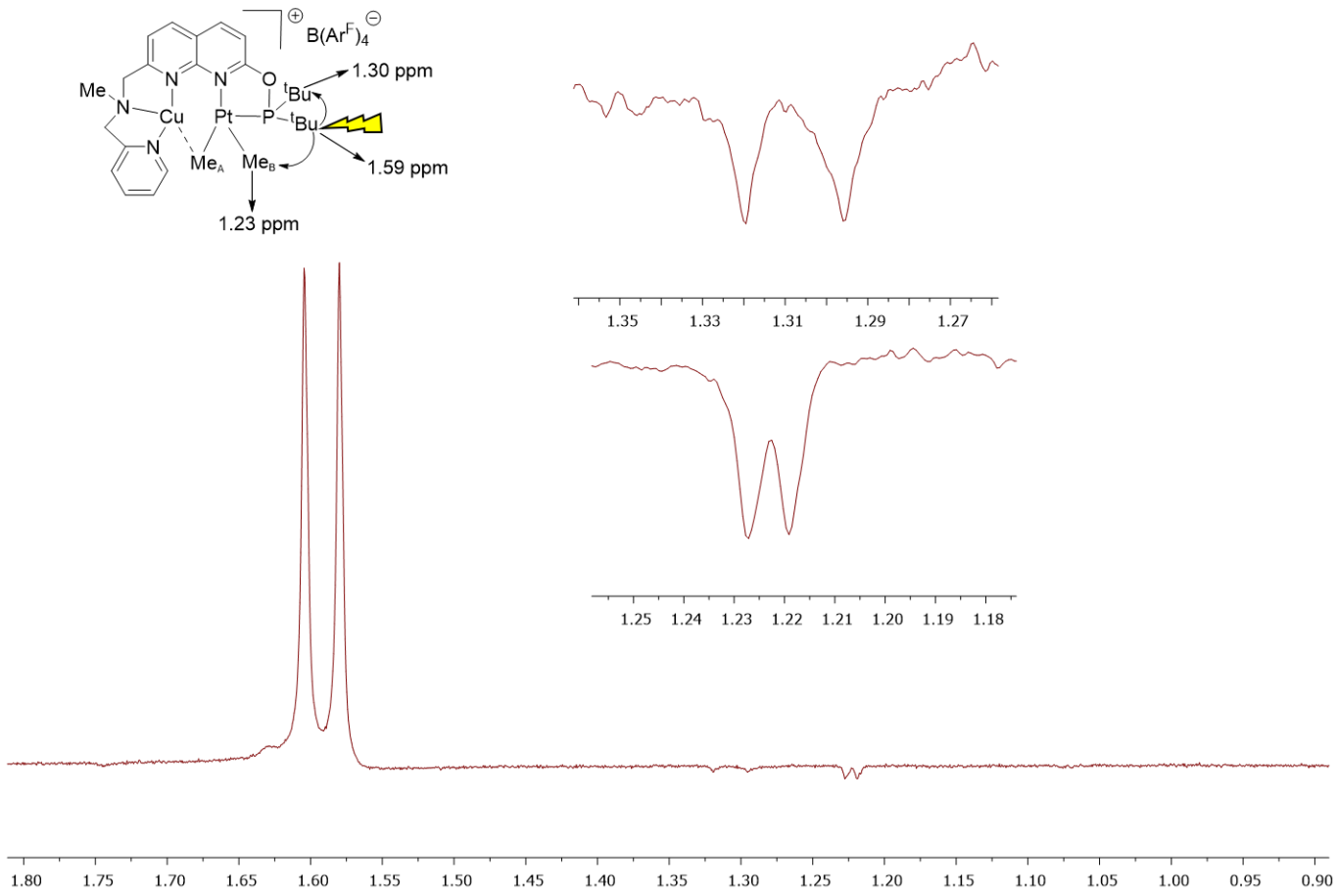

Figure S61. 1D-NOE NMR spectrum of **3**·[B(Ar^F)$_4$] in THF-d_8 at -25 °C.

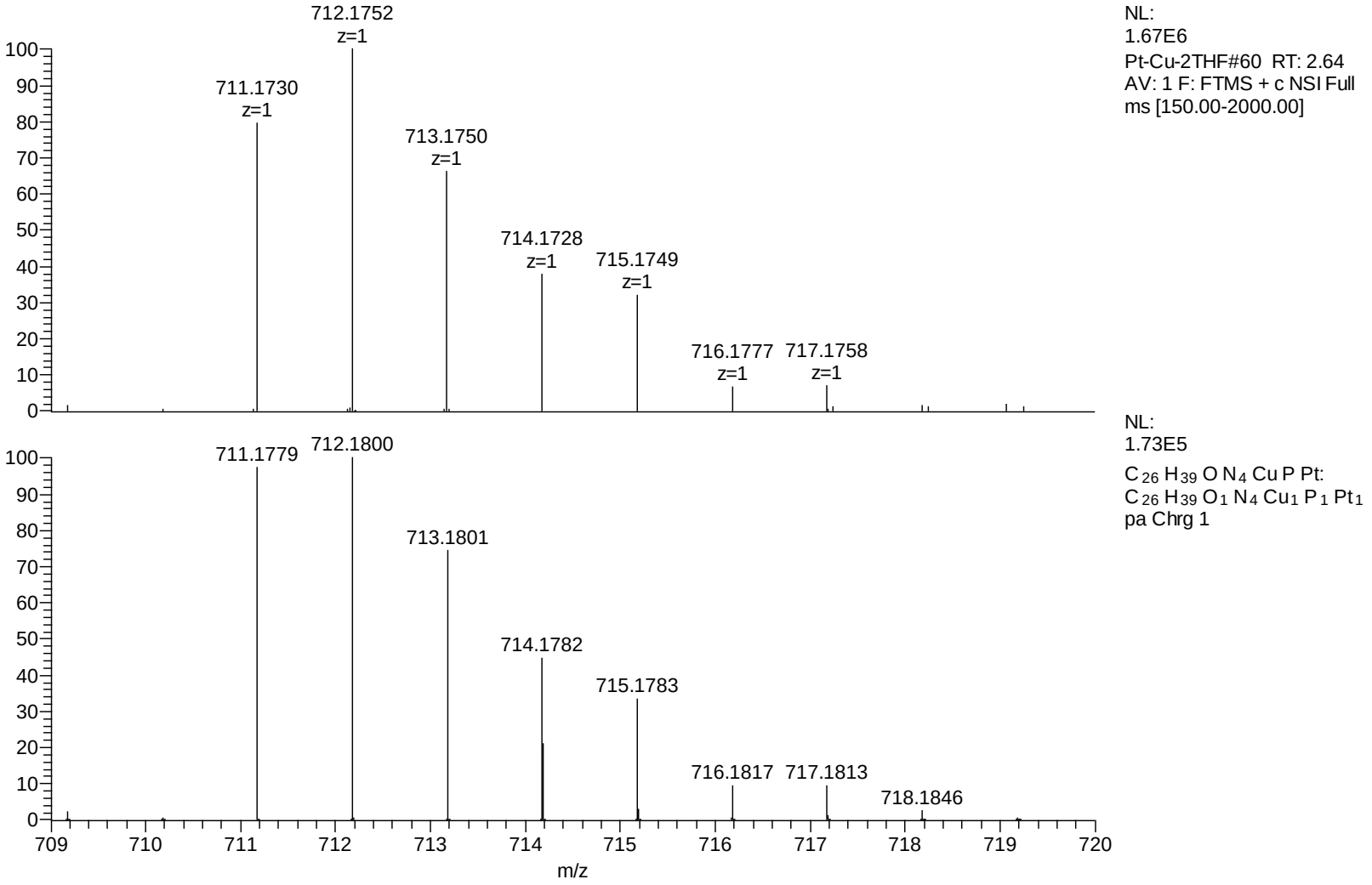

Figure S62. ESI-(HR)MS spectrum of a THF solution of **3**[B(Ar^F)$_4$] (top) and simulated spectrum for $C_{26}H_{39}ON_4PPtCu^+$ (bottom).

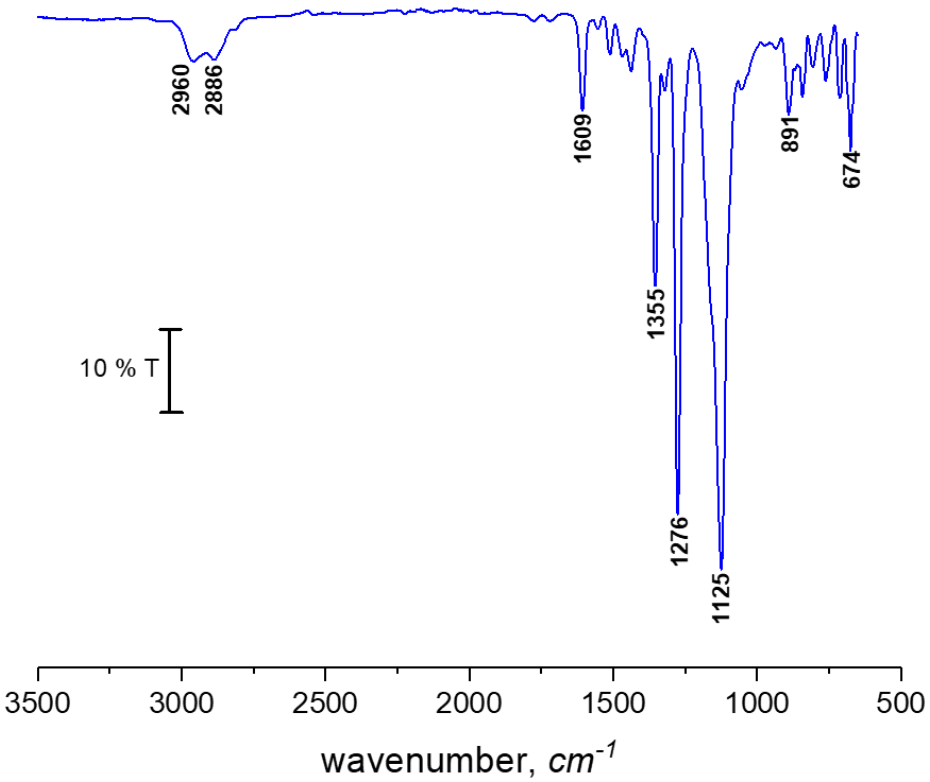

Figure S63. ATR FT-IR transmittance spectrum of **3**[B(Ar^F)$_4$].

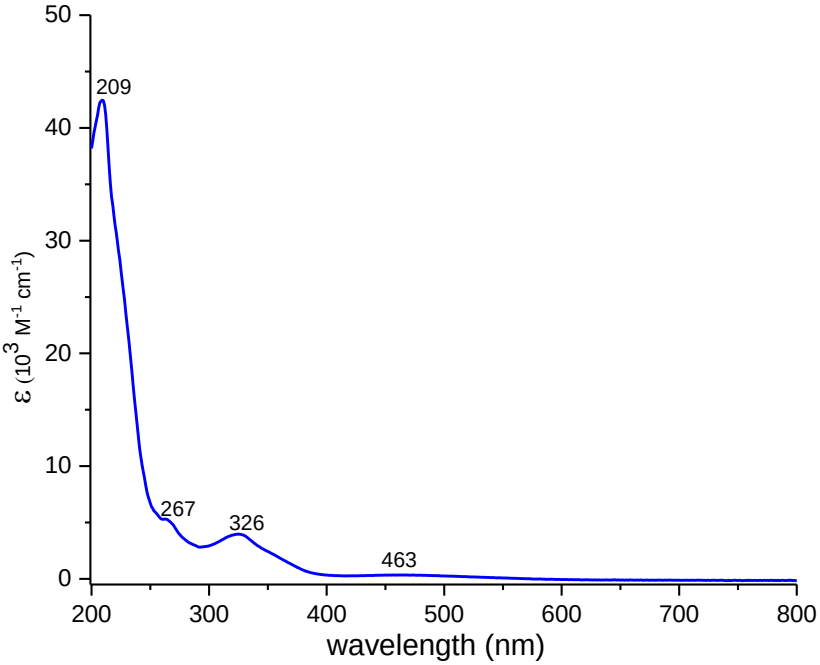

Figure S64. UV-vis absorbance spectrum for **3**[B(Ar^F)$_4$] in MeCN.

Synthesis of [(L)CuPtMe$_2$][BF$_4$], 3[BF$_4$]

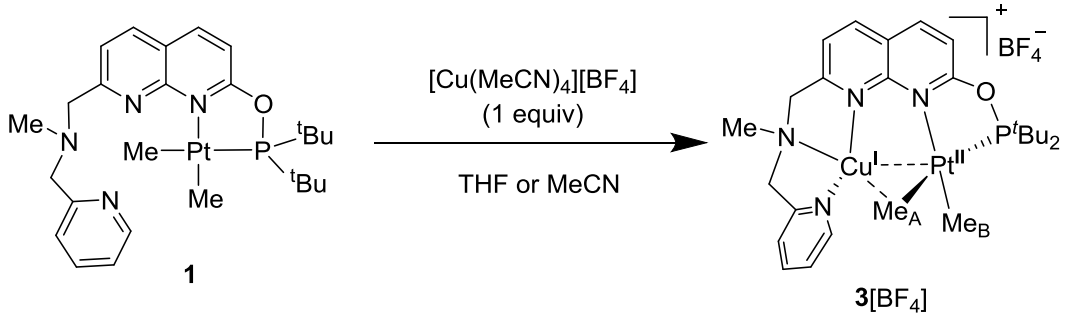

Scheme **S7.** Formation of **3**·[BF$_4$].

In a 20 mL vial, [Cu(MeCN)$_4$][BF$_4$] (48.5 mg, 0.0778 mmol) and **1** (24.4 mg, 0.0778 mmol) were dissolved in THF (4 mL) to give a brown solution which was stirred at RT for 20 min. The solvent is removed under vacuum, and the brown color viscous liquid was then dissolved in minimum amount of THF (1 mL) and precipitated with hexane (4 x 2 mL). The remaining liquid was decanted, and brown color solid was dried vacuum to give complex **3**·[BF$_4$] (44.3 mg, 0.0553 mmol, 71%). Crystal suitable for X-ray diffraction study were grown by slow evaporation of a THF solution at –30 °C inside the glovebox fridge. For the NMR analysis the sample was prepared *in situ* in THF-d_8 or CD_3CN to avoid slight decomposition of the complex **3**[BF$_4$] observed during prolonged evaporation and workup.

^{1}H NMR (600 MHz, THF-d_8, -25 °C) δ: 8.93 (d, $^3J_{HH}$ = 8.7 Hz, 1H, CH_{Naph}), 8.80 (d, $^3J_{HH}$ = 4.8 Hz, 1H, CH_{Py}), 8.77 (d, $^3J_{HH}$ = 8.2 Hz, 1H, CH_{Naph}), 7.95 (td, $^3J_{HH}$ = 7.7 Hz, $^4J_{HH}$ = 1.5 Hz, 1H, CH_{Py}), 7.78 (d, $^3J_{HH}$ = 8.2 Hz, 1H, CH_{Naph}), 7.65 (d, $^3J_{HH}$ = 8.7 Hz, 1H, CH_{Naph}), 7.59 (d, $^3J_{HH}$ = 7.7 Hz, 1H, CH_{Py}), 7.52 (t, $^3J_{HH}$ = 6.2 Hz, 1H, CH_{Py}), 4.34 (m, AB system, 2H, CH_2), 3.84 (d, $^2J_{HH}$ = 15.2 Hz, 1H, CH_2), 3.76 (d, $^2J_{HH}$ = 15.2 Hz, 1H, CH_2), 2.64 (s, 3H, N-CH_3), 1.57 (d, $^3J_{PH}$ = 14.4 Hz, 9H, C(CH_3)$_3$), 1.25 (d, $^3J_{PH}$ = 14.4 Hz, 9H, C(CH_3)$_3$), 1.18 (d, $^3J_{PH}$ = 5.1 Hz, $^2J_{PtH}$ = 82.4 Hz, 3H, Pt-Me_B), 1.04 (d, $^3J_{PH}$ = 3.8 Hz, $^2J_{PtH}$ = 36.2 Hz, 3H, Pt-Me_A).

^{13}C{^{1}H} NMR (151 MHz, THF-d_8, -25 °C) δ: 167.79 ($C_{q,Naph}$), 162.55 ($C_{q,Naph}$), 159.28 ($C_{q,Py}$), 150.70 ($C_{q,Naph}$), 150.35 ($C_{H,Py}$), 144.76 ($C_{H,Naph}$), 140.93 ($C_{H,Naph}$), 139.17 ($C_{H,Py}$), 125.75 ($C_{H,Py}$), 125.22 ($C_{H,Py}$), 123.09 ($C_{H,Naph}$), 122.27 ($C_{q,Naph}$), 113.80 ($C_{H,Naph}$), 62.16 (CH_2), 61.81 (CH_2), 44.11 (N-CH_3), 43.15 (d, $^1J_{PC}$ = 5.5 Hz, ***C***(CH_3)$_3$), 39.80 (d, $^1J_{PC}$ = 18.9 Hz, ***C***(CH_3)$_3$), 27.79 (d,$^2J_{PC}$ = 4.9 Hz, C(***C***H_3)$_3$), 27.20 (d,$^2J_{PC}$ = 6.1 Hz, C(***C***H_3)$_3$), -5.62 (d, $^2J_{PC}$ = 99.4 Hz, Pt-Me_A), -21.32 (d, $^2J_{PC}$ = 3.5 Hz, $^1J_{PtC}$ = 719.5 Hz, Pt-Me_B). Pt satellite for -5.62 ppm signal were not clearly seen due to low intensity.

^{31}P{^{1}H} NMR (242 MHz, THF-d_8, -25 °C) δ: 184.9 ($^1J_{PtP}$ = 2866 Hz).

^{195}Pt{^{1}H} NMR (129 MHz, THF-d_8, -25 °C) δ: -3971.4 (d, $^1J_{PtP}$ = 2866 Hz).

^{1}H NMR (600 MHz, CD_3CN, -25 °C) δ: 8.70 (d, $^3J_{HH}$ = 4.9 Hz, 1H, CH_{Py}), 8.55 (d, $^3J_{HH}$ = 8.7 Hz, 1H, CH_{Naph}), 8.45 (d, $^3J_{HH}$ = 8.2 Hz, 1H, CH_{Naph}), 7.86-7.82 (m, 1H, CH_{Py}), 7.50 (d, $^3J_{HH}$ = 8.2 Hz, 1H, CH_{Naph}), 7.46 (d, $^3J_{HH}$ = 8.7 Hz, 1H, CH_{Naph}), 7.44-7.41 (m, 1H, CH_{Py}), 7.38 (d, $^3J_{HH}$ = 7.8 Hz, 1H, CH_{Py}), 4.18 (d, $^2J_{HH}$ = 16.7 Hz, 1H, CH_2), 4.08 (d, $^2J_{HH}$ = 16.7 Hz, 1H, CH_2), 3.59 (m, AB system, 2H, CH_2), 2.52 (s, 3H, N-CH_3), 1.48 (d, $^3J_{PH}$ = 14.6 Hz, 9H, C(CH_3)$_3$), 1.18 (d, $^3J_{PH}$ = 14.6 Hz, 9H, C(CH_3)$_3$), 1.08 (d, $^3J_{PH}$ = 5.1 Hz, $^2J_{PtH}$ = 84.1 Hz, 3H, Pt-Me_B), 0.90 (d, $^3J_{PH}$ = 3.7 Hz, $^2J_{PtH}$ = 44.1 Hz, 3H, Pt-Me_A).

^{13}C{^{1}H} NMR (151 MHz, CD_3CN, -25 °C) δ: 167.41 ($C_{q,Naph}$), 161.28 ($C_{q,Naph}$), 158.15 ($C_{q,Py}$), 150.43 ($C_{q,Naph}$), 150.30 ($C_{H,Py}$), 143.17 ($C_{H,Naph}$), 139.76 ($C_{H,Naph}$), 138.73 ($C_{H,Py}$), 125.06 ($C_{H,Py}$), 122.15

($C_{H,Naph}$), 121.60 ($C_{q,Naph}$), 113.81 ($C_{H,Naph}$), 61.66 (CH_2), 61.43 (CH_2), 43.6 (N-CH_3), 42.71 (d, $^1J_{PC}$ = 3.9 Hz, ***C***$(CH_3)_3$), 39.15 (d, $^1J_{PC}$ = 18.8 Hz, ***C***$(CH_3)_3$), 27.30 (d,$^2J_{PC}$ = 2.8 Hz, C(***C***$H_3)_3$), 26.73 (d,$^2J_{PC}$ = 5.4 Hz, C(***C***$H_3)_3$), -6.37 (d, $^2J_{PC}$ = 99.1 Hz, $^1J_{PtC}$ = 504.78, Pt-Me_A), -21.87 (d, $^2J_{PC}$ = 3.5 Hz, $^1J_{PtC}$ = 710.8 Hz, Pt-Me_B). Two pyridine carbon signals overlap with each other at *ca.* 125 ppm confirmed by HMQC experiment.

Elemental Analysis: Expt (Calc): [$C_{30}H_{47}BCuN_4O_2F_4PPt$]: C 41.13 (41.32), H 5.50 (5.43), N 6.96 (6.42).
ESI-HRMS (m/z pos): Found (Calcd): $C_{26}H_{39}ON_4P^{195}Pt^{63}Cu^+$: 712.1762 (712.1800).
FT-IR (ATR, solid): 2955 (br, w), 2879 (br, w), 1729 (w), 1601 (s), 1581 (m), 1318 (m), 1059 (s), 862 (m), 765 (m) cm^{-1}.
UV-vis (MeCN), λ, nm (ε, $M^{-1}\cdot cm^{-1}$) : 328 (2170), 209 (19620).

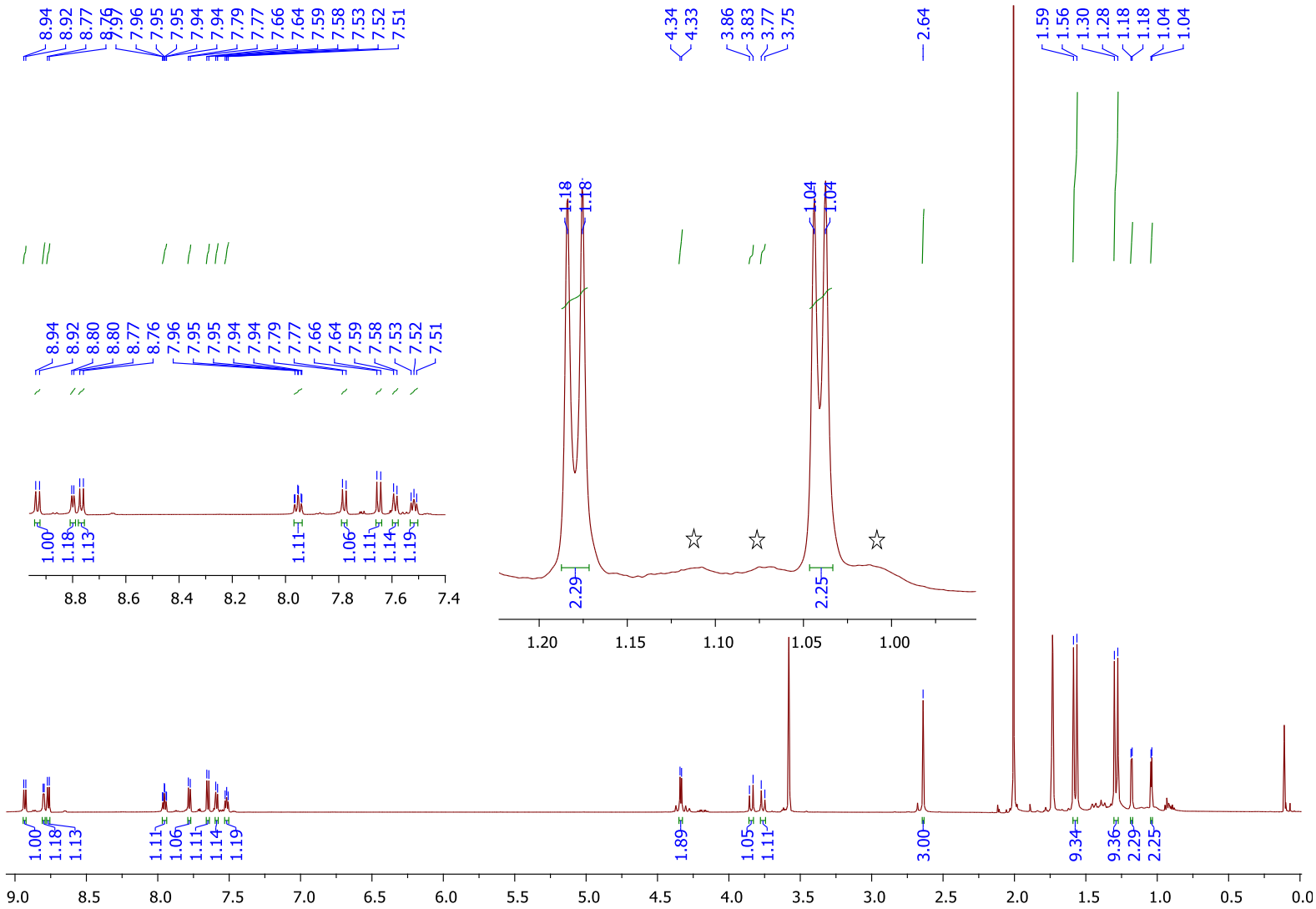

Figure S65. ^{1}H NMR spectrum of **3**[BF_4] in THF-d_8 at -25 °C. The peak at 2 ppm corresponds to free MeCN in the solution of *in situ* generated **3**·[BF_4] formed by dissociation from [$Cu(MeCN)_4$][BF_4] precursor. Pt satellites are marked with stars.

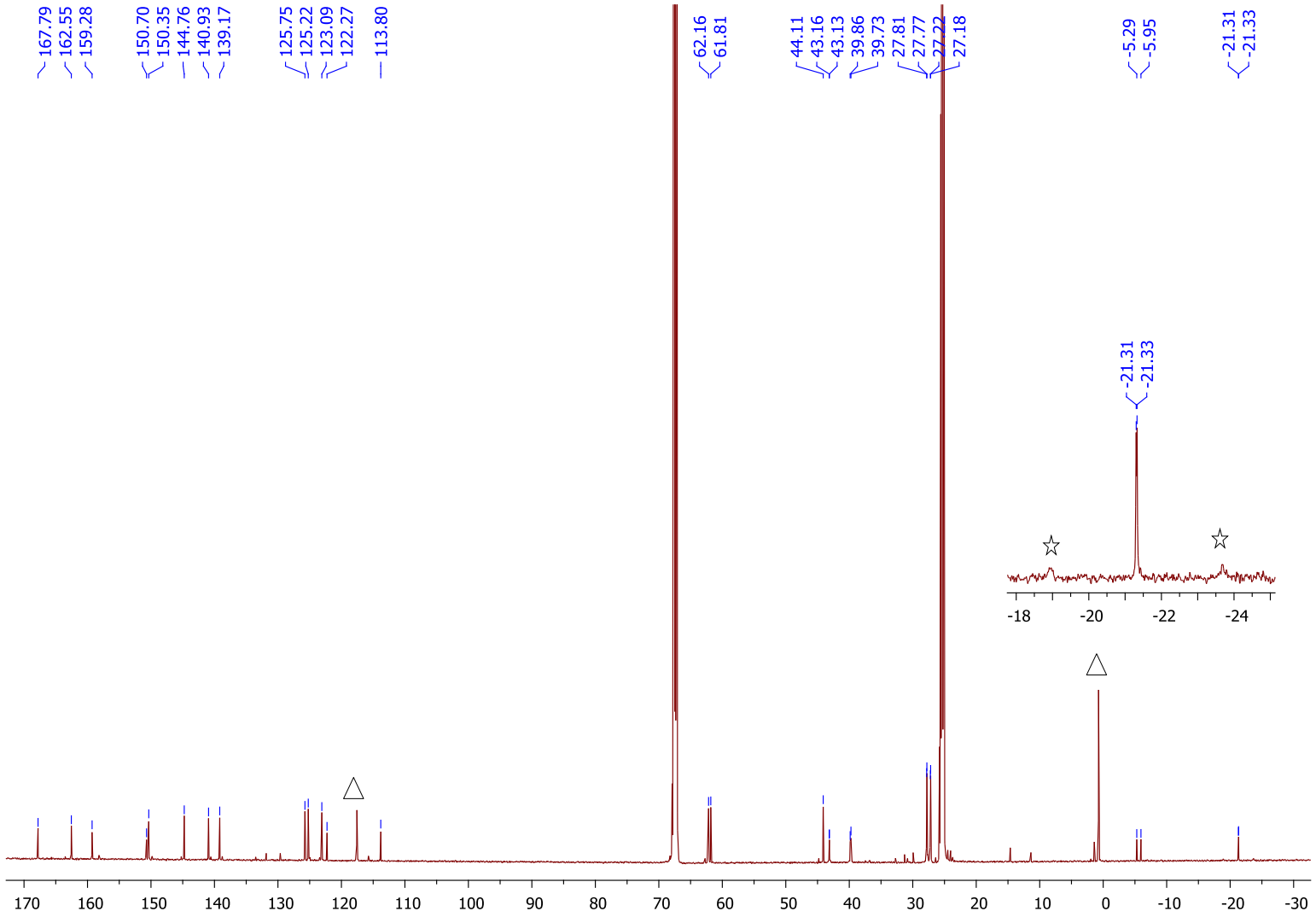

Figure S66. $^{13}C\{^{1}H\}$ NMR spectrum of **3**[BF_4] in THF-d_8 at -25 °C. The peaks marked by triangles correspond to free MeCN in the solution of *in situ* generated **3**·[BF_4] formed by dissociation from [$Cu(MeCN)_4$][BF_4] precursor. Pt satellites are marked with stars.

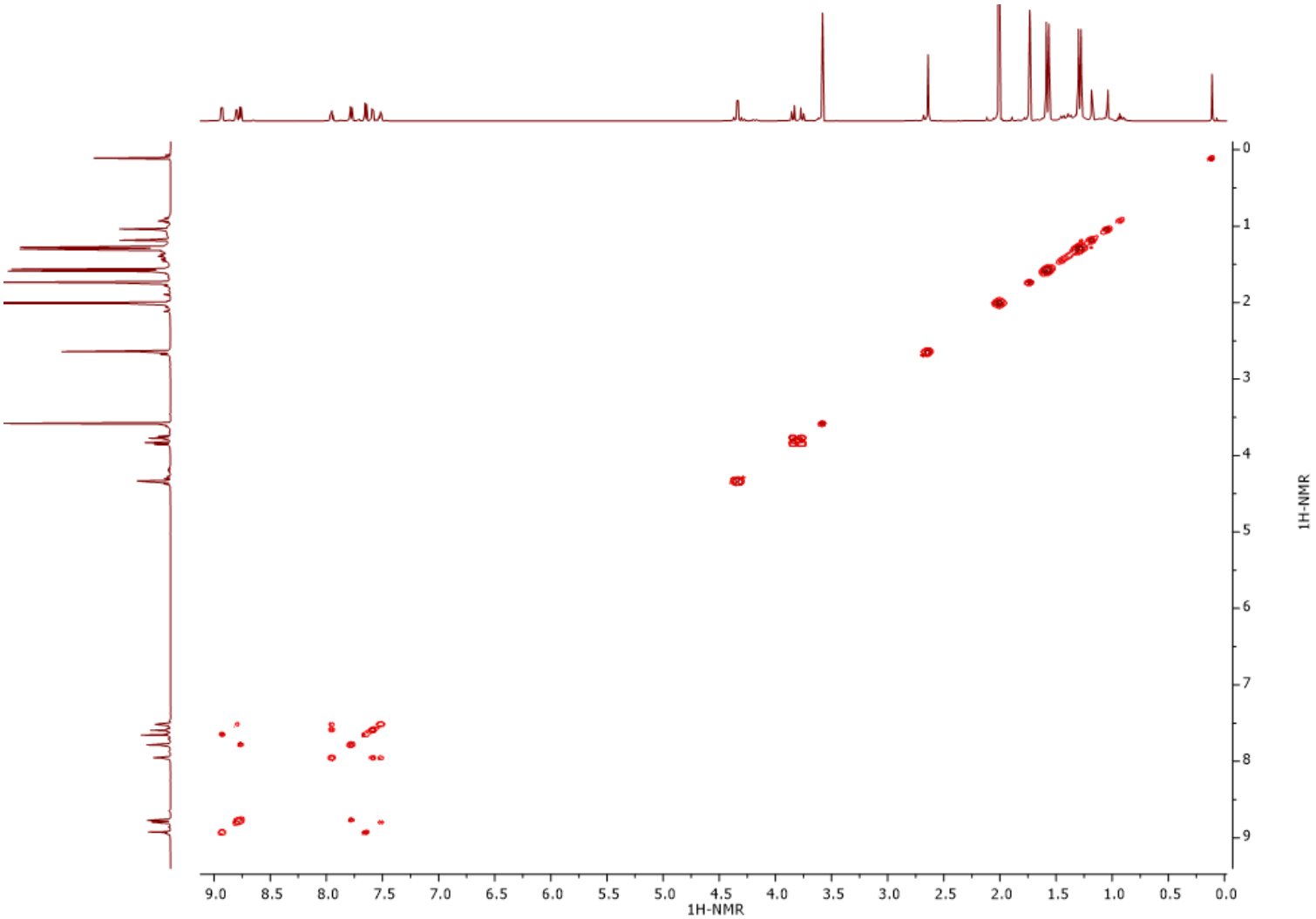

Figure S67. ^{1}H-^{1}H COSY spectrum of **3**[BF_4] in THF-d_8 at -25 °C.

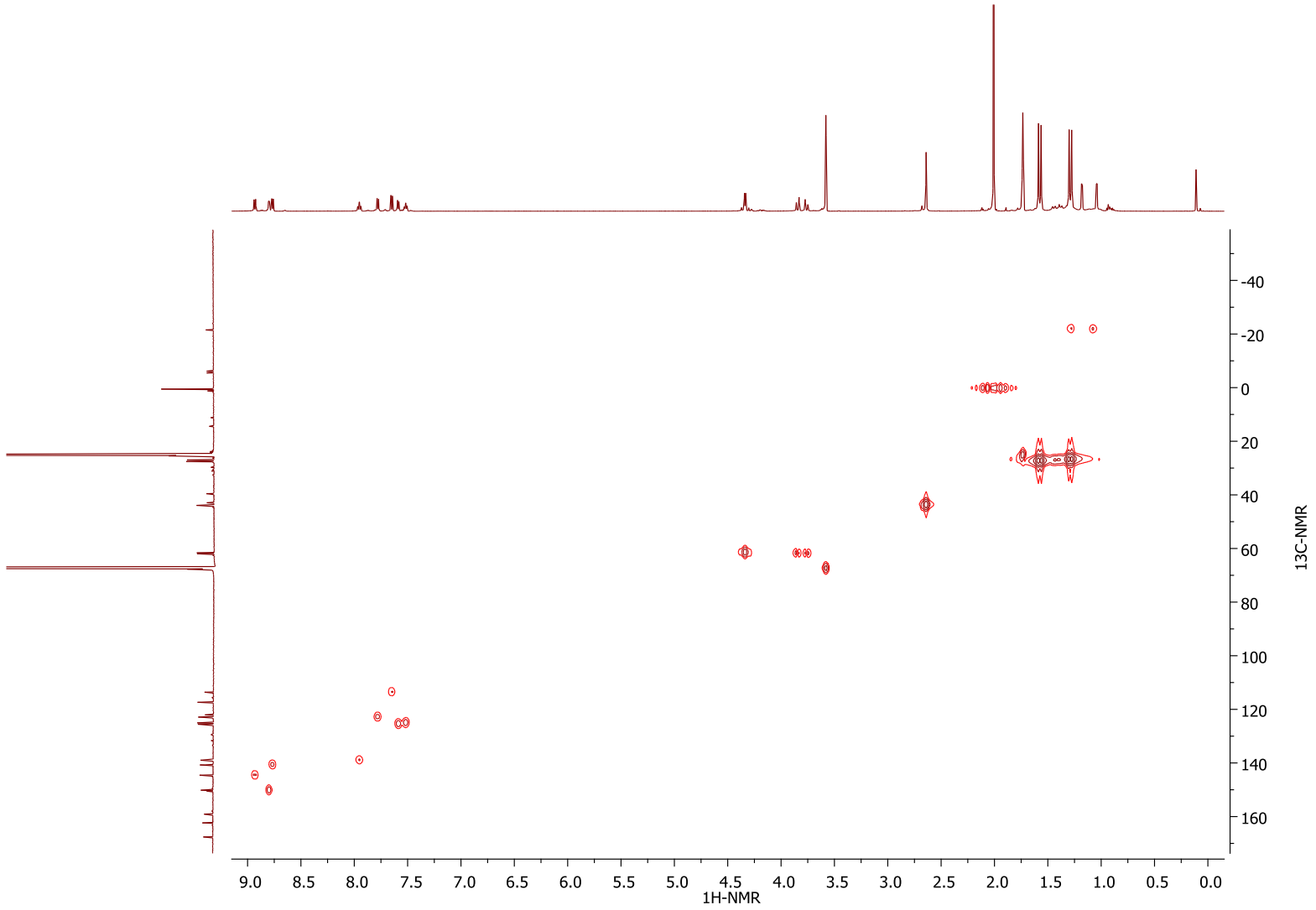

Figure S68. ^{1}H-^{13}C HMQC spectrum of **3**[BF_4] in THF-d_8 at -25 °C.

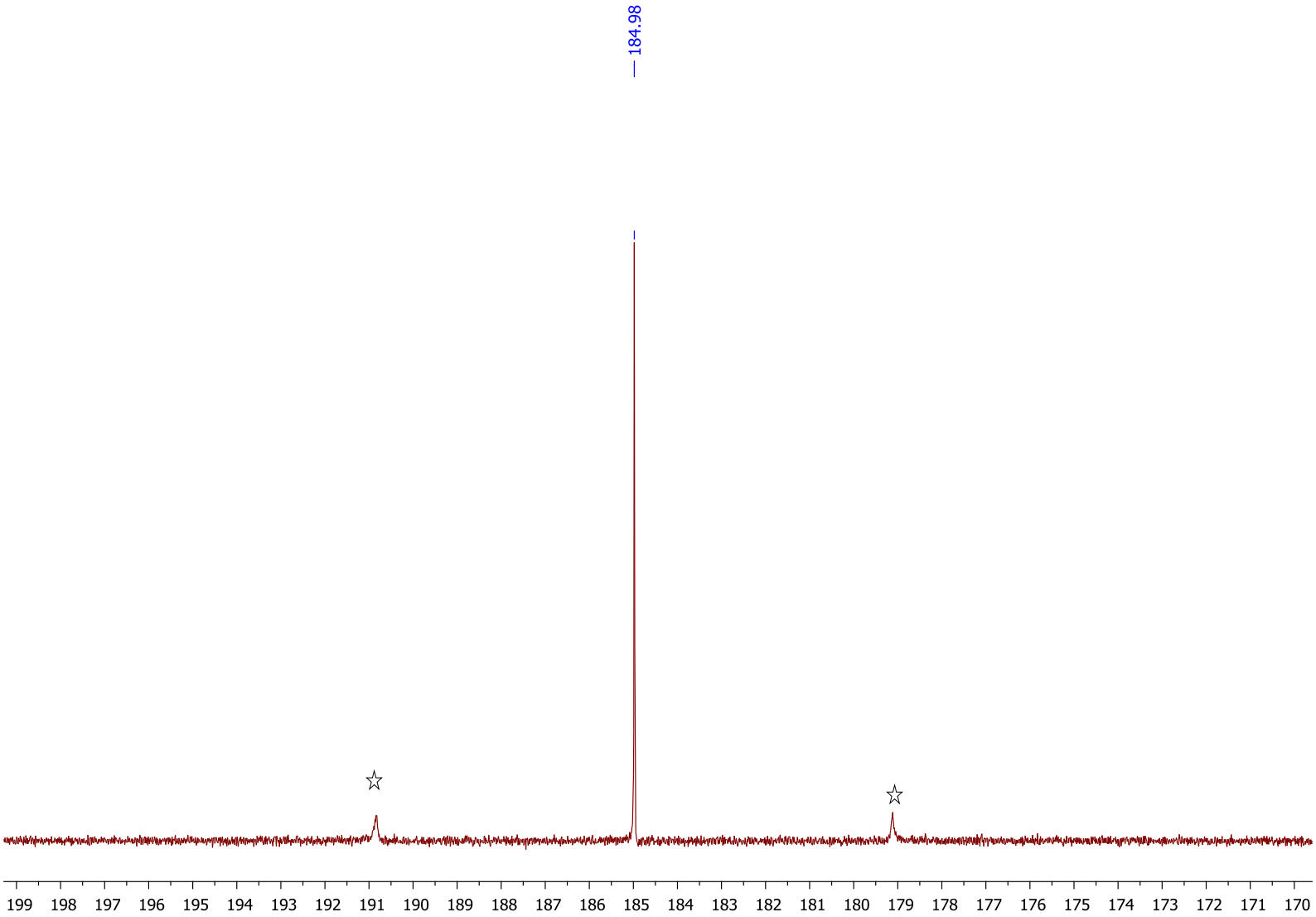

Figure S69. $^{31}P\{^{1}H\}$ NMR spectrum of **3**[BF_4] in THF-d_8 at -25 °C. Pt satellites are marked with stars.

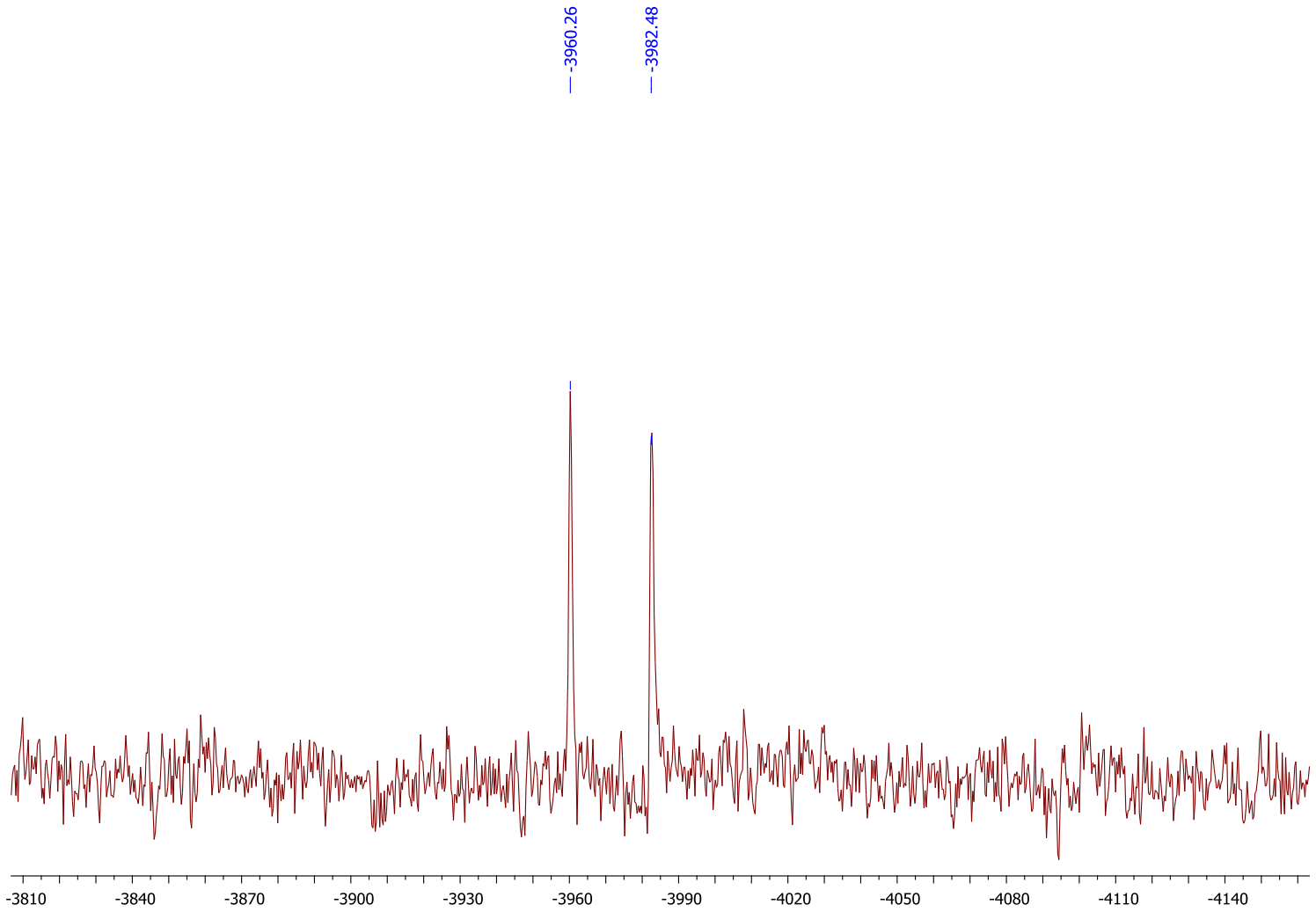

Figure S70. $^{195}Pt\{^{1}H\}$ NMR spectrum of **3**[BF_4] in THF-d_8 at -25 °C.

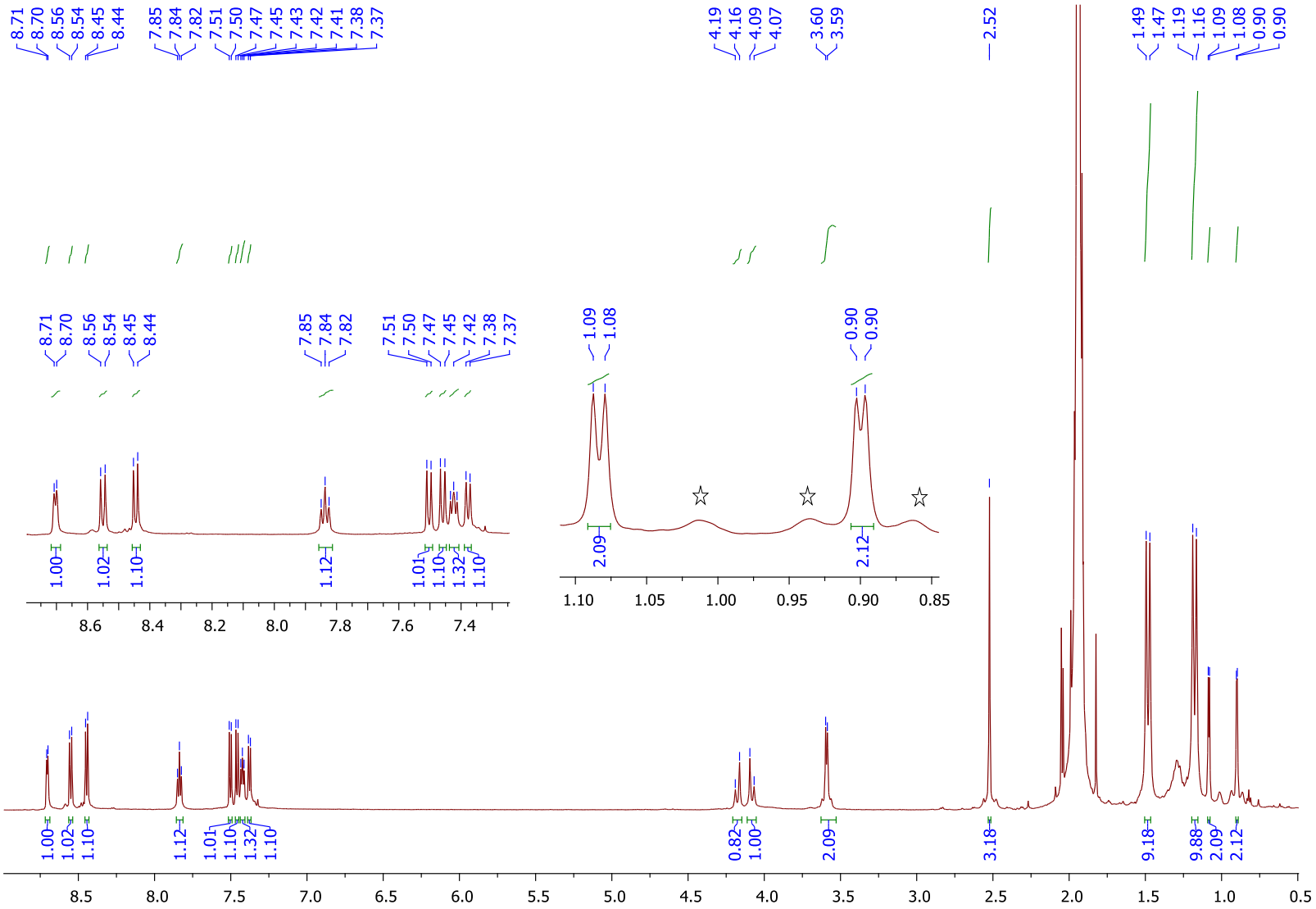

Figure S71. ^{1}H NMR spectrum of **3**[BF_4] in CD_3CN at -25 °C. Pt satellite are marked with stars.

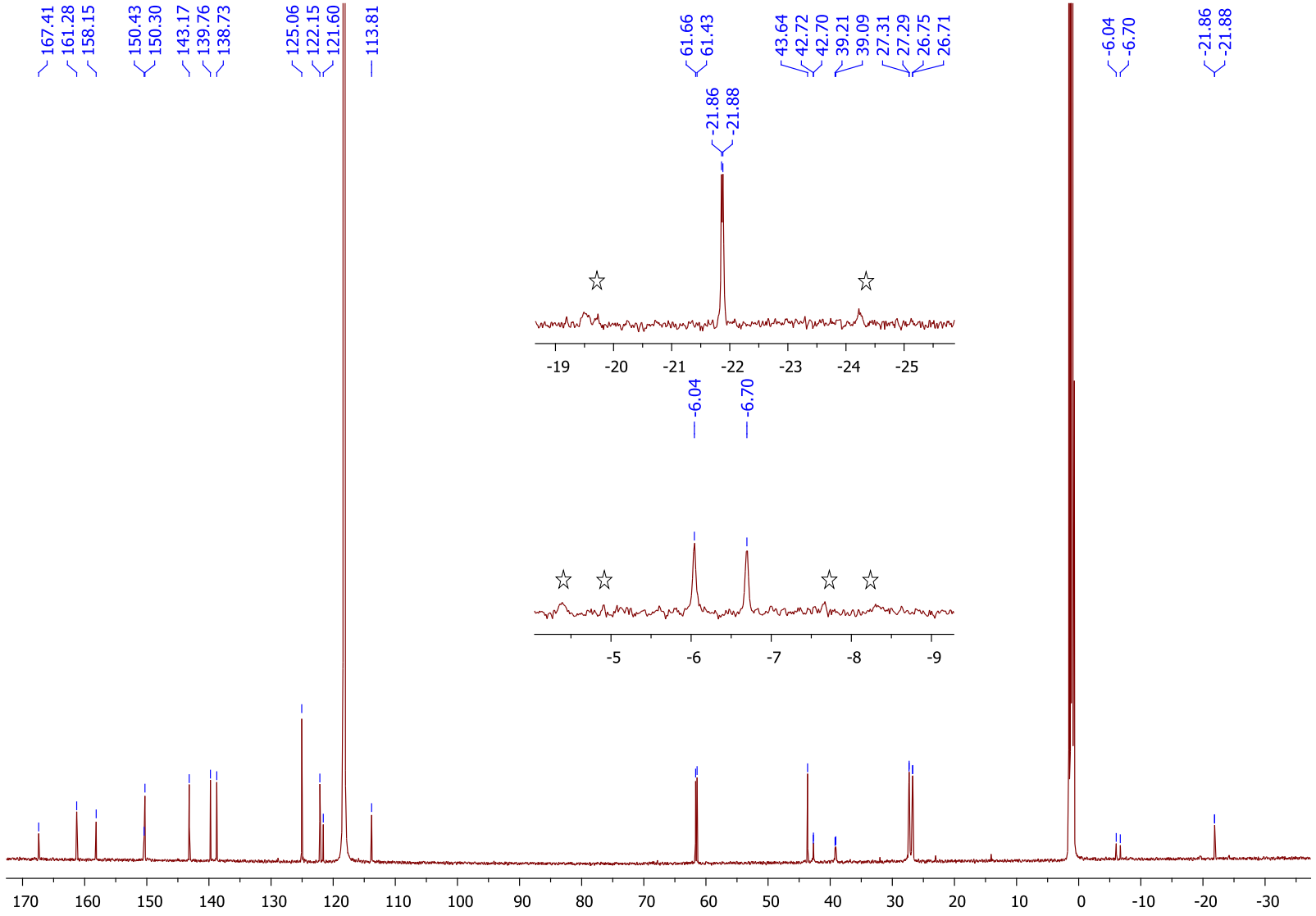

Figure S72. $^{13}C\{^{1}H\}$ NMR spectrum of **3**[BF_4] in CD_3CN at -25 °C. Pt satellites are marked with stars.

Selective 1D-difference NOE experiments of 3[BF_4] in THF-d_8:

The orientation of the methyl group relative to the *tert*-butyl group was determined by difference NOE 1D experiments. Irradiation of a resonance at 1.18 ppm corresponding to one of the Pt-methyl group induced enhancement (positive NOE) of the *tert*-butyl groups at 1.25 ppm, 1.57 ppm and also shows positive enhancement for methyl group at 1.04 ppm. In another experiment Irradiation of the resonance of another Pt-Me group at 1.04 ppm induced enhancement (positive NOE) of another methyl at 1.18 ppm and no other peaks showed NOE.

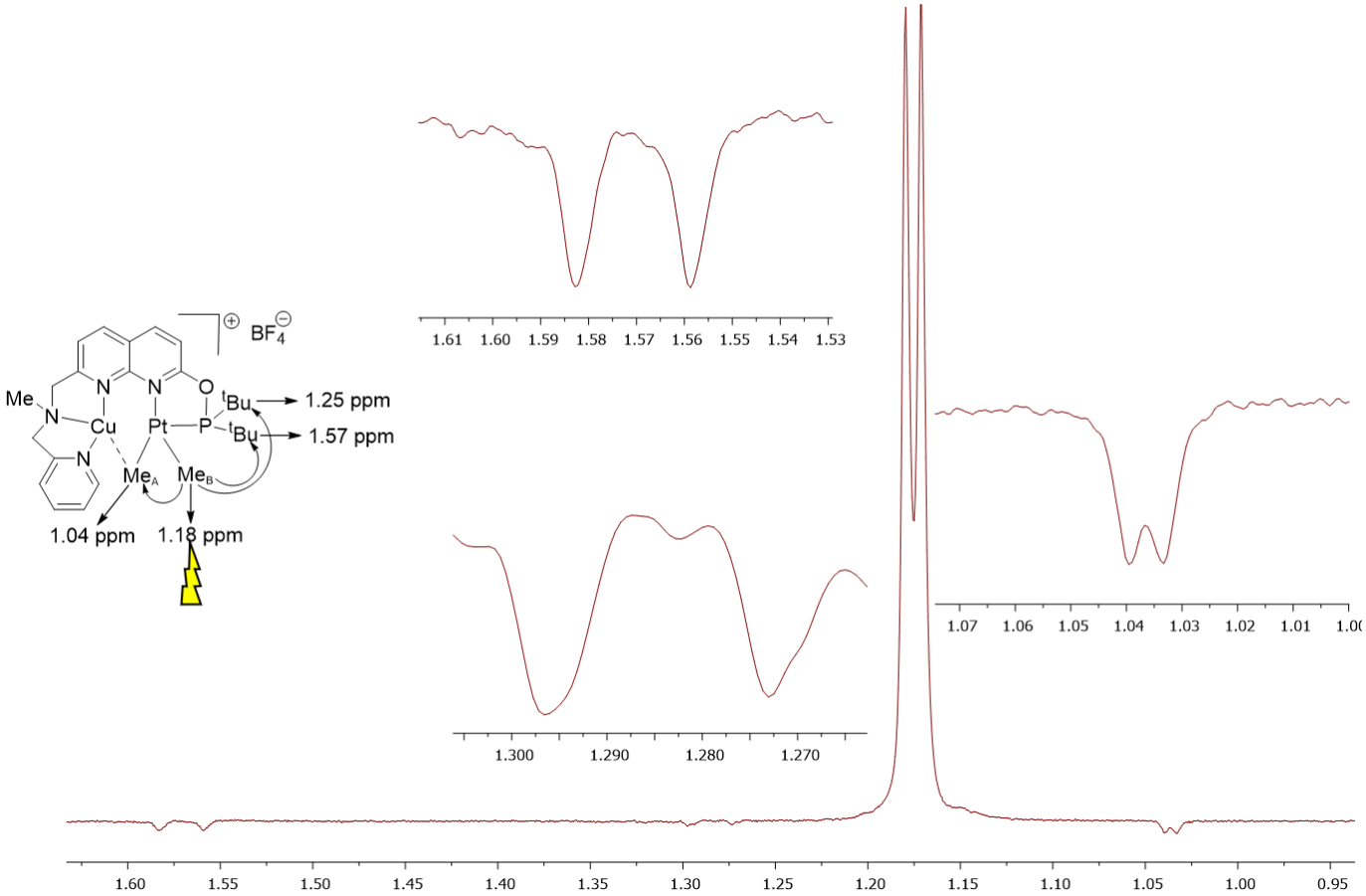

Figure S73. 1D-NOE NMR spectrum of **3**[BF_4] in THF-d_8 at -25 °C.

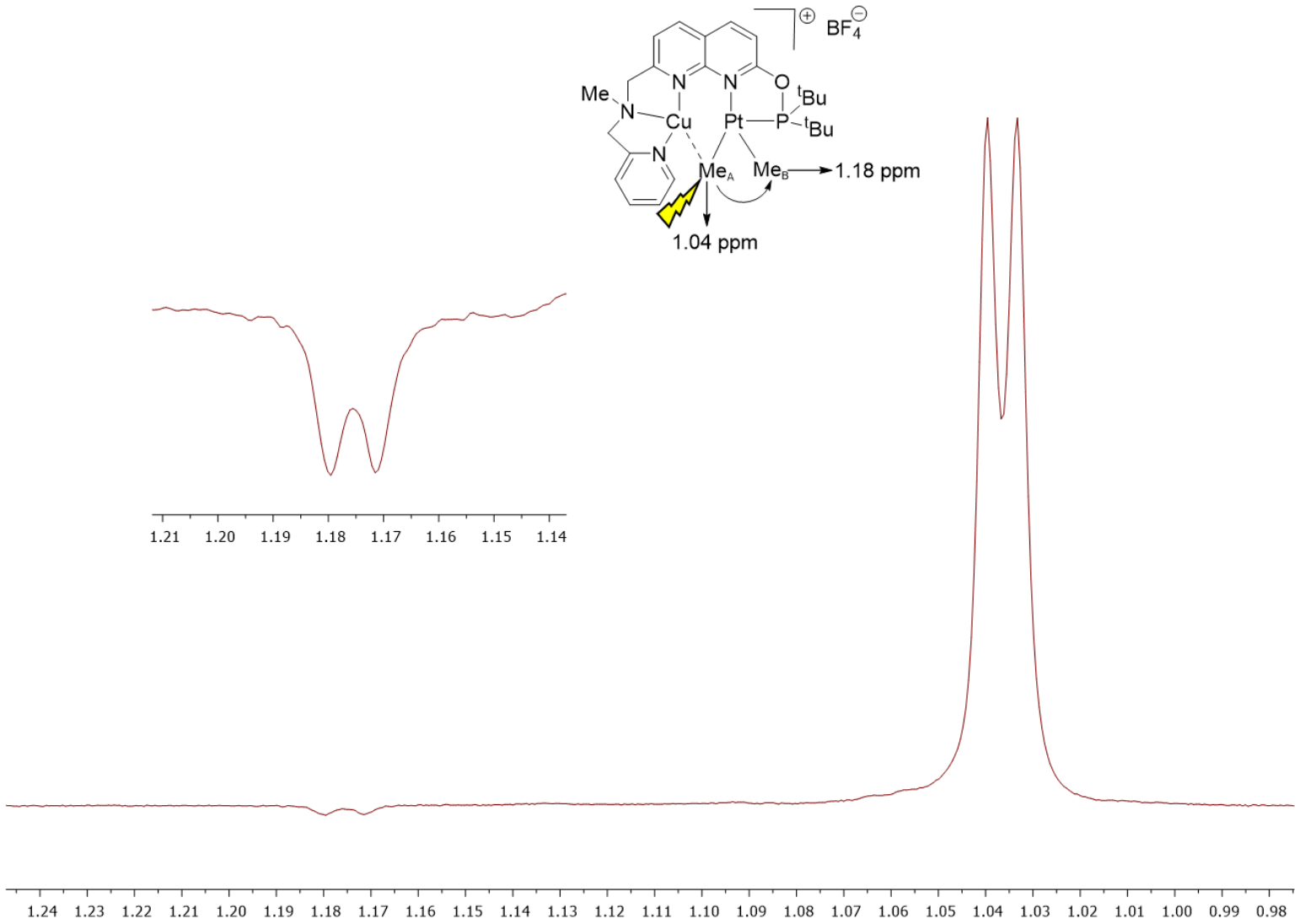

Figure S74. 1D-NOE NMR spectrum of **3**[BF_4] in THF-d_8 at -25 °C.

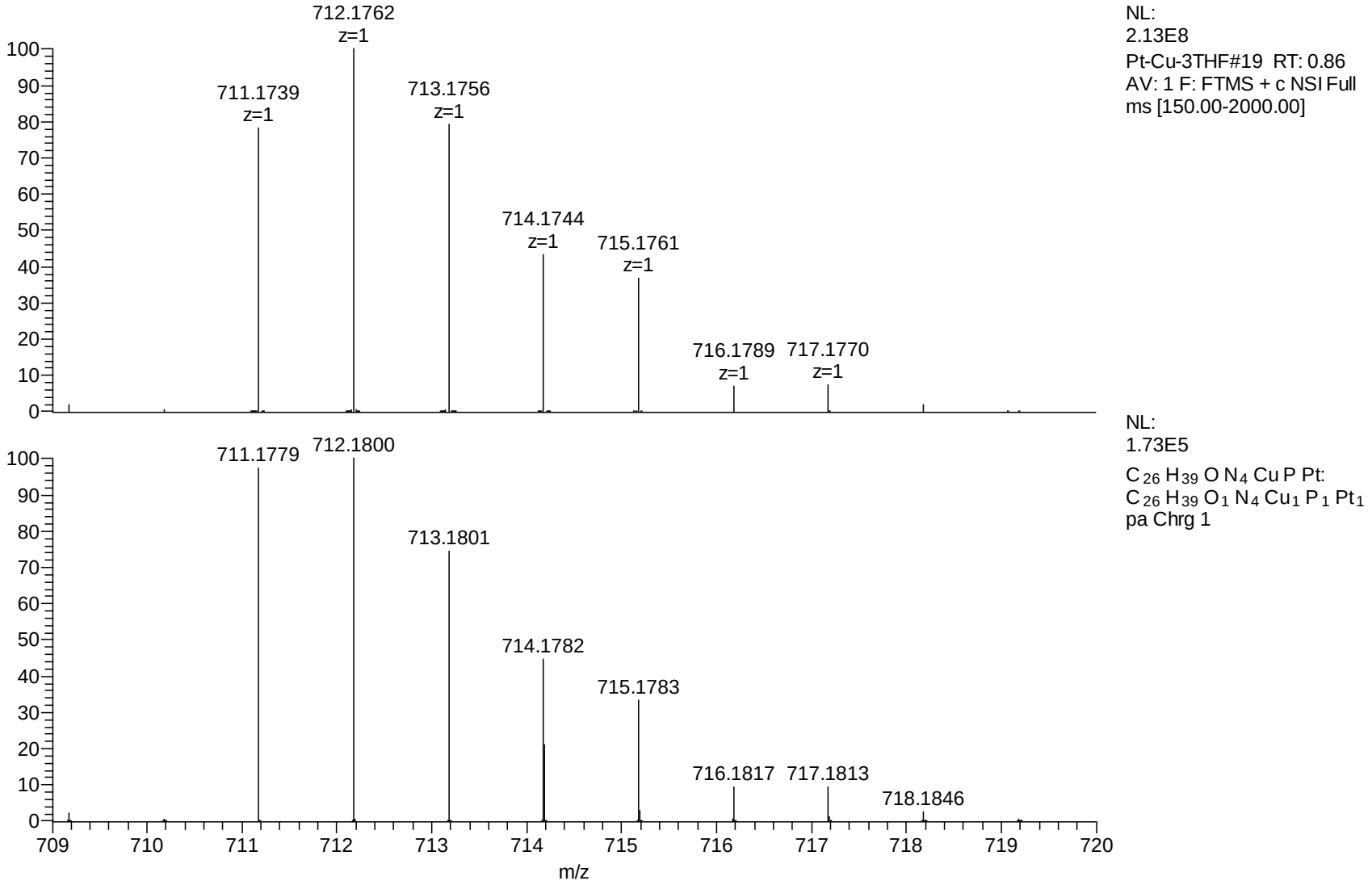

Figure S75. ESI-(HR)MS spectrum of a THF solution of **3**[BF_4] (top) and simulated spectrum for $C_{26}H_{39}ON_4PPtCu^+$ (bottom).

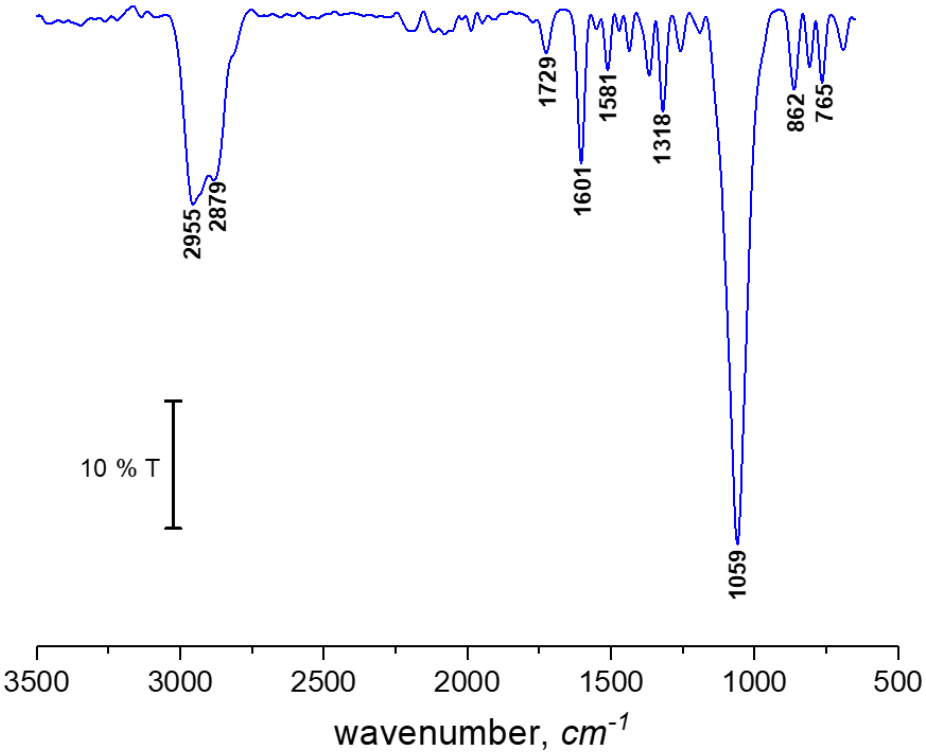

Figure S76. ATR FT-IR transmittance spectrum of **3**[BF_4].

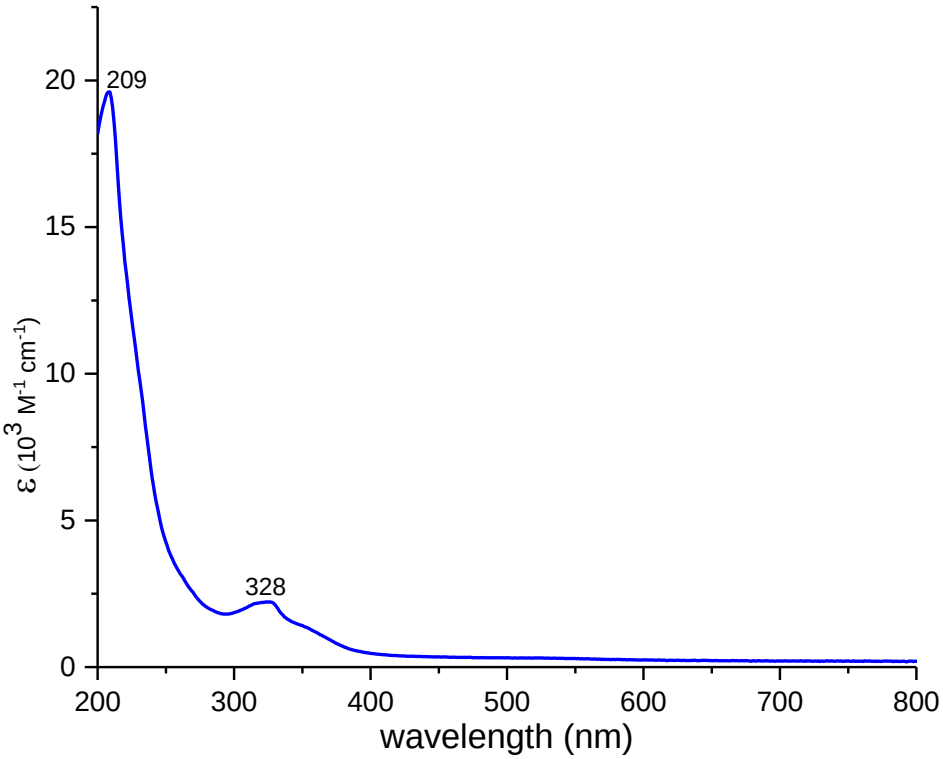

Figure S77. UV-vis absorbance spectrum for **3**[BF_4] in MeCN.

Synthesis of 4

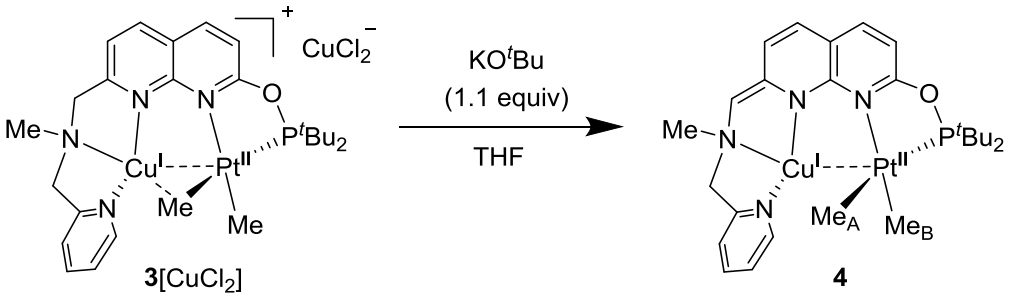

Scheme **S8.** Formation of **4**.

In a 20 mL vial **3**[$CuCl_2$] (100.7 mg, 0.1187 mmol) and KO^{t}Bu (14.6 mg, 0.1306 mmol) were dissolved in THF (4 mL) giving a red solution which was stirred at RT for 1 hour. Inorganic salts were removed via filtration and the solvent is removed under vacuum. The red color viscous solid was dissolved again in ether and left it for crystallization at -30 °C, yielding red color crystals (57.6 mg, 0.0808 mmol, 68 % yield).

^{1}H NMR (600 MHz, THF-d_8, -25 °C) δ: 8.82 (d, $^3J_{HH}$ = 4.9 Hz, 1H, CH_{Py}), 7.87-7.83 (m, 1H, CH_{Py}), 7.45-7.41 (m, 2H, CH_{Py}), 6.74 (d, $^3J_{HH}$ = 7.4 Hz, 1H, CH_{Naph}), 6.25 (d, $^3J_{HH}$ = 9.2 Hz, 1H, CH_{Naph}), 5.80 (d, $^3J_{HH}$ = 9.2 Hz, 1H, CH_{Naph}), 5.69 (d, $^3J_{HH}$ = 7.4 Hz, 1H, CH_{Naph}), 4.83 (s, 1H, $CH_{dearomatized}$), 3.63-3.61 (m, 2H, CH_2), 2.31 (s, 3H, N-CH_3), 1.44 (d, $^3J_{PH}$ = 13.5 Hz, 9H, C(CH_3)$_3$), 1.25 (d, $^3J_{PH}$ = 13.5 Hz, 9H, C(CH_3)$_3$), 0.88 (d, $^3J_{PH}$ = 5.3 Hz, $^2J_{PtH}$ = 83.6 Hz, 3H, Pt-Me_B), 0.82 (d, $^3J_{PH}$ = 6.1 Hz, $^2J_{PtH}$ = 56.5 Hz, 3H, Pt-Me_A).

^{13}C{^{1}H} NMR (151 MHz, THF-d_8, -25 °C) δ: 164.11 ($C_{q,Naph}$), 160.95 ($C_{q,Naph}$), 158.89 ($C_{q,Py}$), 150.70 ($C_{H,Py}$), 147.17 ($C_{q,Naph}$), 137.80 ($C_{H,Py}$), 133.98 ($C_{H,Naph}$), 126.95 ($C_{H,Naph}$), 125.23 ($C_{H,Py}$), 124.94 ($C_{H,Py}$), 122.01 ($C_{H,Naph}$), 116.30 ($C_{q,Naph}$), 113.71 ($CH_{dearomatized}$), 91.67 (d, $^3J_{PC}$ = 3.2 Hz, $C_{H,Naph}$), 66.54 (CH_2), 42.92 (N-CH_3), 41.96 (***C***(CH_3)$_3$), 37.54 (d, $^1J_{PC}$ = 26.1 Hz, ***C***(CH_3)$_3$), 28.05-27.82 (C(***C***H_3)$_3$), 3 (d, $^2J_{PC}$ = 107.9 Hz, $^1J_{PtC}$ = 357.2 Hz, Pt-Me), -20.20 (d, $^2J_{PC}$ = 4.5 Hz, Pt-Me). Pt satellite for -20.20 ppm signal were not clearly seen due to low intensity.

^{31}P{^{1}H} NMR (242 MHz, THF-d_8, -25 °C) δ: 175.9 ($^1J_{PtP}$ = 2467 Hz).

^{195}Pt{^{1}H} NMR (129 MHz, THF-d_8, -25 °C) δ: -3980.1 (d, $^1J_{PtP}$ = 2467 Hz).

FT-IR (ATR, solid): 2975 (br, w), 2870 (br, w), 1620 (w), 1532 (s), 1465 (m), 1327 (s), 1089 (w), 882 (br), 797 (m) cm^{-1}.

UV-vis (MeCN), λ, nm (ε, $M^{-1}\cdot cm^{-1}$) : 332 (4400), 228 (15100).

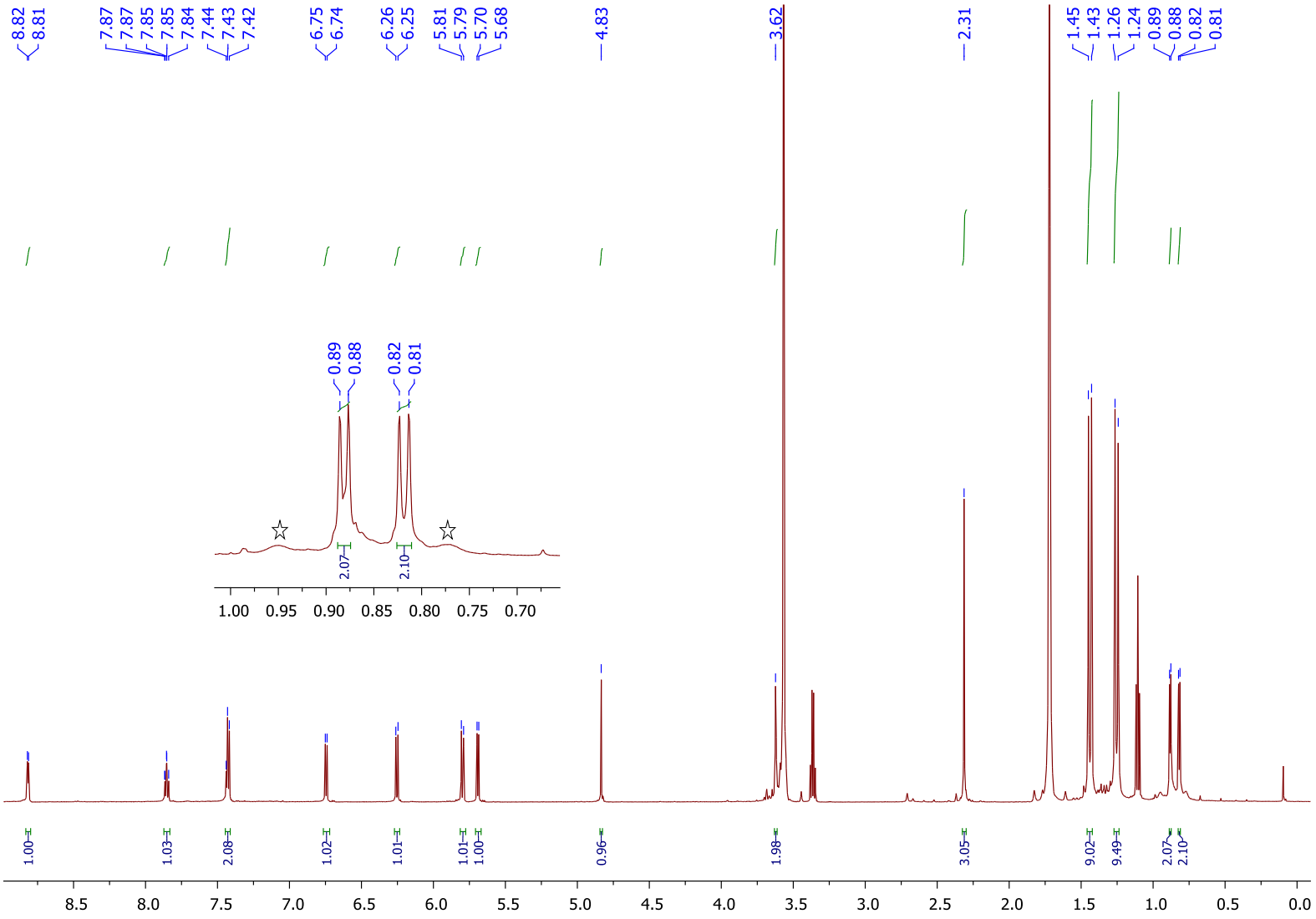

Figure S78. ^{1}H NMR spectrum of **4** in THF-d_8 at -25 °C. Pt satellites are marked with stars.

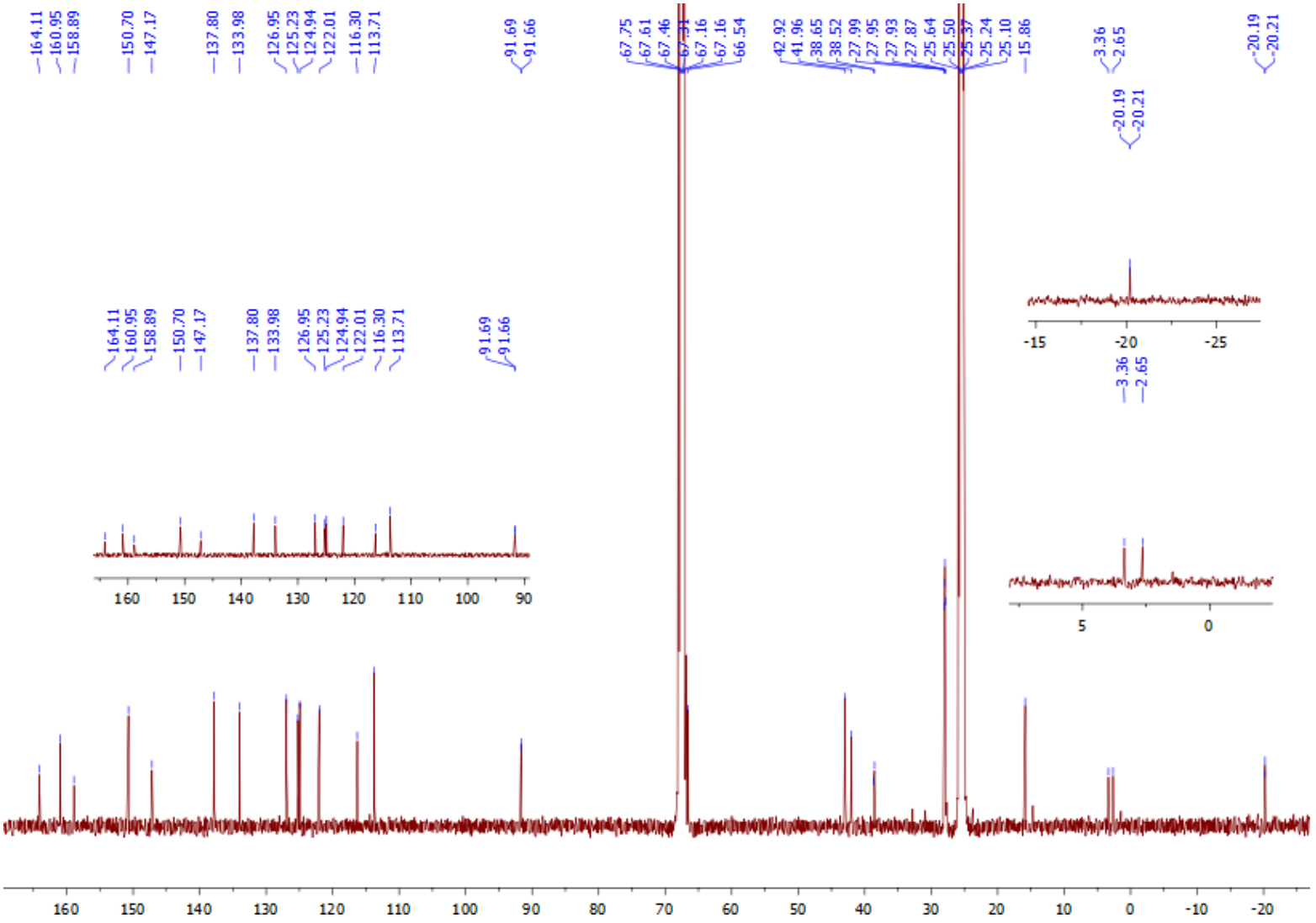

Figure S79. $^{13}C\{^{1}H\}$ NMR spectrum of **4** in THF-d_8 at -25 °C.

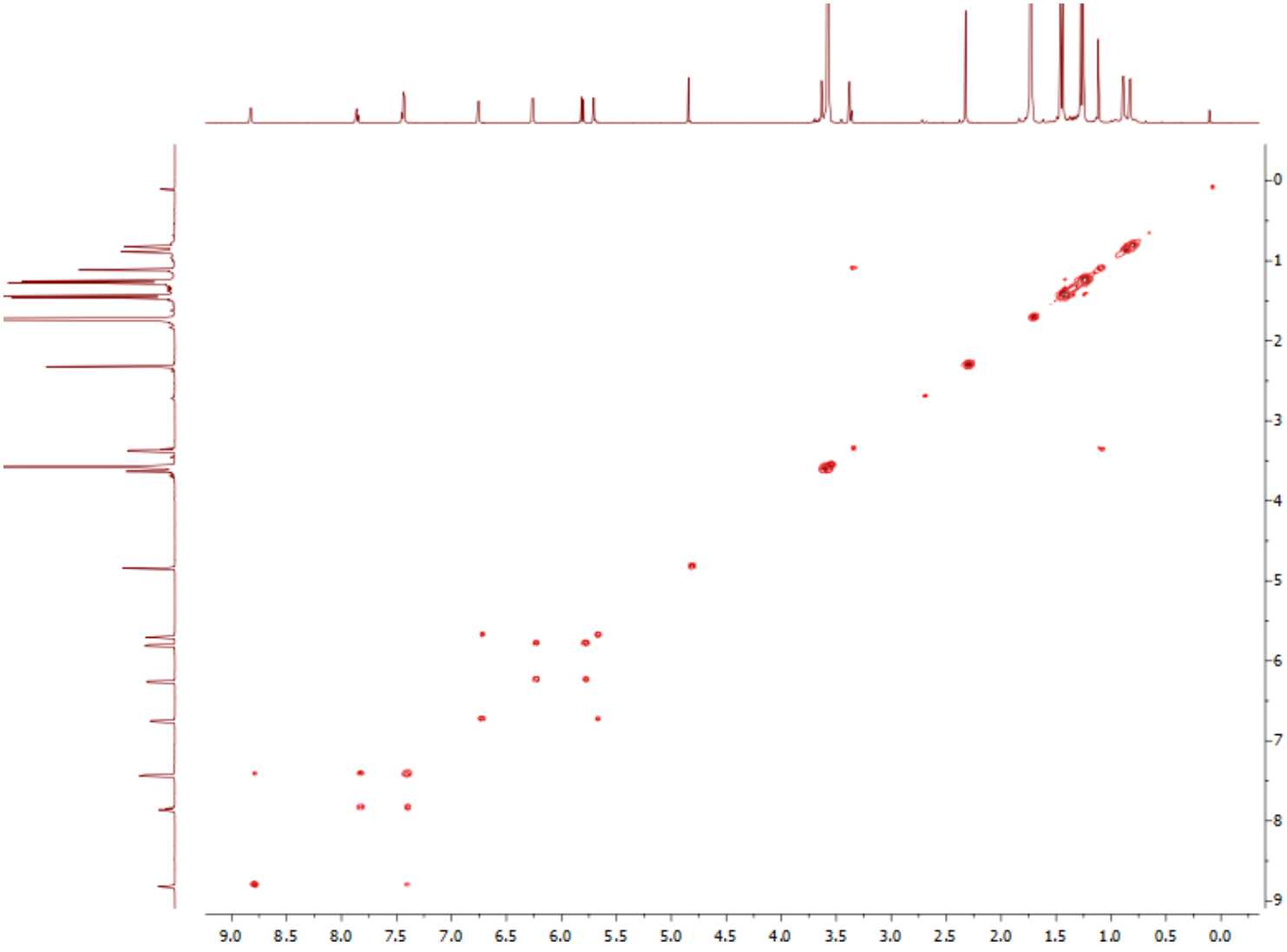

Figure S80. ^{1}H-^{1}H COSY spectrum of **4** in THF-d_8 at -25 °C.

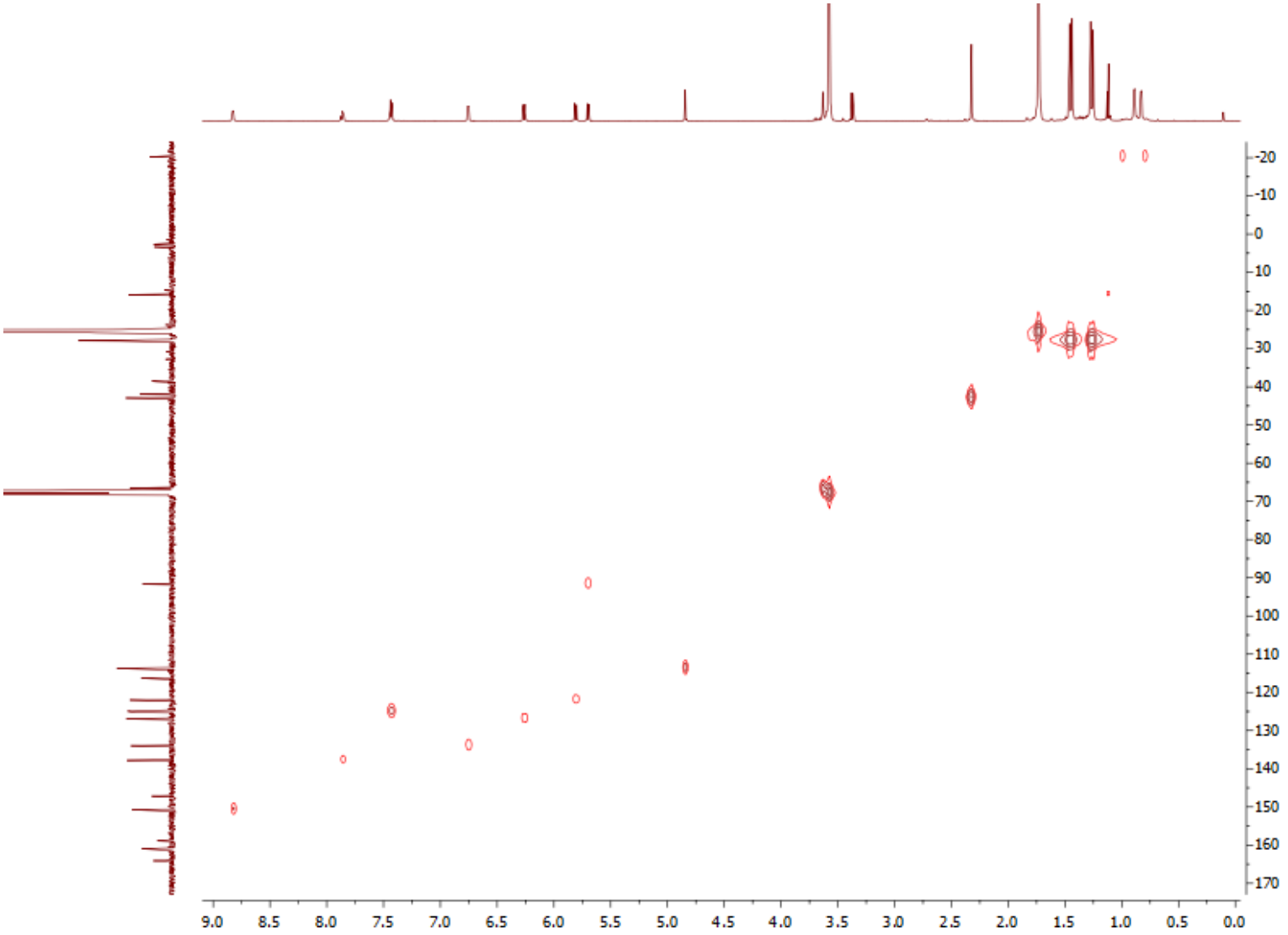

Figure S81. ^{1}H-^{13}C HMQC spectrum of **4** in THF-d_8 at -25 ℃.

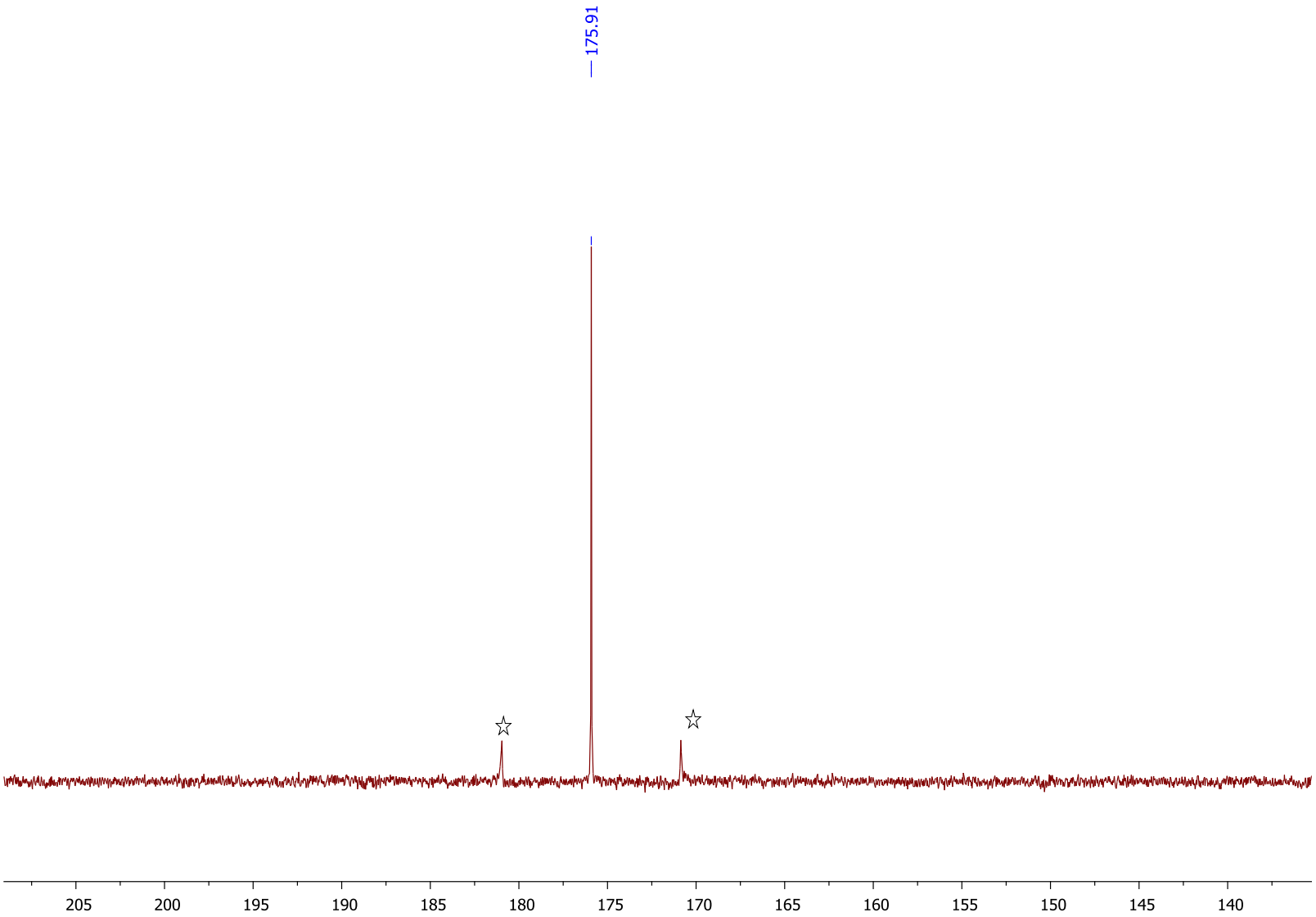

Figure S82. $^{31}P\{^{1}H\}$ NMR spectrum of **4** in THF-d_8 at -25 °C. Pt satellites are marked with stars.

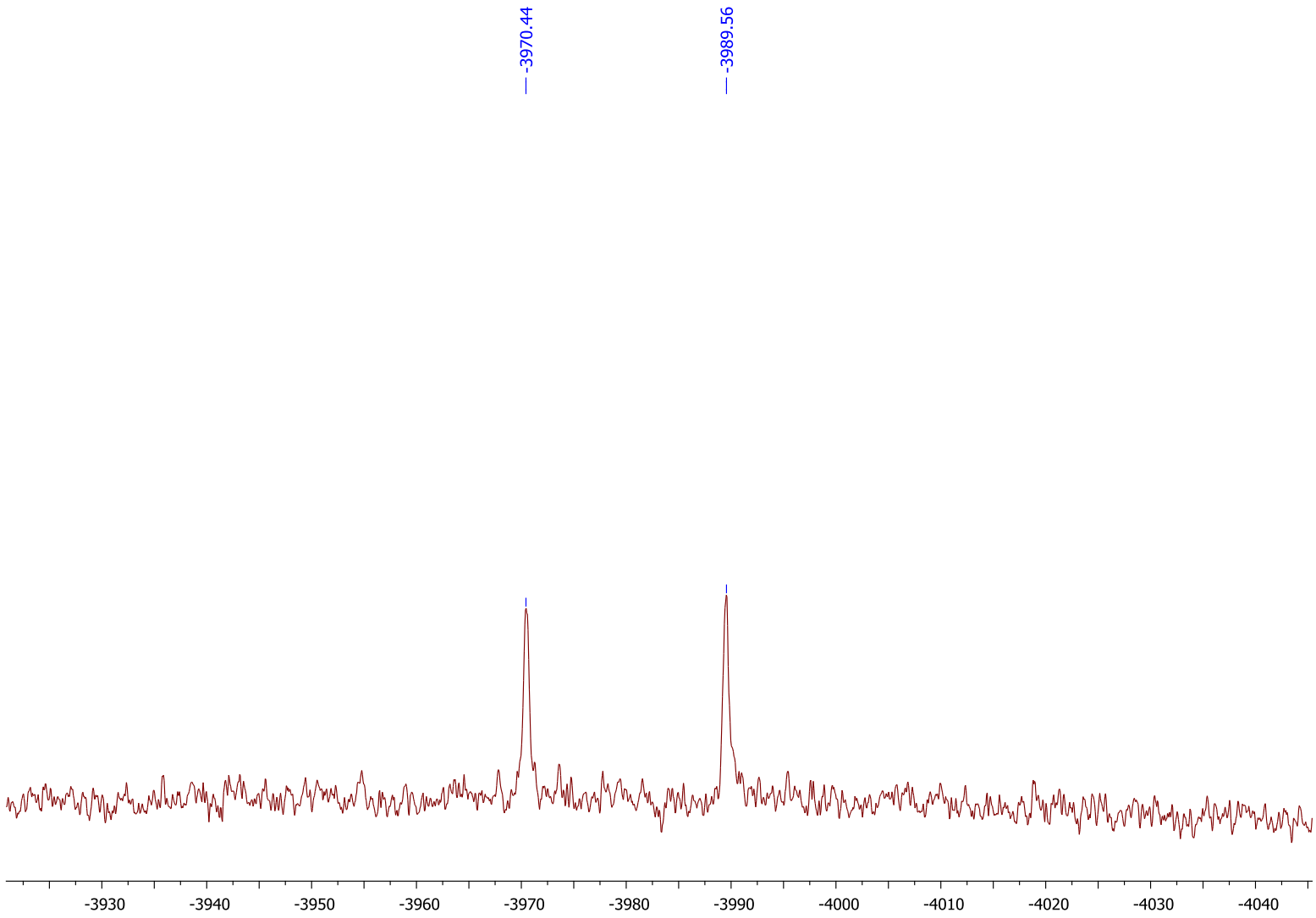

Figure S83. $^{195}Pt\{^{1}H\}$ NMR spectrum of **4** in THF-d_8 at -25 °C.

Selective 1D-difference NOE experiments of 4 in THF-d_8:

Experiments were performed using mixing time 0.44 s and delay time 2.2 s. The orientation of the methyl group relative to the *tert*-butyl group was determined by difference NOE 1D experiments. Irradiation of a resonance at 1.44 ppm corresponding to a *tert*-butyl group induced enhancement (positive NOE) of another *tert*-butyl signal at 1.25 ppm and one of the Pt- methyl groups at 0.88 ppm.

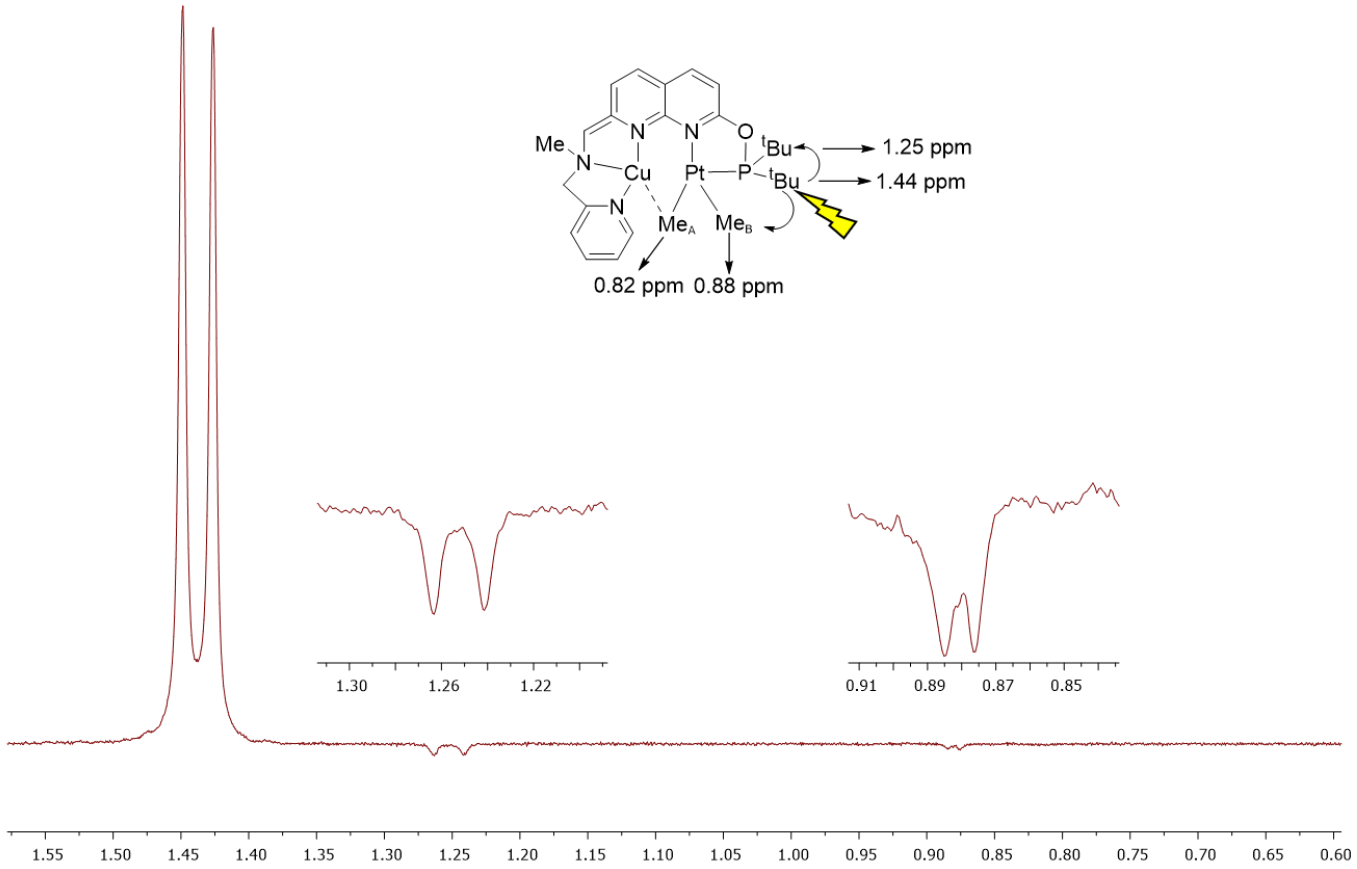

Figure S84. 1D-NOE NMR spectrum of **4** in THF-d_8 at -25 °C.

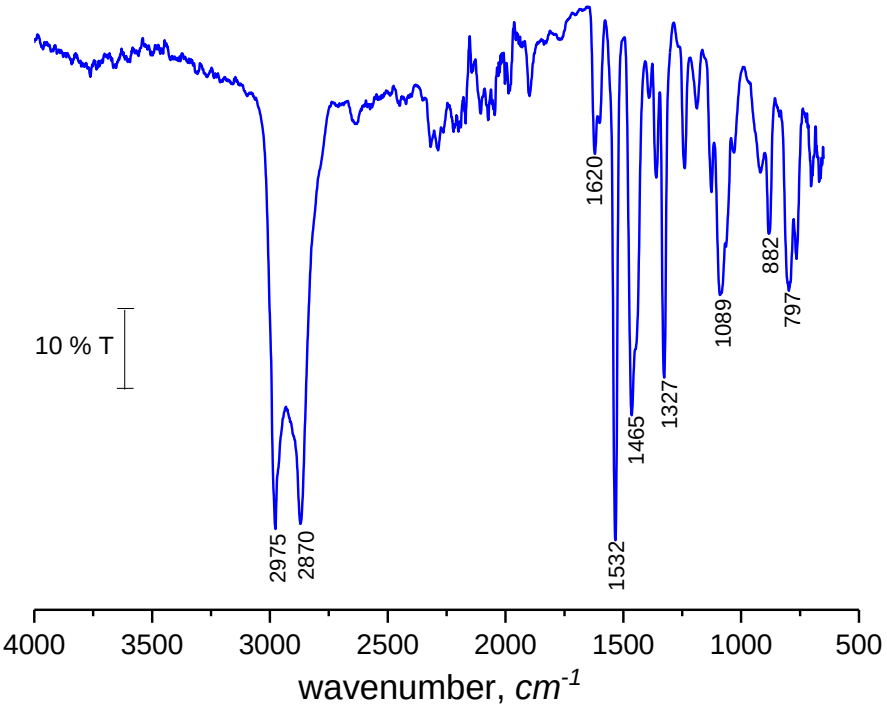

Figure S85. ATR FT-IR transmittance spectrum of **4**.

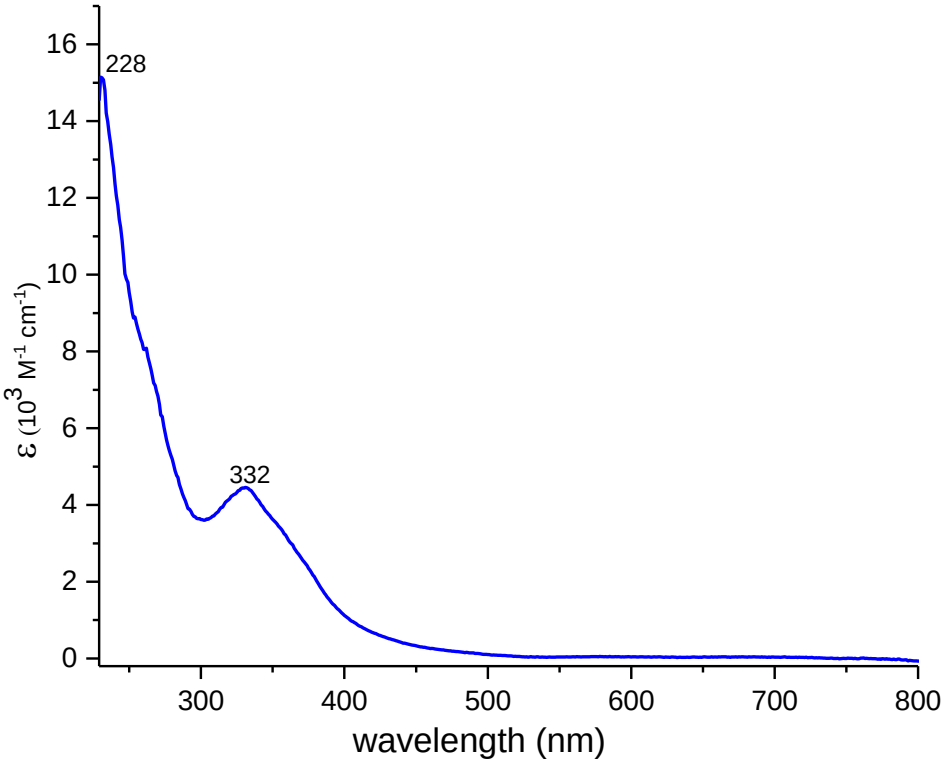

Figure S86. UV-vis absorbance spectrum for **4** in THF.

Comparison of NMR spectra of complexes 1, 3[$CuCl_2$], 3[$B(Ar^F)_4$], 3[BF_4] and 4

Table S1. Comparison of chemical shifts and coupling constant for complexes **1**, **3**[$CuCl_2$], **3**[$B(Ar^F)_4$], **3**[BF_4] and **4** in THF-d_8 and CD_3CN solutions.

Complex	Fragment	^{1}H		^{13}C		^{195}Pt	
		δ_H ($^2J_{H,Pt}$) in THF-d_8	δ_H ($^2J_{H,Pt}$) in CD_3CN	δ_C ($^2J_{C,Pt}$) in THF-d_8	δ_C ($^2J_{C,Pt}$) in CD_3CN	δ_{Pt} ($^1J_{Pt,P}$) in THF-d_8	δ_{Pt} ($^1J_{Pt,P}$) in CD_3CN
1	Pt-Me_A Pt-Me_B	0.93 (66) 0.96 (94)	0.81 (67) 0.91 (95)	-21.94 (805) 15.74 (662)	-22.13 (791) 15.27 (659)	-3894 (2006)	-3815 (2043)
3[$CuCl_2$]	Pt-Me_A Pt-Me_B	n.d.	0.97 (46) 1.14 (85)	n.d.	-21.57 (711) -5.95 (490)	n.d.	-3978 (2850)
3[$B(Ar^F)_4$]	Pt-Me_A Pt-Me_B	1.10 (44) 1.23 (86)	(0.94, 45) 1.12 (87)	-5.95 (491) -21.34 (711)	-6.41 (n.d.) -21.88 (714)	-3971 (2877)	-3977 (2794)
3[BF_4]	Pt-Me_A Pt-Me_B	1.04 (36) 1.18 (82)	0.90 (44) 1.08 (84)	-5.62 (n.d.) -21.32 (719)	-6.37 (505) -21.87 (711)	-3971 (2866)	-3976 (2846)
4	Pt-Me_A Pt-Me_B	0.82 (56) 0.88 (84)	n.d.	3.00 (357) -20.20 (n.d.)	n.d.	-3980 (2467)	n.d.

n.d. - not determined due to low intensity

Thermolysis of [(L)PtMe$_2$] (1) in benzene to generate 5

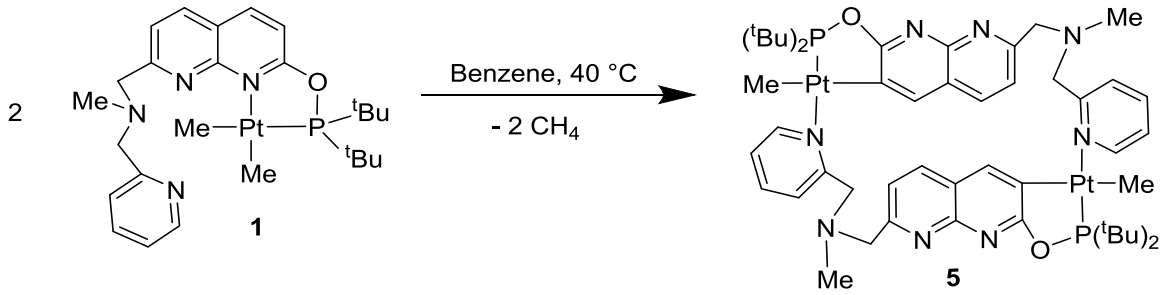

Scheme S9. Formation of **5.**

A Schlenk flask (50 mL) was charged with **1** (100.6 mg, 0.1548 mmol) and distilled benzene (5 mL) to give a yellow solution. The Schlenk flask was submerged in an oil bath at 40 °C for three days. There was a visual change in the color of solution from yellow to pale green. The Schlenk flask was then transferred inside the glovebox and the solvent was removed under vacuum. The crude residue was dissolved in a minimum amount of benzene (1 mL), followed by addition of pentane (5 x 2 mL) to precipitate a powder. Then the solvent was decanted and the solid was dried under vacuum to obtain complex **5** (119.7 mg, 0.0944 mmol, 61% yield). For NMR analysis, the powder was dissolved in C_6D_6 to give broad signals in the NMR spectra. Crystals suitable for X-ray diffraction study were obtained by vapor diffusion technique in benzene/pentane at RT. According to X-ray and ESI-MS, the product was identified as the rollover cyclometallation product **5**. Elemental analysis is also consistent with this assignment.

^{1}H NMR (400 MHz,C_6D_6, 23 °C) δ: 8.54-8.24 (br m), 7.62-7.41 (br m), 6.67-6.49 (br m), 6.43-6.35 (br m), 4.06-3.70 (br m), 2.37-2.04 (br m), 1.82-1.57 (br m), 1.51-1.07 (br m), 0.98 (br d), 0.89 (t). All peaks were significantly broadened, likely due to oligomeric nature of **5**. Attempts to characterize the cyclometallation product in coordinating solvents did not result in resolved NMR spectra.

Elemental Analysis: Expt (Calc): [$C_{26}H_{39}N_4OPPt$]: C 47.46 (47.39), H 5.82 (5.57), N 8.34 (8.84).

ESI-HRMS (m/z pos): Found (Calcd): Found (Calcd): $C_{50}H_{70}O_2N_8P_2{}^{195}Pt_2$: 1267.4469 (1267.4446).

FT-IR (ATR, solid): 2968 (br, w), 2857 (br, w), 1464 (s), 1381 (m), 1175 (m), 1064 (s), 907 (br, s) cm^{-1}.

UV-vis (THF), λ, nm (ε, $M^{-1}\cdot cm^{-1}$) : 345 (15000), 335 (14000).

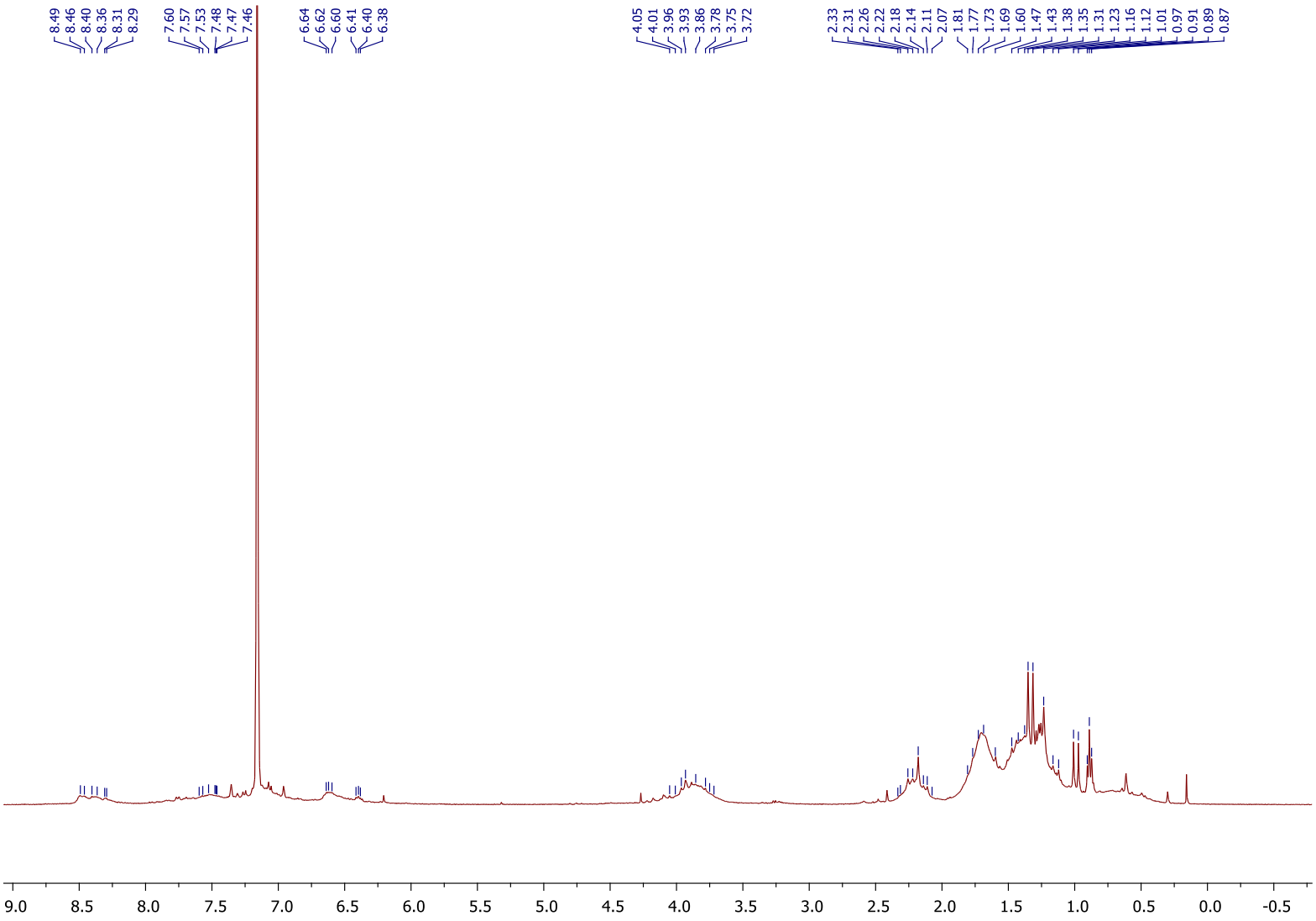

Figure S87. ^{1}H NMR spectrum of **5** in C_6D_6 at 23 °C.

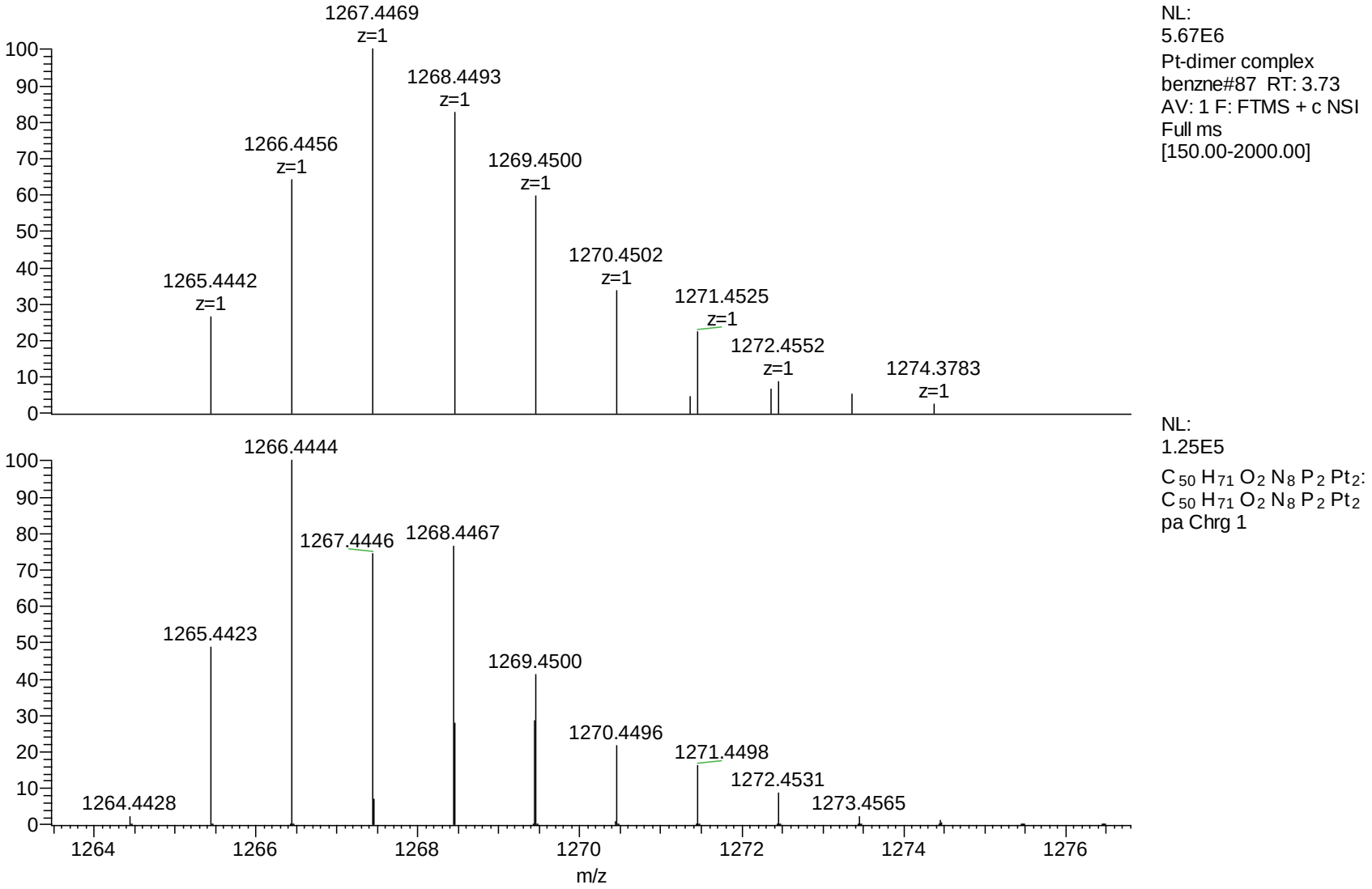

Figure S88. ESI-(HR)MS spectrum of **5** (top) and simulated spectrum for $C_{50}H_{70}O_2N_8P_2Pt_2$ (bottom).

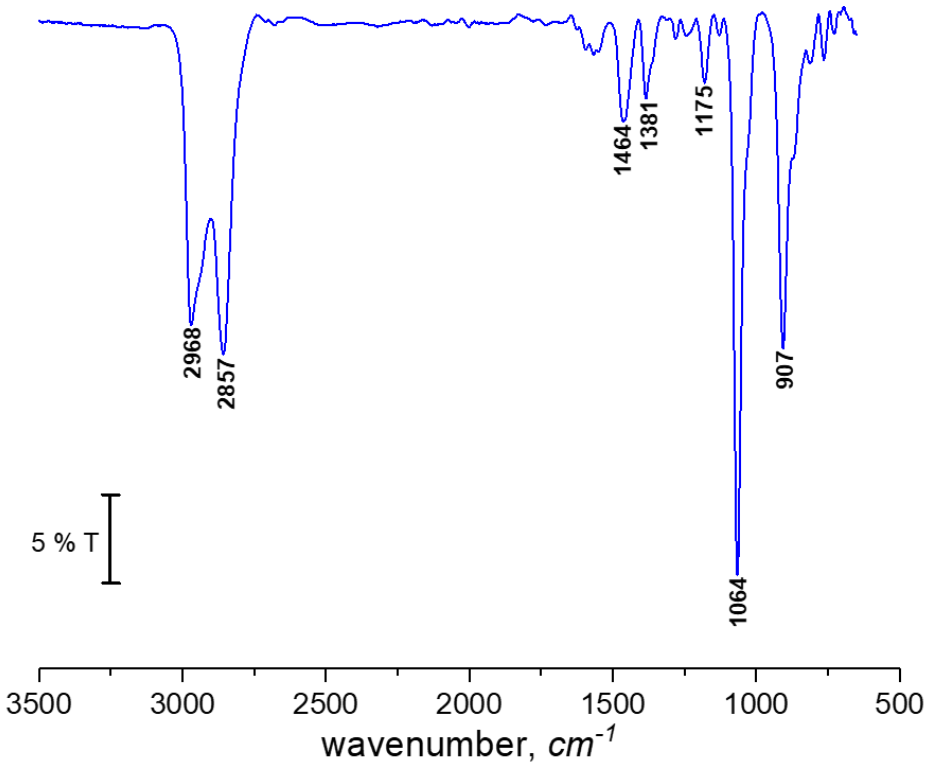

Figure S89. ATR FT-IR transmittance spectrum of **5.**

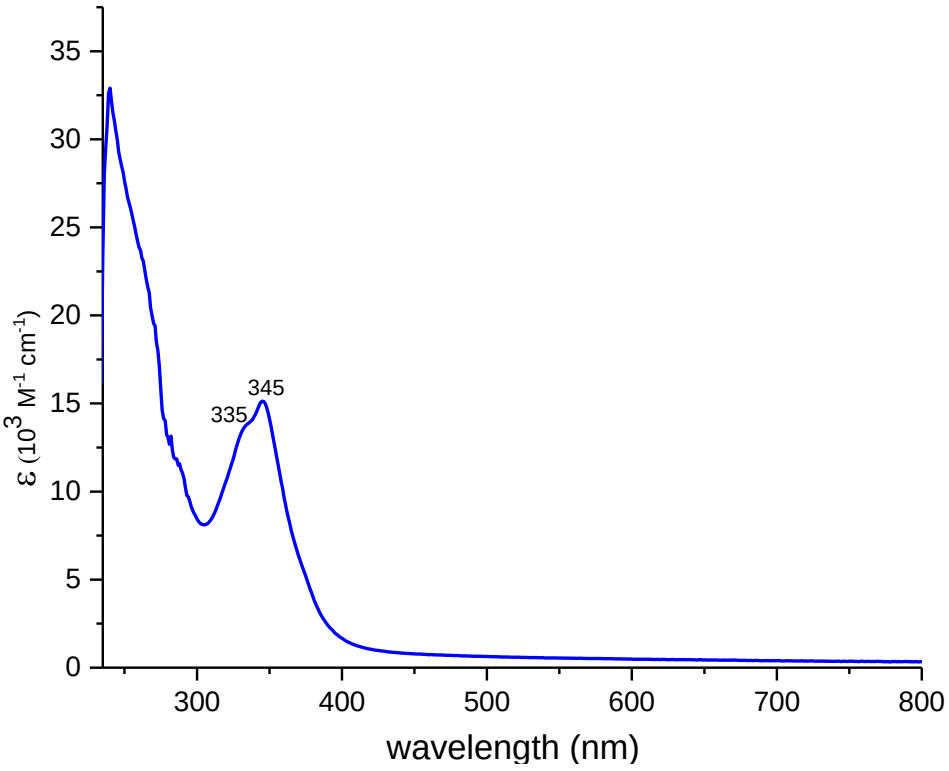

Figure S90. UV-vis absorbance spectra for **5** in THF.

Formation of 6[B(Ar^F)$_4$]

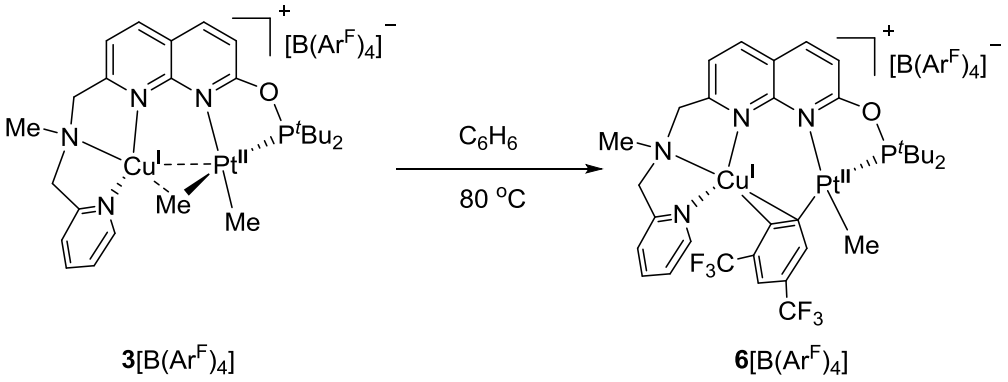

3[B(Ar^F)$_4$] **6**[B(Ar^F)$_4$]

Scheme S10. Formation of **6**[B(Ar^F)$_4$].

A Schlenk flask (50 ml) was charged with **3**[B(Ar^F)$_4$] (50.6 mg, 0.0321 mmol) and distilled benzene (5 mL) yielding a brown solution. The Schlenk flask was submerged in an oil bath at 80 °C for 18 hours. After a Schlenk flask was then transferred inside the glovebox, the solvent was removed under vacuum. The crude was dissolved in a minimum amount of THF (1 mL) a followed by addition of pentane (5 x 2 mL) to precipitate a brown-colored powder. Solvent removal yielded complex **6**[B(Ar^F)$_4$] (40.8 mg). The yield (46 %) of the product was measured in the presence of mesitylene added as an internal standard (see Figure S91).
Crystals suitable for X-ray diffraction study were obtained via vapor diffusion in THF/pentane at -30 °C.

^{1}H NMR (600 MHz, THF-d_8, 23 °C) δ: 9.14 (d, $^3J_{HH}$ = 4.9 Hz, 1H, CH_{Py}), 8.83 (d, $^3J_{HH}$ = 8.9 Hz, 1H, CH_{Naph}), 8.68 (d, $^3J_{HH}$ = 8.1 Hz, 1H, CH_{Naph}), 8.00-7.97 (m, 1H, CH_{Py}), 7.82 (s, 11H +3H, o-CH_{BArF}, o-CH_{ArF-Pt} + unknown), 7.78-7.76 (m, 1H, CH_{Naph}), 7.62 (s, 6H + 2H, *p*-CH_{BArF}, *p*-CH_{ArF-Pt}, CH_{Py} + unknown), 7.54-7.51 (m, 1H, CH_{Naph}), 7.45 (d, $^3J_{HH}$ = 7.7 Hz, 1H, CH_{Py}), 4.01 (d, $^2J_{HH}$ = 16.5 Hz, 1H, CH_2), 3.52 (d, $^2J_{HH}$ = 16.5 Hz, 1H, CH_2), 3.47 (m, AB system, 2H, CH_2), 2.08 (s, 3H, N-CH_3), 1.61 (d, $^3J_{PH}$ = 14.8 Hz, 9H, C(*C*H$_3$)$_3$), 1.40 (d, $^3J_{PH}$ = 14.8 Hz, 9H, C(*C*H$_3$)$_3$), 1.23 (d, $^3J_{PH}$ = 5.1 Hz, $^2J_{PtH}$ = 63.6 Hz, 3H, Pt-Me).

^{13}C NMR (151 MHz, THF-d_8, -25 °C) δ: 168.45 ($C_{q,Naph}$), 162.64 ($C_{q,BArF}$), 160.82 ($C_{q,Naph}$), 157.93 ($C_{q,Py}$), 150.53 ($C_{H,Naph}$), 149.97 ($C_{q,Naph}$), 144.56 ($C_{H,Py}$), 144.37 ($C_{q,Naph}$), 141.08 ($C_{H,Naph}$), 139.79 ($C_{H,Py}$), 135.29 ($C_{H,BArF}$), 129.76 ($C_{q,BArF}$), 127.96 ($C_{q,BArF}$), 126.15 (Pt-Ar_{ortho}), 125.60 ($C_{H,Naph}$), 124.99 ($C_{H,Py}$), 124.35 (Pt-Ar_{para}), 121.99 ($C_{H,Naph}$), 118.07 ($C_{H,BArF}$), 114.99 ($C_{H,Py}$), 62.37 (CH_2), 61.27 (CH_2), 44.19 (N-CH_3), 42.68 (m, ***C***(CH$_3$)$_3$), 39.64 (m, ***C***(CH$_3$)$_3$), 27.71 (d, $^2J_{PC}$ = 2.9 Hz, C(***C***H$_3$)$_3$), 26.98 (d, $^2J_{PC}$ = 4.8 Hz, C(***C***H$_3$)$_3$), -18.03 (d, $^2J_{PC}$ = 3.7 Hz, $^1J_{PtC}$ = 298.41, Pt-Me). Assignment of Pt- $ArCF_3$ and Pt- ArC_{ipso} could not be picked due to low intensity.

^{31}P{^{1}H} NMR (262 MHz, THF-d_8, -25 °C) δ: 182.1 ($^1J_{PtP}$ = 2731 Hz).

^{195}Pt{^{1}H} NMR (129 MHz, THF-d_8, -25 °C) δ: -4016 ($^1J_{PtP}$ = 2731 Hz).

ESI-HRMS (m/z pos): Found (Calcd): $C_{33}H_{39}ON_4PF_6{}^{195}Pt^{63}Cu^+$: 910.1700 (910.1704).

FT-IR (ATR, solid): 2964 (br, w), 2898 (br, w), 1611 (s), 1438 (m), 1354 (s), 1276 (s), 1123 (s), 889 (m), 678 (m) cm^{-1}.

UV-vis (THF), λ, nm (ε, M^{-1}·cm^{-1}) : 320 (6100), 239 (19500).

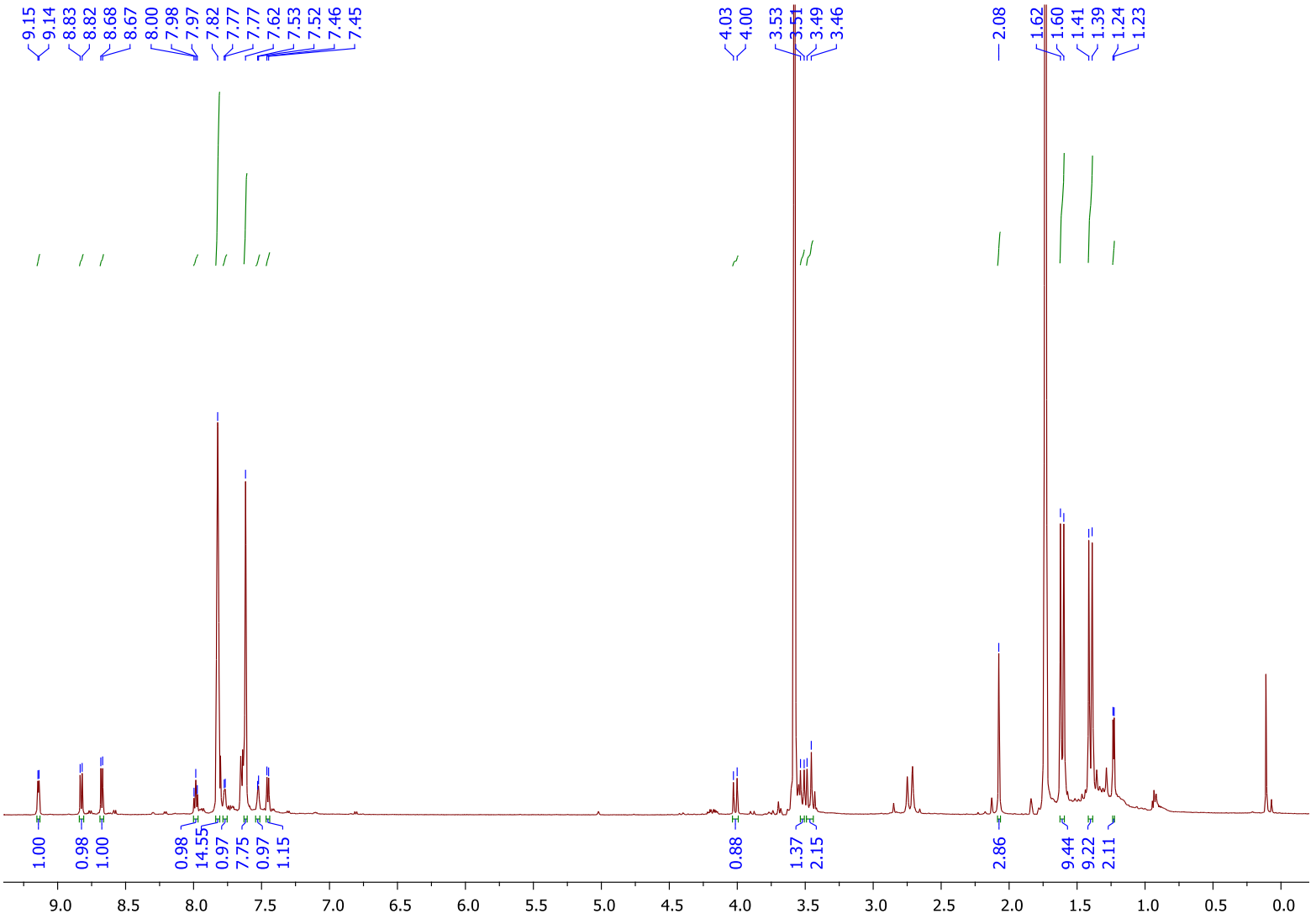

Figure S91.[1]H NMR spectrum of **6**[B(Ar^F)$_4$] in THF-d_8 at -25 °C.

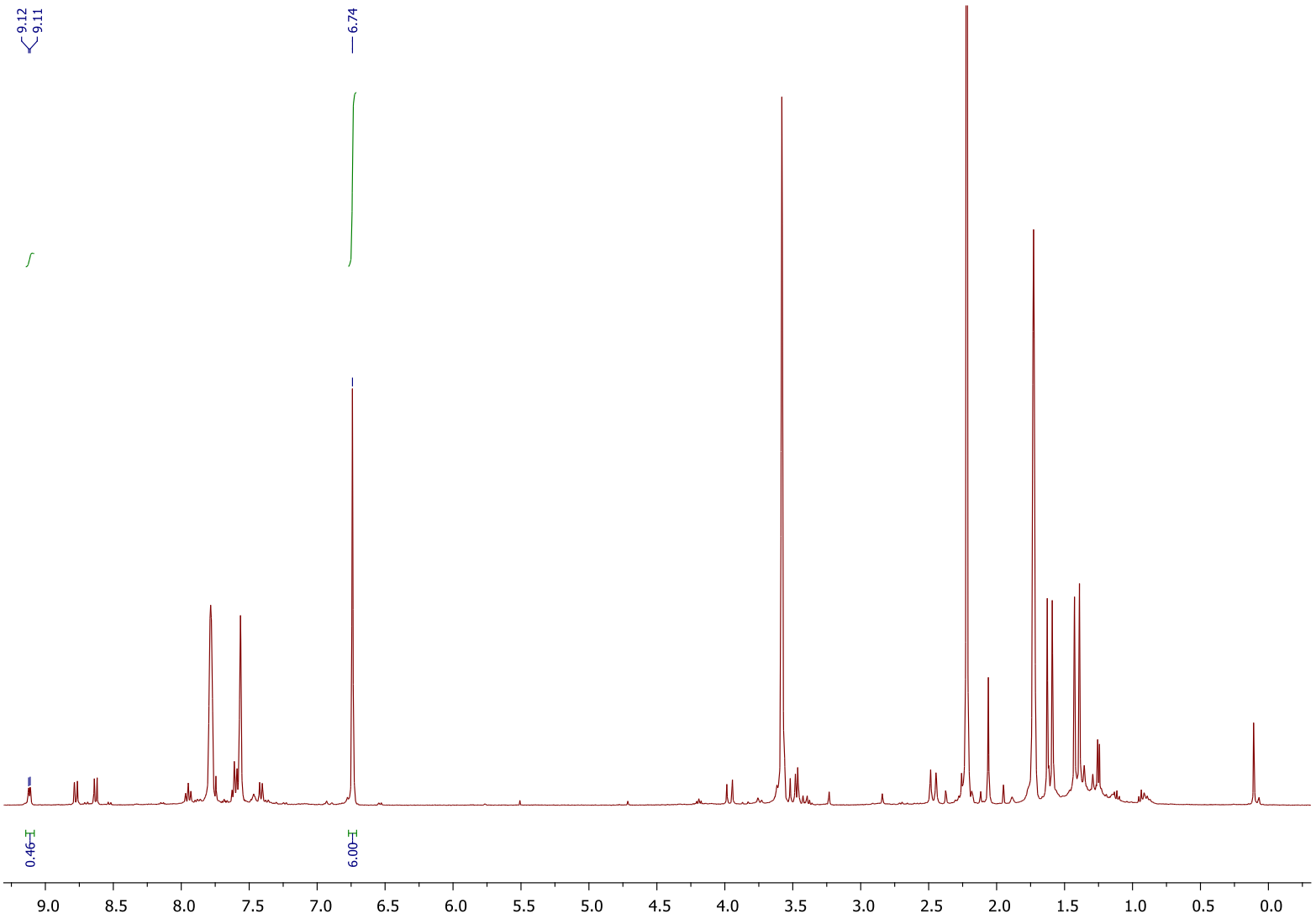

Figure S92.[1]H NMR spectrum of **6**[B(Ar^F)$_4$] in THF-d_8 at 25 °C.Quantification of yield by integrating the peak at 9.12 ppm vs mesitylene peak (2 equivalent) at 6.74 ppm which act as an internal standard.

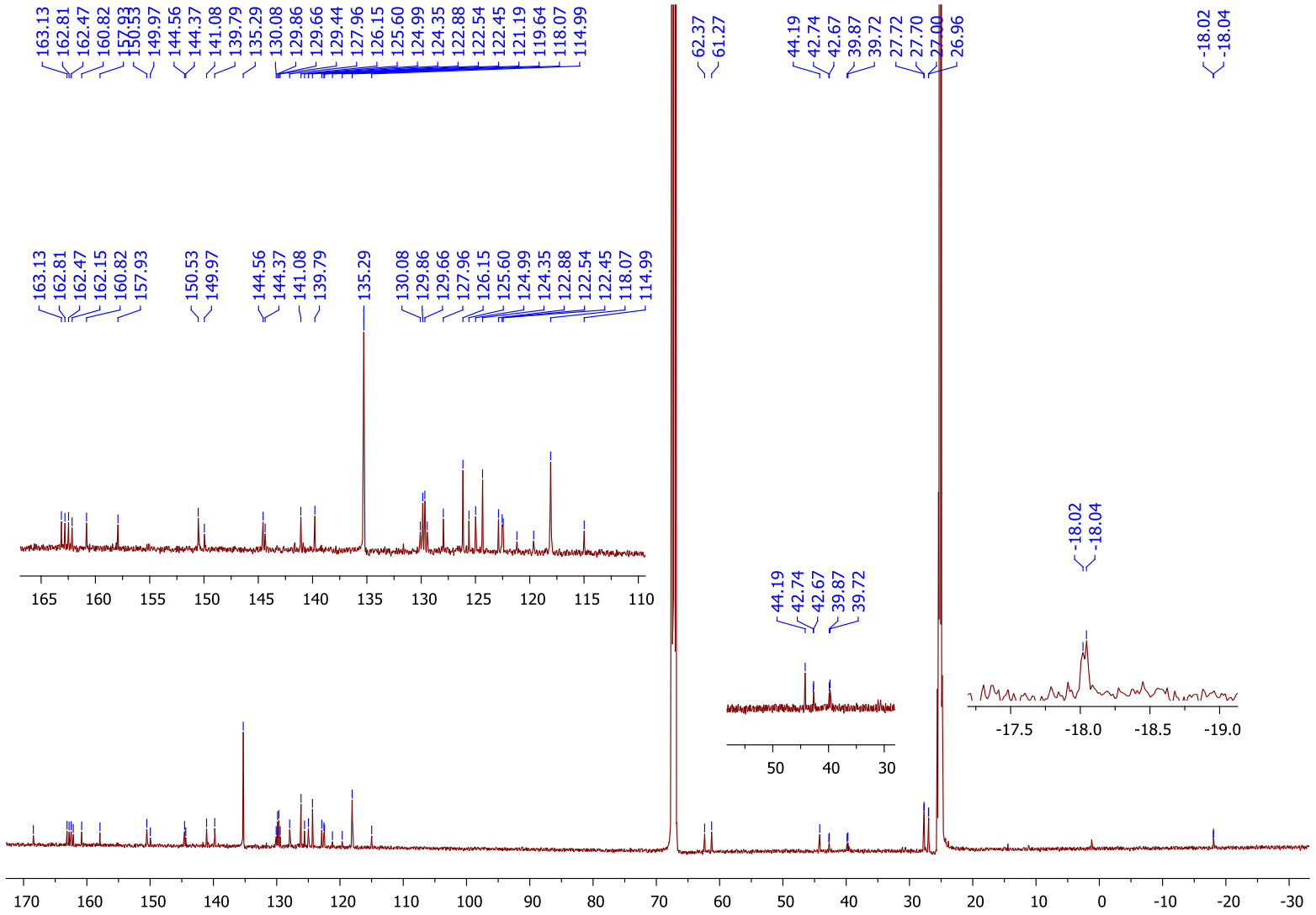

Figure S93. ^{13}C NMR spectrum of **6**[B(Ar^{F})$_4$] in THF-d_8 at -25 °C.

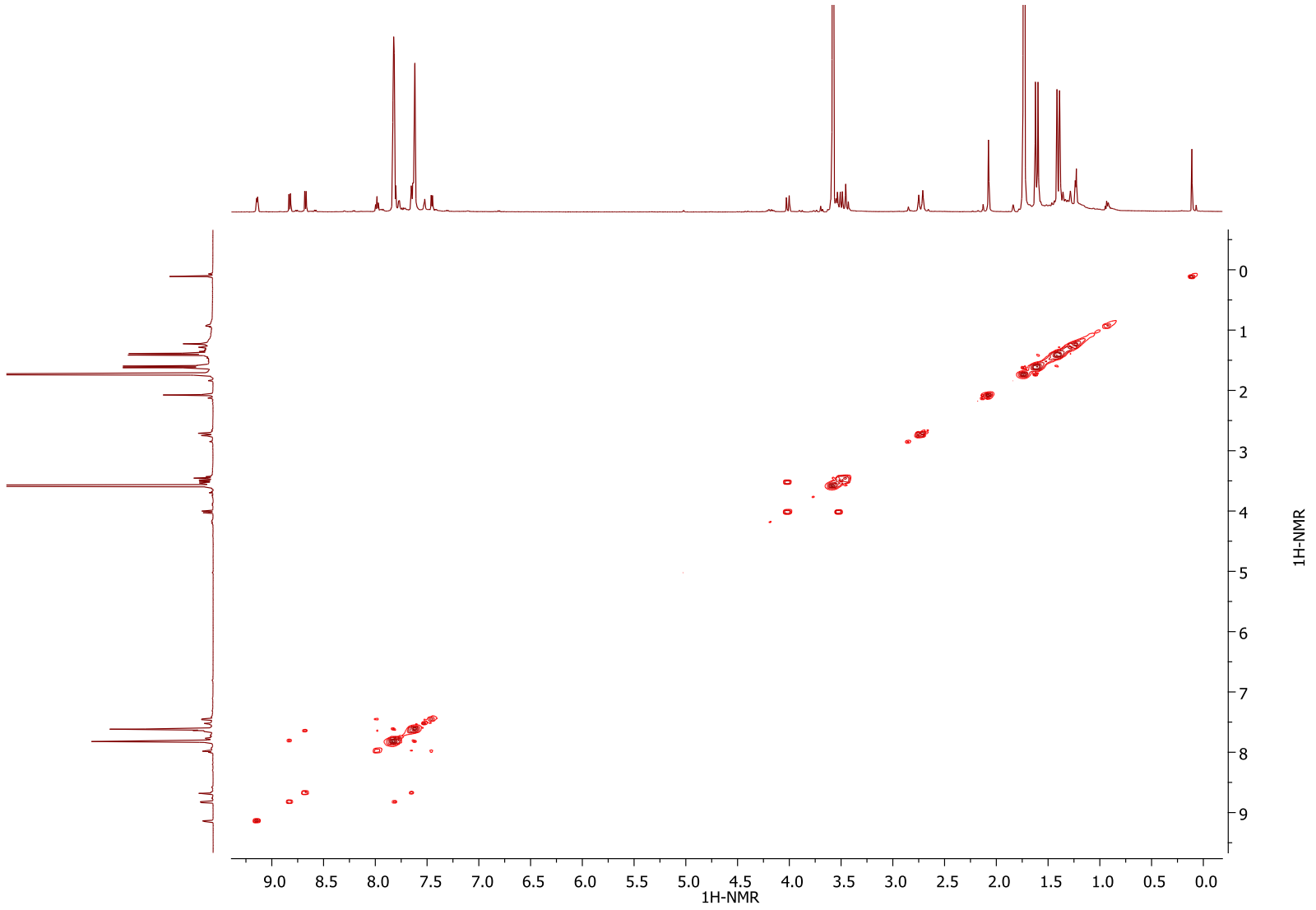

Figure S94. ^{1}H-^{1}H COSY spectrum of **6**[B(Ar^{F})$_4$] in THF-d_8 at -25 °C.

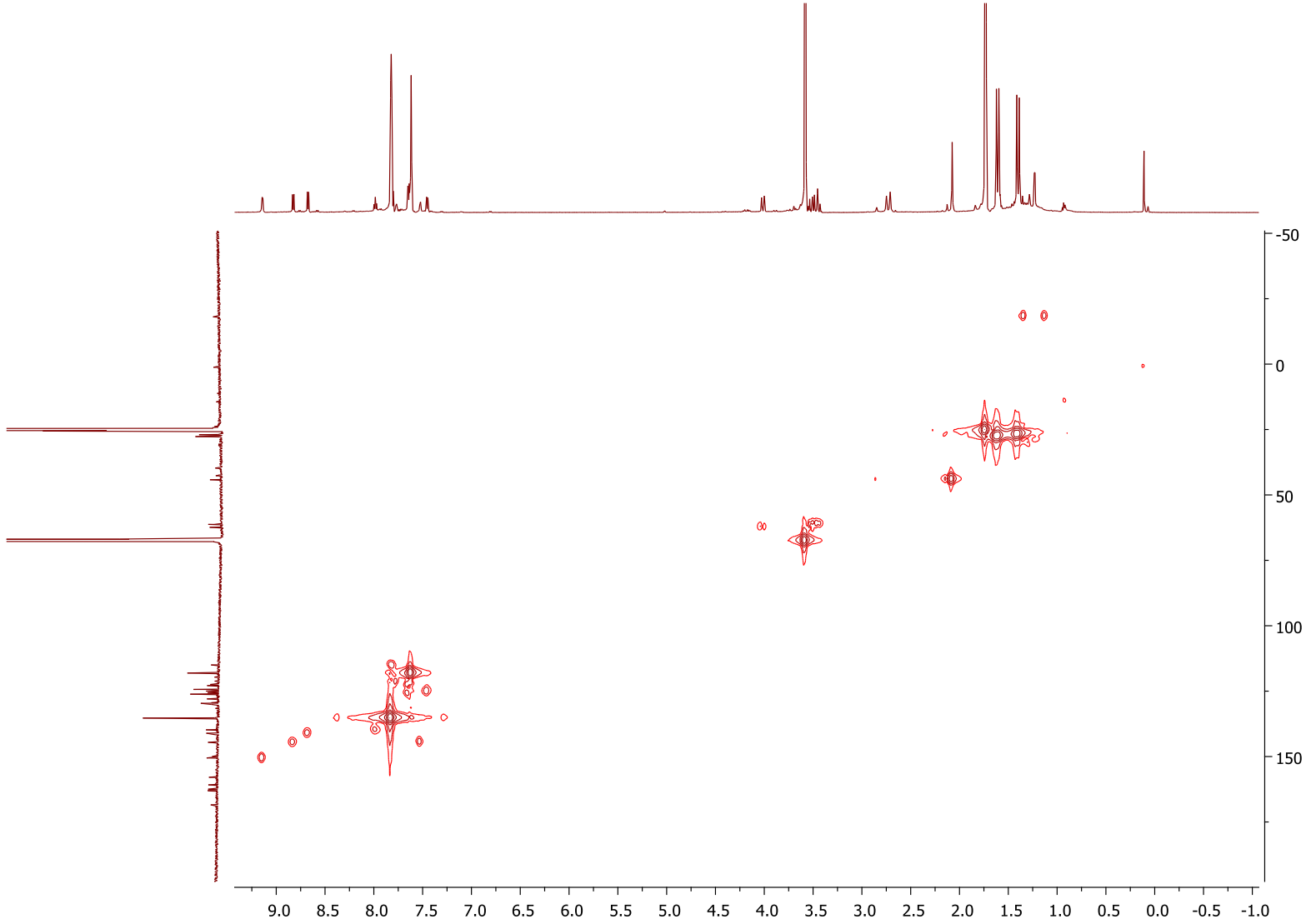

Figure S95. ^{1}H-^{13}C HMQC spectrum of **6**[B(Ar^{F})$_4$] in THF-d_8 at -25 °C.

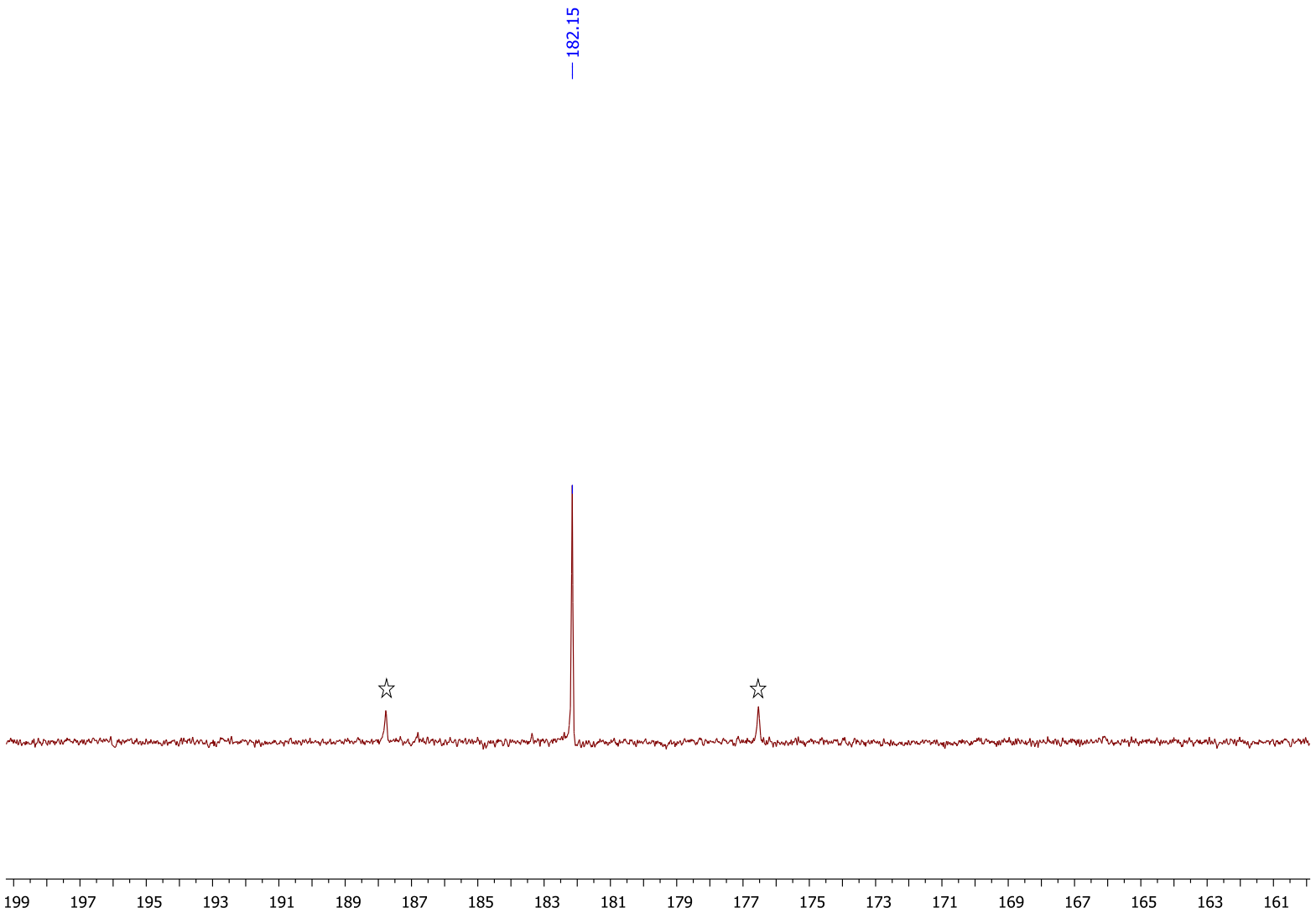

Figure S96. $^{31}P\{^{1}H\}$ NMR spectrum of **6**[$B(Ar^F)_4$] in THF-d_8 at -25 °C. Pt satellites are marked with stars.

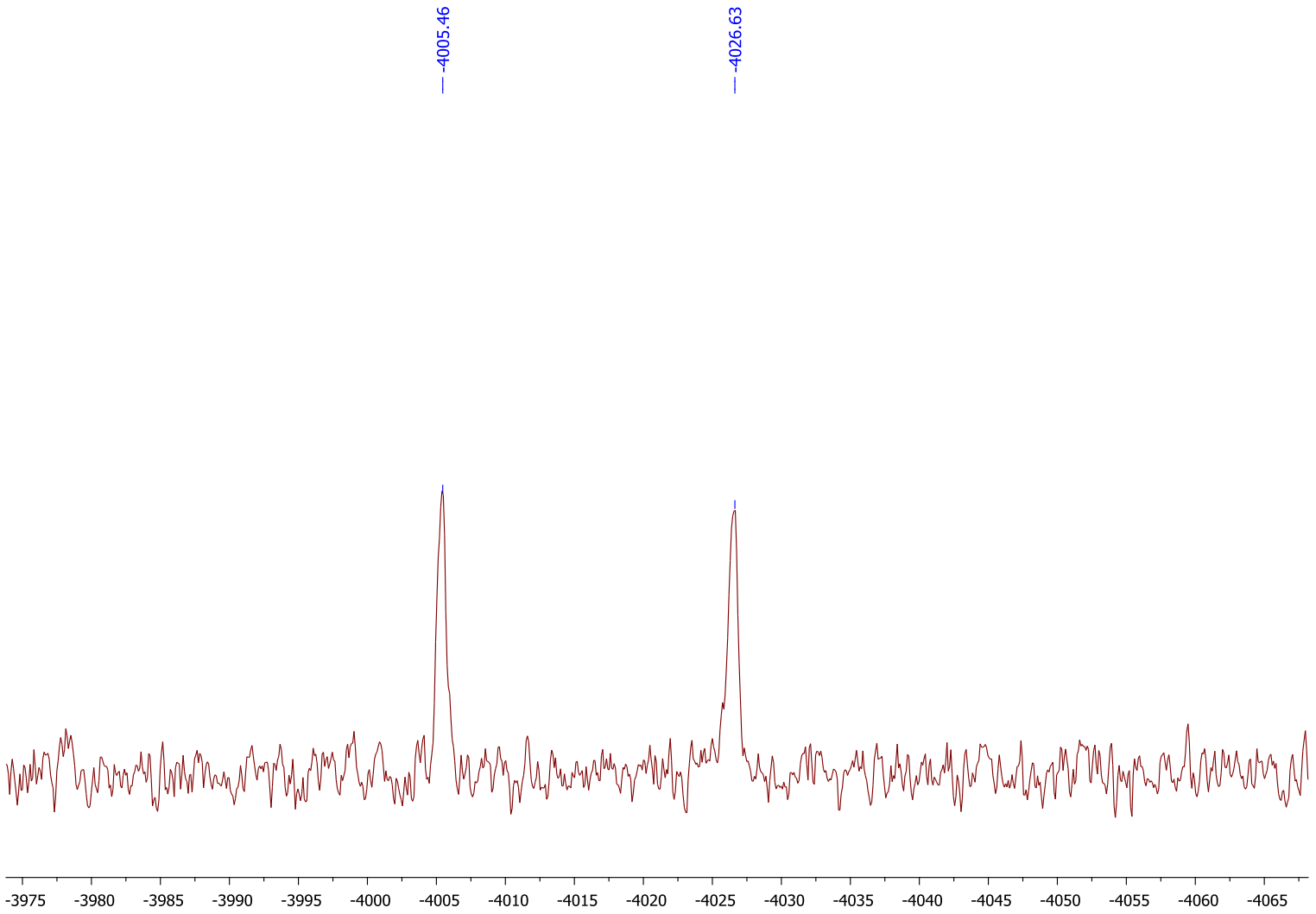

Figure S97. $^{195}Pt\{^{1}H\}$ NMR spectrum of **6**[$B(Ar^{F})_4$] in THF-d_8 at -25 °C.

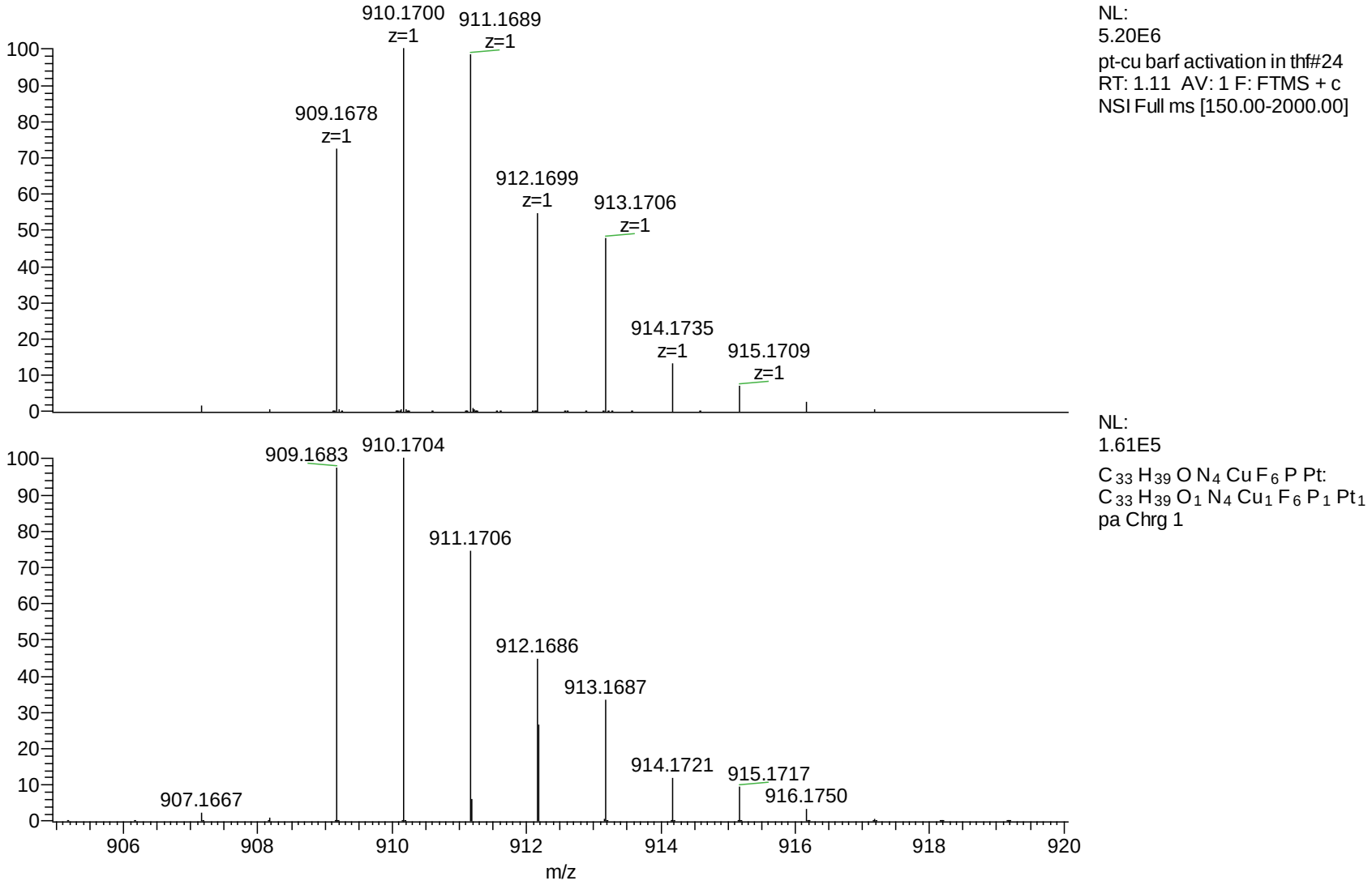

Figure S98. ESI-(HR)MS spectrum of a THF solution of **6**[B(Ar^{F})$_4$] and simulated spectrum for $C_{33}H_{39}ON_4PF_6PtCu^+$ (bottom).

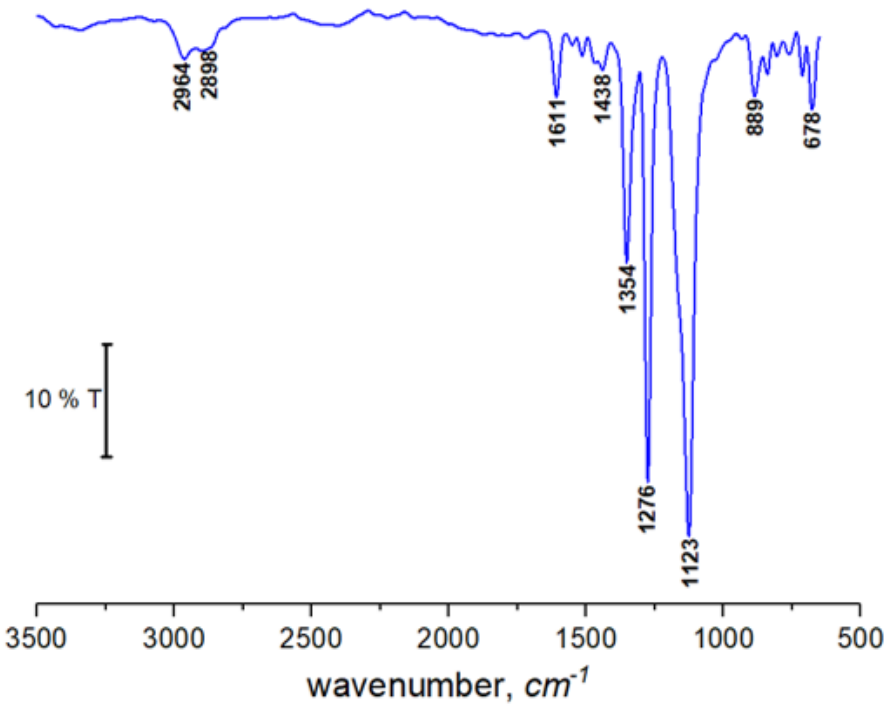

Figure S99. ATR FT-IR transmittance spectrum of **6**[B(Ar^F)$_4$].

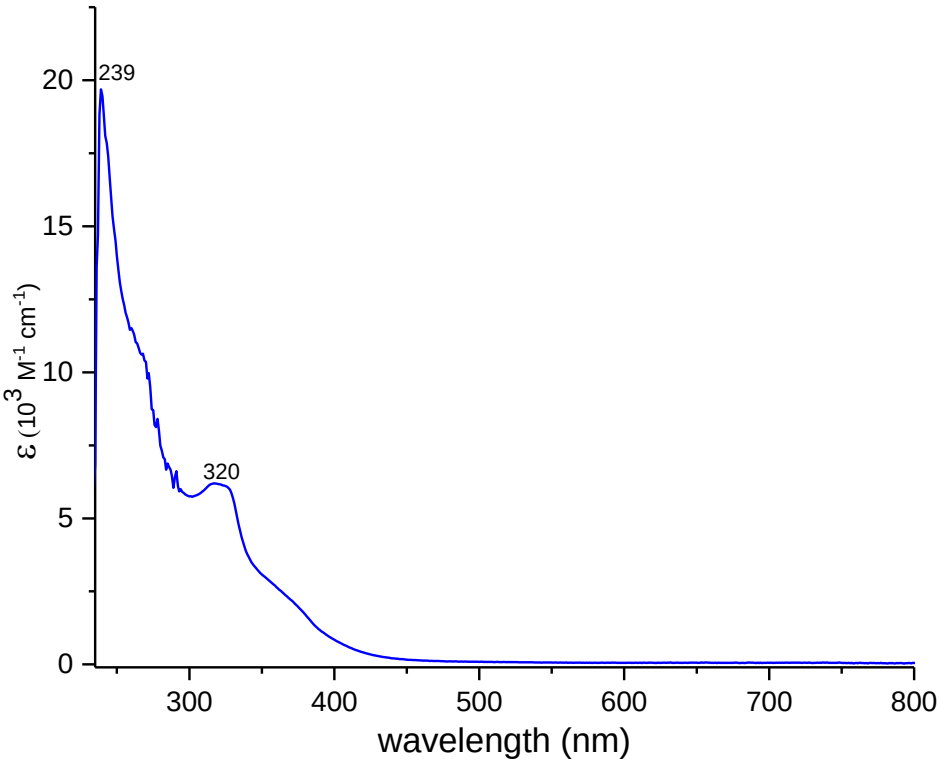

Figure S100. UV-vis absorbance spectra for **6**[B(Ar^F)$_4$] in THF.

Attempted detection of boron-containing by-product of aryl group transfer from $BAr^F_4^-$ to form complex 6[BAr^F_4]

Complex **3**[$B(Ar^F)_4$] (6.1 mg, 0.0038 mmol) was dissolved in benzene (500 μL) in a J. Young NMR tube. The NMR spectrum were recorded, further the NMR tube was then heated in an oil bath at 80 °C for 18 hours. After cooling down to RT, the NMR tube was then transferred inside the glovebox and the solvent was removed under vacuum. To the solid residue THF-d_8 (400 μL) was added to record the ^{19}F and ^{11}B NMR spectra. Only a strong signal corresponding to $[B(Ar^F)_4]^-$ anion was observed clearly, with no new peaks that could be clearly assigned to another boron-containing product.

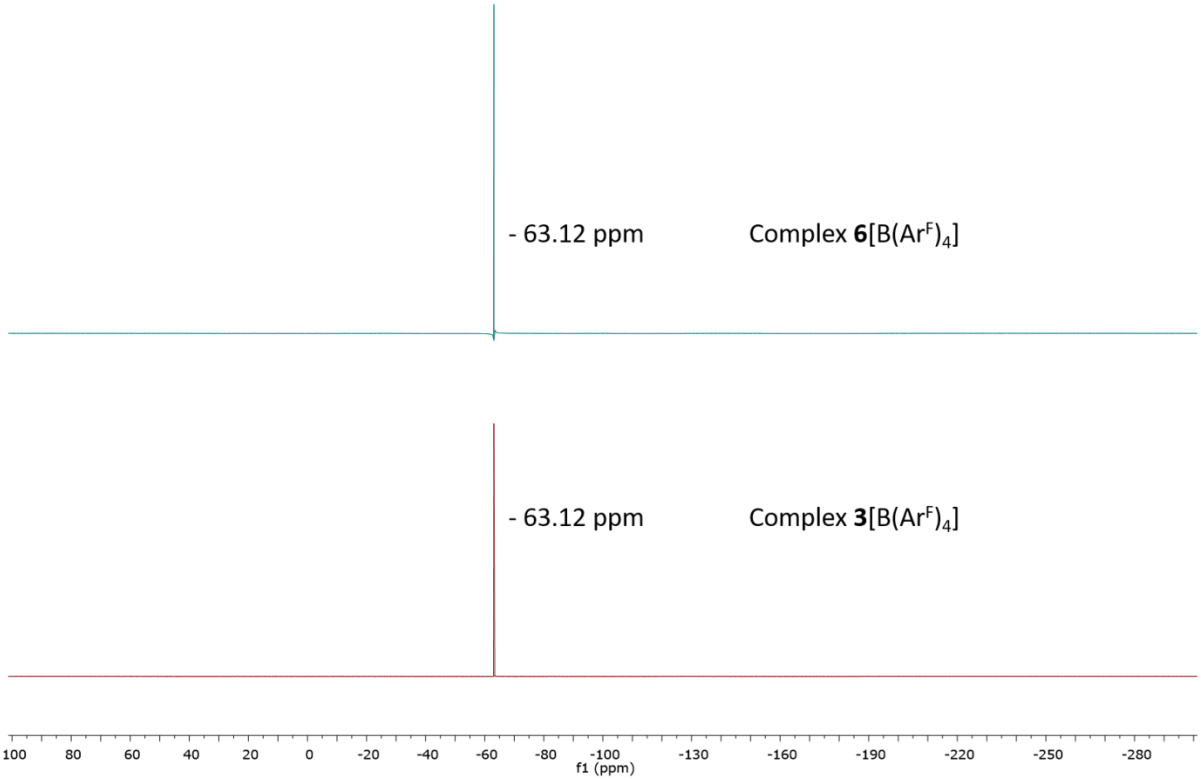

Figure 101. Comparison of ^{19}F NMR spectra of the reaction mixture of the formation of **6**[$B(Ar^F)_4$] in THF-d_8 (blue line, top) and complex **3**[$B(Ar^F)_4$] in C_6D_6 (red line, bottom).

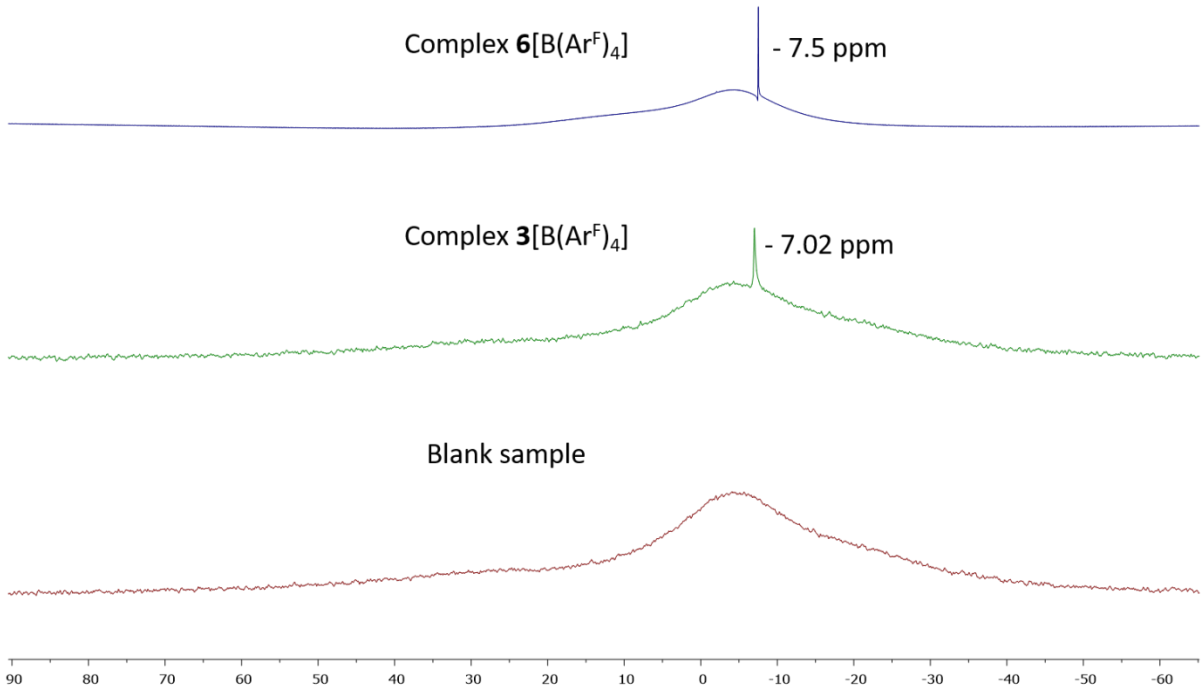

Figure 102. Comparison of ^{11}B NMR spectra of the reaction mixture of the formation of **6**[B(Ar^F)$_4$] in THF-d_8 (blue line, top), starting material **3**[B(Ar^F)$_4$] (green line, middle) and blank tube (red line, bottom). The broad background signal is from NMR tube glass.

Thermolysis of 3[BF_4] in benzene at 80 °C

Complex **3**[BF_4] (8.1 mg, 0.010 mmol) was dissolved in C_6D_6 (400 μL) (partially soluble at RT) in a J. Young NMR tube. The solution was then heated in an NMR tube at 80 °C. After 18 hours, significant (>80%) degradation of the starting material was observed yielding a mixture of unidentified products.

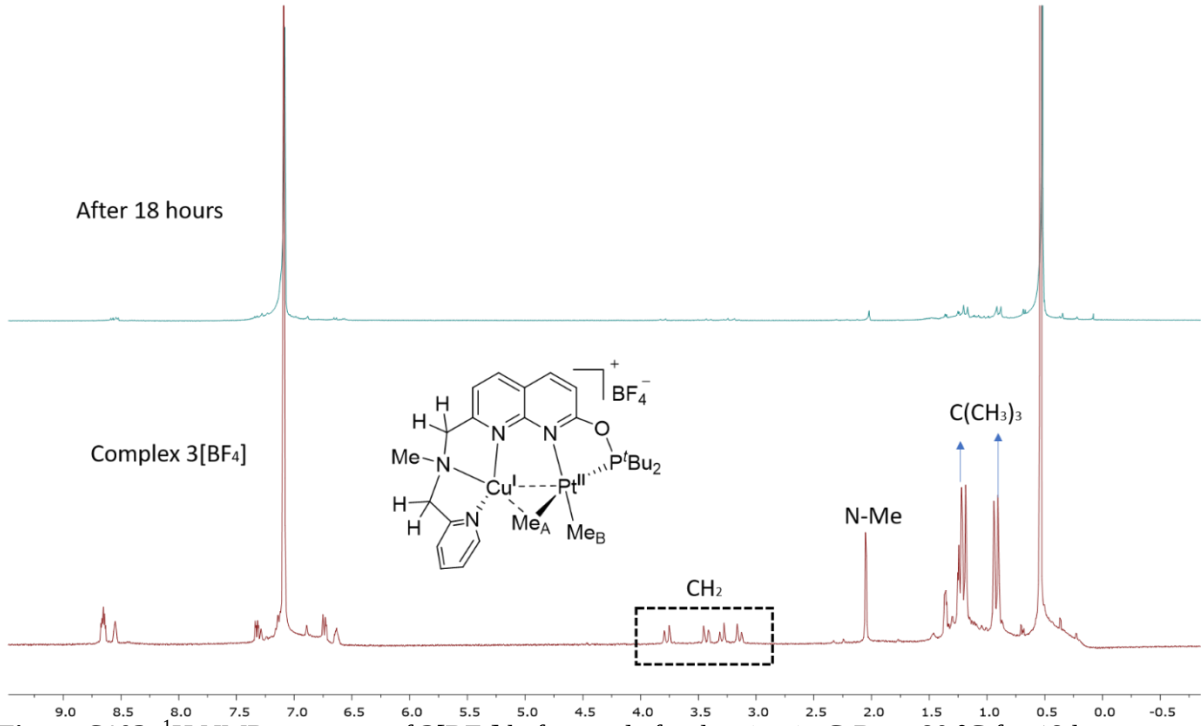

Figure S103. ^{1}H NMR spectrum of **3**[BF_4] before and after heating in C_6D_6 at 80 °C for 18 h.

Attempted reactivity of 1 with 4-ethynylanisole

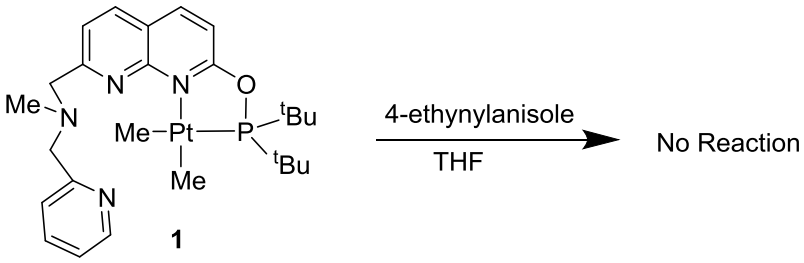

To a solution of **1** (10 mg, 0.015 mmol) in THF-d_8 (500 μL) in a J. Young NMR tube, 4-ethynylanisole (4 μL , 0.03 mmol) was added and the reaction was stirred at RT for 6 h. No color changes and no changes in 1H NMR spectrum were observed under these conditions showing only unreacted **1**.

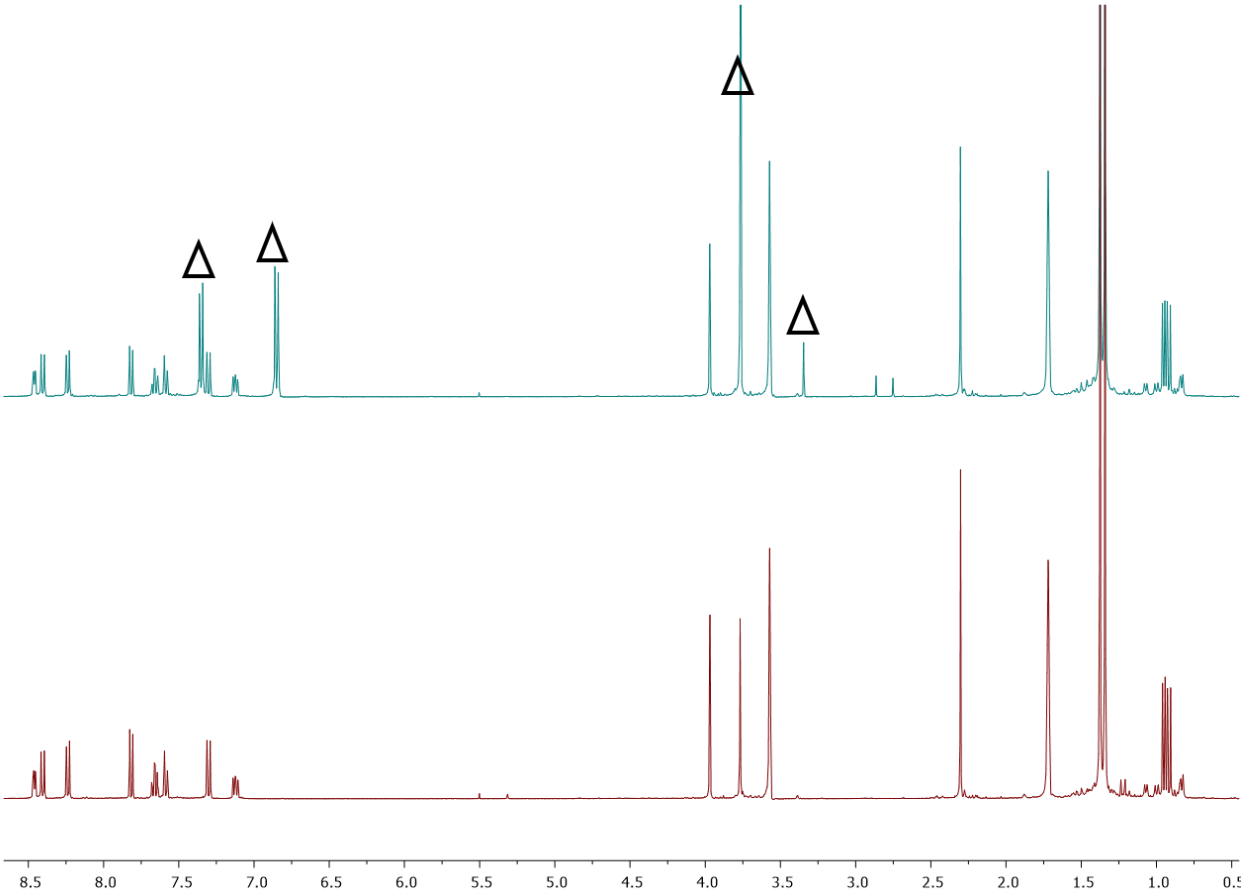

Figure S104. ^{1}H NMR spectrum of **1** (red line, bottom) and the spectrum of solution containing **1** in a mixture with 4-ethynyl anisole after reacting for 6 h at RT (green line, top). Peaks marked with triangles belong to an unreacted 4- ethynylanisole.

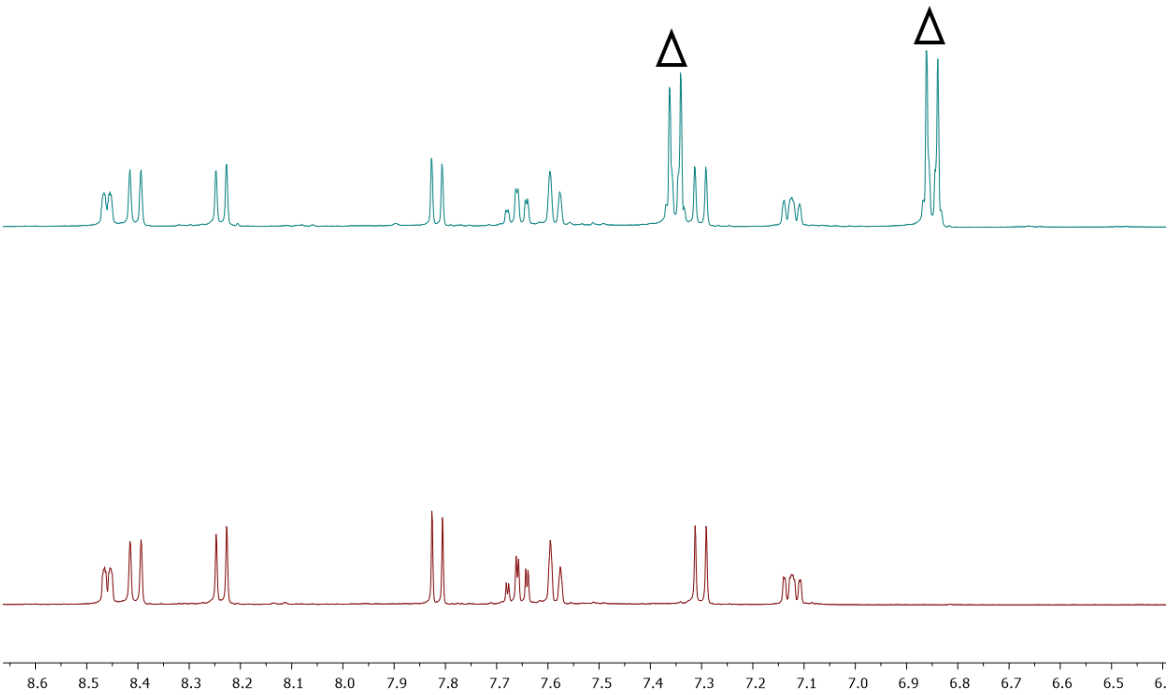

Figure S105. Expanded aromatic region of ^{1}H NMR spectrum of of **1** (red line, bottom) and the spectrum of solution containing **1** in a mixture with 4-ethynyl anisole after reacting for 6 h at RT (green line, top). Peaks marked with triangles belong to an unreacted 4- ethynylanisole.

Thermolysis of 1 in the presence of 4-ethynylanisole after prolonged heating

To a solution of **1** (5 mg, 0.007 mmol) in THF-d_8 (400 μL) in a J. Young NMR tube, 4-ethynylanisole (2 μL , 0.015 mmol) was added and the NMR tube was submerged in an oil bath at 40 °C.The reaction was periodically monitored by NMR spectroscopy over prolonged period of time. While the complex **1** did not show significant decomposition for up to 6 h (vide supra), eventually after prolonged heating decomposition to an intractable mixture of product was observed.

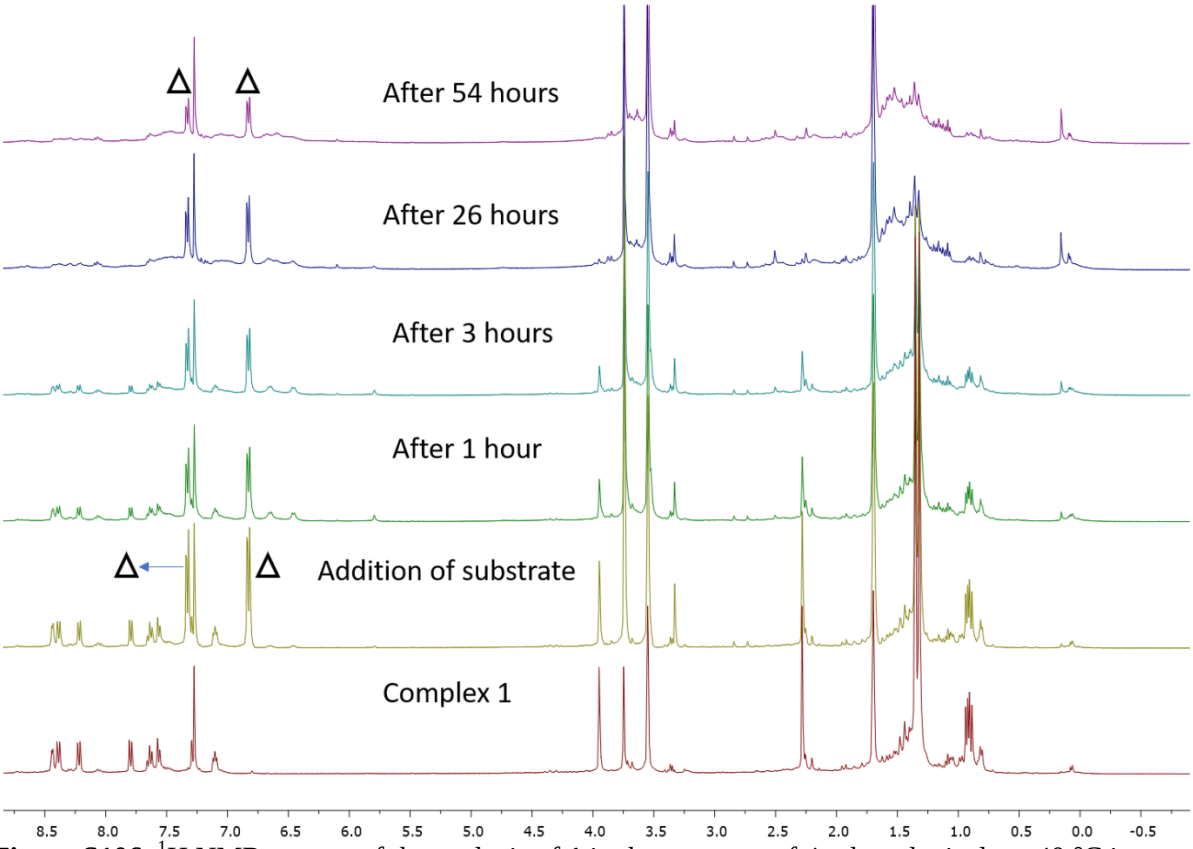

Figure S106. ^{1}H NMR spectra of thermolysis of **1** in the presence of 4-ethynylanisole at 40 ℃ in THF-d_8. Bottom spectrum is the spectrum of **1** before addition of 4-ethynylanisole.

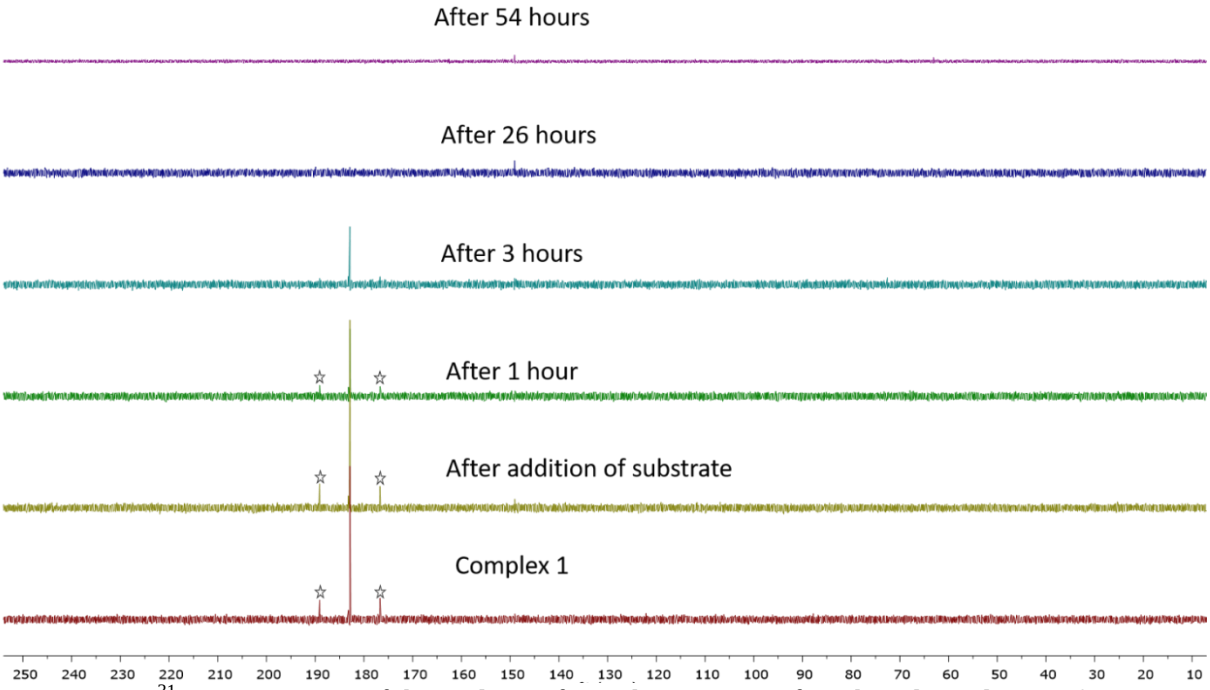

Figure S107. ^{31}P NMR spectra of thermolysis of **1** in the presence of 4-ethynylanisole at 40 ℃ in THF-d_8. Bottom spectrum is the spectrum of **1** before addition of 4-ethynylanisole.

Reaction of 3[BF_4] with 2 equiv of 4-ethynylanisole to give 7[BF_4]

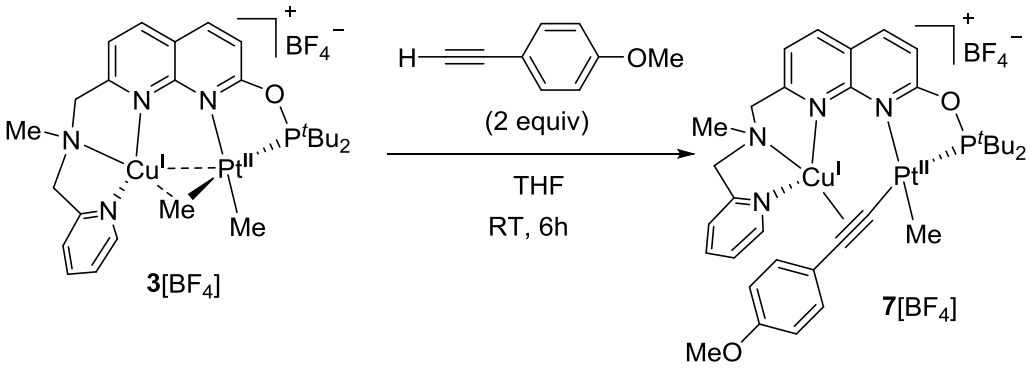

Scheme S11. Formation of **7.**

To a 20 mL vial containing solution of **3**[BF_4] (85.2 mg, 0.10 mmol) in THF (5 mL), 4-ethynylanisole (27.6 μL, 0.21 mmol) was added. The reaction mixture was stirred at RT for 6 h. The color of solution changed from brown to deep red-orange. After 6 h the reaction mixture was filtered through celite. The resulting solution was layered with pentane (12 mL) and left to crystallize at -30 °C, yielding orange crystals. Crystals were washed with excess amount of cold penatne to obtain complex **7**[BF_4], 57.6 mg, 0.06 mmol, 59% yield.

^{1}H NMR (600 MHz, CD_3CN, -25 °C) δ: 8.99 (d, $^3J_{HH}$ = 4.9 Hz, 1H, CH_{Py}), 8.57 (d, $^3J_{HH}$ = 8.7 Hz, 1H, CH_{Naph}), 8.49 (d, $^3J_{HH}$ = 8.2 Hz, 1H, CH_{Naph}), 7.84 (td, $^3J_{HH}$ = 7.7 Hz, $^4J_{HH}$ = 1.2 Hz, 1H, CH_{Py}), 7.58 (d, $^3J_{HH}$ = 8.2 Hz, 1H, CH_{Naph}), 7.51 (d, $^3J_{HH}$ = 8.7 Hz, 1H, CH_{Naph}), 7.50 - 7.46 (m, 1H, CH_{Py}), 7.31 (d, $^3J_{HH}$ = 7.7 Hz, 1H, CH_{Py}), 7.21 (d, $^3J_{HH}$ = 8.6 Hz, 2H, C_6H_4-OMe), 6.80 (d, $^3J_{HH}$ = 8.6 Hz, 2H, C_6H_4-OMe), 4.37 (d, $^2J_{HH}$ = 16.4 Hz, 1H, CH_2), 4.17 (d, $^2J_{HH}$ = 16.4 Hz, 1H, CH_2), 3.73 (s, 3H,O*Me*), 3.57 (d, $^2J_{HH}$ = 15.2 Hz, 1H, CH_2), 3.51 (d, $^2J_{HH}$ = 15.2 Hz, 1H, CH_2), 2.38 (s, 3H, N-CH_3), 1.52 (d, $^3J_{PH}$ = 14.8 Hz, 9H, $C(CH_3)_3$), 1.34 (d, $^3J_{PH}$ = 5.9 Hz, $^2J_{PtH}$ = 40.2 Hz, 3H, Pt-Me), 1.24 (d, $^3J_{PH}$ = 14.8 Hz, 9H, $C(CH_3)_3$).

$^{13}C\{^1H\}$ NMR (151 MHz, CD_3CN, -25 °C) δ: 167.69 ($C_{q,\ Naph}$), 160.65 ($C_{q,\ Naph}$), 158.92 ($C_{q,\ Naph}$), 157.28 ($C_{q,\ Naph}$), 150.97 (C_q of C_6H_4-OMe), 149.93 (CH_{Py}), 144.14 (CH_{Naph}), 140.21 (CH_{Naph}), 138.81 (CH_{Py}), 132.68 (*C*H of C_6H_4-OMe), 128.88 (C_q of C_6H_4-OMe), 124.85 (CH_{Py}), 123.92 (CH_{Py}), 122.59 (CH_{Naph}), 121.93 ($C_{q,\ Py}$), 114.44 (CH_{Naph}), 114.35 (*C*H of C_6H_4-OMe), 67.80 (Pt-C≡*C*), 63.76 (CH_2), 61.84 (CH_2), 55.42 (O*Me*), 45.37 (N-CH_3), 42.13 – 42.03 (br m, *C*$(CH_3)_3$), 39.37 – 39.21 (br m,*C*$(CH_3)_3$), 27.44 (d, $^2J_{PC}$ = 3.5 Hz, C(*C*$H_3)_3$), 26.72 (d, $^2J_{PC}$ = 5.3 Hz, C(*C*$H_3)_3$), 25.77 (Pt-*C*≡C), -27.22 (d, $^2J_{PC}$ = 3.9 Hz, Pt-Me). Pt satellite for -27.22 ppm Pt-Me signal were not clearly seen due to low intensity.

$^{31}P\{^1H\}$ NMR (242 MHz, CD_3CN, -25 °C) δ: 175.5 ($^1J_{PtP}$ = 3220 Hz).

$^{195}Pt\{^1H\}$ NMR (129 MHz, CD_3CN, -25 °C) δ: -4126.6 ($^1J_{PtP}$ = 3220 Hz).

ESI-HRMS (m/z pos): Found (Calcd): $C_{34}H_{43}O_2N_4P^{195}Pt^{63}Cu^+$ 828.2063 (828.2063).

FT-IR (ATR, solid): 2955 (br, w), 2879 (br, w), 1729 (w), 1601 (s), 1581 (m), 1318 (m), 1059 (s), 862 (m), 765 (m) cm^{-1}.

UV-vis (THF), λ, nm (ε, $M^{-1}\cdot cm^{-1}$) : 321 (10600), 242 (20000).

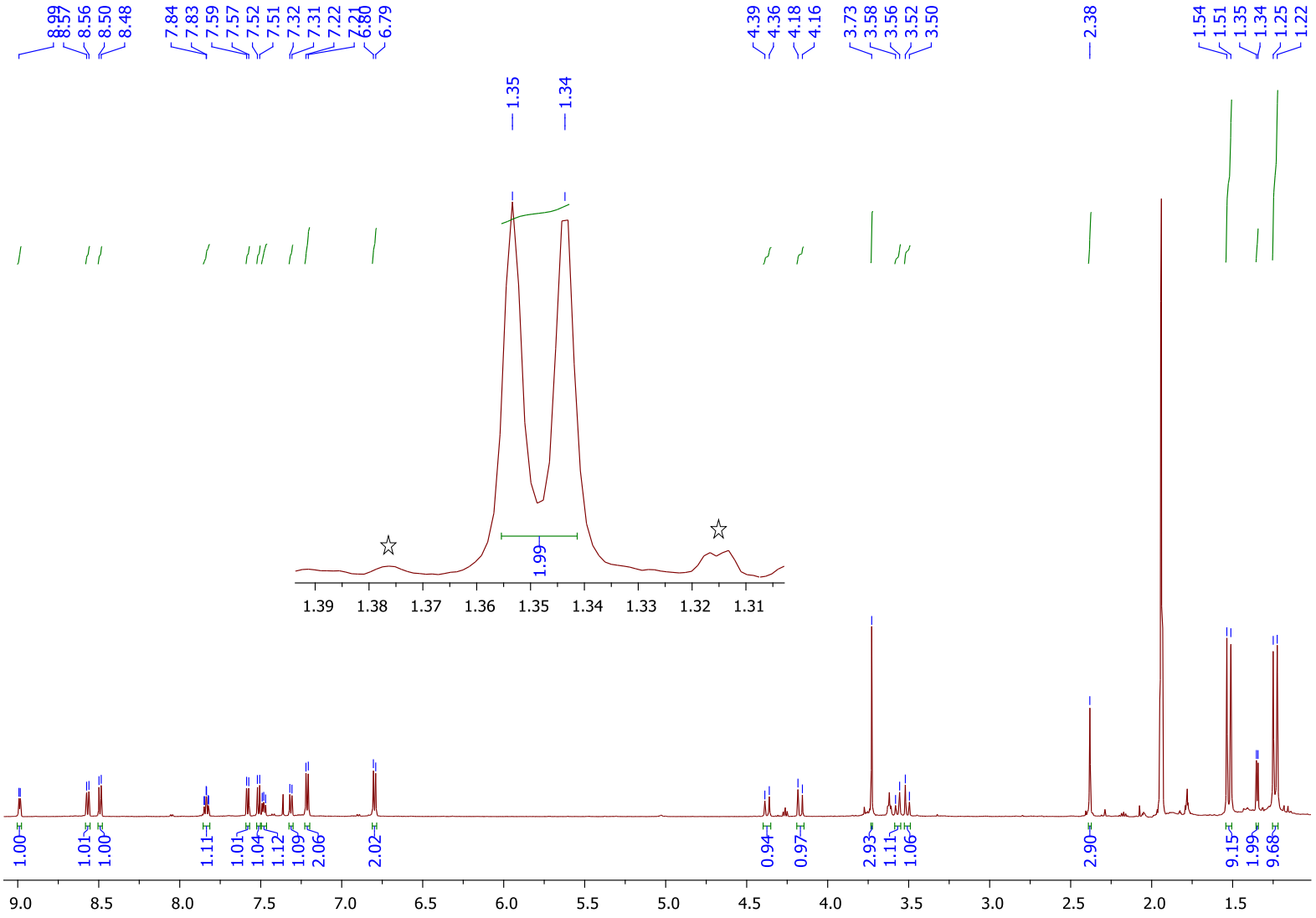

Figure S108. ^{1}H NMR spectrum of **7**[BF_4] in CD_3CN at -25 °C. Pt satellites are marked with stars.

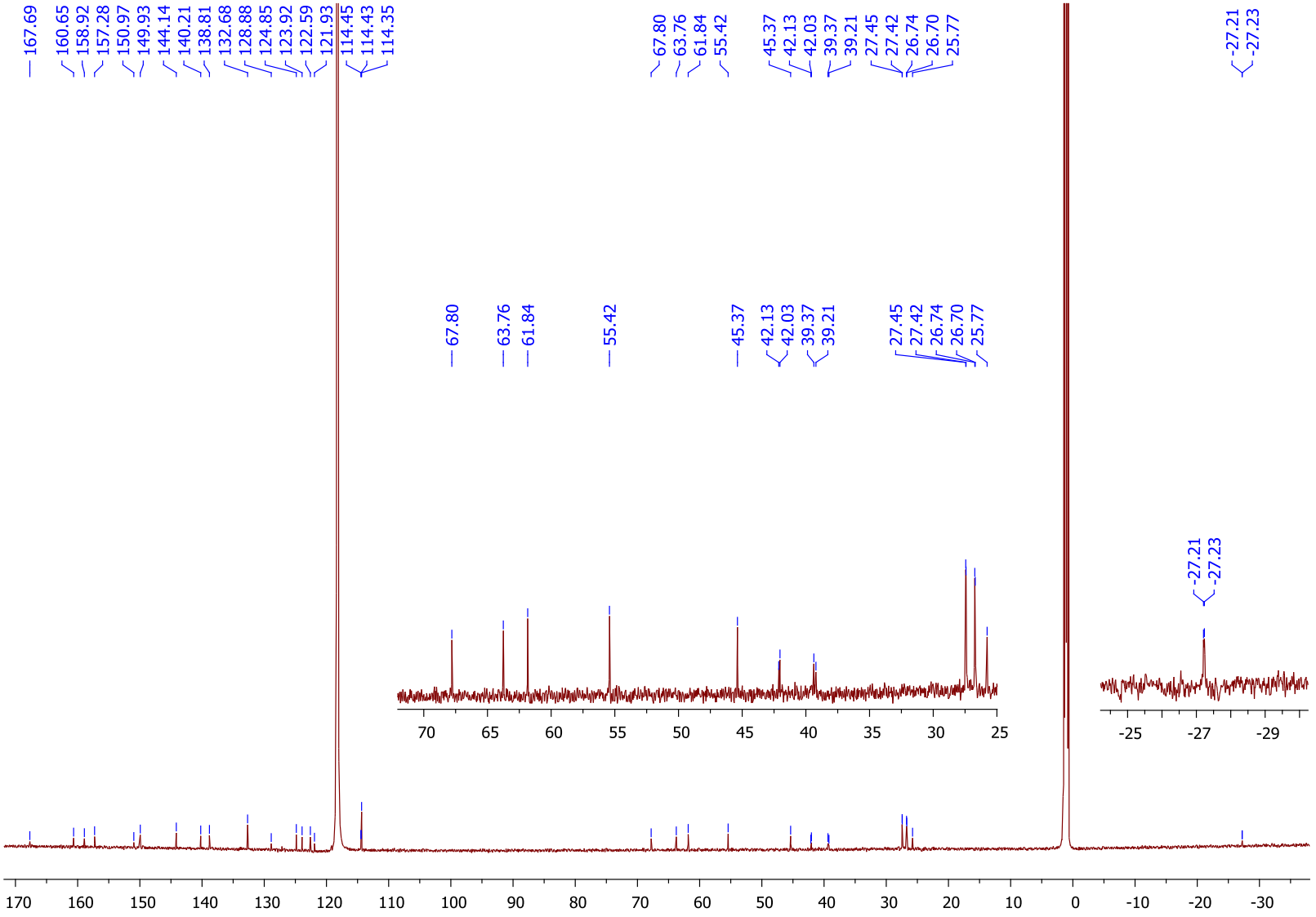

Figure S109. $^{13}C\{^{1}H\}$ NMR spectrum of **7**[BF_4] in CD_3CN at -25 °C.

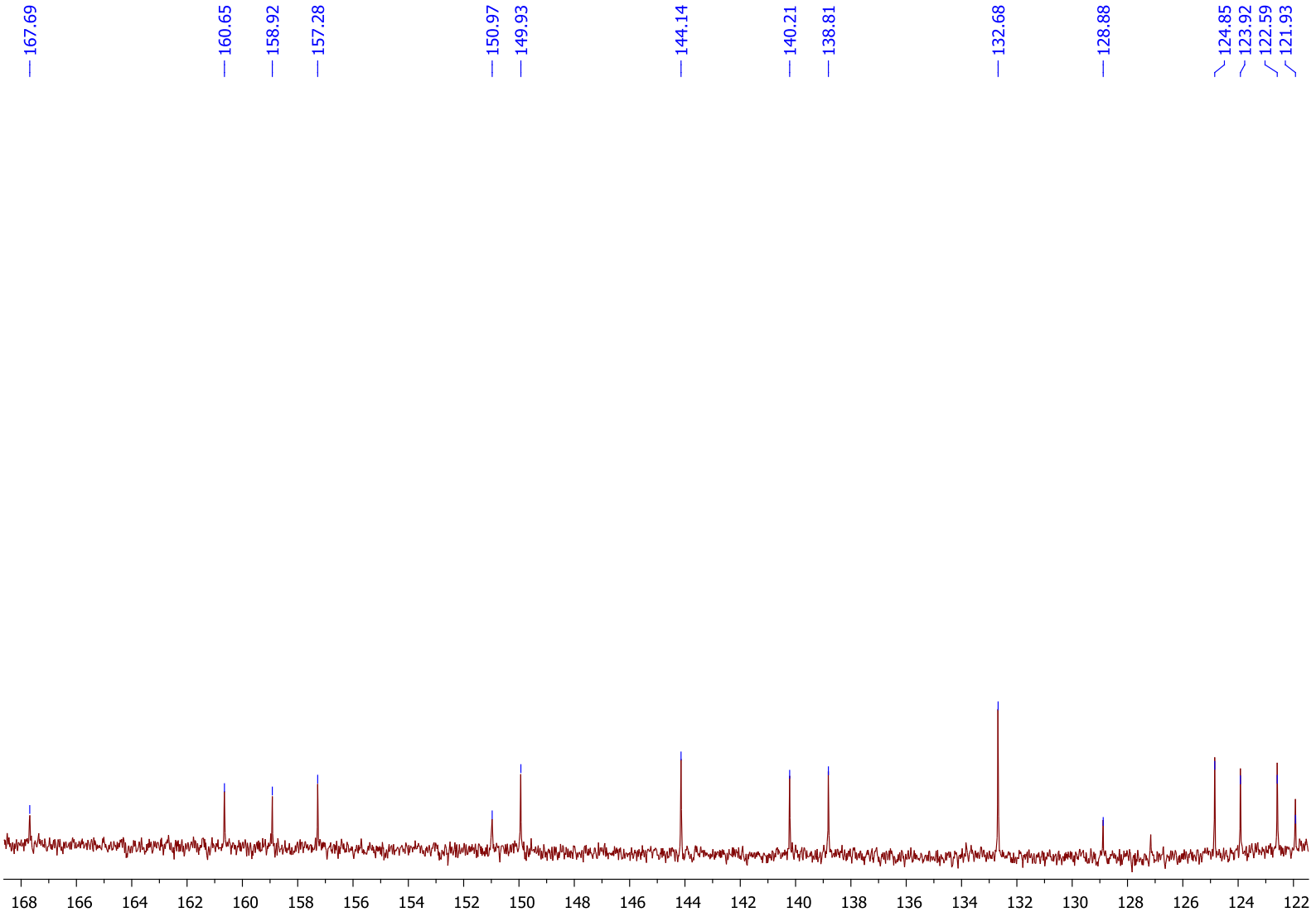

Figure S110. Expanded aromatic region of the $^{13}C\{^{1}H\}$ NMR spectrum of **7**[BF_4] in CD_3CN at -25 °C.

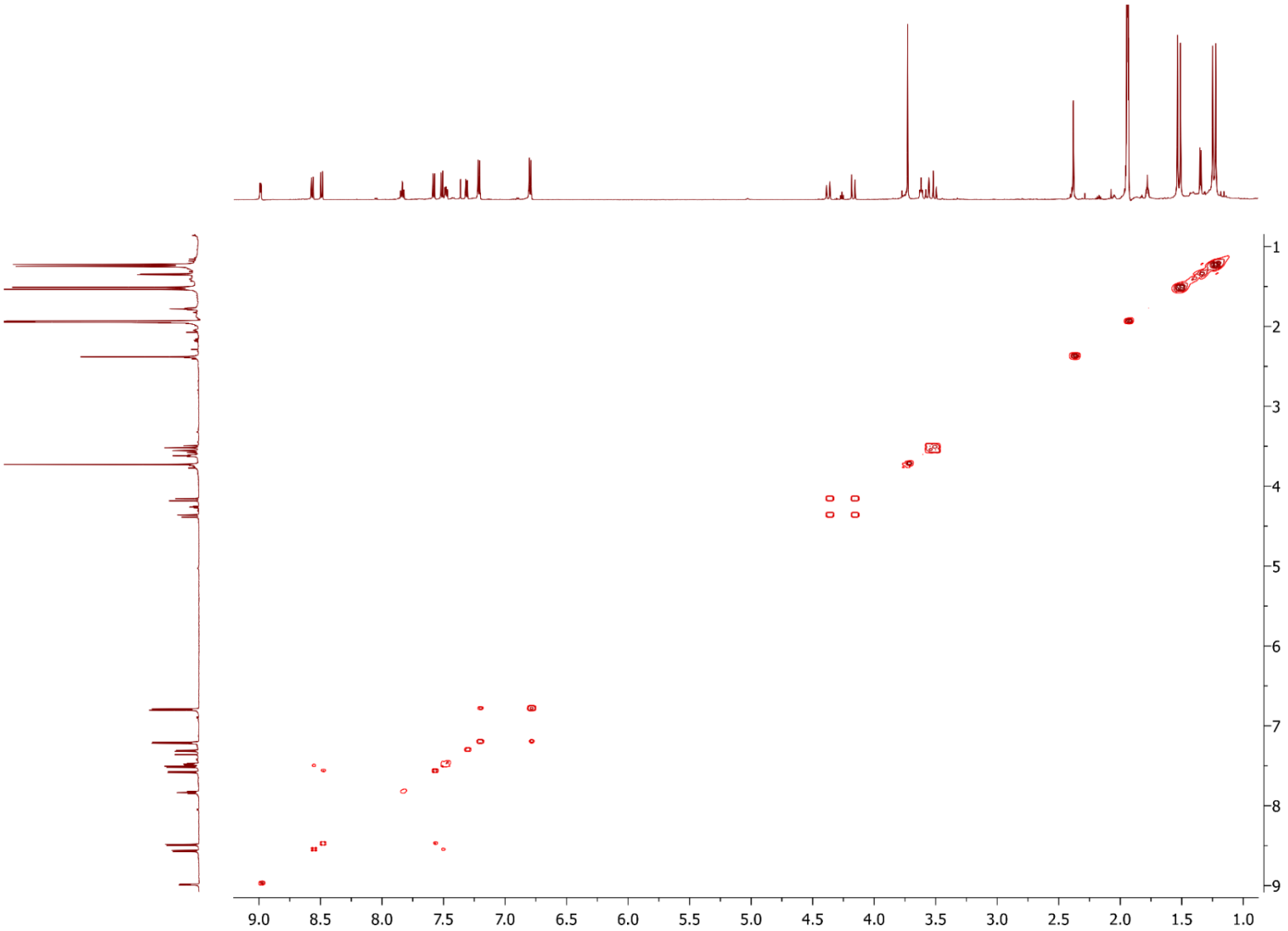

Figure S111. ^{1}H-^{1}H COSY spectrum of **7**[BF_4] in CD_3CN at -25 °C.

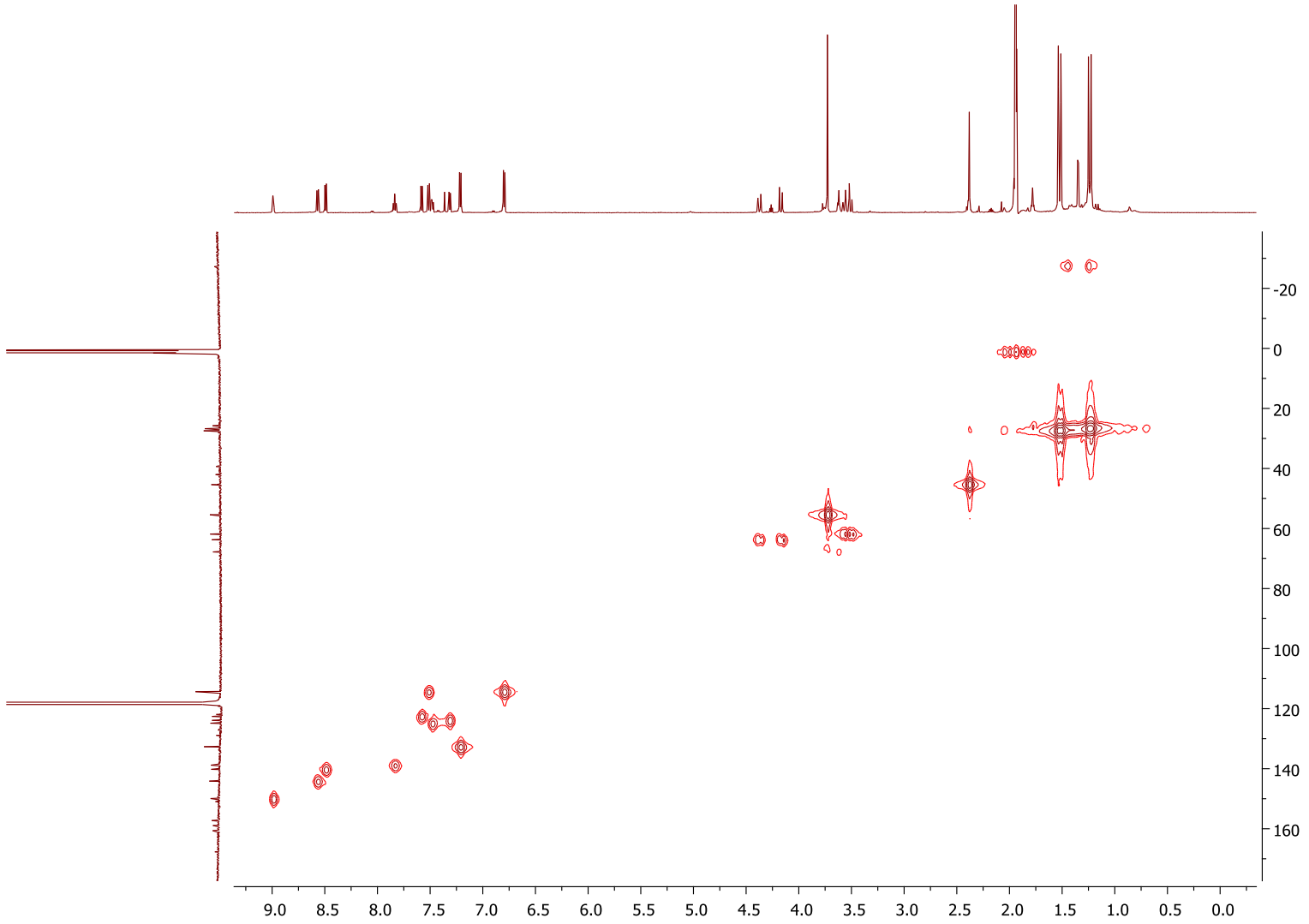

Figure S112. ^{1}H-^{13}C HMQC spectrum of **7**[BF_4] in CD_3CN at -25 °C.

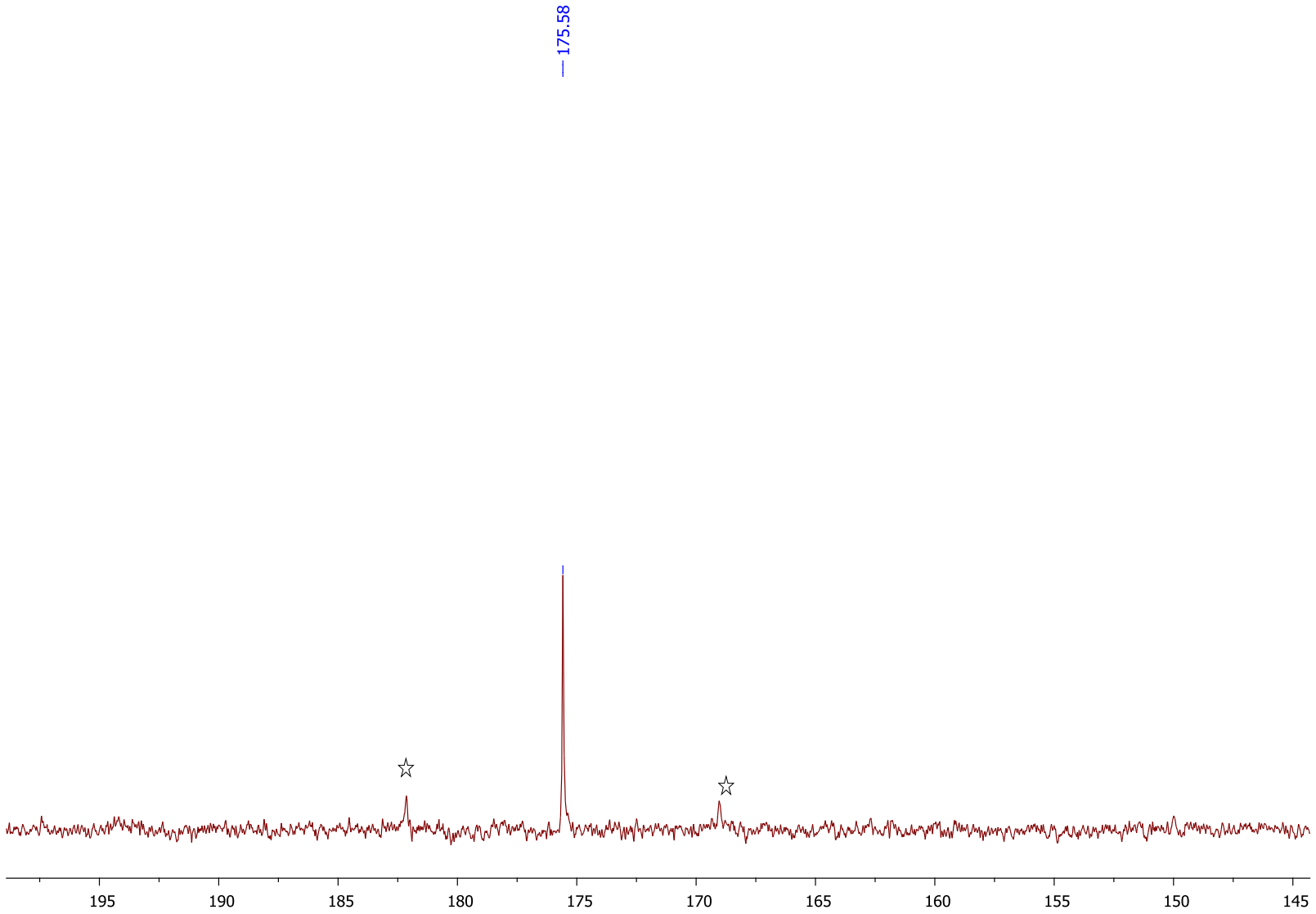

Figure S113. $^{31}P\{^{1}H\}$ NMR spectrum of **7**[BF_4] in CD_3CN at -25 °C. Pt satellites are marked with stars.

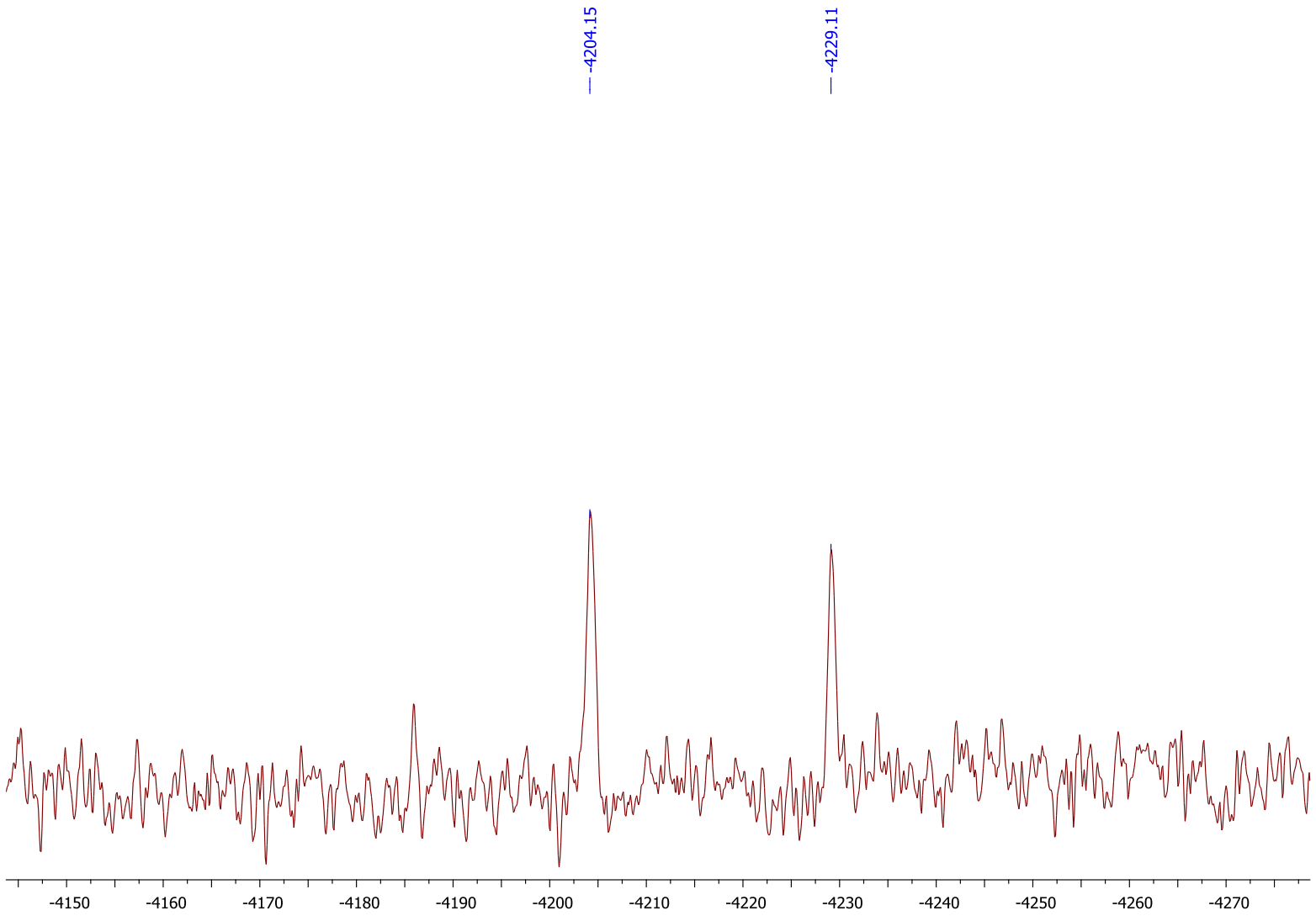

Figure S114. $^{195}Pt\{^{1}H\}$ NMR spectrum of **7**[BF_4] in CD_3CN at -25 °C.

Selective 1D-difference NOE experiments of 7[BF_4] in CD_3CN:
Experiments were performed using mixing time 0.9 s and delay time 4.5 s. The orientation of the methyl grouprelative to the *tert*-butyl group was confirmed by difference NOE 1D experiments. Irradiation of a resonance at 1.52 ppm corresponding to a *tert*-butyl group induced enhancement (positive NOE) of a Pt-Me signal at 1.34 ppm confirming its *cis*-orientation relative to the P-donor.

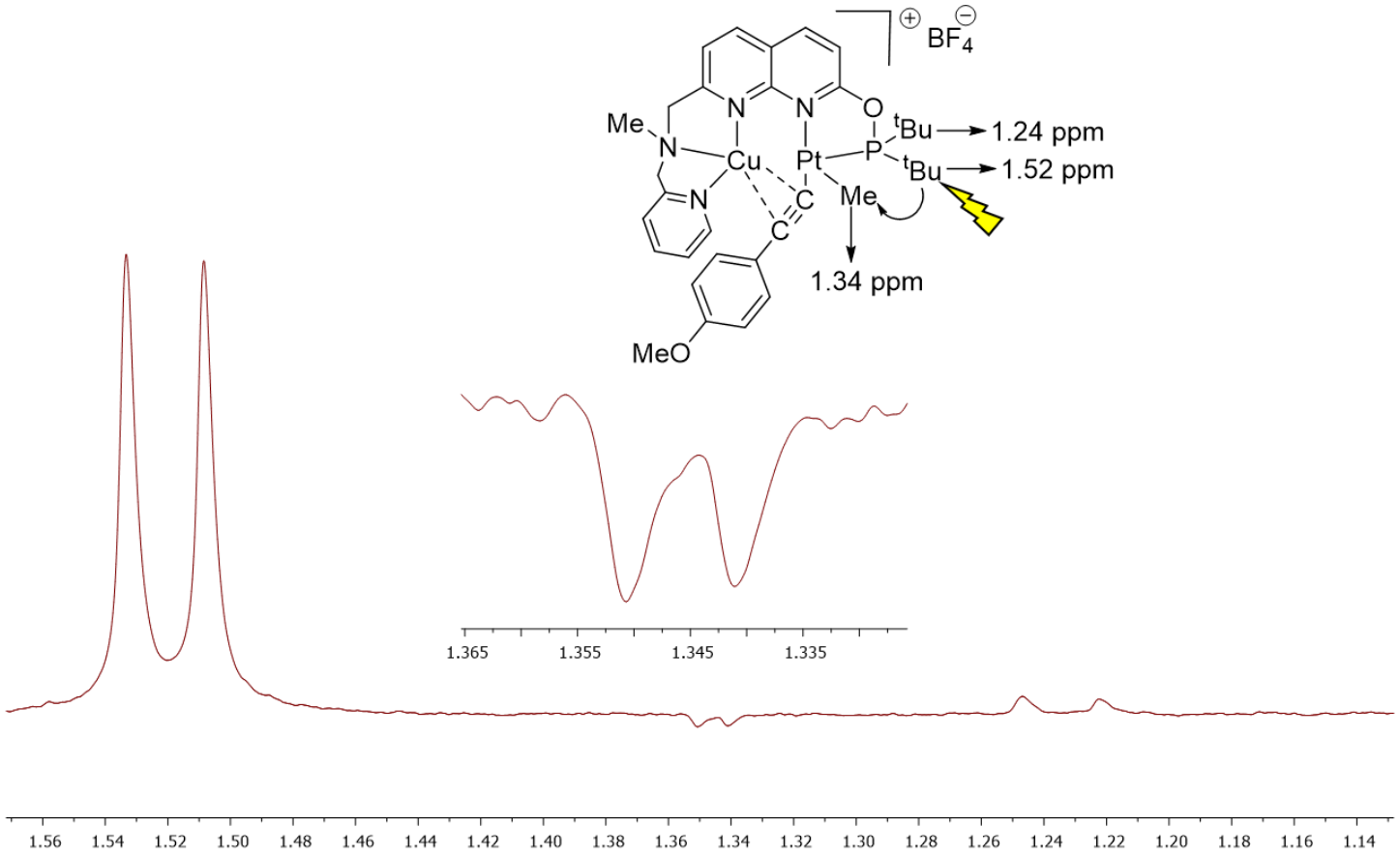

Figure S115. 1D-NOE NMR spectrum of **7**·[BF_4] in CD_3CN at -25 °C.

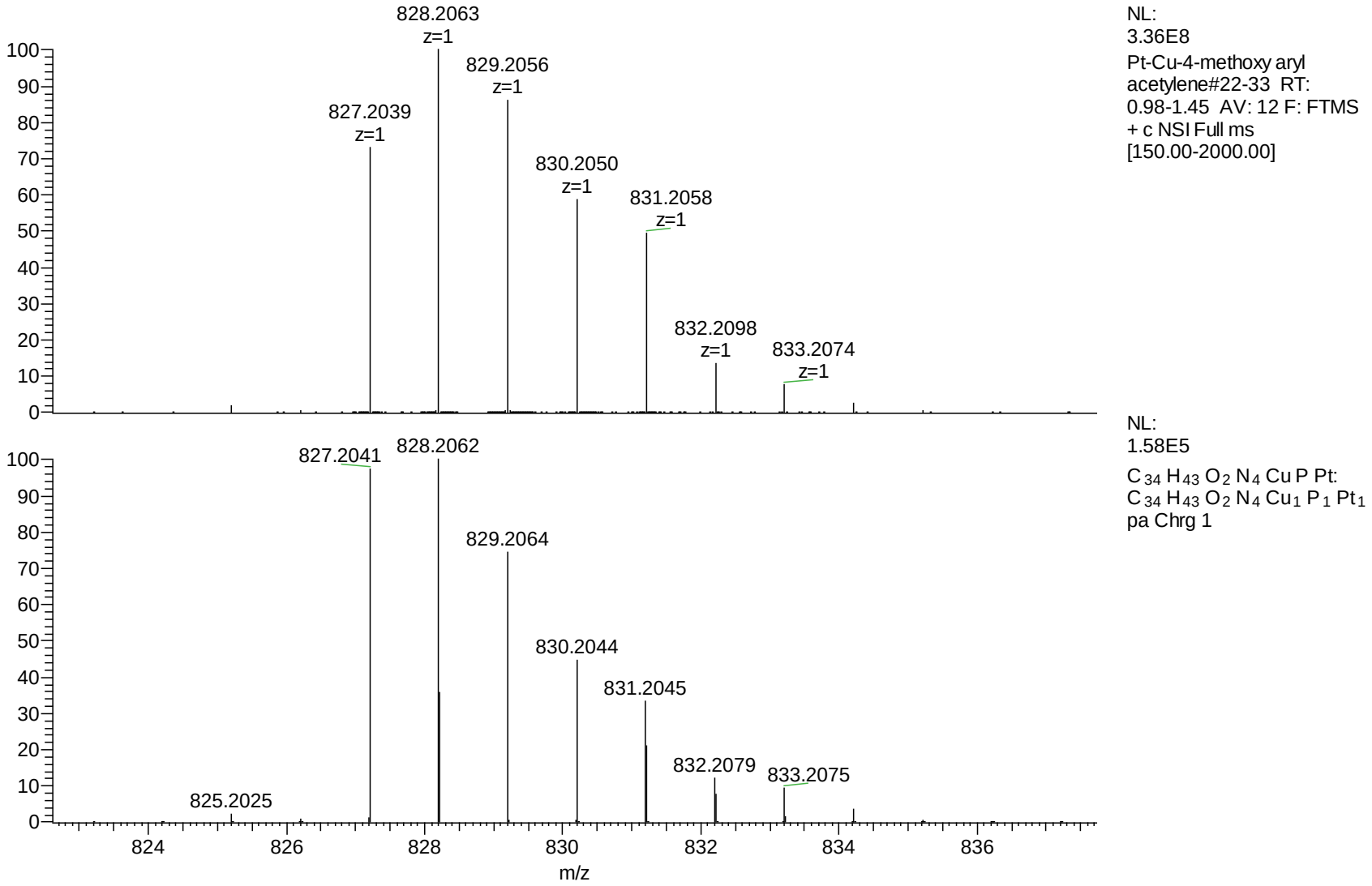

Figure S116. ESI-(HR)MS spectrum of a THF solution of **7**[BF_4] (top) and simulated spectrum for $C_{34}H_{43}O_2N_4PPtCu^+$ (bottom).

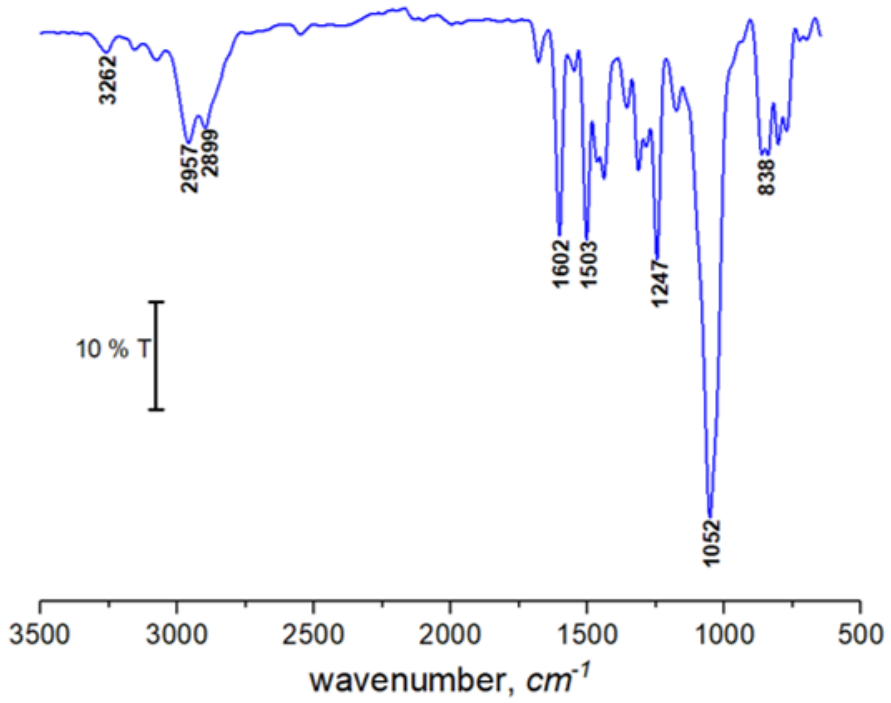

Figure S117. ATR FT-IR transmittance spectrum of **7**[BF_4]**.**

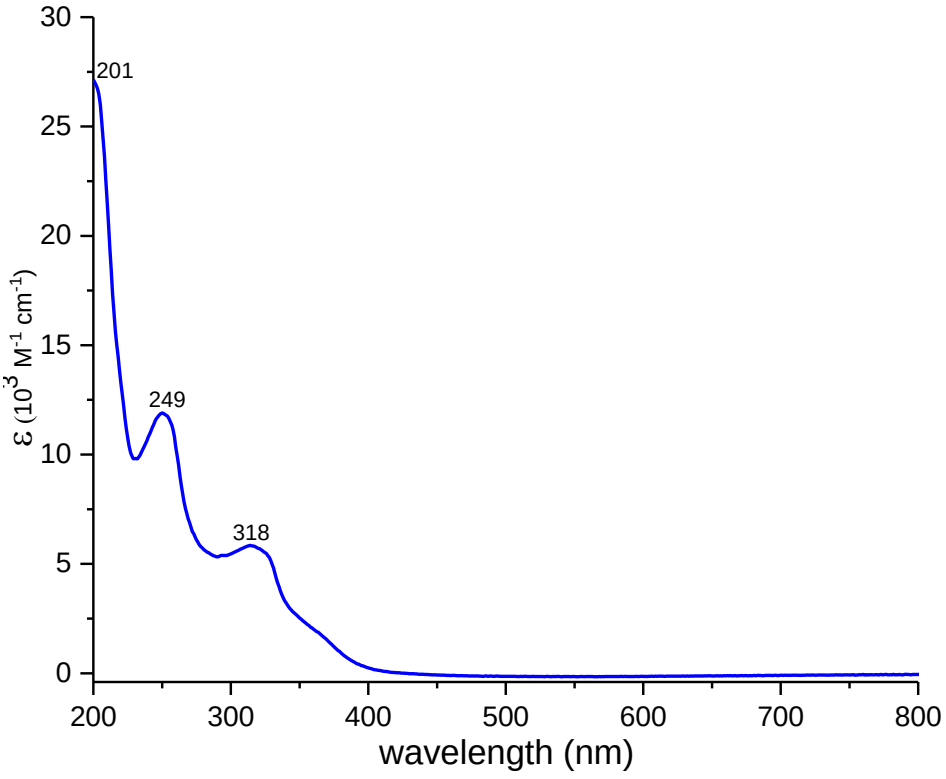

Figure S118. UV-vis absorbance spectrum for **7**[BF_4] in MeCN.

Reaction of 3[BF_4] with 1 equiv of 4-ethynylanisole

Complex **3**[BF_4] (8.5 mg, 0.010 mmol) was dissolved in THF-d_8 (400 μL) in a J. Young NMR tube in the presence of 4-ethynylanisole (1.4 μL, 0.010 mmol, 1 equiv). The solution was then stirred in an NMR tube at room temperature and periodically monitored by NMR spectroscopy. Incomplete conversion was observed after 16 h at RT, and starting material, **3**[BF_4] and unreacted alkyne, still remained in solution as observed by ^{1}H and ^{31}P NMR spectroscopy.

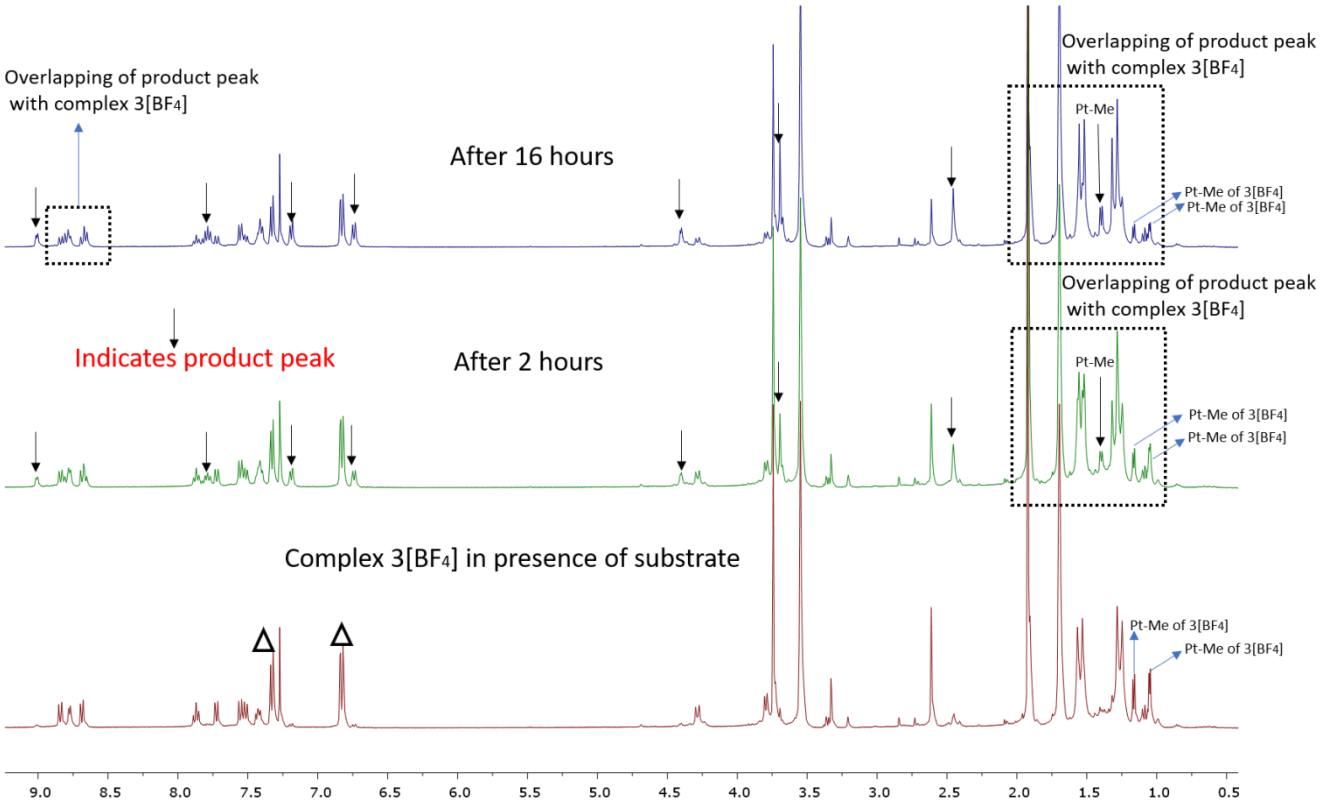

Figure S119. ^{1}H NMR spectra of **3**[BF_4] in the reaction mixture containing 1 equiv of 4-ethynylanisole. Bottom: immediately after mixing; middle: after 2 h; top: after 16 h at RT. Aromatic peaks of 4-ethynylanisole are labeled with triangles; arrows indicate the peaks of the product **7**[BF_4].

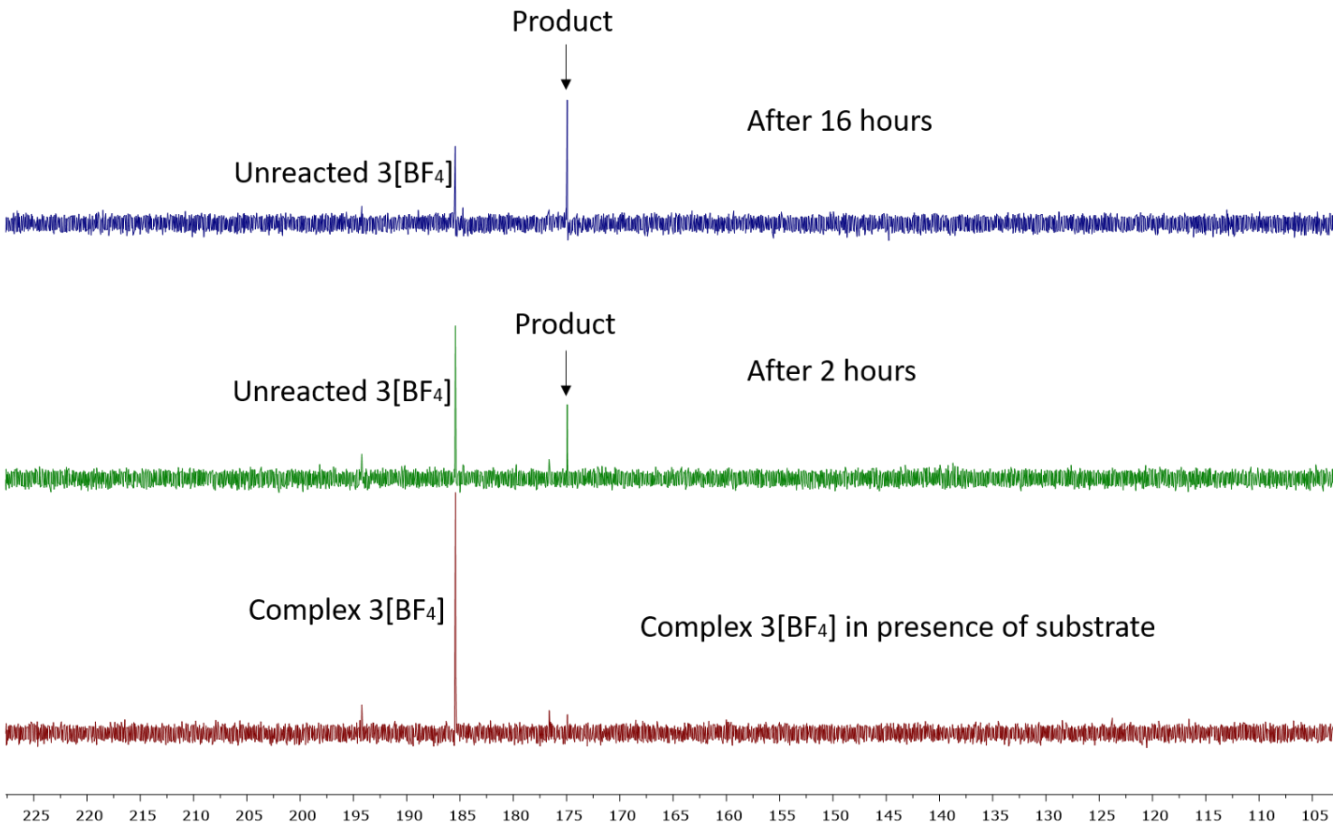

Figure S120. ^{31}P NMR spectra of **3**[BF_4] in the reaction mixture containing 1 equiv of 4-ethynylanisole. Bottom: immediately after mixing; middle: after 2 h; top: after 16 h at RT.

Formation of 6[B(Ar^F)$_4$] in the presence of Na[B(Ar^F)$_4$]

Complex **3**[B(Ar^F)$_4$] (7.1 mg, 0.0045 mmol) was dissolved in benzene (600 μL) in a J. Young NMR tube; Na[B(Ar^F)$_4$] (15.9 mg, 0.0179 mmol) was added. The NMR tube was then heated in an oil bath at 80 °C for 18 hours. After cooling down to RT, the NMR tube was then transferred inside the glovebox and the solvent was removed under vacuum. To the solid residue THF-d_8 (400 μL) was added in the presence of mesitylene added as an internal standard (1.9 μL, 0.013 mmol) to determine the yield of **6**[B(Ar^F)$_4$]. Integration against the internal standard gives the yield of **6**[B(Ar^F)$_4$] determined as 80% relative to the amount of starting material, **3**·[B(Ar^F)$_4$].

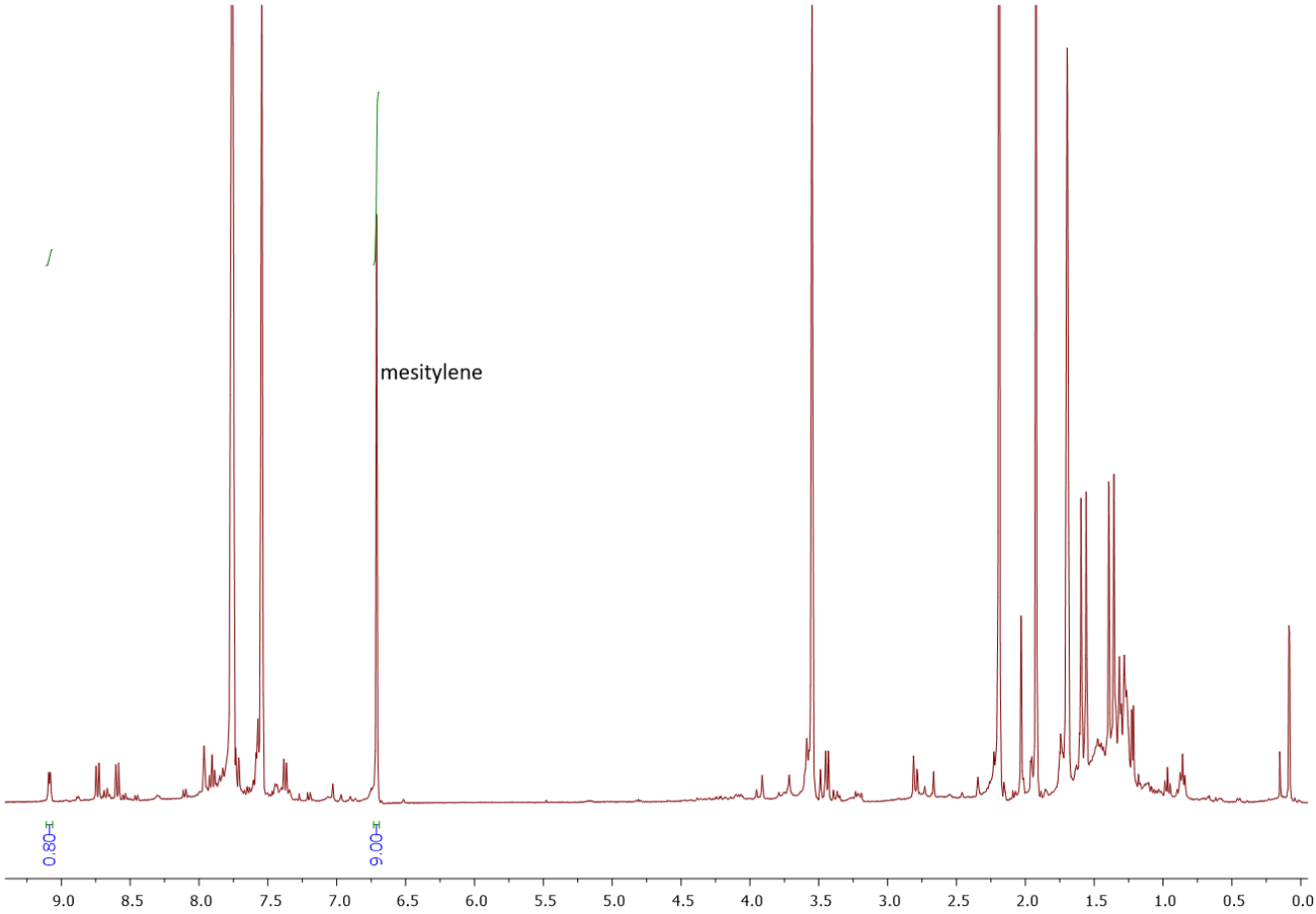

Figure S121.^{1}H NMR spectrum of **6**[B(Ar^F)$_4$] in THF-d_8 at 25 °C. Quantification of yield by integrating the peak at 9.12 ppm vs mesitylene peak (3 equivalents) at 6.74 ppm which act as an internal standard.

Comparison of stability of complexes 1, 3[BF_4] and 3[$B(Ar^F)_4$]

Stability of 1 in THF-d_8 and C_6D_6:
Complex **1** (8.7 mg, 0.015 mmol) was dissolved in THF-d_8 (400 μL) in a J. Young NMR tube in the presence of mesitylene as an internal standard. Complex **1** was heated at 40 °C and the reaction was periodically checked by ^{1}H NMR spectroscopy. After 12 hours, complete disappearance of Pt-Me signals was observed indicating that >95% of the complex has degraded under these conditions.

In the analogous way, stability of the solution of complex **1** (8.3 mg, 0.012 mmol) in C_6D_6 (400 μL) was monitored by ^{1}H NMR spectroscopy. Similarly, no signals of the starting materials could be detected after heating for 12 h, and broadened signals of the cyclometalated product started appearing.

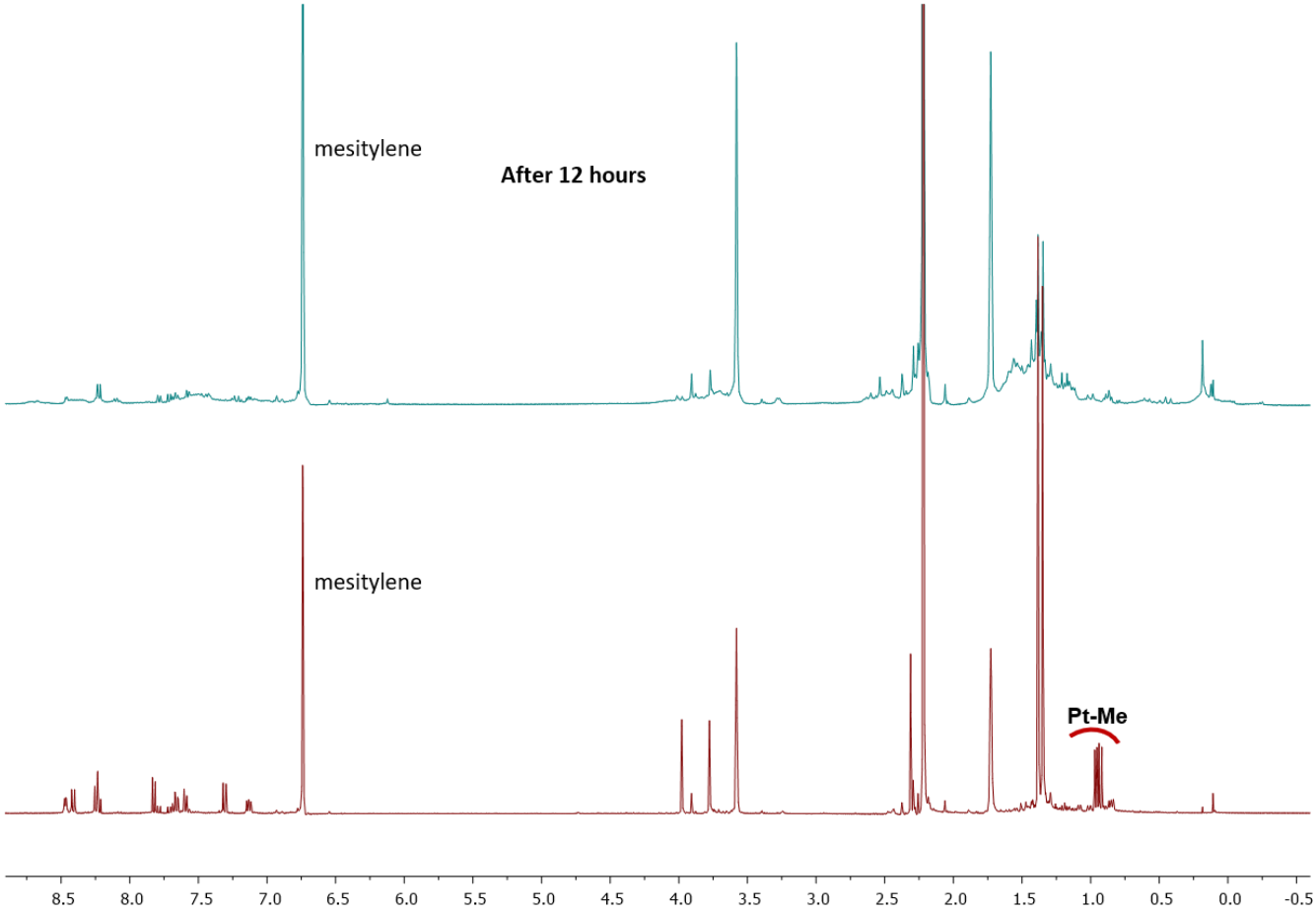

Figure S122. ^{1}H NMR spectra of **1** in THF-d_8 in the presence of mesitylene before heating (brown line, bottom) and after heating for 12 hours (blue line, top).

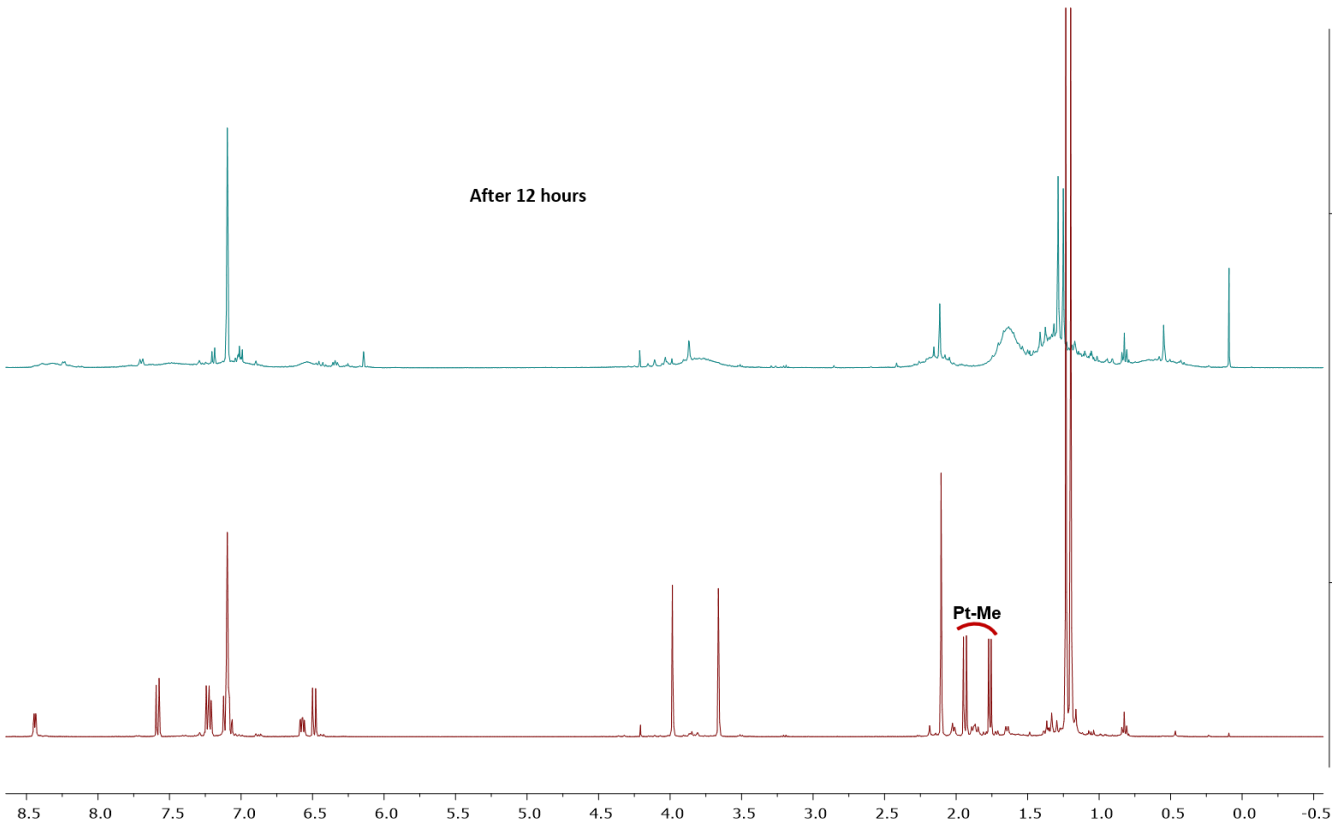

Figure S123. ^{1}H NMR spectra of **1** in C_6D_6 in the presence of mesitylene before heating (brown line, bottom) and after heating for 12 hours (blue line, top).

Stability of 3[BF_4] in THF-d_8:

Complex **3**[BF_4] (8.1 mg, 0.010 mmol) was dissolved in THF-d_8 (400 μL) in a J. Young NMR tube in the presence of mesitylene as an internal standard. The solution was then heated in an NMR tube at 40 °C and the reaction was periodically monitored by NMR spectroscopy.
According to ^{1}H NMR integration of the aromatic peak at 8.93 ppm vs. mesitylene standard, less than 1% decomposition is observed after heating for 12 h. No changes were observed in ^{1}H and ^{31}P spectra after heating indicating stability of the starting material under these conditions.

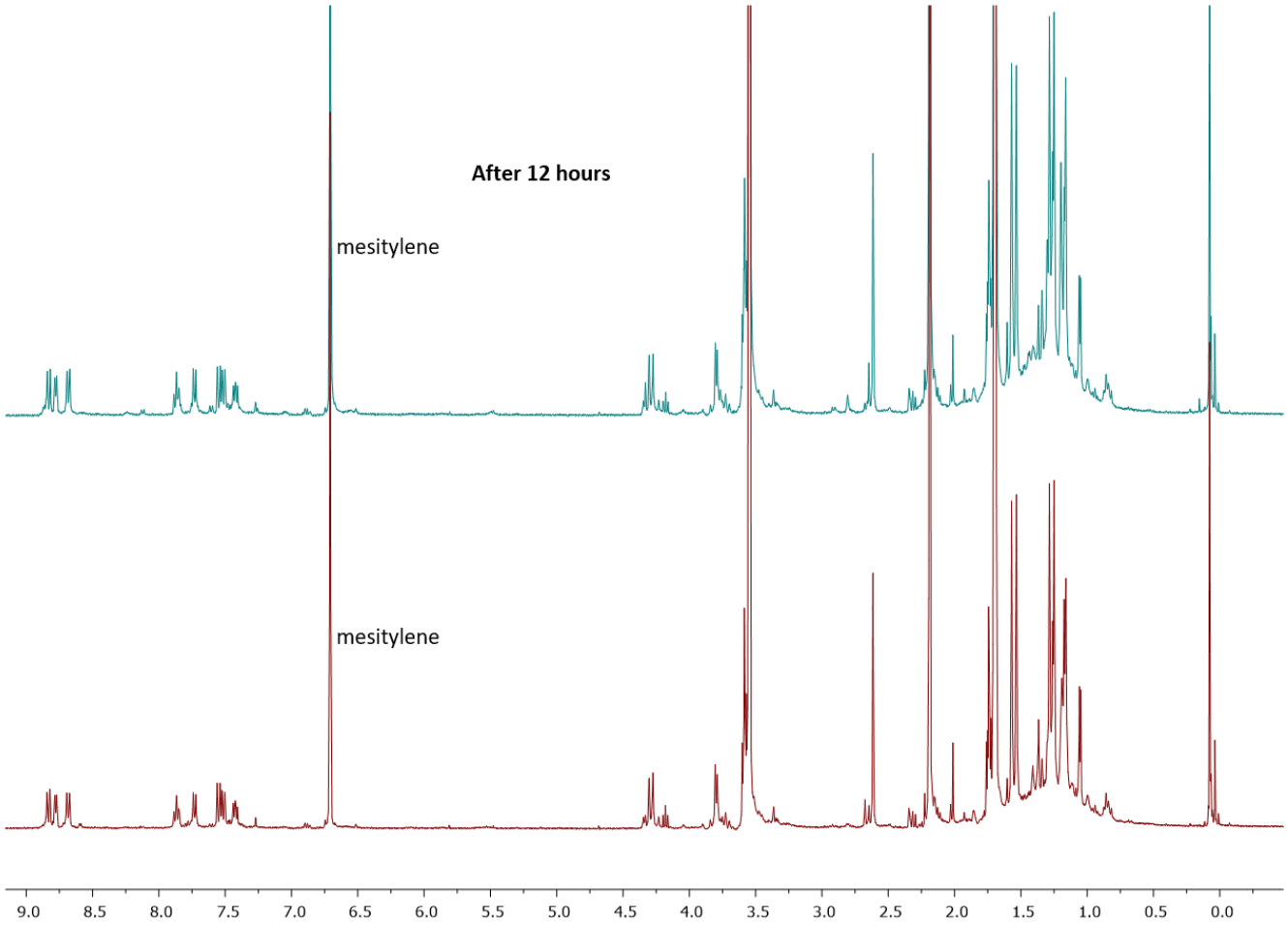

Figure S124. ^{1}H NMR spectra of **3**[BF_4] in THF-d_8 in the presence of mesitylene before heating (brown line, bottom) and after heating for 12 hours (blue line, top).

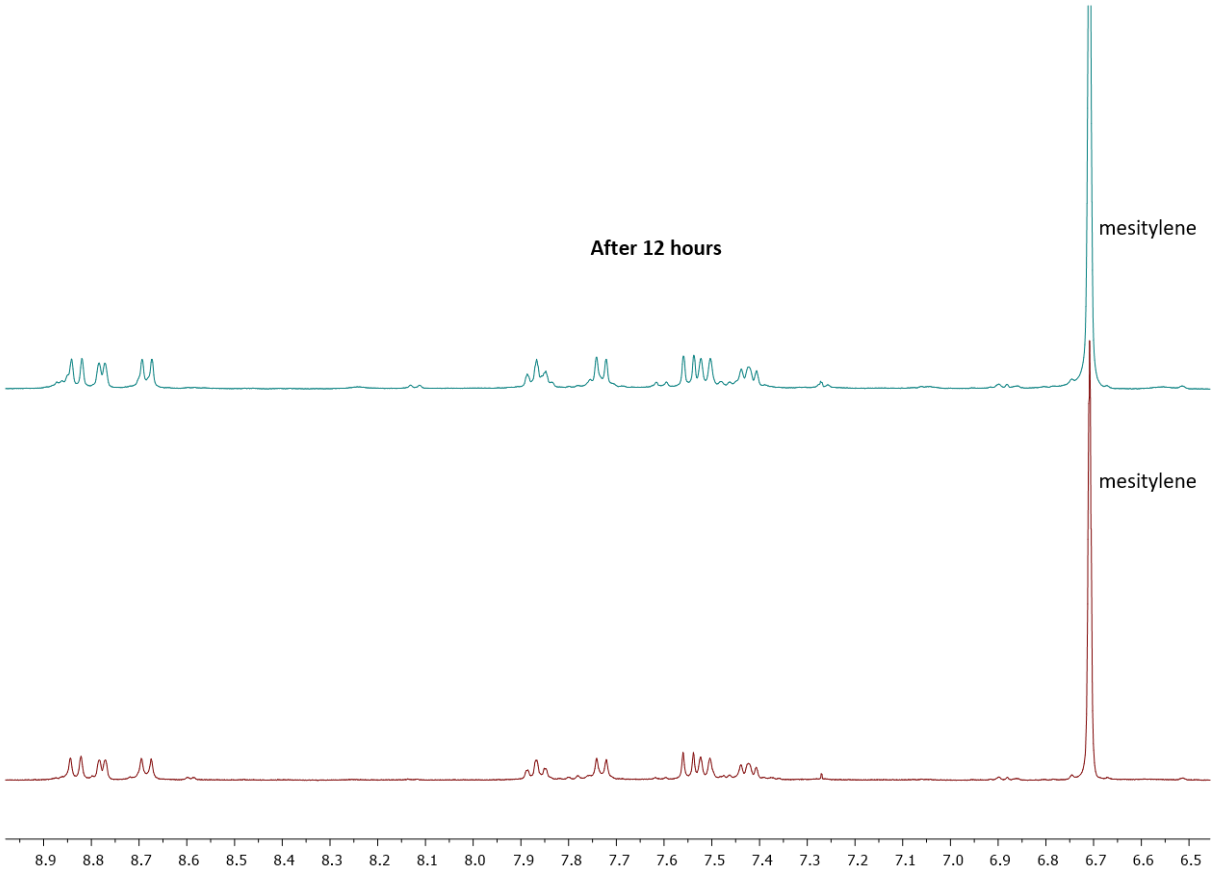

Figure S125. Expanded ^{1}H NMR spectra of **3**[BF_4] in THF-d_8 in the presence of mesitylene before heating (brown line, bottom) and after heating for 12 hours (blue line, top).

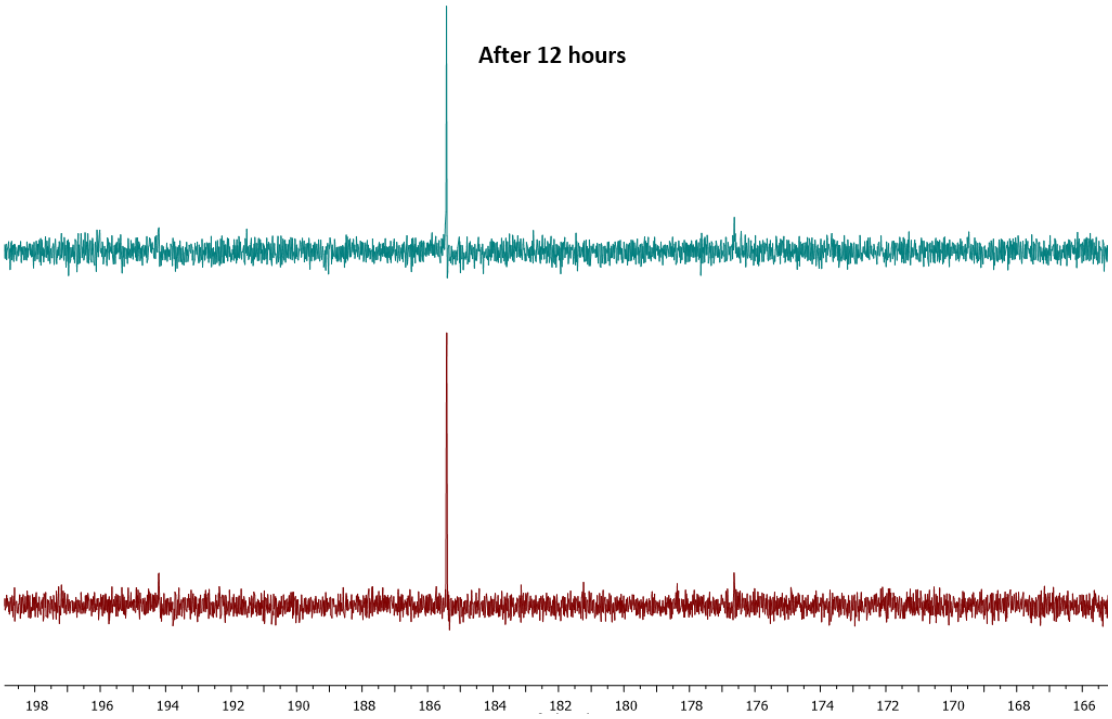

Figure S126. ^{31}P{^{1}H} NMR spectraof **3**[BF_4] in THF-d_8 in the presence of mesitylene before heating (brown line, bottom) and after heating for 12 hours (blue line, top).

Stability of 3[B(Ar^F)$_4$] in THF-d_8:

Complex **3**[B(Ar^F)$_4$] (8.4 mg, 0.005 mmol) was dissolved in THF-d_8 (400 µL) in a J. Young NMR tube. The solution was then heated in an NMR tube at 40 °C and the reaction was periodically monitored by NMR spectroscopy.
According to ^{1}H NMR integration of the aromatic peak at 8.84 ppm vs. solvent peak at 3.58 ppm before and after heating, less than 2% decomposition is observed after heating for 12 h. No changes were observed in ^{1}H and ^{31}P spectra after heating indicating stability of the starting material under these conditions.

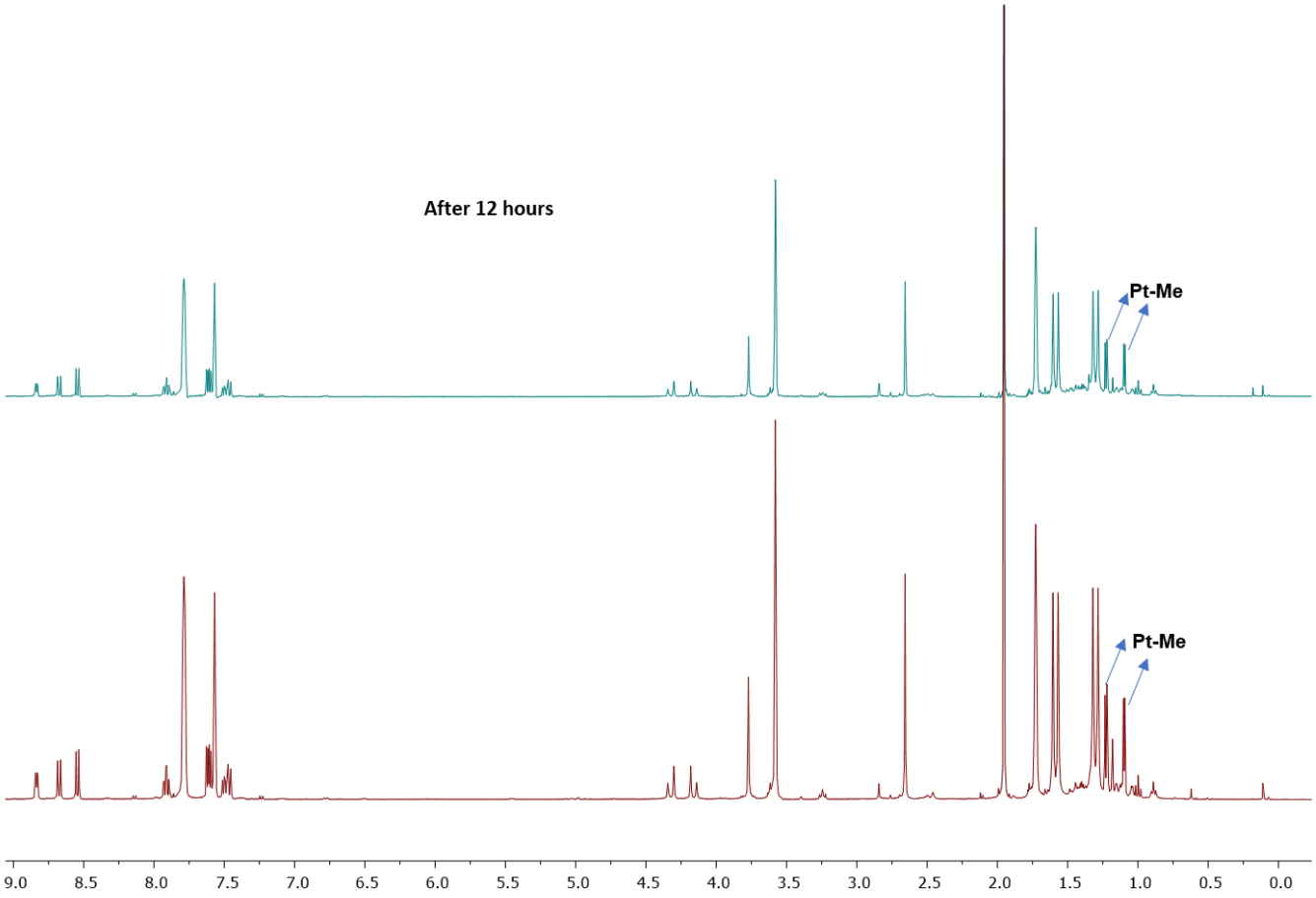

Figure S127. ^{1}H NMR spectra of **3**[B(Ar^F)$_4$] in THF-d_8 before heating (brown line, bottom) and after heating for 12 hours (blue line, top).

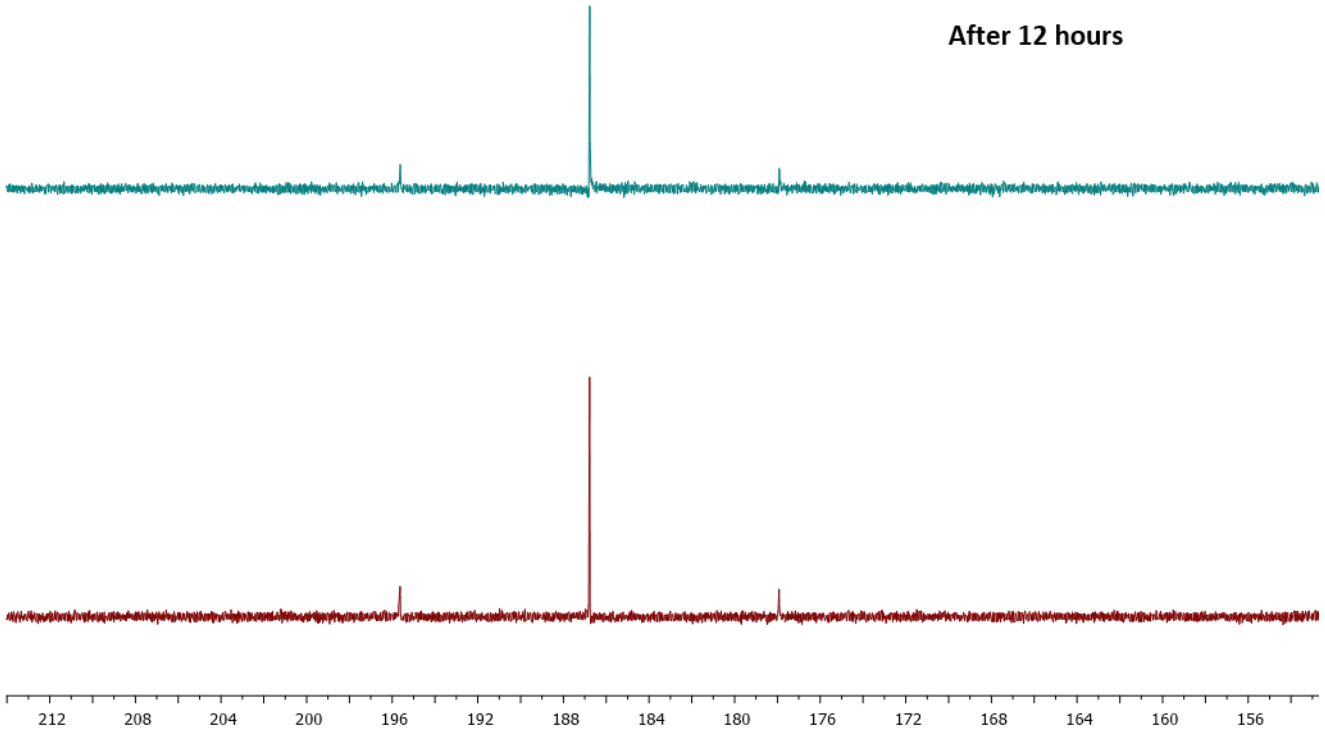

Figure S128. $^{31}P\{^{1}H\}$ NMR spectra of **3**[$B(Ar^F)_4$] in THF-d_8 in the presence of mesitylene before heating (brown line, bottom) and after heating for 12 hours (blue line, top).

Thermolysis of 4 in benzene-d_6.

Complex **4** (7.2 mg, 0.010 mmol) was dissolved in benzene-d_6 (400 μL) in a Teflon-sealed J. Young NMR tube. The solution was heated at 40 °C and the reaction was monitored by ^{1}H NMR and ^{31}P NMR spectroscopy. There was no sign of decomposition for 14 hours at 40 °C. The temperature was then raised up to at 60 °C, however, no changes were observed by NMR for 2 h. Upon further heating at 80 °C, complex **4** shows decomposition within several hours evident by changes in NMR spectra to give a mixture of unidentified products, among which cyclometalated product could not be reliably detected.

Attempted reactivity of 4 with 4-ethynylanisole

Complex **4** (5.3 mg, 0.007 mmol) was dissolved in THF-d_8 (400 μL) in a Teflon sealed J. Young NMR tube. After cooling down to -50 °C, 4-ethynylanisole (2.0 μL, 0.014 mmol,) was added and the NMR tube was quickly transferred to the NMR with pre-cooled probe. At -50 °C, slow formation of two new products is observed, however, upon warming to -40 °C, an intractable mixture of several unidentified products was formed, and complete degradation is observed at -25 °C.
When the reaction was performed at 20 °C, similarly, an intractrable mixture of several products formed. Among these products, complex **7** could not be reliably detected by NMR.
The absence of well-defined products in the case of **4** is likely due to its significantly higher reactivity due to presence of dearomatized ligand arm, which might lead to ligand-centered reactivity, and reduced ability to bind acetylene due to electron-rich Cu-center stabilized by an amide donor.

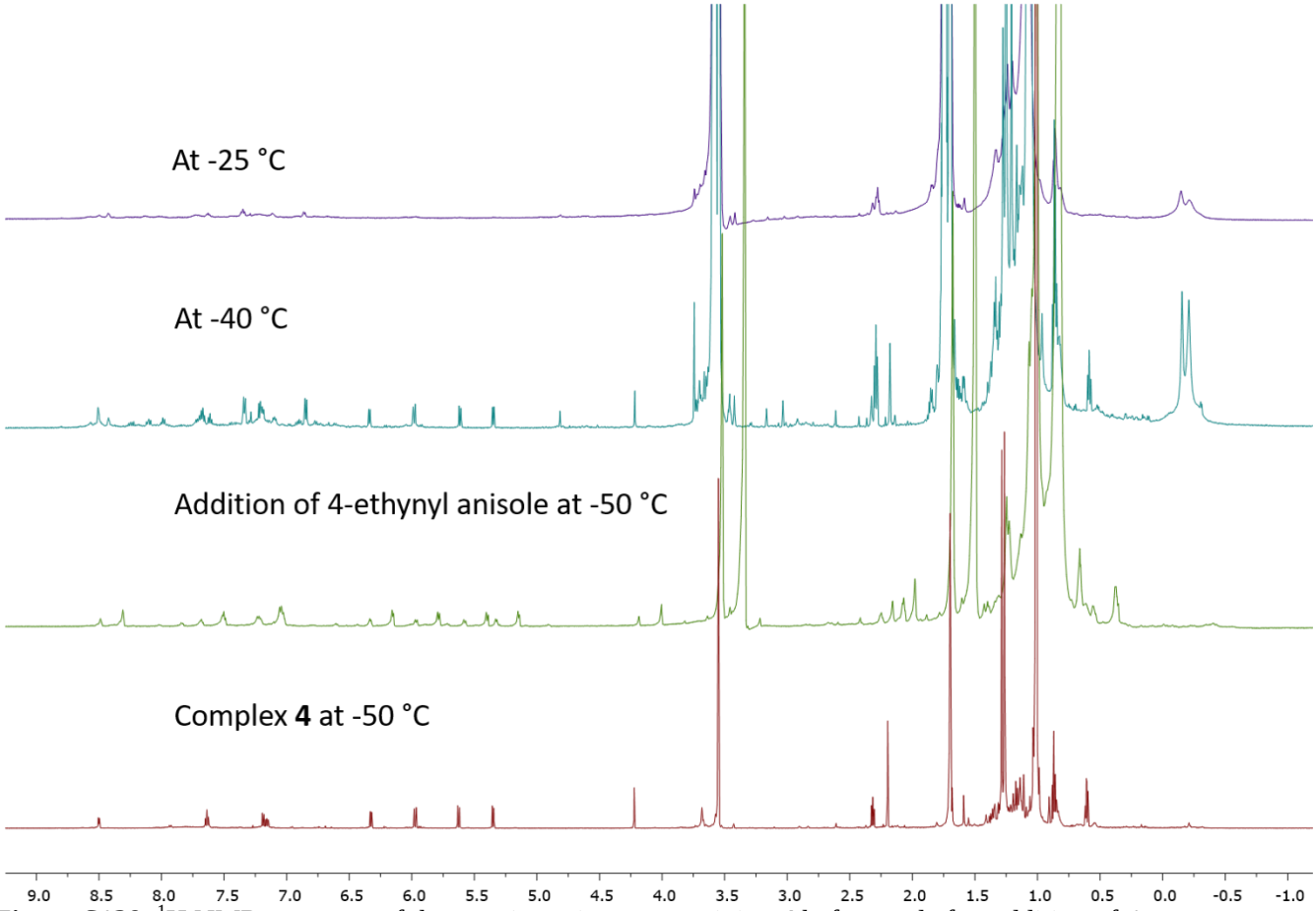

Figure S129. ^{1}H NMR spectrum of the reaction mixture containing **4** before and after addition of 4-ethynylanisole. Brown trace: 4 before addition of 4-ethynylanisole at -50 °C; green: after addition of 4-ethynylanisole at -50 °C; cyan: after warming up to -40 °C; purple: after warming up to -25 °C.

Kinetic Isotope Effect measurements

In a glovebox, complex **3**[BF_4] (4.4 mg) was dissolved in THF-d_8 (500 µL) in a septum-sealed NMR tube in the presence of an internal standard mesitylene (1.5 µL). Then the tube was transferred to a low temperature bath at -40 °C, followed by addition of phenylacetylene (6 µL, 10 equiv). The sample was quickly transferred at low temperature NMR pre-cooled at -10 °C and the measurement was started after short temperature equilibration to reach -10 °C. The NMR spectra were recorded every 180 s and the reaction was followed until ca. 80% conversion of the starting material. The most upfield peak of the Pt-Me group of the starting material was intergrated against the peak of the Me group of mesitylene standard, and the disappearance of the starting material was followed to estimate pseudo-first order reaction rate constant. Low temperature was used to obtain optimal conditions for the kinetic measurements under pseudo-first order conditons (10-fold excess of phenylacetylene). Each measurement was repeated two times and the average was used to estimate the pseudo-first order reaction rate constant. The analogous procedure was used for the reaction with phenylacetylene-d_1 (PhCCD).

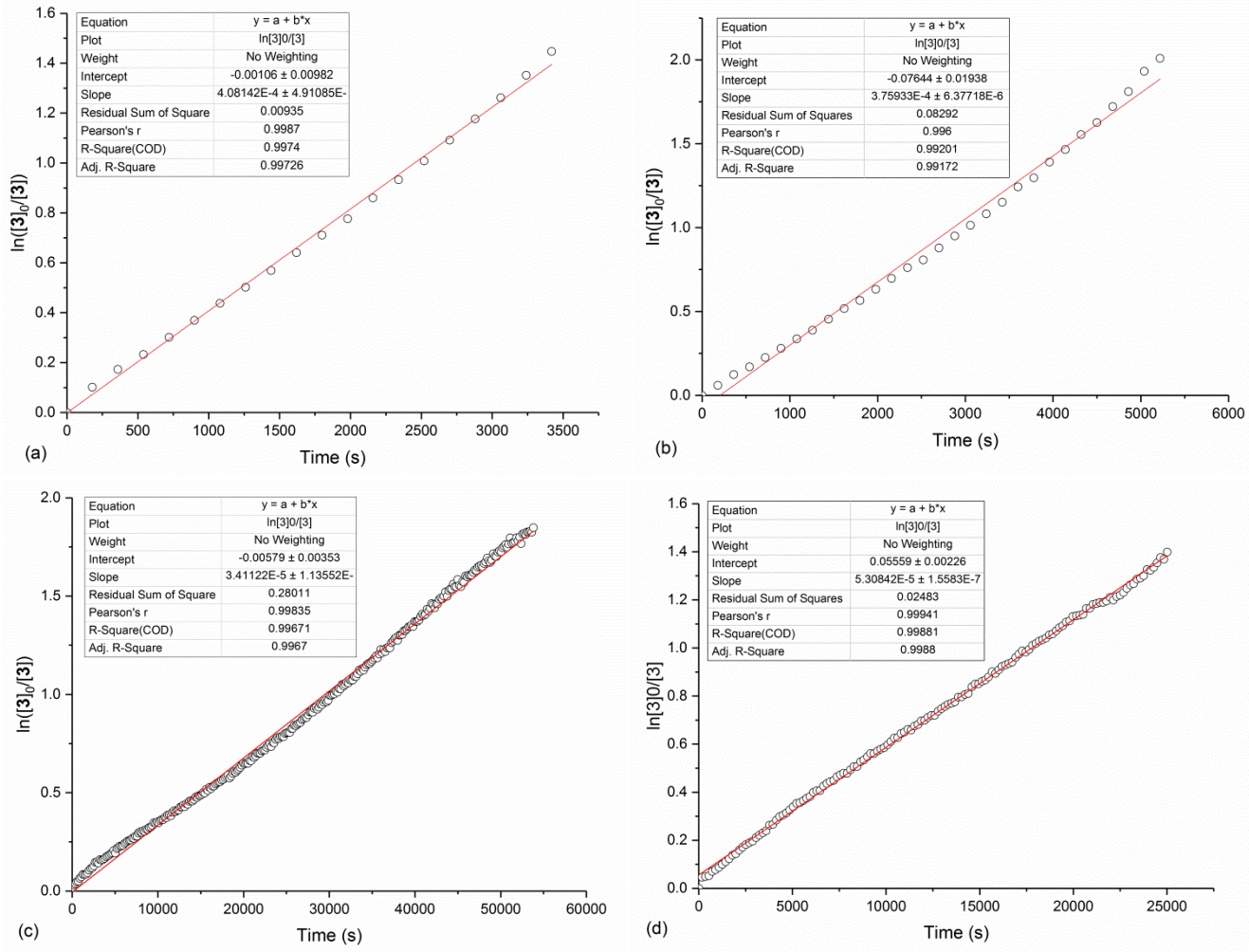

Figure S130. Kinetic plots of the reaction of **3**[BF_4] with phenylacetylene (a and b) and phenylacetylene-d_1 (c and d) at -10 °C.

The product of the reaction with phenylacetylene was identified as the phenylacetylide methyl complex analogous to **7**[BF_4], and it was characterized by NMR, HRMS and IR spectroscopy.

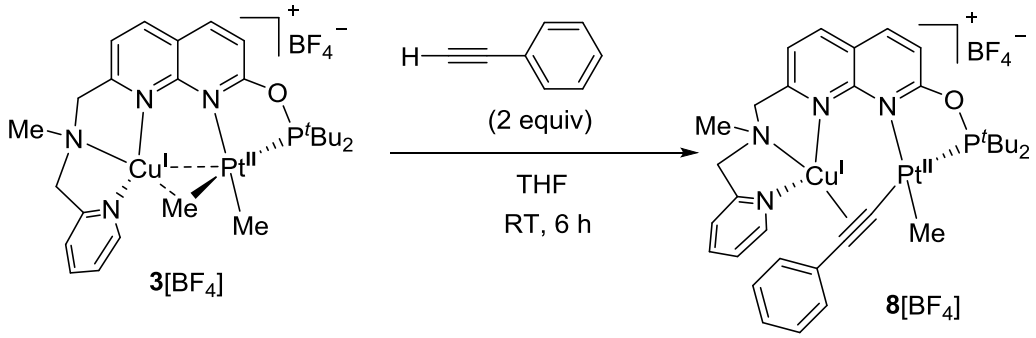

Scheme S12. Reaction with phenylacetylene.

The complex used for complete NMR characterization was synthesized as follows.
To a 20 mL vial containing solution of **3**[BF_4] (20.2 mg, 0.025 mmol) in THF (5 mL), phenylacetylene (5.5 µL, 0.050 mmol) was added. The reaction mixture was stirred at room temperature for 6 h. The color of the solution changed from brown to deep orange. After 6 h the reaction mixture was filtered out through celite. The resulting solution was removed under vacuum and the orange color viscous oil was dissolved in 1 mL of cold acetonitrile. The desired complex was precipitated with hexane (3 x 2 mL). The solvent removal under vacuum yields complex **8**[BF_4] as an orange solid (12.3 mg, 0.013 mmol, 55%).

^{1}H NMR (600 MHz, THF-d_8, 23 °C) δ: 9.05 (d, $^3J_{HH}$ = 4.9 Hz, 1H, CH_{Py}), 8.83 (d, $^3J_{HH}$ = 8.7 Hz, 1H, CH_{Naph}), 8.70 (d, $^3J_{HH}$ = 8.2 Hz, 1H, CH_{Naph}), 7.85-7.81 (m, 2H, overlapping of CH_{Py} and CH_{Naph}), 7.60 (d, $^3J_{HH}$ = 8.7 Hz, 1H, CH_{Naph}), 7.46 - 7.43 (m, 2H, CH_{Py}), 7.31-7.29 (m, 2H, C_6H_5), 7.19 (t, $^3J_{HH}$ = 7.4 Hz, 2H, C_6H_5), 7.13 (t, $^3J_{HH}$ = 7.4 Hz, 1H, C_6H_5).
4.49-4.43 (m, 2H, CH_2), 3.77-3.70 (m, 2H, CH_2), 2.51 (s, 3H, N-CH_3), 1.57 (d, $^3J_{PH}$ = 14.6 Hz, 9H, $C(CH_3)_3$), 1.43 (d, $^3J_{PH}$ = 5.8 Hz, $^2J_{PtH}$ = 43 Hz, 3H, Pt-Me), 1.34 (d, $^3J_{PH}$ = 14.6 Hz, 9H, $C(CH_3)_3$).

^{13}C{^{1}H} NMR (151 MHz, THF-d_8, 23 °C) δ: 167.96 ($C_{q,\ Naph}$), 162.15 ($C_{q,\ Naph}$), 158.35 (C_q of C_6H_5), 151.26 ($C_{q,\ Naph}$), 149.79 (CH_{Py}), 145.39 (CH_{Naph}), 141.17 (CH_{Naph}), 138.79 (CH_{Py}), 131.47 (*C*H of C_6H_5), 128.77 (*C*H of C_6H_5), 128.36 ($C_{q,\ Py}$) 126.90 (*C*H of C_6H_5), 124.50 (CH_{Py}), 124.33 (CH_{Py}), 123.51 (C_{Naph}), 122.47 (CH_{Naph}), 114.01 (CH_{Naph}), 67.71 (Pt-C≡*C*), 64.24 (CH_2), 62.43 (CH_2), 45.95 (N-CH_3), 42.18 – 42.10 (br m, *C*$(CH_3)_3$), 40.16 – 40 (br m, *C*$(CH_3)_3$), 27.82 (d, $^2J_{PC}$ = 4.9 Hz, C(*C*$H_3)_3$), 27.29 (d, $^2J_{PC}$ = 5.7 Hz, C(*C*$H_3)_3$), 25.59 (Pt-*C*≡C), -27.17 (d, $^2J_{PC}$ = 4 Hz, Pt-Me). Pt satellite for -27.17 ppm Pt-Me signal were not clearly seen due to low intensity.

^{31}P{^{1}H} NMR (242 MHz, THF-d_8, -25 °C) δ: 174.8 ($^1J_{PtP}$ = 3117 Hz).

ESI-HRMS (m/z pos): Found (Calcd): $C_{33}H_{41}ON_4P^{195}Pt^{63}Cu^+$ 799.1954 (799.1958).

FT-IR (ATR, solid): 2963 (br, w), 1605 (s), 1478 (m), 1318 (m), 1060 (s), 875 (s), 762 (s) cm^{-1}.

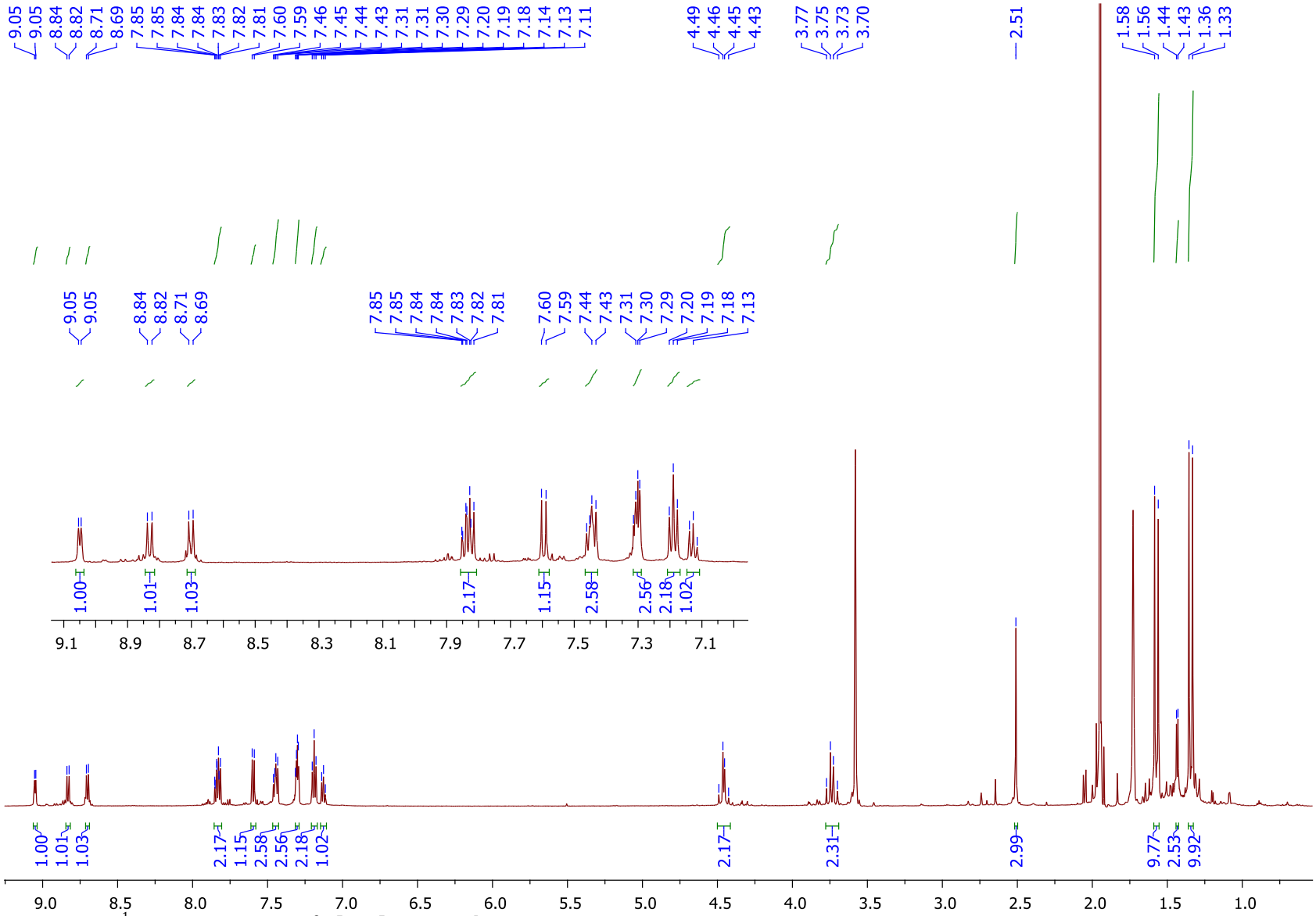

Figure S131. ^{1}H NMR spectrum of **8**[BF_4] in THF-d_8 at 23 °C.

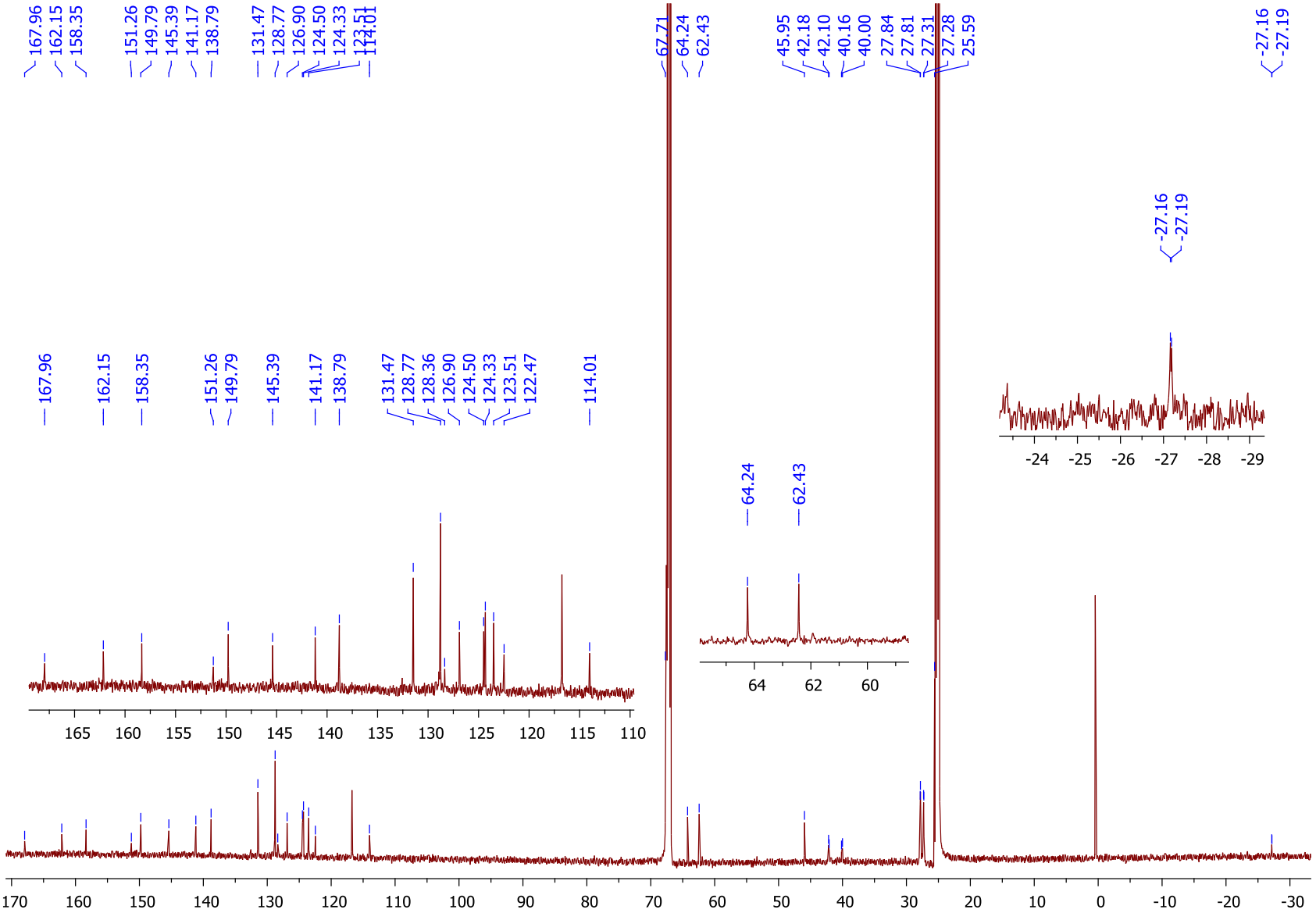

Figure S132. ^{13}C NMR spectrum of **8**[BF_4] in THF-d_8 at 23 °C.

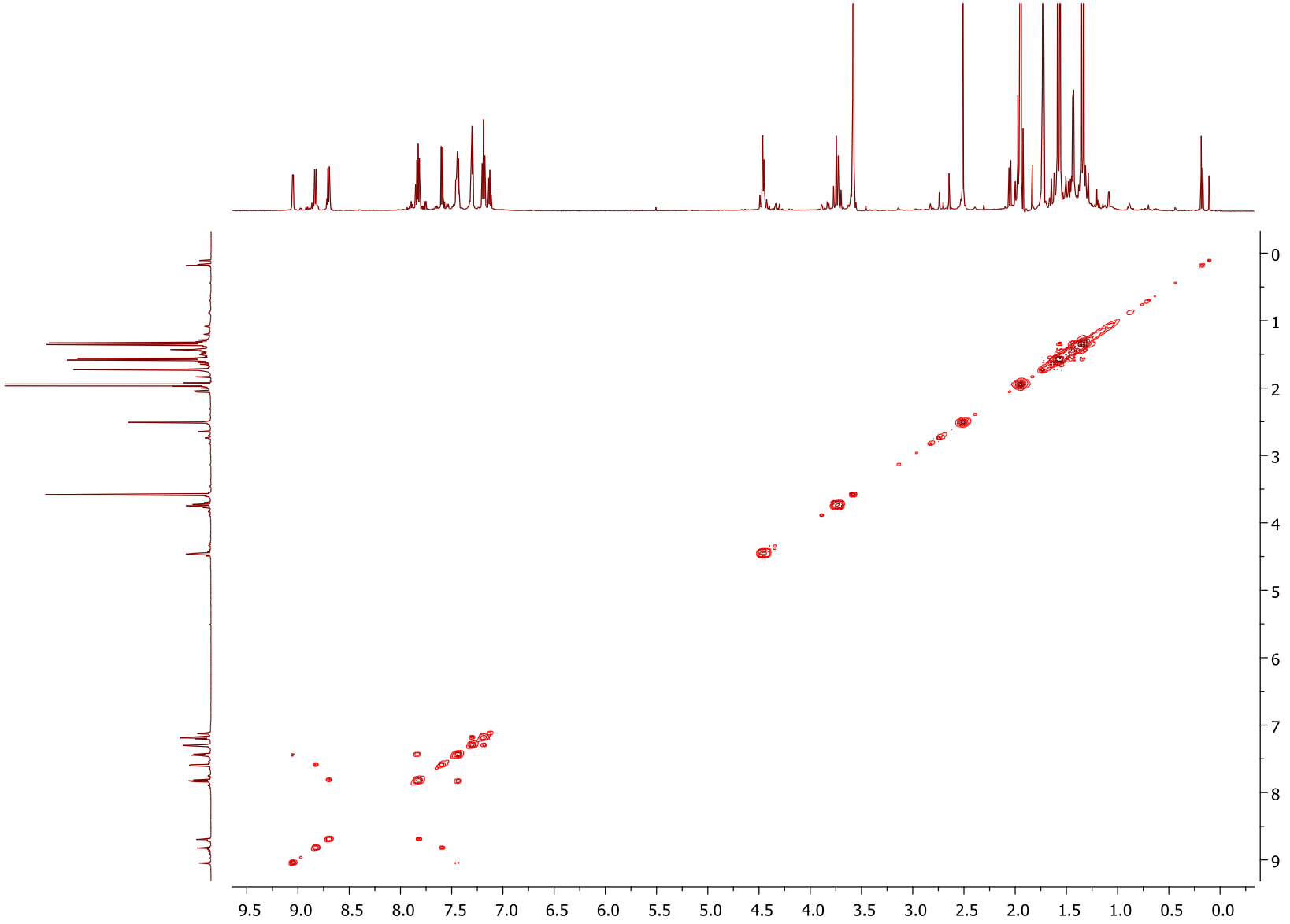

Figure S133. ^{1}H-^{1}H COSY spectrum of **8**[BF_4] in THF-d_8 at 23 °C.

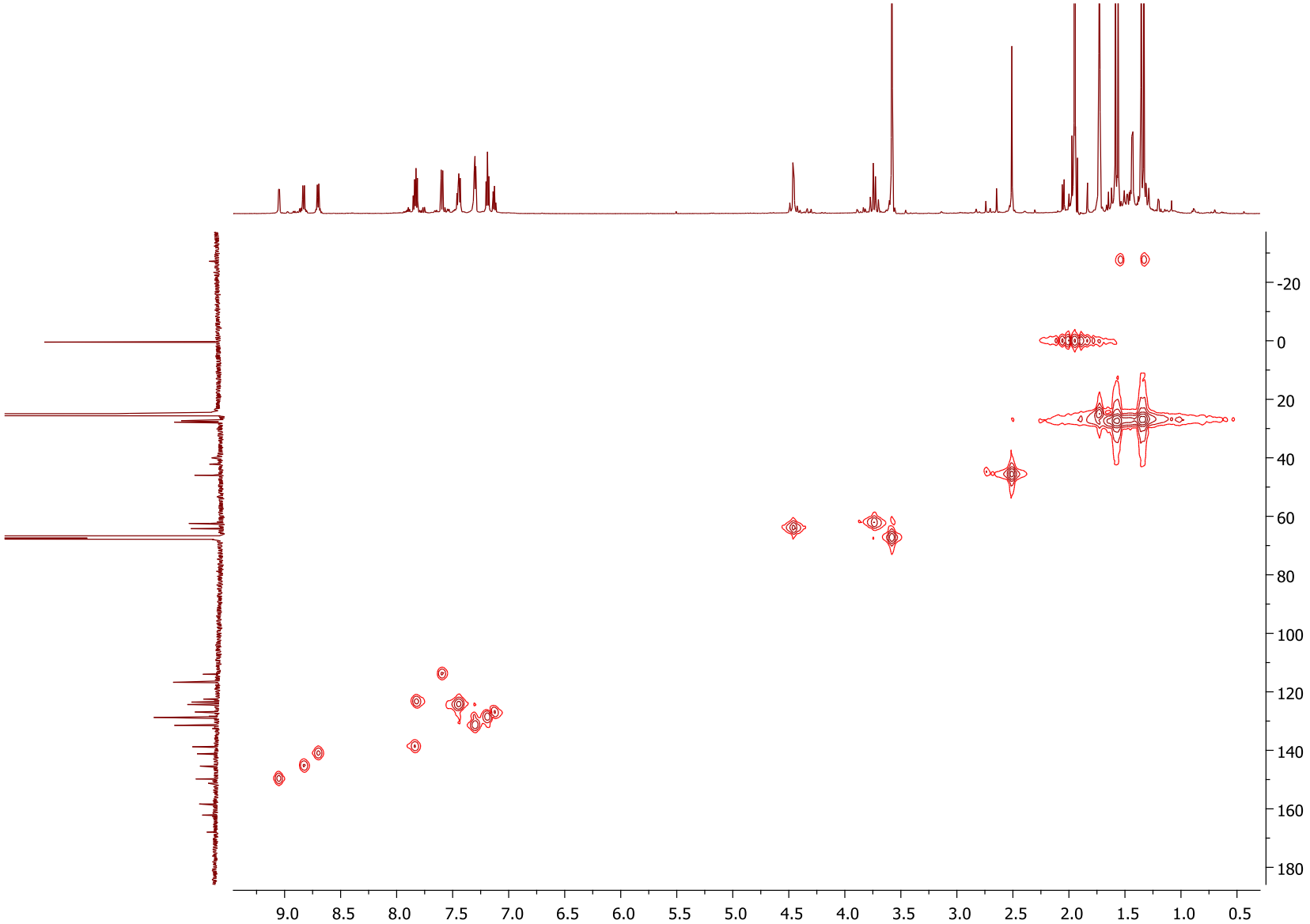

Figure S134. ^{1}H-^{13}C HMQC spectrum of **8**[BF_4] in THF-d_8 at 23 °C.

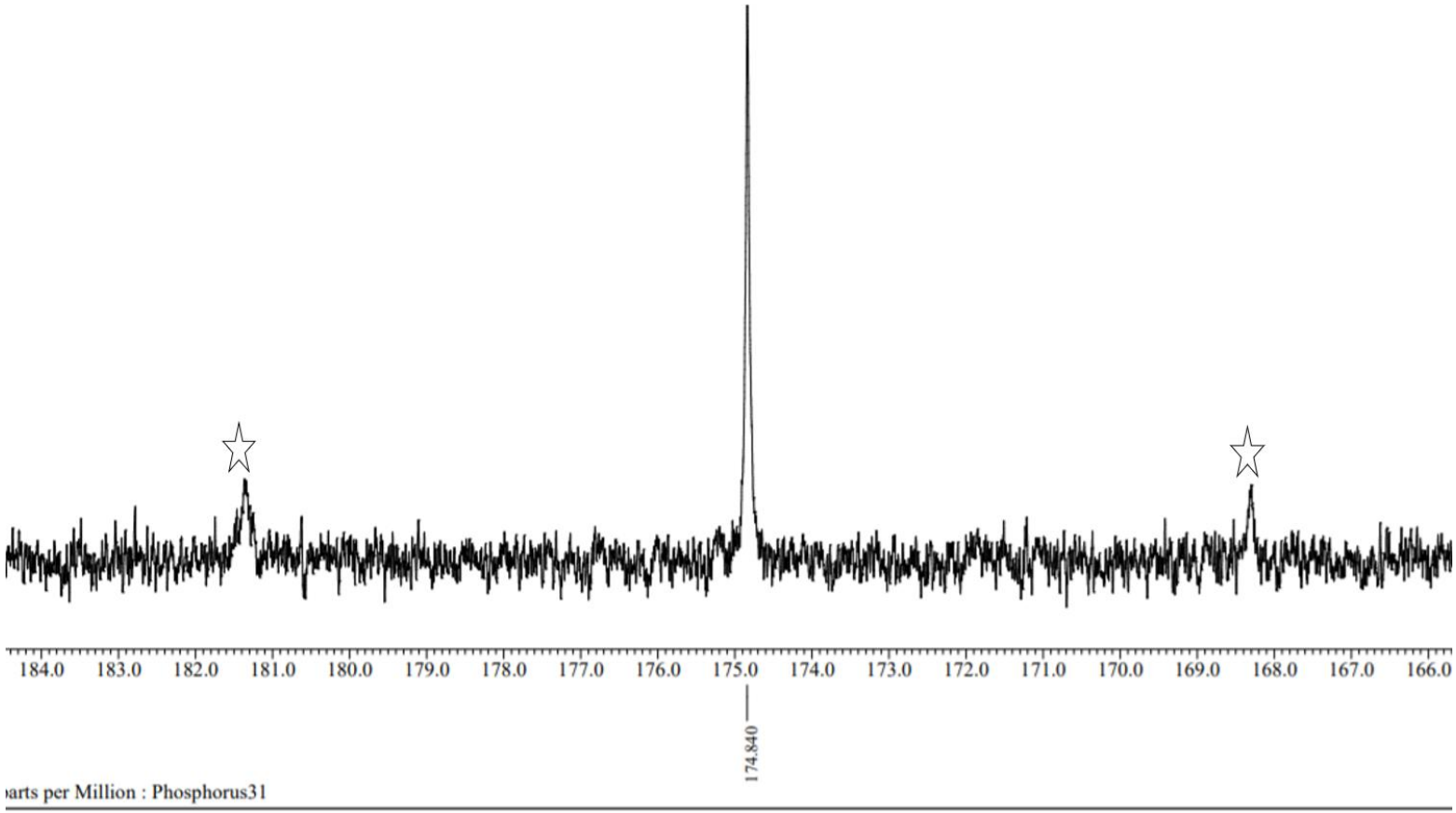

Figure S135. $^{31}P\{^{1}H\}$ NMR spectrum of **8**[BF_4] in THF-d_8 at 23 °C. Pt satellites are marked with stars.

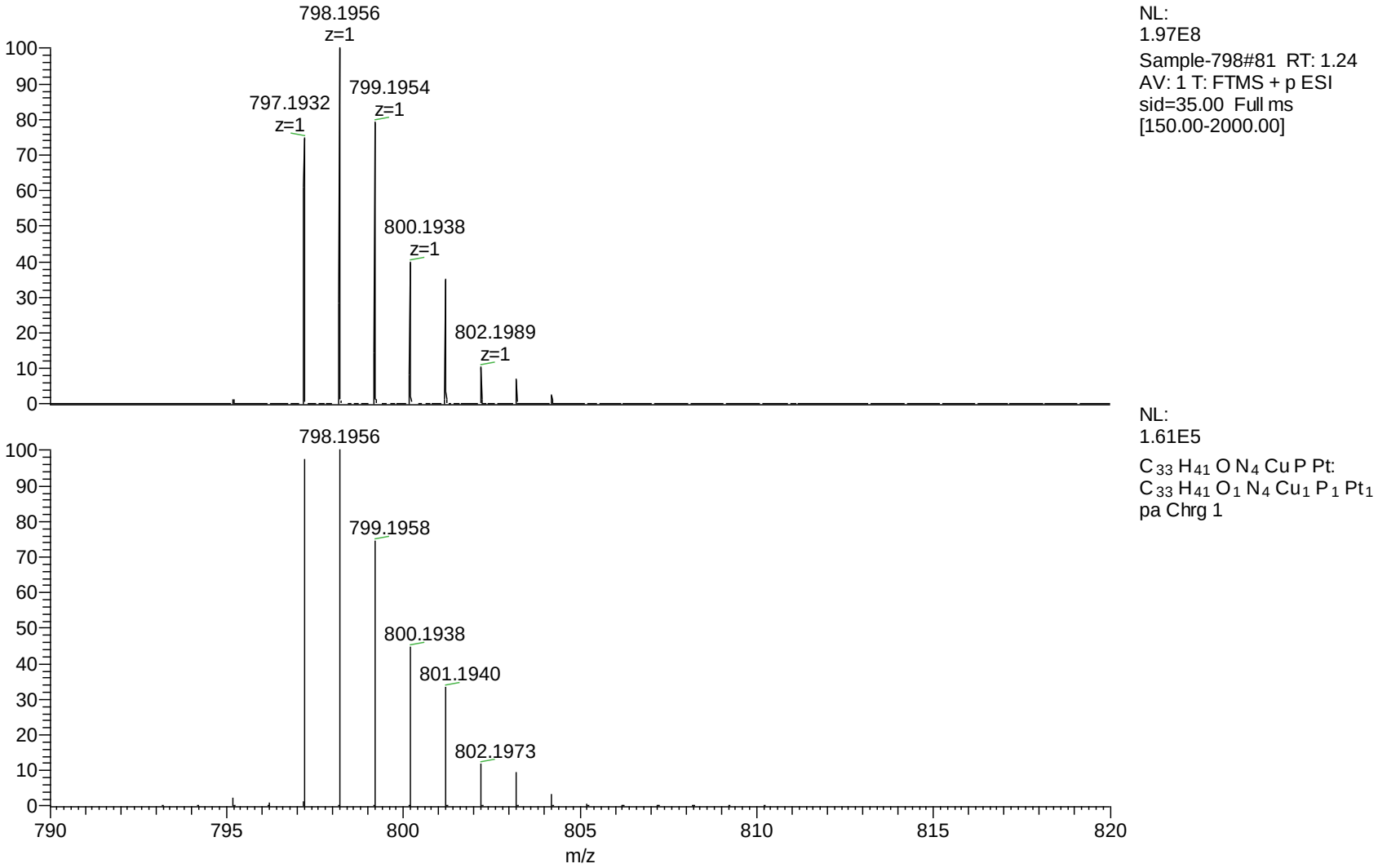

Figure S136. ESI-(HR)MS spectrum of a THF solution of **8**[BF_4] (top) and simulated spectrum for $C_{33}H_{41}ON_4PPtCu^+$ (bottom).

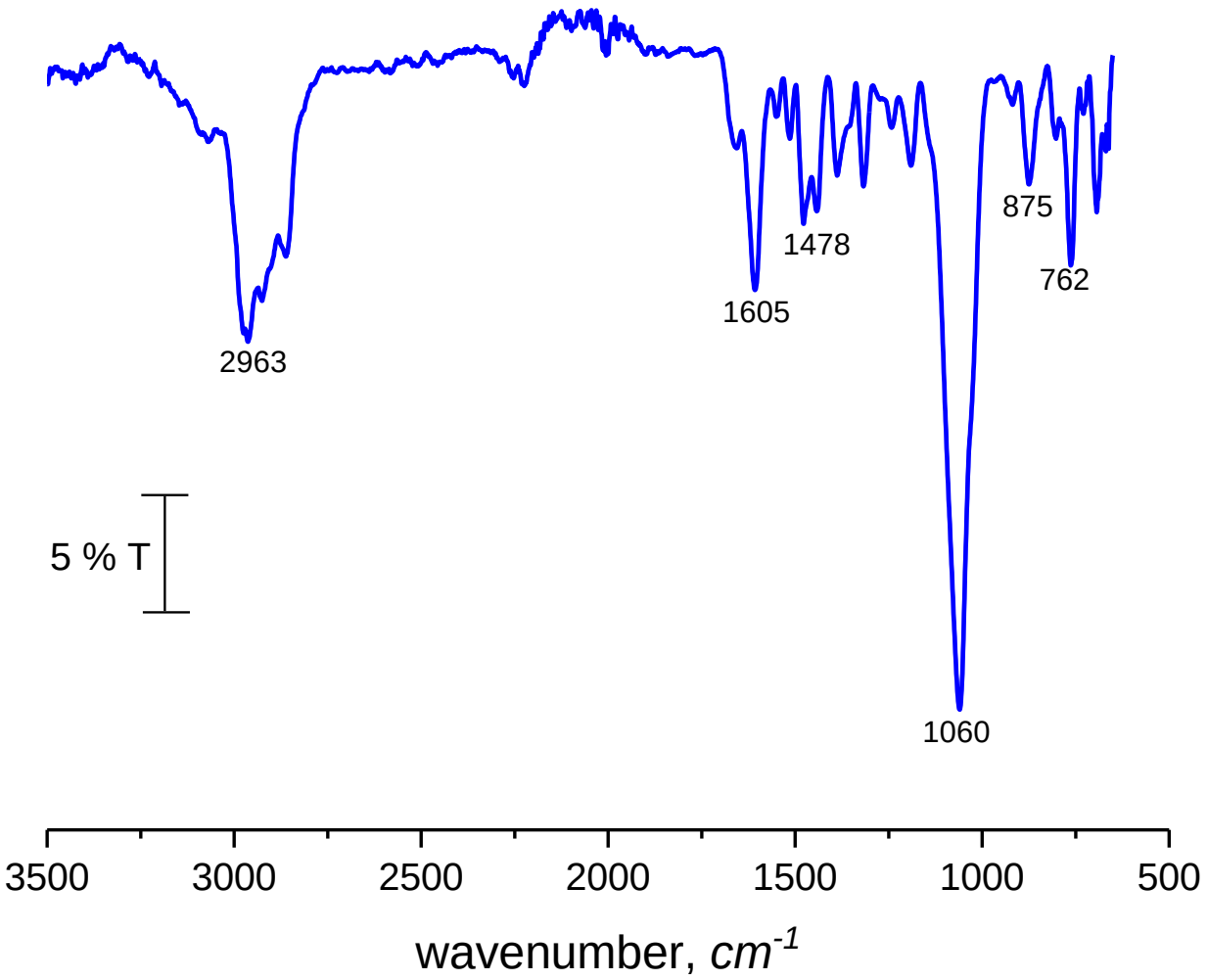

Figure S137. ATR FT-IR spectrum of **8**[BF_4].

X-Ray Structure Determination Details

The X-ray diffraction data for the single crystals were collected on a Rigaku XtaLab PRO instrument (κ-goniometer) with a PILATUS3 R 200K hybrid pixel array detector using Mo*Kα* (0.71073 Å) or Cu*Kα* (1.54184 Å) radiation monochromated by means of multilayer optics. The performance mode of MicroMax™-003 microfocus sealed X-ray tubes was 50 kV, 0.60 mA. The diffractometer was equipped with a Rigaku GN2 system for low temperature experiments. Suitable crystals of appropriate dimensions were mounted on MiTeGen loops in random orientations. Preliminary unit cell parameters were determined with three sets of a total of 10 narrow frame scans in the case of a Mo-source and six sets of a total of 10 narrow frame scans at two different 2θ positions in the case of a Cu-source. The data were collected according to recommended strategies in an ω scan mode. Final cell constants were determined by global refinement of reflections from the complete data sets using the Lattice wizard module. Images were indexed and integrated with "smart" background evaluation using the *CrysAlis*^{Pro} data reduction package (1.171.39.46, Rigaku Oxford Diffraction, 2018). Analysis of the integrated data did not show any decay. Data were corrected for systematic errors and absorption using the *ABSPACK* module: Numerical absorption correction based on Gaussian integration over a multifaceted crystal model and empirical absorption correction based on spherical harmonics (according to the point group symmetry using equivalent reflections). The *GRAL* module and the *ASSIGN SPACEGROUP* routine of the *WinGX* suite were used for analysis of systematic absences and space group determination.

The structures were solved by the direct methods using *SHELXT*-2018/2[4] and refined by the full-matrix least-squares on F^2 using *SHELXL*-2018/3,[5] which uses a model of atomic scattering based on spherical atoms. Calculations were mainly performed using the *WinGX*-2018.3 suite of programs.[6] Non-hydrogen atoms were refined anisotropically. The positions of the hydrogen atoms bonded to C1 (for **3**[$CuCl_2$] and **3**[$B(Ar^F)_4$]) and C11, C12, C13, C111, C112, and C113 (for **4**) were determined by difference Fourier maps, and the C–H distances were restrained to the values of 0.980 Å and 0.950 Å; these atoms were refined isotropically. The positions of the other hydrogen atoms of methyl groups were found using rotating group refinement with idealized tetrahedral angles. The other hydrogen atoms were inserted at the calculated positions and refined as riding atoms.

The unit cell of **5** contains highly disordered solvent molecules of pentane and/or benzene, which were treated as a diffuse contribution to the overall scattering without specific atom positions by *PLATON*/SQUEEZE-220119.[7] Squeezed solvent info is not included in the formulae and related items such as molecular weights and calculated densities.

It is noteworthy that some solvent molecules (**3**[BF_4], **4**, **7**[BF_4]), some trifluoromethyl groups of tetrakis[3,5-bis(trifluoromethyl)phenyl]borate anions (**3**[$B(Ar^F)_4$], **6**[$B(Ar^F)_4$]), P1-pivot *tert*-butyl groups (**5**), tetrafluoroborate anion (**7[BF_4]**), and 1,8-naphthyridin-2-one moiety (**7**[BF_4]) are found to be disordered. The disorder was resolved using free variables and reasonable restraints on geometry and anisotropic displacement parameters. All the compounds studied have no unusual bond lengths and angles.

Interestingly, studied complexes **4** and **5** crystallize with three molecules ($Z' = 3$) and a half of the molecule ($Z' = 0.5$) in the asymmetric cells, respectively.

Molecular structures of the investigated complexes in the crystalline phase as well as accepted partial numbering are presented as ORTEP diagrams in Figures S138-S145. Selected geometrical parameters are appended to the captions. Accepted abbreviations are as follows: ORTEP, Oak Ridge Thermal Ellipsoid Plot; SC-XRD, single crystal X-ray diffraction.

Crystallographic data for 2.

$C_{27}H_{42}N_4OPPt^{1+}\ I^{1-} \times C_6H_6$, pale yellow plate (0.114 × 0.113 × 0.020 mm^3), formula weight 869.71; orthorhombic, *Pccn* (No. 56), a = 24.4749(4) Å, b = 22.6183(4) Å, c = 12.7406(2) Å, V = 7053.0(2) Å^3, Z = 8, Z' = 1, T = 95(2) K, d_{calc} = 1.638 g cm^{-3}, μ(MoK_α) = 4.930 mm^{-1}, F(000) = 3424; $T_{max/min}$ = 1.000/0.567; 105399 reflections were collected (2.452° ≤ θ ≤ 30.500°, index ranges: –34 ≤ h ≤ 34, –32 ≤ k ≤ 31, –17 ≤ l ≤ 18), 10733 of which were unique, R_{int} = 0.0545, R_σ = 0.0295; completeness to θ of 25.242° 99.9 %. The refinement of 380 parameters with no restraints converged to R_1 = 0.0370 and wR_2 = 0.0770 for 8565 reflections with $I > 2\sigma(I)$ and R_1 = 0.0533 and wR_2 = 0.0832 for all data with S = 1.090 and residual electron density, $\rho_{max/min}$ = 3.154 and –1.079 e Å^{-3}. The crystals were grown by vapor diffusion of pentane into a benzene solution at room temperature.

Crystallographic data for 3[$CuCl_2$].

$C_{26}H_{39}CuN_4OPPt^{1+}\ Cl_2Cu^{1-}$, yellow plate (0.073 × 0.046 × 0.022 mm^3), formula weight 847.65; monoclinic, $P2_1/c$ (No. 14), a = 12.7739(2) Å, b = 8.98822(13) Å, c = 27.1150(4) Å, β = 100.7026(16)°, V = 3059.03(9) Å^3, Z = 4, Z' = 1, T = 93(2) K, d_{calc} = 1.841 g cm^{-3}, μ(MoK_α) = 6.193 mm^{-1}, F(000) = 1664; $T_{max/min}$ = 0.968/0.732; 61309 reflections were collected (2.734° ≤ θ ≤ 32.337°, index ranges: –18 ≤ h ≤ 18, –13 ≤ k ≤ 13, –36 ≤ l ≤ 40),

10168 of which were unique, R_{int} = 0.0448, R_σ = 0.0310; completeness to θ of 25.242° 99.9 %. The refinement of 354 parameters with 3 restraints converged to R_1 = 0.0249 and wR_2 = 0.0535 for 8716 reflections with $I > 2\sigma(I)$ and R_1 = 0.0336 and wR_2 = 0.0558 for all data with S = 1.042 and residual electron density, $\rho_{max/min}$ = 2.417 and –0.726 e Å^{-3}. The crystals were grown by vapor diffusion of pentane into a benzene solution at room temperature.

Crystallographic data for 3[BF$_4$].

$C_{26}H_{39}CuN_4OPPt^{1+}$ BF_4^{1-} × C_4H_8O, amber plate (0.097 × 0.022 × 0.016 mm^3), formula weight 872.12; monoclinic, $P2_1/c$ (No. 14), a = 9.1729(4) Å, b = 30.0139(10) Å, c = 12.3335(3) Å, β = 90.445(3)°, V = 3395.5(2) Å^3, Z = 4, Z' = 1, T = 96(2) K, d_{calc} = 1.706 g cm^{-3}, μ(CuK_α) = 9.284 mm^{-1}, F(000) = 1736; $T_{max/min}$ = 1.000/0.528; 30688 reflections were collected (2.945° ≤ θ ≤ 68.233°, index ranges: –9 ≤ h ≤ 11, –36 ≤ k ≤ 36, –14 ≤ l ≤ 14), 6162 of which were unique, R_{int} = 0.0569, R_σ = 0.0343; completeness to θ of 67.684° 99.2 %. The refinement of 452 parameters with 236 restraints converged to R_1 = 0.0832 and wR_2 = 0.2262 for 5091 reflections with $I > 2\sigma(I)$ and R_1 = 0.0943 and wR_2 = 0.2402 for all data with S = 1.048 and residual electron density, $\rho_{max/min}$ = 4.359 and –2.792 e Å^{-3}. The crystals were grown by slow evaporation of a THF solution at –30°C.

Crystallographic data for 3[B(Ar^F)$_4$].

$C_{26}H_{39}CuN_4OPPt^{1+}$ $C_{32}H_{12}BF_{24}^{1-}$, yellow plate (0.239 × 0.042 × 0.021 mm^3), formula weight 1576.43; monoclinic, $P2_1/c$ (No. 14), a = 14.66021(18) Å, b = 16.24537(17) Å, c = 26.9484(4) Å, β = 103.6804(13)°, V = 6235.98(13) Å^3, Z = 4, Z' = 1, T = 93(2) K, d_{calc} = 1.679 g cm^{-3}, μ(MoK_α) = 2.722 mm^{-1}, F(000) = 3112; $T_{max/min}$ = 1.000/0.392; 279547 reflections were collected (1.922° ≤ θ ≤ 31.500°, index ranges: –21 ≤ h ≤ 21, –23 ≤ k ≤ 23, –39 ≤ l ≤ 39), 20630 of which were unique, R_{int} = 0.0668, R_σ = 0.0272; completeness to θ of 25.242° 99.9 %. The refinement of 924 parameters with 240 restraints converged to R_1 = 0.0321 and wR_2 = 0.0819 for 17554 reflections with $I > 2\sigma(I)$ and R_1 = 0.0418 and wR_2 = 0.0874 for all data with S = 1.029 and residual electron density, $\rho_{max/min}$ = 4.685 and –1.242 e Å^{-3}. The crystals were grown by slow evaporation of a pentane solution at –30°C.

Crystallographic data for 4.

$C_{26}H_{38}CuN_4OPPt$ × 0.167(C_6H_{14}) × 0.333($C_4H_{10}O$), red needle (0.308 × 0.031 × 0.026 mm^3), formula weight 751.27; monoclinic, $P2_1/c$ (No. 14), a = 9.14540(11) Å, b = 34.4731(5) Å, c = 28.8368(4) Å, β = 90.3193(11)°, V = 9091.2(2) Å^3, Z = 12, Z' = 3, T = 93(2) K, d_{calc} = 1.647 g cm^{-3}, μ(MoK_α) = 5.394 mm^{-1}, F(000) = 4492; $T_{max/min}$ = 1.000/0.216; 138269 reflections were collected (2.414° ≤ θ ≤ 30.000°, index ranges: –12 ≤ h ≤ 12, –46 ≤ k ≤ 48, –40 ≤ l ≤ 39), 26269 of which were unique, R_{int} = 0.0807, R_σ = 0.0602; completeness to θ of 25.242° 99.5 %. The refinement of 1114 parameters with 181 restraints converged to R_1 = 0.0449 and wR_2 = 0.0862 for 22296 reflections with $I > 2\sigma(I)$ and R_1 = 0.0564 and wR_2 = 0.0892 for all data with S = 1.094 and residual electron density, $\rho_{max/min}$ = 2.358 and –1.662 e Å^{-3}. The crystals were grown by diffusion of hexane into a diethyl ether solution at –30°C.

Crystallographic data for 5.

The unit cell contains highly disordered solvent molecules of pentane and/or benzene, which were treated as a diffuse contribution to the overall scattering without specific atom positions by *PLATON*/SQUEEZE-220119. Squeezed solvent info is not included in the formulae and related items such as molecular weights and calculated densities. $C_{50}H_{70}N_8O_2P_2Pt_2$, colorless prism (0.433 × 0.158 × 0.079 mm^3), formula weight 1267.26; tetragonal, $I4_1/a$ (No. 88), a = 20.4659(2) Å, b = 20.4659(2) Å, c = 27.7779(4) Å, V = 11634.8(3) Å^3, Z = 8, Z' = 0.5, T = 94(2) K, d_{calc} = 1.447 g cm^{-3}, μ(MoK_α) = 4.900 mm^{-1}, F(000) = 5024; $T_{max/min}$ = 1.000/0.157; 73384 reflections were collected (2.032° ≤ θ ≤ 32.291°, index ranges: –30 ≤ h ≤ 26, –29 ≤ k ≤ 30, –40 ≤ l ≤ 41), 9735 of which were unique, R_{int} = 0.0440, R_σ = 0.0276; completeness to θ of 25.242° 99.9 %. The refinement of 375 parameters with 276 restraints converged to R_1 = 0.0347 and wR_2 = 0.0824 for 7957 reflections with $I > 2\sigma(I)$ and R_1 = 0.0482 and wR_2 = 0.0891 for all data with S = 1.027 and residual electron density, $\rho_{max/min}$ = 3.375 and –1.590 e Å^{-3} The crystals were grown by vapor diffusion of pentane into a benzene solution at room temperature.

Crystallographic data for 6[B(Ar^F)$_4$].

$C_{33}H_{39}CuF_6N_4OPPt^{1+}$ $C_{32}H_{12}BF_{24}^{1-}$, orange prism (0.102 × 0.060 × 0.044 mm^3), formula weight 1774.51; monoclinic, $P2_1/c$ (No. 14), a = 20.7797(2) Å, b = 19.37993(18) Å, c = 17.2379(2) Å, β = 105.4400(13)°, V = 6691.33(13) Å^3, Z = 4, Z' = 1, T = 90(2) K, d_{calc} = 1.761 g cm^{-3}, μ(MoK_α) = 2.560 mm^{-1}, F(000) = 3496; $T_{max/min}$ = 1.000/0.800; 149456 reflections were collected (2.033° ≤ θ ≤ 30.050°, index ranges: –29 ≤ h ≤ 29, –27 ≤ k ≤ 27, –22 ≤ l ≤ 24), 19569 of which were unique, R_{int} = 0.0836, R_σ = 0.0407; completeness to θ of 25.242° 99.9 %. The refinement of 995 parameters with 156 restraints converged to R_1 = 0.0379 and wR_2 = 0.0954 for 15814 reflections with $I > 2\sigma(I)$ and R_1 = 0.0530 and wR_2 = 0.1074 for all data with S = 1.041 and residual electron density, $\rho_{max/min}$ = 3.858 and –3.456 e Å^{-3}. The crystals were grown vapor diffusion of pentane into a THF solution at –30°C.

Crystallographic data for 7[BF$_4$].

$C_{34}H_{43}CuN_4O_2PPt^{1+}$ BF_4^{1-} × 2(C_4H_8O), pale orange plate (0.131 × 0.089 × 0.030 mm^3), formula weight 1060.34; triclinic, $P\bar{1}$ (No. 2), a = 11.34455(16) Å, b = 12.7555(3) Å, c = 15.58801(18) Å, α = 97.0654(13)°, β = 96.2303(10)°, γ = 94.2103(15)°, V = 2216.69(7) $Å^3$, Z = 2, Z' = 1, T = 95(2) K, d_{calc} = 1.589 g cm^{-3}, μ(CuK_α) = 7.264 mm^{-1}, F(000) = 1068; $T_{max/min}$ = 1.000/0.474; 141001 reflections were collected (2.877° ≤ θ ≤ 72.342°, index ranges: $-14 \le h \le 194$, $-15 \le k \le 15$, $-19 \le l \le 19$), 8680 of which were unique, R_{int} = 0.0729, R_σ = 0.0205; completeness to θ of 67.684° 99.5 %. The refinement of 893 parameters with 1901 restraints converged to R_1 = 0.0558 and wR_2 = 0.1416 for 8285 reflections with $I > 2\sigma(I)$ and R_1 = 0.0573 and wR_2 = 0.1442 for all data with S = 1.044 and residual electron density, $\rho_{max/min}$ = 4.069 and –2.687 e $Å^{-3}$. The crystals were grown by vapor diffusion of pentane into a THF solution at –30°C.

Detailed information about crystal structure determination can be accessed via supplementary cif files. The crystallographic data for the investigated compounds have been deposited in the Cambridge Crystallographic Data Centre as supplementary publication numbers CCDC 1975187 (**2a**), 1975188 (**3**[$CuCl_2$]), 1975189 (**3**[BF_4]), 1975190 (**3**[$B(Ar^F)_4$]), 1975191 (**4**), 1975192 (**5**), 1975193 (**6**[$B(Ar^F)_4$]), and 1975194 (**7**[BF_4]). These data can be obtained free of charge via https://www.ccdc.cam.ac.uk/structures/.

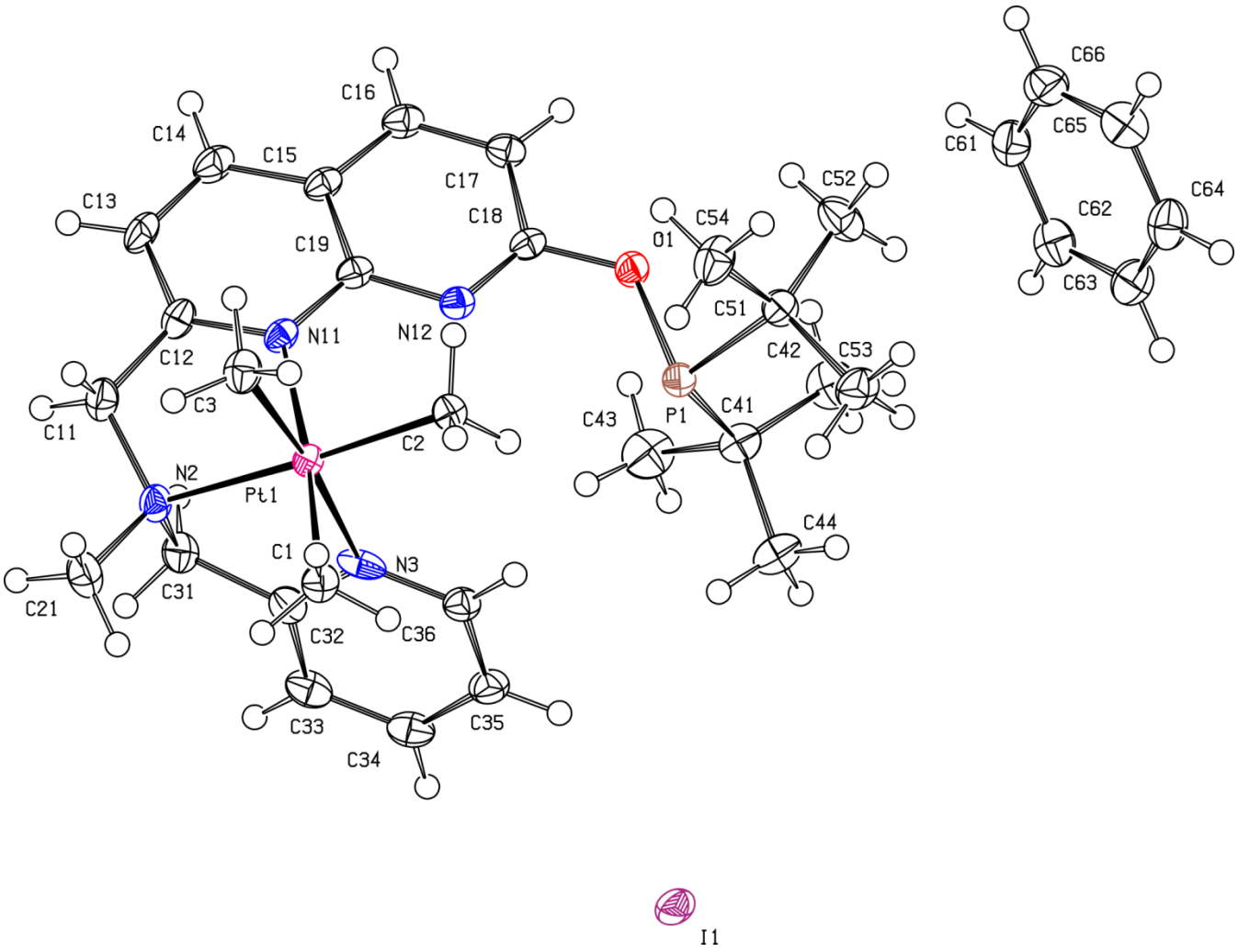

Figure S138. ORTEP at 50 % probability anisotropic displacement ellipsoids of non-hydrogen atoms for compound **2** according to SC-XRD. Selected interatomic distances [Å]: Pt1–N11 2.193(3), Pt1–N2 2.226(3), Pt1–N3 2.137(3), Pt1–C1 2.041(4), Pt1–C2 2.053(4), Pt1–C3 2.047(4).

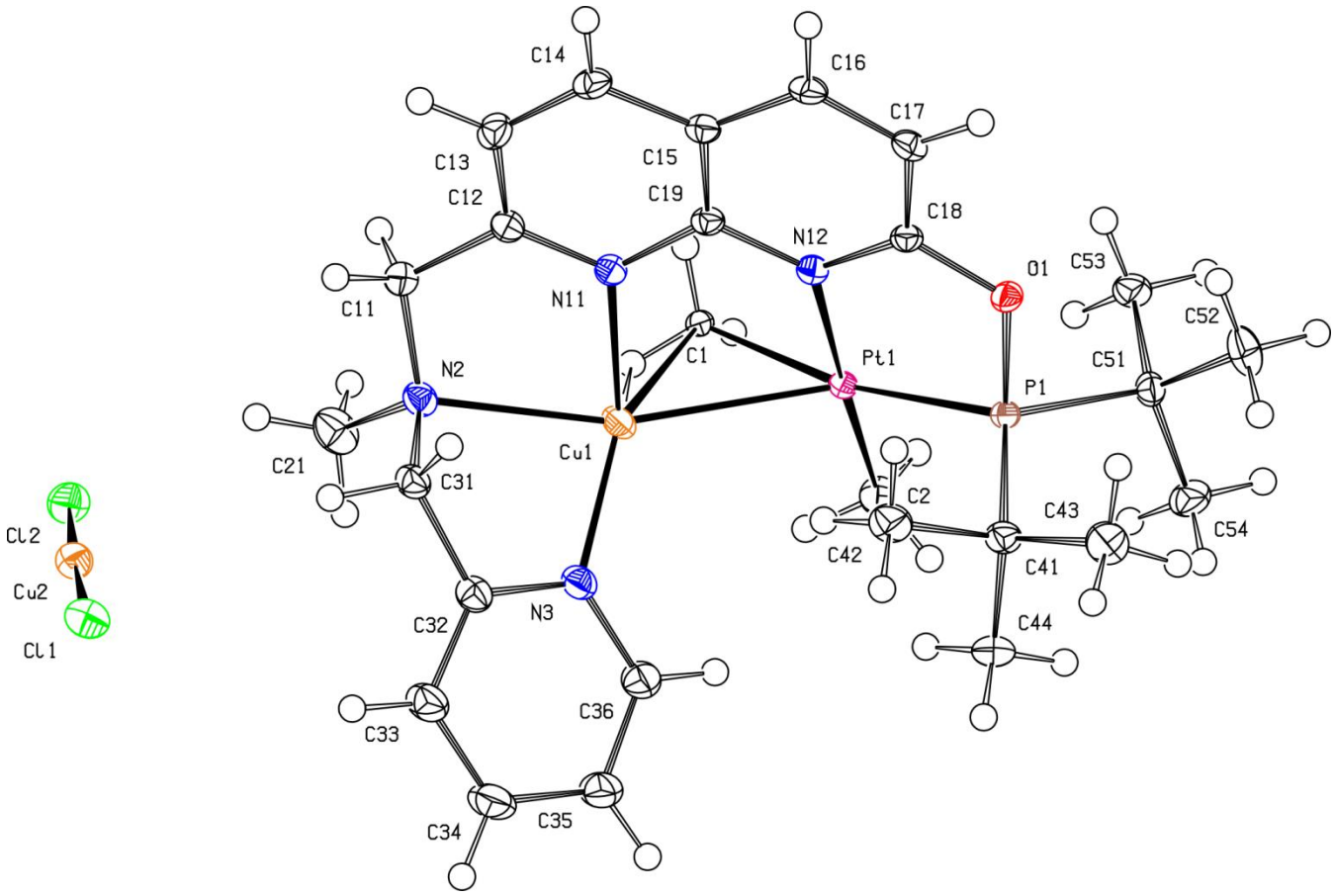

Figure S139. ORTEP at 50 % probability anisotropic displacement ellipsoids of non-hydrogen atoms for compound **3**[$CuCl_2$] according to SC-XRD data. Selected interatomic distances [Å] and angles [°]: Pt1–Cu1 2.6486(3), Pt1–P1 2.2280(6), Pt1–N12 2.1823(19), Pt1–C1 2.201(2), Pt1–C2 2.050(2), Cu1–N11 2.064(2), Cu1–N2 2.320(2), Cu1–N3 1.966(2), Cu1–C1 2.277(2), Cu1–H1A 1.95(4); Cu1–H1A–C1 99(2).

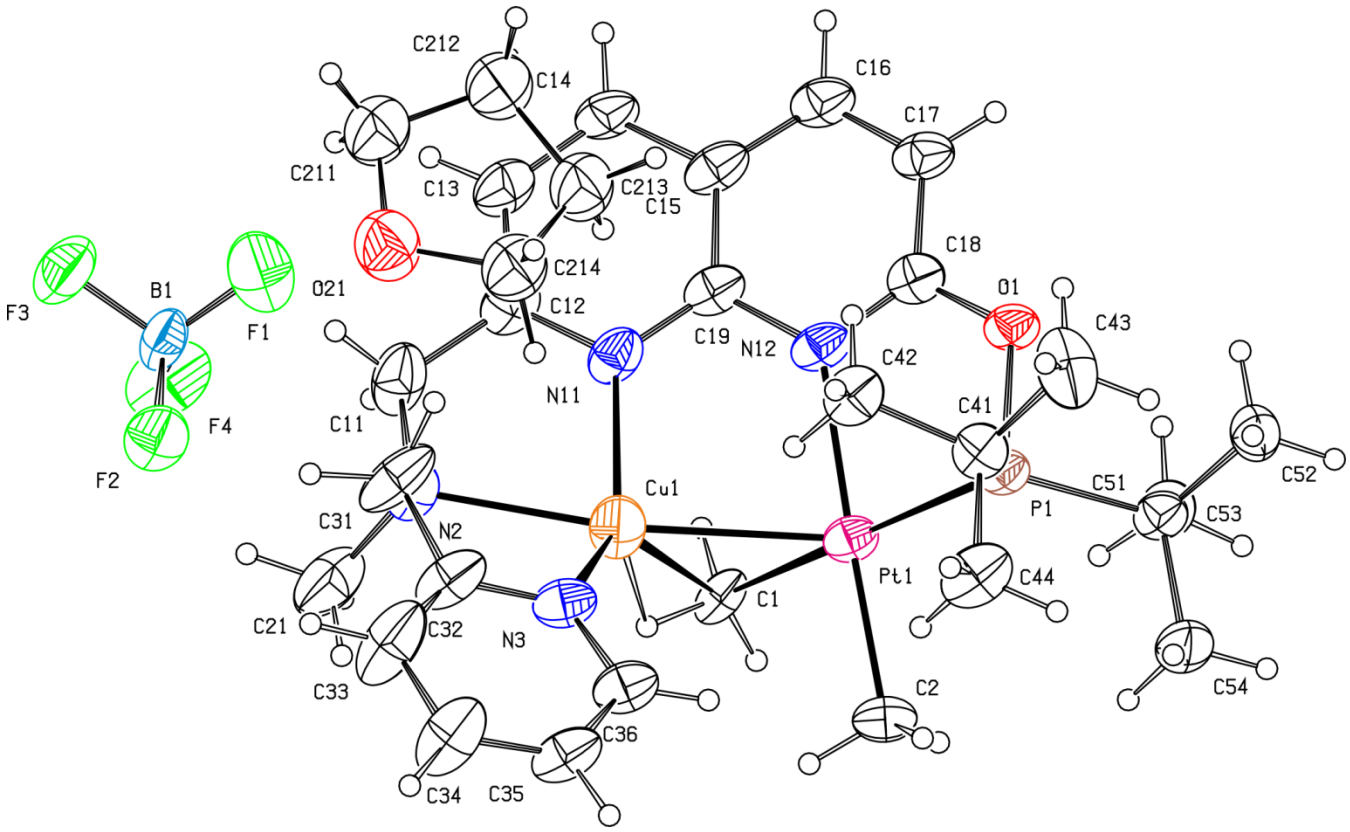

Figure S140. ORTEP at 30 % probability anisotropic displacement ellipsoids of non-hydrogen atoms for compound **3**[BF_4] according to SC-XRD data. The minor disordered component of the THF molecule is omitted for clarity. Selected interatomic distances [Å] and angles [°]: Pt1–Cu1 2.625(2), Pt1–P1 2.228(3), Pt1–N12 2.172(9), Pt1–C1 2.251(12), Pt1–C2 2.048(11), Cu1–N11 2.038(10), Cu1–N2 2.335(11), Cu1–N3 1.982(10), Cu1–C1 2.362(9), Cu1–H1A 1.886(3); Cu1–H1A–C1 106.7(7).

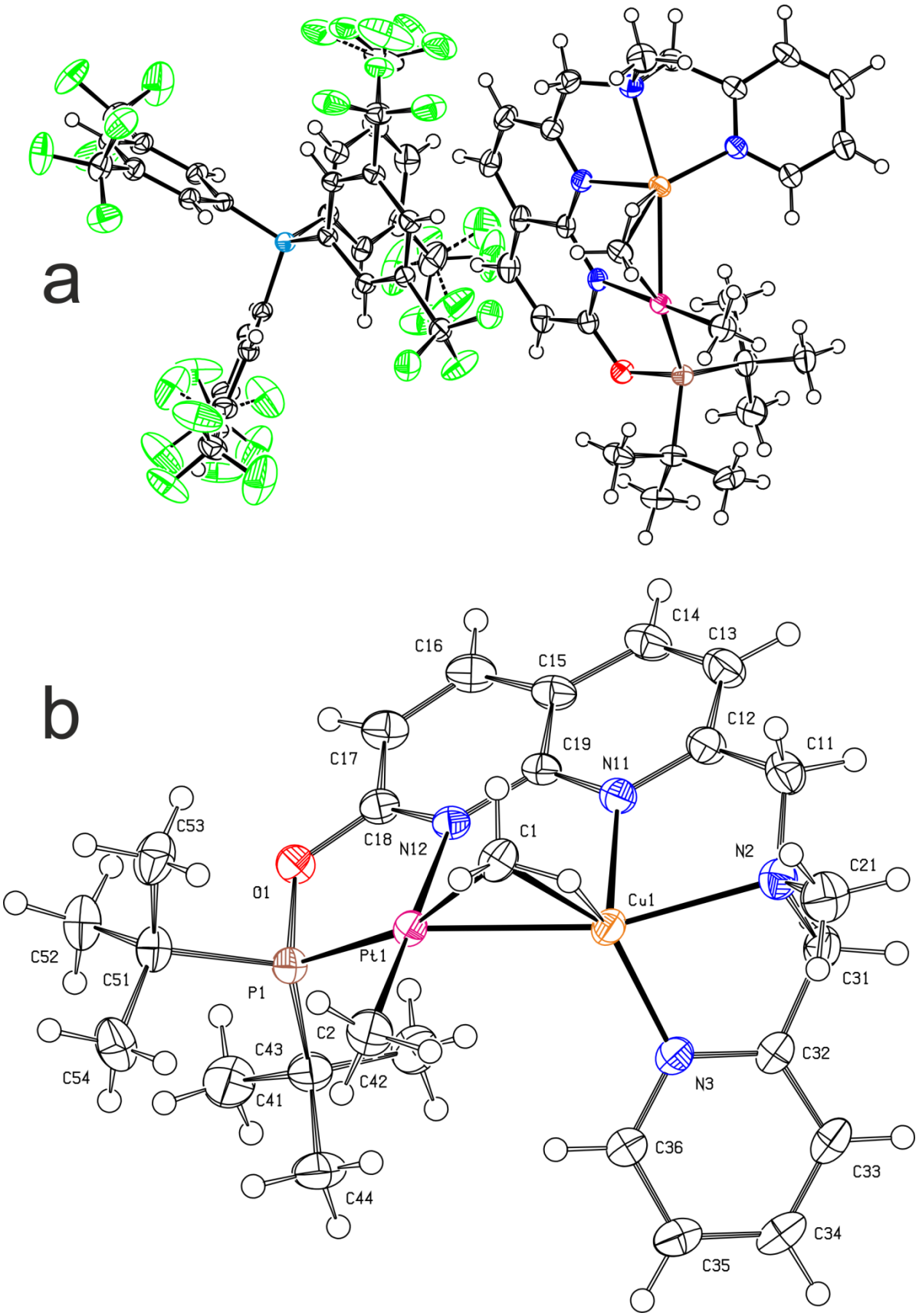

Figure S141. ORTEP at 50 % probability anisotropic displacement ellipsoids of non-hydrogen atoms for compound **3**[B(Ar^F)$_4$] (a) and for its cationic part (b) according to SC-XRD data. Selected interatomic distances [Å] and angles [°]: Pt1–Cu1 2.6119(3), Pt1–P1 2.2180(6), Pt1–N12 2.1894(19), Pt1–C1 2.164(3), Pt1–C2 2.048(3), Cu1–N11 2.076(2), Cu1–N2 2.322(2), Cu1–N3 1.953(2), Cu1–C1 2.160(3), Cu1–H1A 1.77(3); Cu1–H1A–C1 99(2). The minor disordered component is shown by dotted lines.

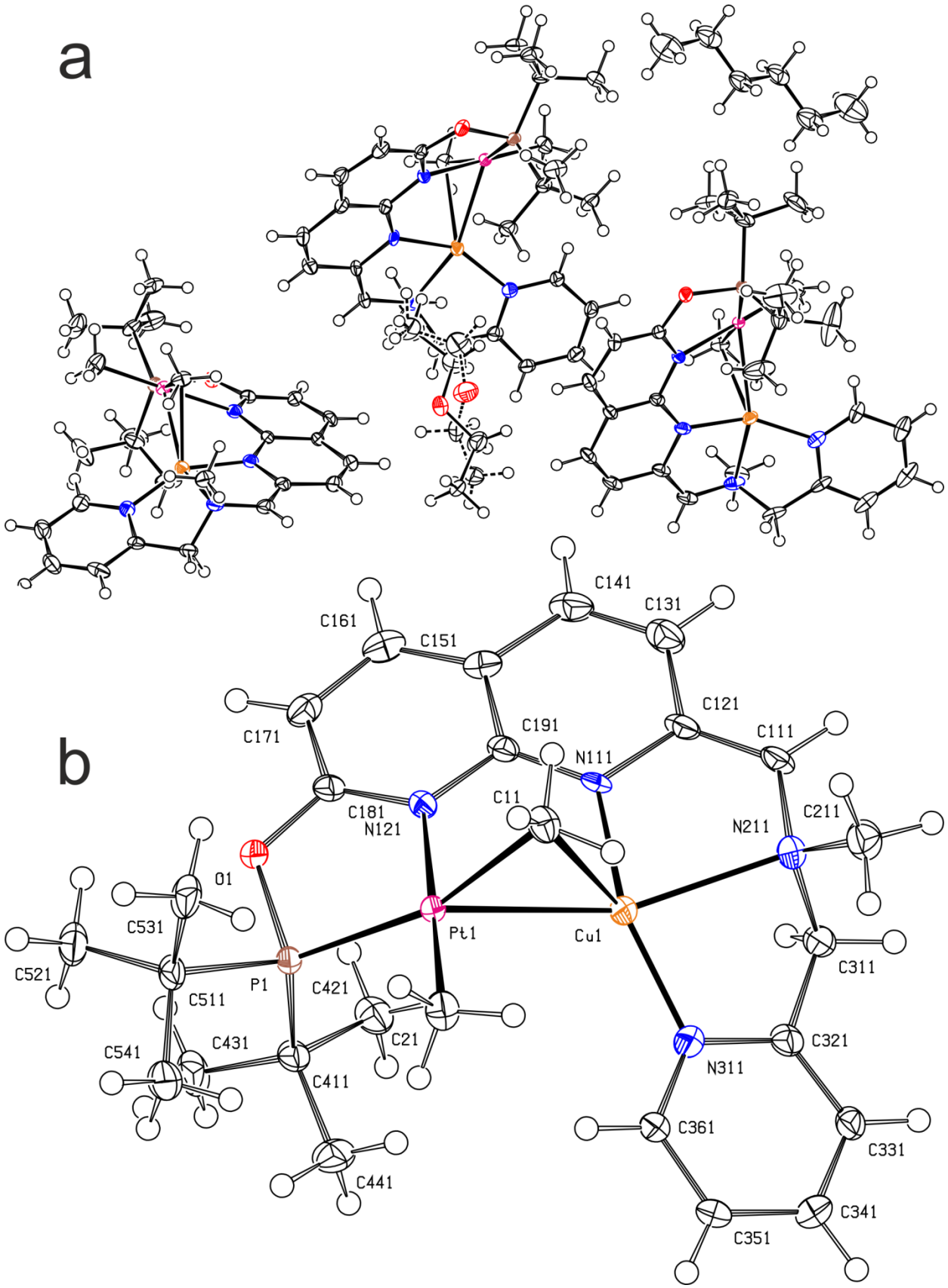

Figure S142. ORTEP at 50 % probability anisotropic displacement ellipsoids of non-hydrogen atoms for compound **4** (a) and for one of three independent molecules (b) according to SC-XRD data. Selected interatomic distances [Å] and angles [°]: Pt1–Cu1 2.6890(5), Pt1–P1 2.2371(11), Pt1–N121 2.156(3), Pt1–C11 2.109(5), Pt1–C21 2.062(5), Cu1–N111 1.933(4), Cu1–N211 2.346(4), Cu1–N311 1.925(4), Cu1–C11 2.558(5), Cu1–H11A 2.25(4); Cu1–H11A–C1 97(3). The minor disordered component is shown by dotted lines.

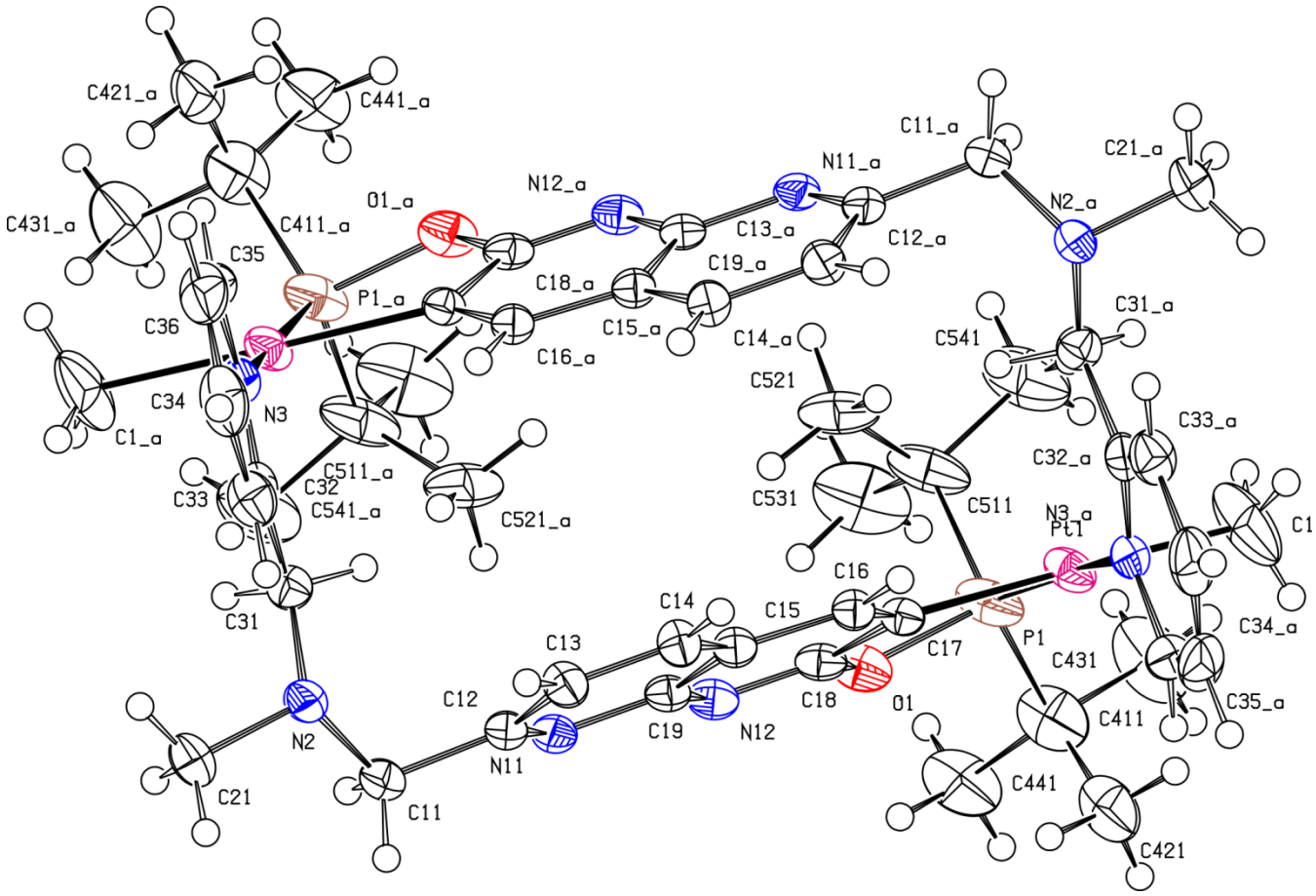

Figure S143. ORTEP at 50 % probability anisotropic displacement ellipsoids of non-hydrogen atoms for the main disordered component of compound **5** according to SC-XRD data. Selected interatomic distances [Å]: Pt1–P1 2.1745(10), Pt1–N3_a 2.095(3), Pt1–C1 2.136(4), Pt1–C17 2.057(3). Equivalent atoms are labeled by the sign a; symmetry operation (–x+1, –y+1/2, z).

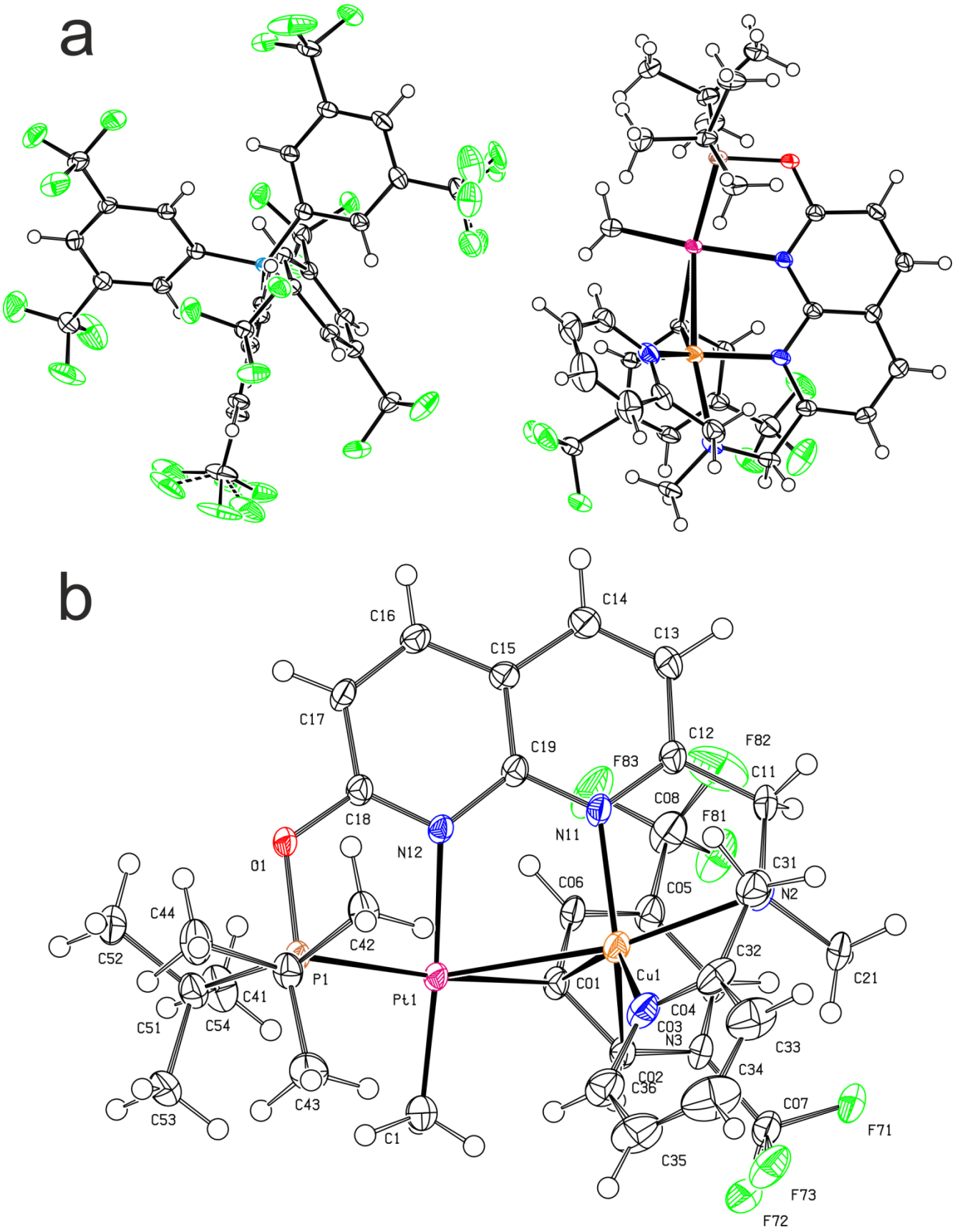

Figure S144. ORTEP at 50 % probability anisotropic displacement ellipsoids of non-hydrogen atoms for compound **6**[B(Ar^F)$_4$] (a) and for its cationic part (b) according to SC-XRD data. Selected interatomic distances [Å]: Pt1–Cu1 2.7745(4), Pt1–P1 2.2396(7), Pt1–N12 2.202(2), Pt1–C1 2.043(3), Pt1–C01 2.083(3), Cu1–N11 2.038(2), Cu1–N2 2.280(3), Cu1–N3 1.999(3), Cu1–C01 2.098(3), Cu1–C02 2.335(3). The minor disordered component is shown by dotted lines.

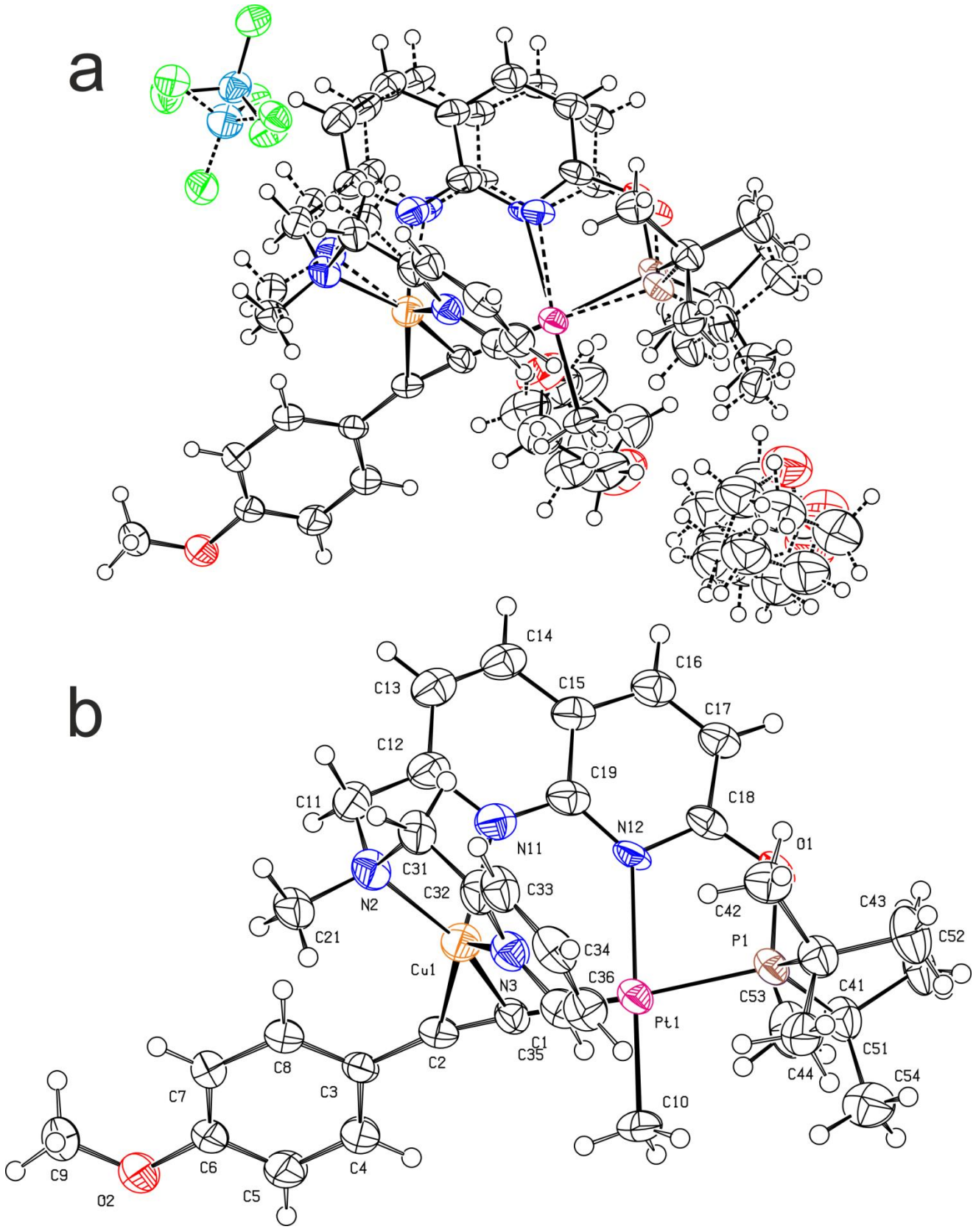

Figure S145. ORTEP at 50 % probability anisotropic displacement ellipsoids of non-hydrogen atoms for compound **7**[BF_4] (a) and for the main disordered component of its cationic part (b) according to SC-XRD data. Selected interatomic distances [Å]: Pt1–Cu1 3.0934(8), Pt1–P1 2.235(7), Pt1–P1' 2.227(8), Pt1–N12 2.282(9), Pt1–N12' 2.214(10), Pt1–C1 2.024(5), Pt1–C10 2.099(5), Cu1–C1 1.982(5), Cu1–N11 2.136(10), Cu1–N11' 2.222(10), Cu1–N2 2.107(10), Cu1–N2' 2.120(10), Cu1–N3 2.079(4), Cu1–C2 2.141(4). The minor disordered component is shown by dotted lines.

Computational Details

All calculations were performed using density functional theory (DFT) as implemented in the Gaussian 16 suite of programs.[8] Geometry optimizations and frequency analyses were carried out in the gas-phase without symmetry restrictions; ground states corresponded to the absence of imaginary frequencies while transition states (TSs) had exactly one imaginary frequency corresponding to the bond making/breaking process. Connectivity of the transition states to preceeding and succeeding intermediates were ascertained with intrinsic reaction coordinate (IRC) calculations. Gibbs free energies are reported as the 'Sum of electronic and thermal free energies'. The following describes the computational methods corresponding to **(1) QTAIM analysis; (2) NBO analysis** and **(3) the reaction profile**.

(1) QTAIM Analysis

Geometry optimizations of charged (**3**, **6**, **7**) and neutral (**4**) Pt/Cu complexes were carried out in the gas phase without symmetry restrictions using the rωB97XD functional.[9] The metal atoms were described with the SDD basis set,[10] while the remaining atoms were represented by the 6-31++g(d,p) basis set.[11] The initial atomic coordinates were taken from the crystal structures determined by SC XRD. The quantum-topological analysis of the calculated electron density of the "gas-phase" structures (provided as a multi-XYZ file named 'QTAIM_Structures.xyz') was performed within the quantum topological theory of atoms in molecules by means of the *AIMAll* package (v 19.10.12).[12] The QTAIM analysis using optimized structures obtained with RPBE1PBE[13] functional and the same basis set led to qualitatively similar conclusions.
According to Quantum Theory of Atoms in Molecules (QTAIM),[14] the bonding between two atoms is indicated by the presence of a bond critical point, bcp (in other words, a (3,-1) critical point of $\rho(\boldsymbol{r})$) along a bond path connecting two neighbouring atoms. The character of the bonding can be characterized by local indicators at the bcp and by the electron delocalization indices (DIs, an average number of electrons shared between pair of atoms) related to the degree of covalence and bond multiplicity.[15] Negative and positive values of the Laplacian at the bcp, $\nabla^2\rho_b$, are characteristics of "shared" and "closed-shell" interactions, respectively.[15-16] The value of ρ at bcp, ρ_b, is characteristic of a bond strength.[17] Metal-metal and metal-ligand interactions are typically characterized by positive values of $\nabla^2\rho_b$ and low ρ_b.[15, 18] Other characteristics are H_b (total energy density, G_b + V_b), G_b (kinetic energy density), V_b (potential energy density) at bcp and the relative ratio of the latter two, $|V_b|/G_b$. The covalent bonds are characterized by $|V_b|/G_b > 2$, the intermediate or transit region is characterized by $1 < |V_b|/G_b < 2$.[15, 19] Metal-metal interactions typically feature negative values for V_b and H_b (with H_b value close to zero), and $G_b \cong |V_b|$.[15-16, 18b, 18c]

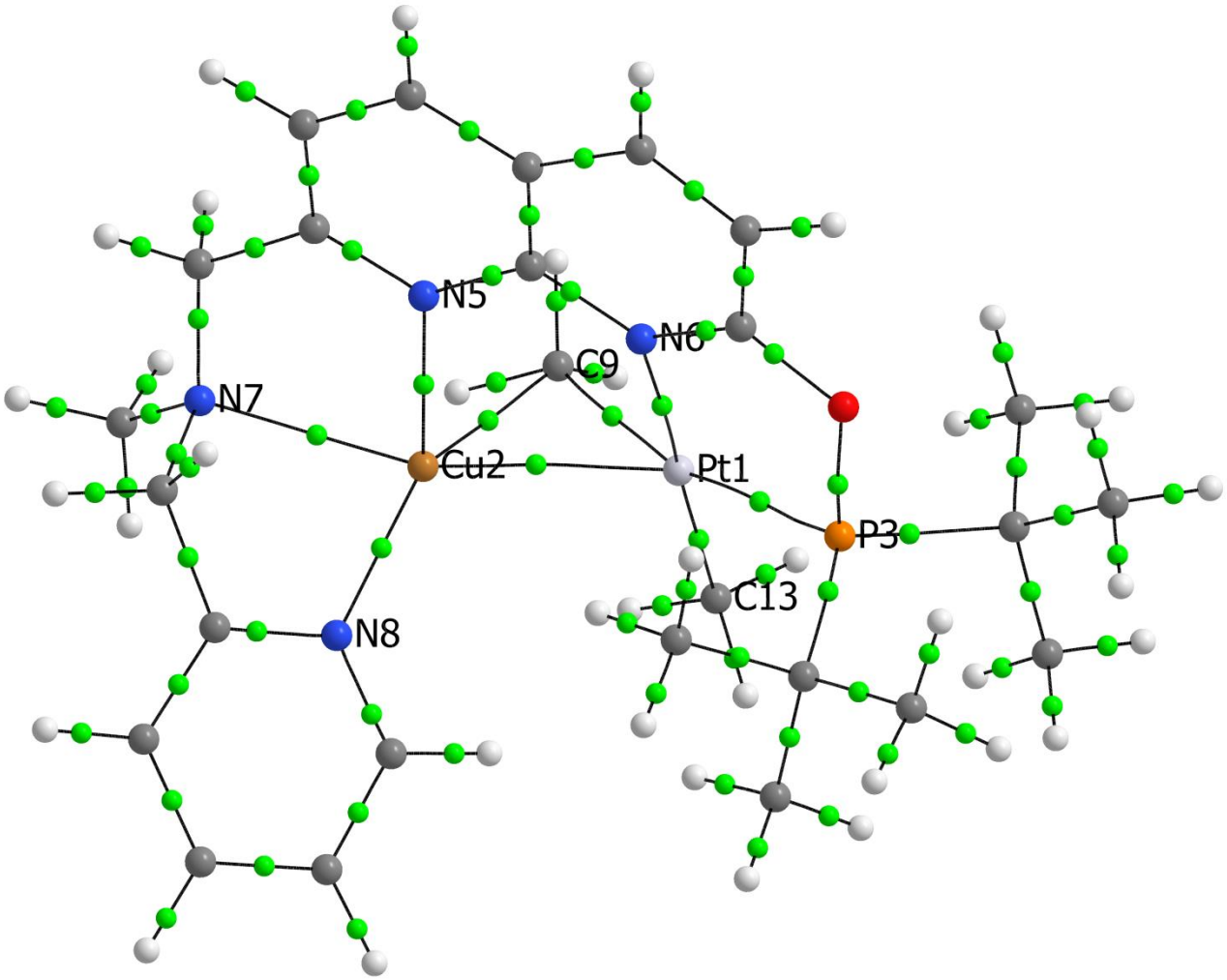

Figure S146. Molecular graph for "gas-phase" DFT-optimized ion $\mathbf{3}^{+}$. Bond critical points (3, –1) with a threshold of $\nabla\rho_b > 0.025$ a.u. and corresponding bond paths are shown with green dots and black lines, respectively.

Table S2. Quantum-topological parameters [in a.u.] at the bond critical points involving metal atoms for "gas-phase" ion $\mathbf{3}^{+}$.

Bonding atoms	ρ_b [a]	$\nabla^2\rho_b$ [b]	λ_1 [c]	λ_2 [c]	λ_3 [c]	ε [d]	V_b [e]	G_b [f]	H_b [g]	DI [h]
Pt1···Cu2	0.045905	0.117584	–0.03425	–0.01428	0.166116	1.399062	–0.04729	0.038343	–0.00895	0.32948
Pt1···P3	0.11322	0.146442	–0.09470	–0.09192	0.333063	0.030232	–0.13802	0.087256	–0.05077	0.95656
Pt1···N6	0.067944	0.302108	–0.05418	–0.05293	0.409215	0.023498	–0.09265	0.084042	–0.00860	0.50772
Pt1···C9	0.108297	0.14162	–0.11148	–0.10717	0.360266	0.040235	–0.12149	0.078384	–0.04310	0.79122
Pt1···C13	0.138535	0.068467	–0.16395	–0.16358	0.395988	0.00226	–0.15330	0.085109	–0.06819	1.00833
Cu2···N5	0.053868	0.280058	–0.06025	–0.05529	0.395595	0.089776	–0.06701	0.068511	0.001504	0.33226
Cu2···N7	0.039709	0.147984	–0.03637	–0.03565	0.220006	0.020075	–0.04138	0.039188	–0.00219	0.23312
Cu2···N8	0.081401	0.477478	–0.10865	–0.10151	0.687636	0.07029	–0.12733	0.123349	–0.00398	0.50735
Cu2···C9	0.05881	0.217788	–0.06007	–0.02767	0.305529	1.170786	–0.06623	0.060337	–0.00589	0.31958

[a]Electron density; [b]Laplacian of electron density; [c]Eigenvalues of the Hessian matrix of $\rho(\boldsymbol{r})$ at the bcp; [d]Bond ellipticity; [e]Potential energy density; [f]Kinetic energy density; [g]Total energy density; [h]Delocalization index. All values are given for the corresponding bcps.

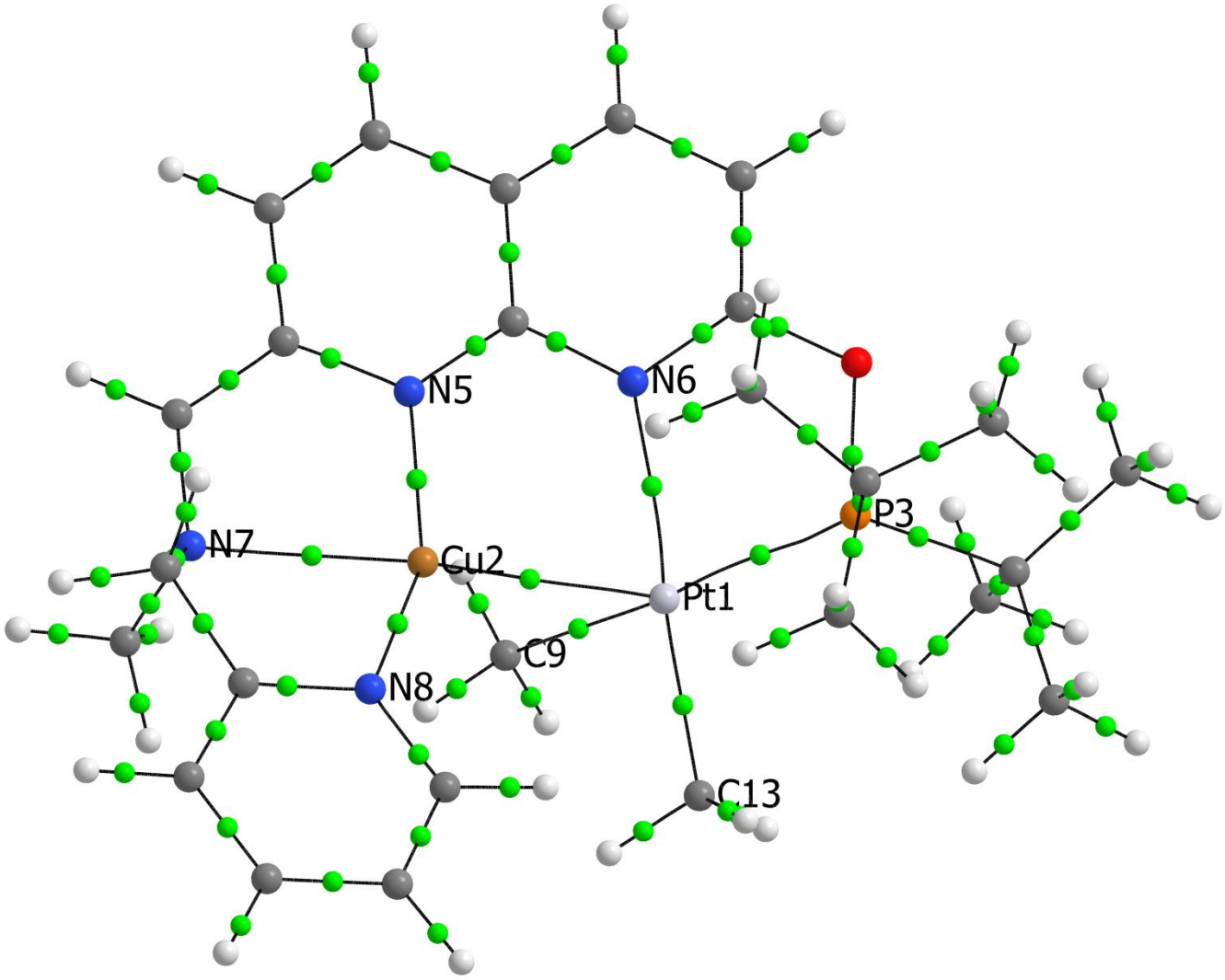

Figure S147. Molecular graph for "gas-phase" DFT-optimized complex **4**. Bond critical points (3, –1) with a threshold of $\nabla\rho_b > 0.025$ a.u. and corresponding bond paths are shown with green dots and black lines, respectively.

Table S3. Quantum-topological parameters [in a.u.] at the bond critical points involving metal atoms for "gas-phase" complex **4**.

Bonding atoms	ρ_b [a]	$\nabla^2\rho_b$ [b]	λ_1 [c]	λ_2 [c]	λ_3 [c]	ε [d]	V_b [e]	G_b [f]	H_b [g]	DI [h,i]
Pt1···Cu2	0.037339	0.08823	–0.02726	–0.02317	0.138659	0.176644	–0.03707	0.029561	–0.00750	0.30527
Pt1···P3	0.108924	0.154615	–0.09148	–0.08655	0.332643	0.056914	–0.13295	0.085748	–0.04720	0.92594
Pt1···N6	0.071072	0.303848	–0.05807	–0.05656	0.418481	0.026674	–0.09599	0.085924	–0.01006	0.52766
Pt1···C9	0.122673	0.124297	–0.13654	–0.13196	0.392797	0.034708	–0.13953	0.085217	–0.05431	0.87970
Pt1···C13	0.136279	0.099210	–0.15671	–0.15605	0.411964	0.004207	–0.15569	0.090133	–0.06555	0.99256
Cu2···N5	0.092452	0.515889	–0.13061	–0.12269	0.76919	0.064551	–0.14854	0.138756	–0.00978	0.53288
Cu2···N7	0.039438	0.14019	–0.03569	–0.03533	0.211211	0.010208	–0.04043	0.037737	–0.00269	0.22104
Cu2···N8	0.089272	0.523422	–0.12527	–0.11797	0.766663	0.061905	–0.14586	0.138360	–0.00750	0.54350

[a]Electron density; [b]Laplacian of electron density; [c]Eigenvalues of the Hessian matrix of $\rho(\boldsymbol{r})$ at the bcp; [d]Bond ellipticity; [e]Potential energy density; [f]Kinetic energy density; [g]Total energy density; [h]Delocalization index; [i]DI(Cu2,C9) = 0.13230.

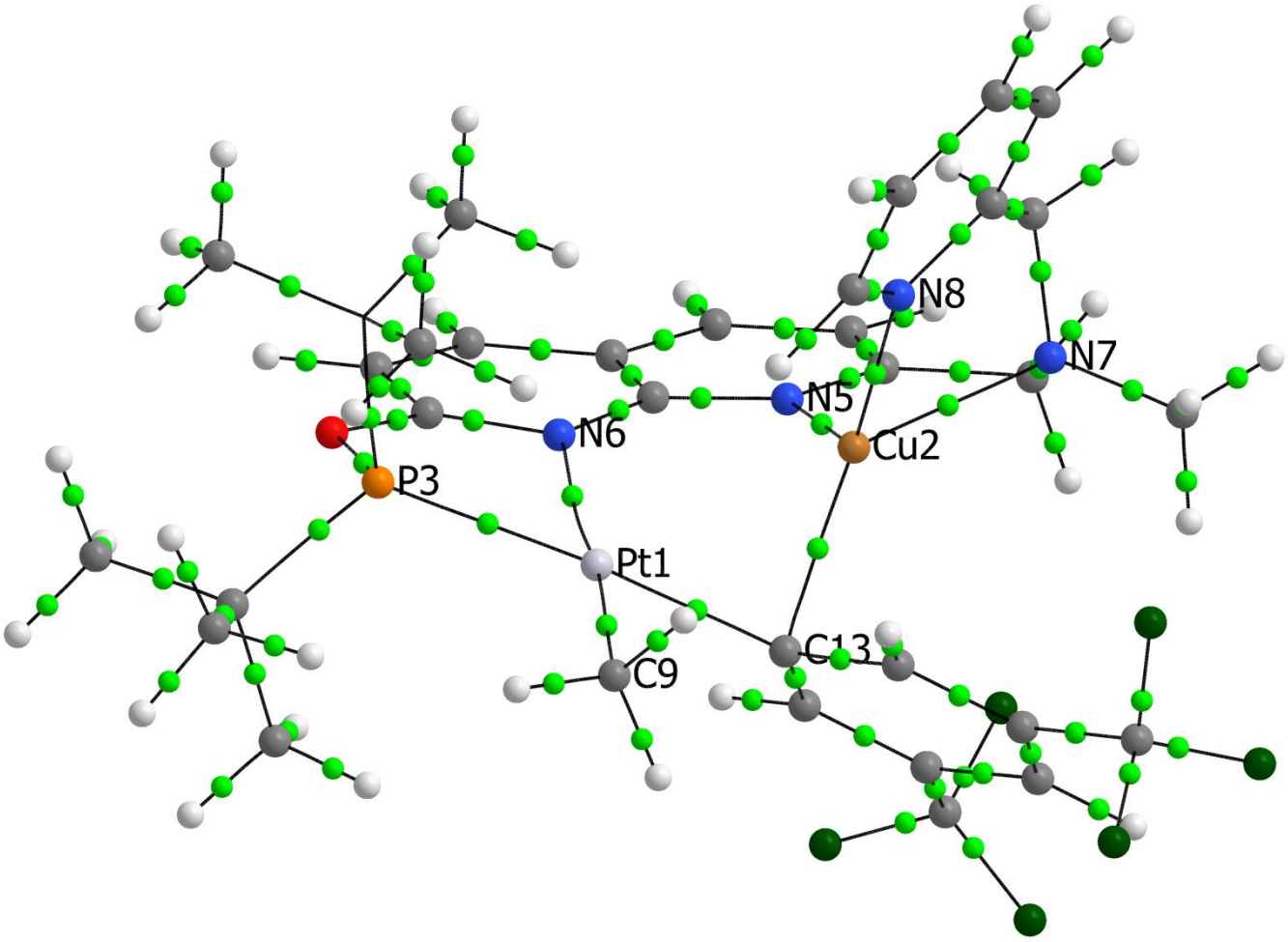

Figure S148. Molecular graph for "gas-phase" DFT-optimized ion $\mathbf{6}^{+}$. Bond critical points (3, –1) with a threshold of $\nabla\rho_b > 0.025$ a.u. and corresponding bond paths are shown with green dots and black lines, respectively.

Table S4. Quantum-topological parameters [in a.u.] at the bond critical points involving metal atoms for "gas-phase" ion $\mathbf{6}^{+}$.

Bonding atoms	ρ_b [a]	$\nabla^2\rho_b$ [b]	λ_1 [c]	λ_2 [c]	λ_3 [c]	ε [d]	V_b [e]	G_b [f]	H_b [g]	DI [h,i]
Pt1···P3	0.110111	0.152084	–0.0892	–0.08736	0.328643	0.02114	–0.13372	0.085809	–0.04791	0.92025
Pt1···N6	0.060801	0.258949	–0.04877	–0.04594	0.353665	0.061526	–0.07805	0.071369	–0.00669	0.46810
Pt1···C9	0.138846	0.063177	–0.16556	–0.16496	0.393702	0.003648	–0.15293	0.084264	–0.06866	1.01393
Pt1···C13	0.12662	0.198660	–0.13869	–0.12831	0.465664	0.080865	–0.16078	0.105090	–0.05569	0.85512
Cu2···N5	0.064222	0.357110	–0.07808	–0.07127	0.50645	0.095562	–0.08789	0.088583	0.000695	0.38095
Cu2···N7	0.045322	0.188665	–0.04475	–0.04407	0.277491	0.015388	–0.04953	0.048347	–0.00118	0.26111
Cu2···N8	0.076828	0.442015	–0.10091	–0.09369	0.636611	0.077089	–0.11552	0.113010	–0.00251	0.47136
Cu2···C13	0.069147	0.213427	–0.07058	–0.05801	0.342017	0.216583	–0.07906	0.066206	–0.01285	0.35972

[a]Electron density; [b]Laplacian of electron density; [c]Eigenvalues of the Hessian matrix of $\rho(\boldsymbol{r})$ at the bcp; [d]Bond ellipticity; [e]Potential energy density; [f]Kinetic energy density; [g]Total energy density; [h]Delocalization index; [i]DI(Pt1,Cu2) = 0.21471.

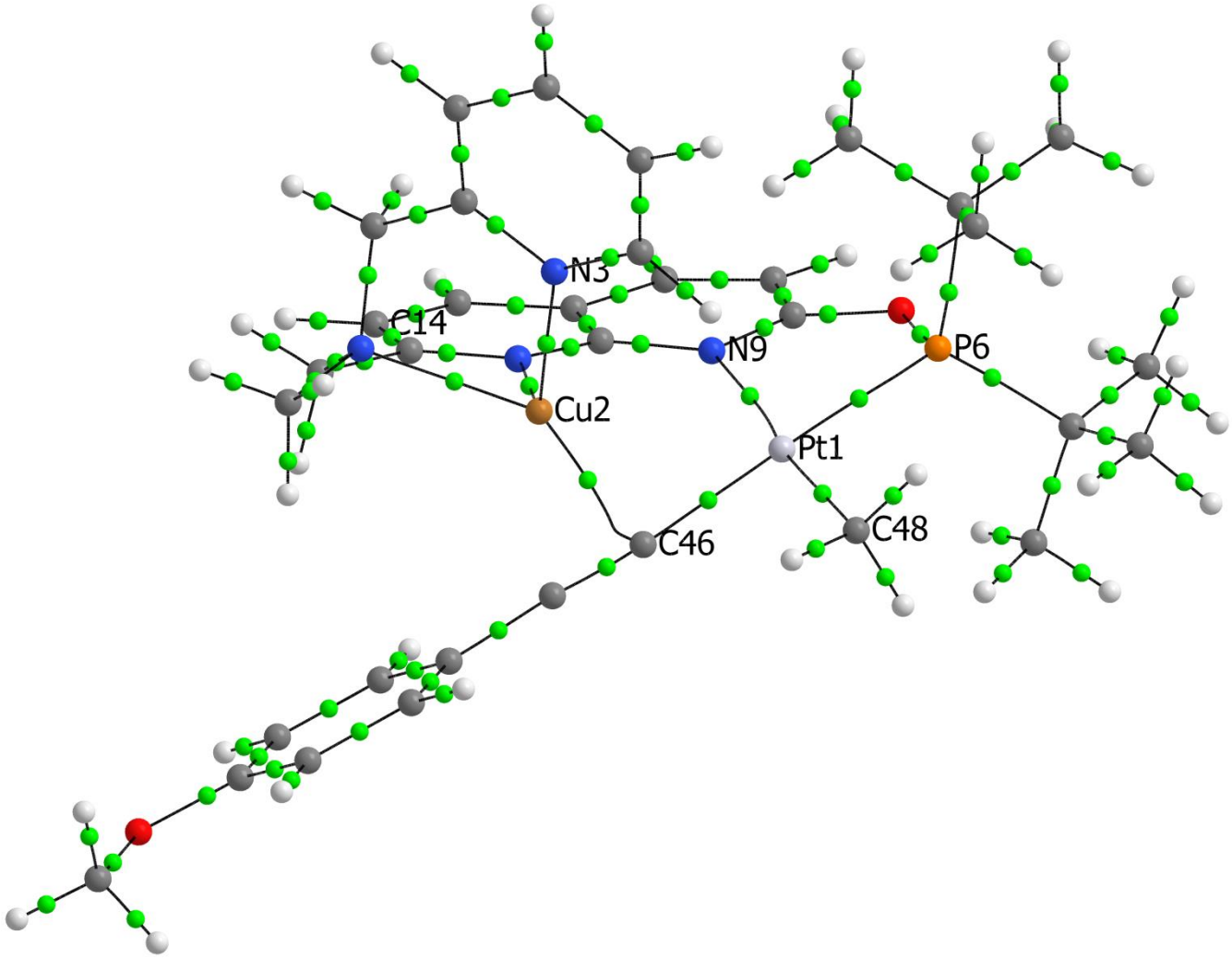

Figure S149. Molecular graph for "gas-phase" DFT-optimized ion $\mathbf{7}^{+}$. Bond critical points (3, –1) with a threshold of $\nabla\rho_b > 0.025$ a.u. and corresponding bond paths are shown with green dots and black lines, respectively.

Table S5. Quantum-topological parameters [in a.u.] at the bond critical points involving metal atoms for "gas-phase" ion $\mathbf{7}^{+}$.

Bonding atoms	ρ_b [a]	$\nabla^2\rho_b$ [b]	λ_1 [c]	λ_2 [c]	λ_3 [c]	ε [d]	V_b [e]	G_b [f]	H_b [g]	DI [h,i]
Pt1···P6	0.114499	0.149117	–0.09387	–0.09133	0.334319	0.027768	–0.14098	0.08906	–0.05192	0.95449
Pt1···N9	0.059616	0.252461	–0.04777	–0.04516	0.345383	0.057861	–0.07567	0.069369	–0.00630	0.46099
Pt1···C46	0.135517	0.284128	–0.14968	–0.13899	0.572798	0.076912	–0.19306	0.131837	–0.06122	0.92207
Pt1···C48	0.137642	0.051282	–0.16593	–0.16434	0.381548	0.009654	–0.14846	0.080553	–0.06791	1.01355
Cu2···N3	0.074277	0.426684	–0.09723	–0.09081	0.614726	0.070669	–0.10961	0.108142	–0.00147	0.45715
Cu2···N8	0.046896	0.223432	–0.04903	–0.04497	0.317424	0.090250	–0.05421	0.055032	0.000827	0.28624
Cu2···N25	0.053608	0.257696	–0.05782	–0.05644	0.371947	0.024433	–0.06475	0.064586	–0.00016	0.30631
Cu2···C46	0.079953	0.290933	–0.09213	–0.05031	0.433365	0.831345	–0.09996	0.086349	–0.01362	0.41472

[a]Electron density; [b]Laplacian of electron density; [c]Eigenvalues of the Hessian matrix of $\rho(\boldsymbol{r})$ at the bcp; [d]Bond ellipticity; [e]Potential energy density; [f]Kinetic energy density; [g]Total energy density; [h]Delocalization index; [i]DI(Pt1,Cu2) = 0.13694.

Comparison of geometry-optimized structures and XRD parameters

Table S6. Comparison of coordination bond distances and metal-metal distances in dimethyl complexes **3[X]** from X-ray data with the geometry-optimized complex $\mathbf{3}^{+}$ according to DFT calculations

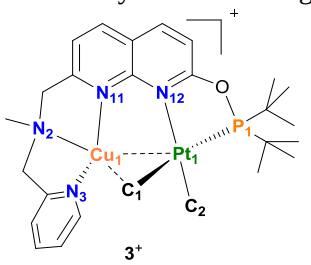

$\mathbf{3}^{+}$

Bond distance (Å)	$\mathbf{3}^{+}$ (DFT)[a]	$\mathbf{3}[CuCl_2]$[b]	$\mathbf{3}[BF_4]$[b]	$\mathbf{3}[BAr^F{}_4]$[b]
Pt1–C1	2.15581	2.201(2)	2.251(12)	2.164(3)
Pt1–C2	2.05033	2.050(2)	2.048(11)	2.048(3)
Pt1–N12	2.26045	2.1823(19)	2.172(9)	2.1894(19)
Pt1–P1	2.28052	2.2280(6)	2.228(3)	2.2180(6)
Cu1–N11	2.18670	2.064(2)	2.038(10)	2.076(2)
Cu1–N2	2.37992	2.320(2)	2.335(11)	2.322(2)
Cu1–N3	2.00408	1.966(2)	1.982(10)	1.953(2)
Cu1–C1	2.19421	2.277(2)	2.362(9)	2.160(3)
Pt1–Cu1	2.60463	2.6486(3)	2.625(2)	2.6119(3)

[a]ωB97XD/6-31++g(d,p),SDD(Cu,Pt). [b]From XRD.

Table S7. Comparison of coordination and metal-metal bond distances in complex **4** from X-ray data (bond distances for each symmetrically independent molecule) with the geometry-optimized complex **4** according to DFT calculations.

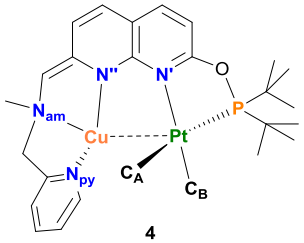

4

Bond distance (Å)	**4** (DFT)[a]	**4**[b,c]	**4**[b,d]	**4**[b,e]
Pt–C_A	2.10410	2.109(5)	2.127(5)	2.124(5)
Pt–C_B	2.05482	2.062(5)	2.050(5)	2.060(5)
Pt–N'	2.24801	2.156(3)	2.174(4)	2.171(3)
Pt–P	2.29449	2.2371(11)	2.2428(11)	2.2427(11)
Cu–N''	1.95497	1.933(4)	1.939(4)	1.939(4)
Cu–N_{am}	2.39025	2.346(4)	2.317(4)	2.301(4)
Cu–N_{py}	1.96410	1.925(4)	1.937(4)	1.941(4)
Cu–C_A	2.58677	2.558(5)	2.518(5)	2.559(5)
Pt–Cu	2.70502	2.6890(5)	2.7459(6)	2.7201(5)

[a]ωB97XD/6-31++g(d,p),SDD(Cu,Pt). [b]From XRD data for the 1st ([c]), 2nd ([d]) and 3rd ([e]) symmetrically independent molecules.

Table S8. Comparison of coordination and metal-metal bond distances in **6**[BAr^F_4] from X-ray data with the geometry-optimized complex **6**$^+$ according to DFT calculations.

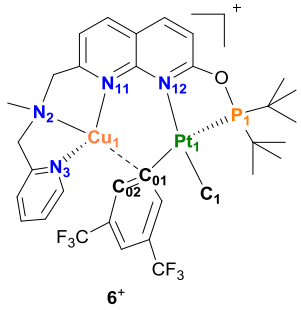

6$^+$

Bond distance (Å)	**6**$^+$ (DFT)[a]	**6**[BAr^F_4][b]
Pt1–C1	2.04826	2.043(3)
Pt1–C01	2.07977	2.083(3)
Pt1–N12	2.31344	2.202(2)
Pt1–P1	2.29772	2.2396(7)
Cu1–N11	2.10720	2.038(2)
Cu1–N2	2.30968	2.280(3)
Cu1–N3	2.03108	1.999(3)
Cu1–C01	2.08958	2.098(3)
Cu1–C02	2.34135	2.335(3)
Pt1–Cu1	2.79943	2.7745(4)

[a]ωB97XD/6-31++g(d,p),SDD(Cu,Pt). [b]From XRD.

Table S9. Comparison of coordination and metal-metal bond distances in **7**[BF_4] from X-ray data with the geometry-optimized complex **7**$^+$ according to DFT calculations.

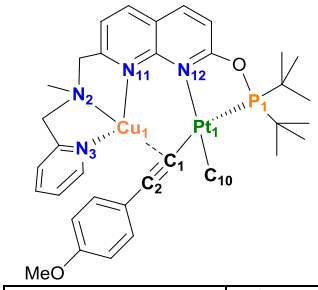

Bond distance (Å)	**7**$^+$ (DFT)[a]	**7**[BF_4][b]
Pt1–C10	2.05305	2.099(5)
Pt1–C1	2.01029	2.024(5)
Pt1–N12	2.32232	2.282(9)
Pt1–P1	2.27850	2.235(7)
Cu1–N11	2.25421	2.136(10)
Cu1–N2	2.21740	2.107(10)
Cu1–N3	2.04506	2.079(4)
Cu1–C1	2.03008	1.982(5)
Cu1–C2	2.18333	2.141(4)
Pt1–Cu1	2.99076	3.0934(8)

[a]ωB97XD/6-31++g(d,p),SDD(Cu,Pt). [b]From XRD data for the main disordered component.

(2) NBO Analysis

Second order perturbation theory analysis data is summarized below using NBO 6.0.[20] The structures for all complexes were optimized as described above in the QTAIM section (ωB97XD/6-31++g(d,p),SDD(Cu,Pt)). The NBO orbitals were visualized using ChemCraft.[21]

Complex 1:

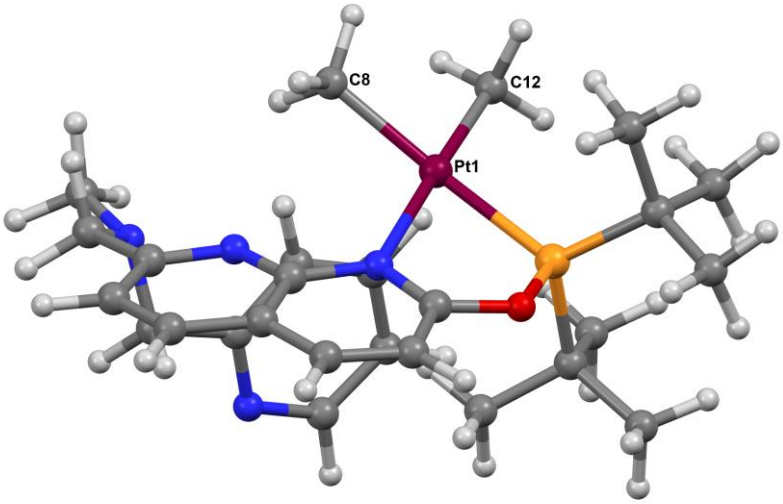

Figure S150. Atom numbering scheme for complex **1** used in the analysis below.

The Pt(1)-C(8) and Pt(1)-C(12) bond lengths of complex **1** are 2.08 and 2.05 Å, respectively, with Natural Binding Indices (NBIs) as detailed below:

Table S10. Natural Binding Indices (NBI) in complex **1**.

	C(8)	**C(12)**
Pt(1)	0.7444	0.8301

The NBOs corresponding to the Pt-CH_3 fragments are detailed/shown below:

#	Orbital	NAO (%contribution)
53	BD(1)Pt1-C8	Pt (36.54%) s(51.19%) p(0.23%) d(48.59%) C (63.46%) s(21.70%) p(78.28%) d(0.02%)
54	BD(1)Pt1-C12	Pt(38.17%) s(43.76%) p(0.24%) d(56.00%) C(61.83%) s(22.25%) p(77.70%) d(0.04%)

53 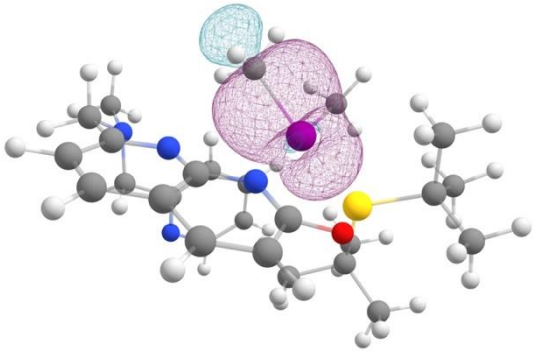

54 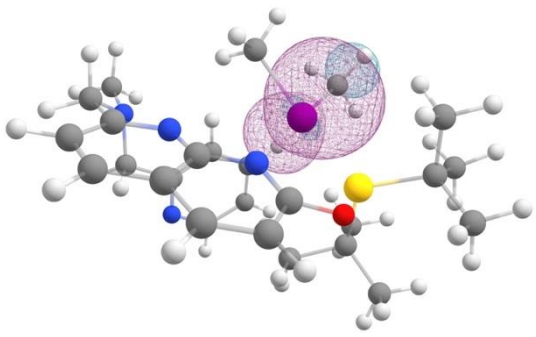

Figure S151. Orbital plots for complex **1**.

Complex 3:

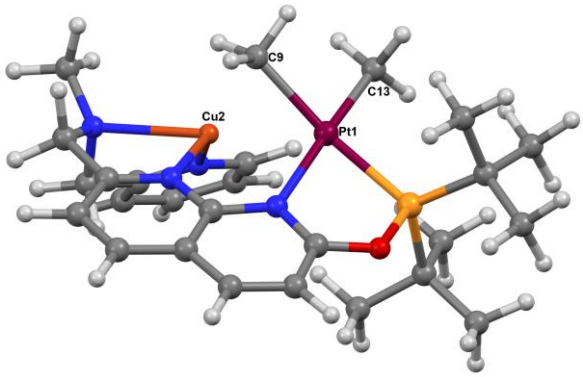

Figure S152. Atom numbering scheme for complex **3** used in the analysis below.

Interactions between Cu and the Pt-CH$_3$ fragments: Complex **3** exhibits strong donation of electrons from the Pt(1)-C(9) fragment to an *s*-type Cu(2)-orbital [$E^{(2)}$ = 89.68 kcal/mol]. A much lower [$E^{(2)}$ = 25.67 kcal/mol] donation is observed from the Pt-C(13) fragment distal to the Cu(2)-center. Two weak interactions corresponding to back-donation of electrons from Cu *d*-type orbitals into the antibonding orbital of the Pt(1)-C(9) fragment were found [$E^{(2)}$ = 6.12 and 5.57 kcal/mol]. In contrast, back-donation from Cu to the antibonding orbital of the distal Pt(1)-C(13) fragment was found to be much weaker [$E^{(2)}$ = 2.62 kcal/mol].
Interactions between Cu and the Pt: Two Pt→Cu interactions [$E^{(2)}$ = 24.49 and 6.6 kcal/mol] involving donation of electrons from Pt *d*-type orbitals into empty *s*-type orbitals on Cu were found.

Table S11. Key interactions in complex **3**.

Donor			**Acceptor**			**$E^{(2)}$ kcal/mol**
#	**Orbital**	**NAO (%contribution)**	**#**	**Orbital**	**NAO (%contribution)**	
62	BD(1)Pt1-C9	Pt(31.79%) s(54.61%) p(0.20%) d(45.19%) C(68.21%) s(23.49%) p(76.50%) d(0.01%)	142	LV(1)Cu2	Cu s(97.33%) p(0.12%) d(2.54%)	89.68
63	BD(1)Pt1-C13	Pt (41.03%) s(40.17%) p(0.24%) d(59.59%) C (58.97%) s(21.48%) p(78.47%) d(0.05%)	142	LV(1)Cu2	Cu s(97.33%) p(0.12%) d(2.54%)	25.67
53	LP(5)Cu2	Cu s(0.67%) p(0.04%) d(99.29%)	144	BD*(1)Pt1-C9	Pt (68.21%) s(54.61%) p(0.20%) d(45.19%) C (31.79%) s(23.49%) p(76.50%) d(0.01%)	6.12
50	LP(2)Cu2	Cu s(0.07%) p(0.02%) d(99.91%)	144	BD*(1)Pt1-C9	Pt (68.21%) s(54.61%) p(0.20%) d(45.19%) C (31.79%) s(23.49%) p(76.50%) d(0.01%)	5.57
50	LP(2)Cu2	Cu s(0.07%) p(0.02%) d(99.91%)	145	BD*(1)Pt1-C13	Pt (58.97%) s(40.17%) p(0.24%) d(59.59%) C (41.03%) s(21.48%) p(78.47%) d(0.05%)	2.62
46	LP(2)Pt1	Pt s(2.62%) p(0.02%) d(97.36%)	142	LV(1)Cu2	Cu s(97.33%) p(0.12%) d(2.54%)	24.49
45	LP(1)Pt1	Pt s(1.18%) p(0.00%) d(98.82%)	142	LV(1)Cu2	Cu s(97.33%) p(0.12%) d(2.54%)	6.6

The interaction of the proximal Pt-CH$_3$ fragment with the Cu-center is reflected in the elongation of the Pt-C(9) bond (2.15 Å) when compared to that distal to the Cu-center(Pt-C(13): 2.05 Å) and to analogous Pt-CH$_3$ fragment in the Cu-free complex **1** (2.08 Å). At the same time, Pt-C distance for the distal Pt-C(13) remains practically unchanged compared to **1** (2.05 Å in complex **1**). This is further reflected in the natural binding indices (NBIs): while an NBI of 0.67 was observed for the Pt-C(9) bond, an NBI of 0.84 was found for the Pt-C(13) bond,

showing significant decrease for the bridging Pt-Me_A, but only minor changes for the distal Pt-Me_B as compared to complex **1** (see above). For the same reasons NBIs of 0.34 and 0.09 were found for Cu(2)-C(9) and Cu(2)-C(13), respectively, indicating that the Cu(2) center interacts predominantly with the proximal Pt(1)-C(9) fragment. The Pt→Cu interactions result in an NBI of 0.26 between the Pt and Cu centers.

Table S12. Natural Binding Indices (NBI) in complex **3**.

	Pt(1)	**Cu(2)**	**C(9)**	**C(13)**
Pt(1)	-	0.2687	0.6760	0.8403
Cu(2)	0.2687	-	0.3476	0.0946

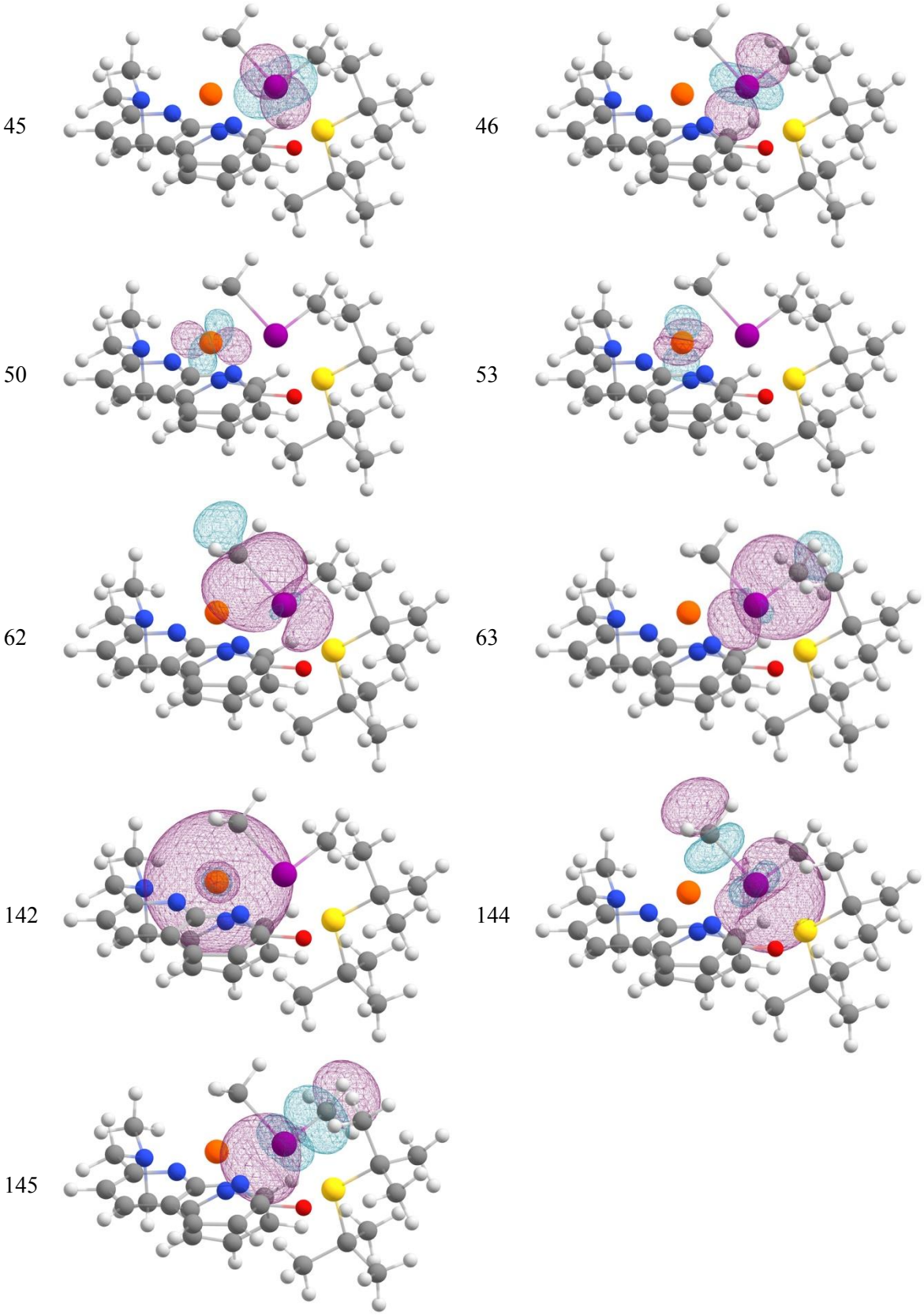

Figure S153. Orbital plots for complex **3**.

Complex 4:

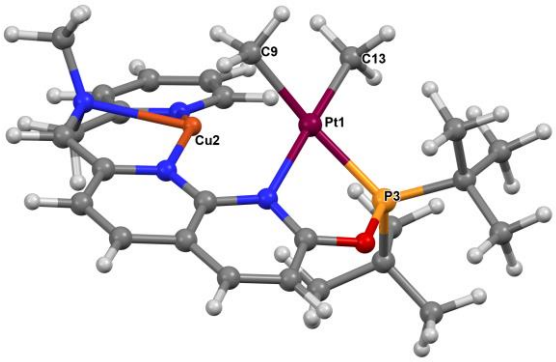

Figure S154. Atom numbering scheme for complex **4** used in the analysis below.

Interactions between Cu and the Pt-CH$_3$ fragments: Complex **4** exhibits moderate donation of electrons from the Pt(1)-C(9) fragment (which is proximal to the Cu-center) to an *s*-type Cu(2)-orbital [$E^{(2)}$ = 44.23 kcal/mol]. In contrast, a much weaker interaction involving donation of electrons from the Pt(1)-C(13) fragment (which is distal to the Cu-center) to an *s*-type Cu(2)-orbital [$E^{(2)}$ = 17.5 kcal/mol] is observed. Two weak interactions corresponding to the back-donation of electrons from a *d*-type Cu orbitals to the antibonding orbital of both the Pt(1)-C(9) and Pt(1)-C(13) fragments [$E^{(2)}$ = 5.13 and 4.03 kcal/mol, respectively] were found.
Interactions between Cu and the Pt: Two Pt→Cu interactions [$E^{(2)}$ = 32.13 and 4.68 kcal/mol] involving donation of electrons from Pt *d*-type orbitals into empty *s*-type orbitals on Cu were found.

Table S13. Key interactions in complex **4**.

Donor			**Acceptor**			$E^{(2)}$ **kcal/mol**
#	**Orbital**	**NAO (%contribution)**	**#**	**Orbital**	**NAO (%contribution)**	
62	BD(1)Pt1-C9	Pt(35.43%) s(52.11%) p(0.20%) d (47.69%) C(64.57%) s(22.15%) p(77.83%) d(0.02%)	142	LV(1)Cu2	Cu s(95.14%) p(0.08%) d(4.78%)	44.23
63	BD(1)Pt1-C13	Pt(37.98%) s(42.39%) p(0.25%) d(57.36%) C(62.02%) s(22.63%) p(77.33%) d(0.04%)	142	LV(1)Cu2	Cu s(95.14%) p(0.08%) d(4.78%)	17.5
52	LP(4)Cu2	Cu s(2.72%) p(0.02%) d(97.26%)	143	BD*(1)Pt1-C9	Pt(64.57%) s(52.11%) p(0.20%) d(47.69%) C(35.43%) s(22.15%) p(77.83%) d(0.02%)	5.13
52	LP(4)Cu2	Cu s(2.72%) p(0.02%) d(97.26%)	144	BD*(1)Pt1-C13	Pt(62.02%) s(42.39%) p(0.25%) d(57.36%) C(37.98%) s(22.63%) p(77.33%) d(0.04%)	4.03
46	LP(2)Pt1	Pt s(3.72%) p(0.03%) d(96.26%)	142	LV(1)Cu2	Cu s(95.14%) p(0.08%) d(4.78%)	32.13
47	LP(3)Pt1	Pt s(0.86%) p(0.01%) d(99.13%)	142	LV(1)Cu2	Cu s(95.14%) p(0.08%) d(4.78%)	4.68

Although the Cu-center in complex **4** interacts with the Pt-C(9) fragment, the intensity of the interaction is much lower than in complex **3**. Thus the Pt-C(9) bond (2.10 Å) is elongated to a lesser extent than in complex **3**. These interactions are reflected in the NBIs.

Table S14. Natural Binding Indices (NBI) in complex **4**.

	Pt(1)	**Cu(2)**	**C(9)**	**C(13)**
Pt(1)	-	0.2498	0.7226	0.8197
Cu(2)	0.2498	-	0.1985	0.0734

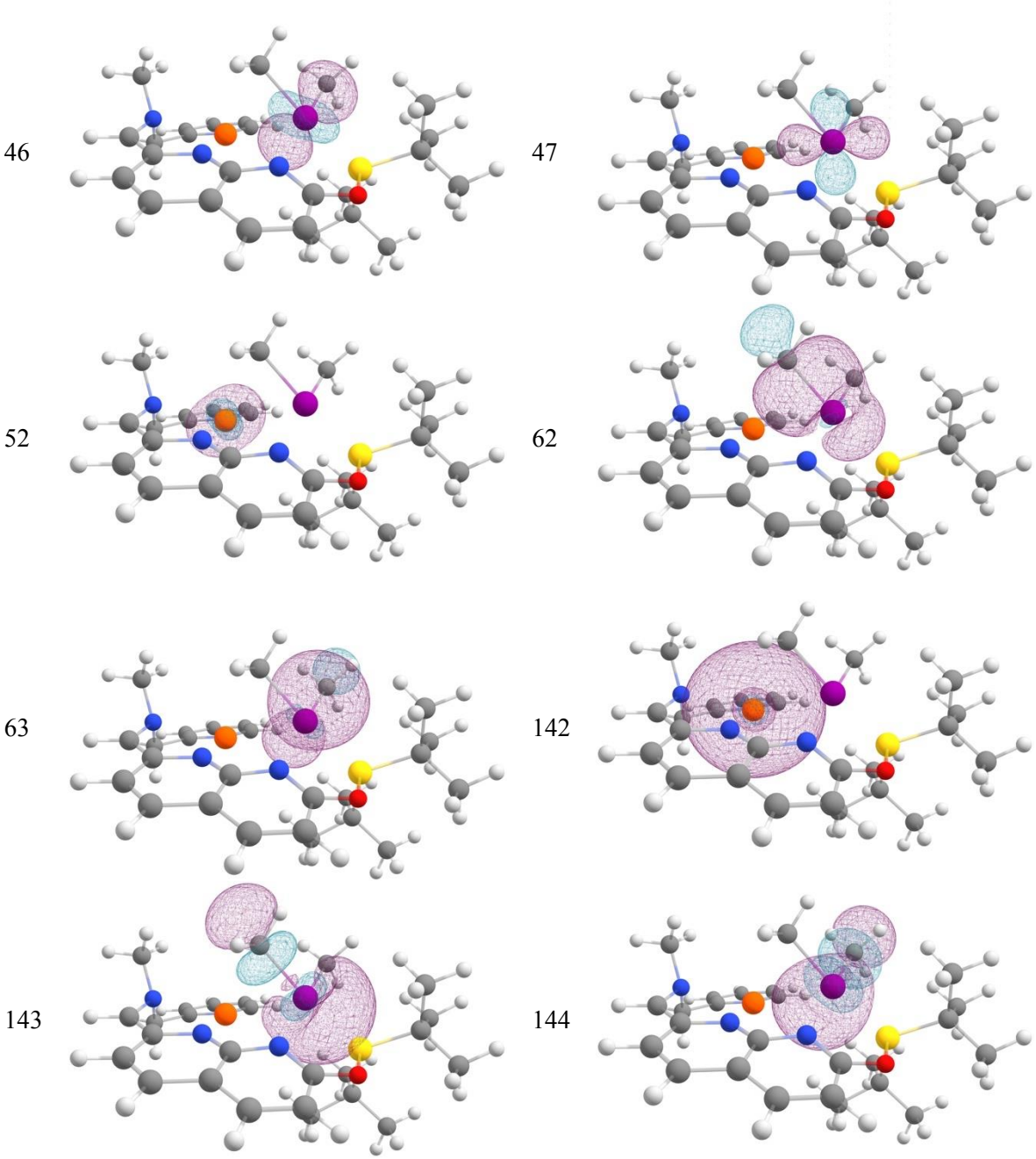

Figure S155. Orbital plots for complex **4**.

Complex 6:

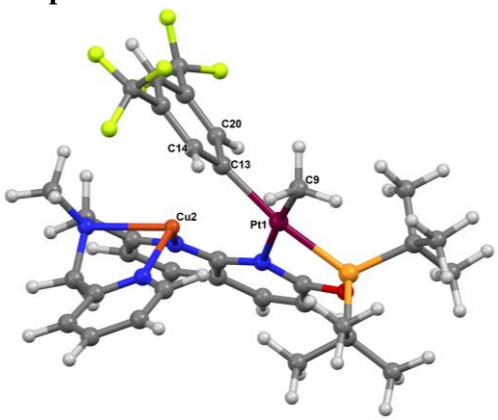

Figure S156. Atom numbering scheme for complex **6** used in the analysis below.

Interaction of the Pt-Me and Pt-Aryl fragments with the Cu-center: A strong donation of electrons from the Pt(1)-C(13) fragment to an *s*-type orbital on the Cu(2)-center [$E^{(2)}$ = 62.36 kcal/mol] was observed. Additionally, the *p*-type orbitals of the C(13)-C(14) π-bond also donate to the Cu(2) center [$E^{(2)}$ = 27.35 kcal/mol]. In contrast, the interaction of the Cu(2)-center with the π-bond of the C(13)-C(20) fragment was found to be extremely weak [$E^{(2)}$ = 0.42 kcal/mol]. Back-donation from the Cu(2)-center to the antibonding orbital of the C(13)-C(14) fragment was observed [$E^{(2)}$ = 15.66 kcal/mol]. A moderate donation of electrons from the Pt(1)-C(9) fragment to the Cu(2)-center [$E^{(2)}$ = 21.65 kcal/mol] was observed. In contrast, back-bonding interactions involving donation of electrons from *d*-type orbitals on the Cu(2)-center to the Pt(1)-C(9) and Pt(1)-C(13) fragments were found to be weak [$E^{(2)}$ = 2.93, 2.51 kcal/mol, respectively].
Interactions between Cu and the Pt: One moderate [$E^{(2)}$ = 18.3 kcal/mol] and one weak [$E^{(2)}$ = 4.87 kcal/mol] Pt→Cu interactions involving donation of electrons from predominantly *d*-type orbitals on Pt(1) to predominantly *s*-type orbitals on Cu(2) were also observed.

Table S15. Key interactions in complex **6**.

Donor			**Acceptor**			**$E^{(2)}$ kcal/mol**
#	**Orbital**	**NAO (%contribution)**	**#**	**Orbital**	**NAO (%contribution)**	
94	BD(1)Pt1-C13	Pt(30.42%) s(53.09%) p(0.13%) d(46.78%) C(69.58%) s(28.97%) p(71.03%) d(0.01%)	190	LV(1)Cu2	Cu s(98.82%) p(0.07%) d(1.11%)	62.36
114	BD(2)C13-C14	C13 (49.47%) s(0.61%) p(99.29%) d(0.09%) C14 (50.53%) s(0.08%) p(99.87%) d(0.05%)	190	LV(1)Cu2	Cu s(98.82%) p(0.07%) d(1.11%)	27.35
115	BD(1)C13-C20	C13 (48.96%) s(35.35%) p(64.57%) d(0.08%) C20 (51.04%) s(36.75%) p(63.17%) d(0.08%)	190	LV(1)Cu2	Cu s(98.82%) p(0.07%) d(1.11%)	0.42
66	LP(5)Cu2	Cu s (0.27%) p(0.03%) d(99.70%)	213	BD*(2)C13-C14	C13(50.53%) s(0.61%) p(99.29%) d(0.09%) C14(49.47%) s(0.08%) p(99.87%) d(0.05%)	15.66
93	BD(1)Pt1-C9	Pt(41.31%) s(41.97%) p(0.22%) d(57.82%)	190	LV(1)Cu2	Cu s(98.82%) p(0.07%) d(1.11%)	21.65

		C(58.69%) s(21.24%) p(78.70%) d(0.05%)				
63	LP(2)Cu2	Cu s(0.32%) p(0.03%) d(99.64%)	192	BD*(1)Pt1-C9	Pt(58.69%) s(41.97%) p(0.22%) d(57.82%) C(41.31%) s(21.24%) p(78.70%) d(0.05%)	2.93
63	LP(2)Cu2	Cu s(0.32%) p(0.03%) d(99.64%)	193	BD*(1)Pt1-C13	Pt(69.58%) s(53.09%) p(0.13%) d(46.78%) C(30.42%) s(28.97%) p (71.03%) d(0.01%)	2.51
59	LP(2)Pt1	Pt s(2.84%) p(0.02%) d(97.13%)	190	LV(1)Cu2	Cu s(98.82%) p(0.07%) d(1.11%)	18.3
58	LP(1)Pt1	Pt s(1.42%) p(0.00%) d(98.58%)	190	LV(1)Cu2	Cu s(98.82%) p(0.07%) d(1.11%)	4.87

Table S16. Natural Binding Indices in complex **6**.

	Pt(1)	**Cu(2)**	**C(9)**	**C(13)**	**C(14)**	**C(20)**
Pt(1)	-	0.2281	0.8425	0.6774	0.1513	0.1385
Cu(2)	0.2281	-	0.0789	0.3530	0.2885	0.1482

58 59

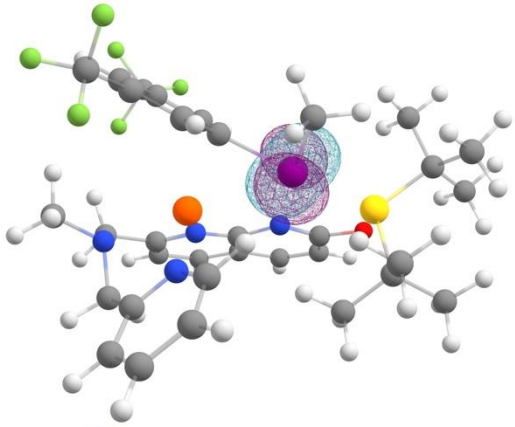

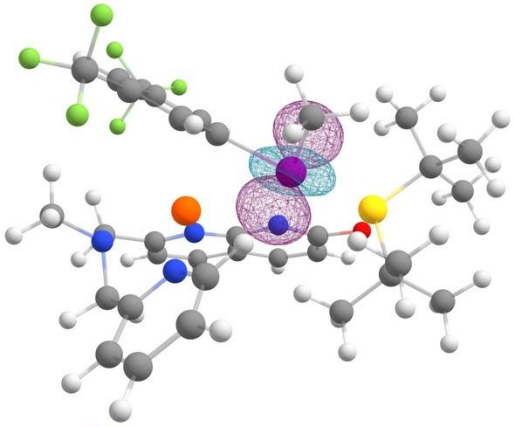

63 66

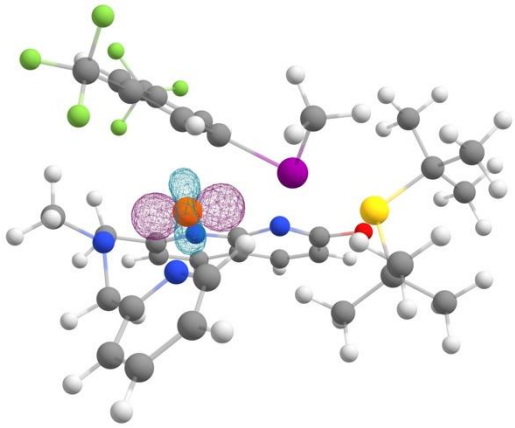

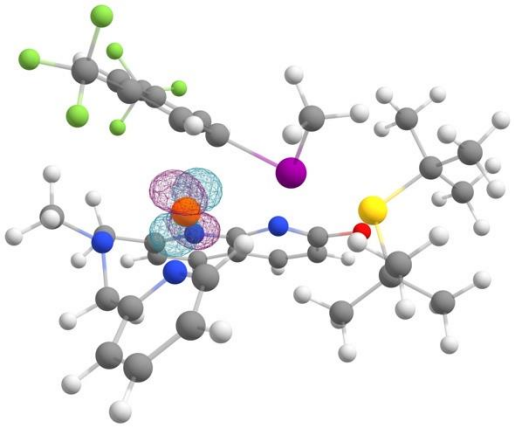

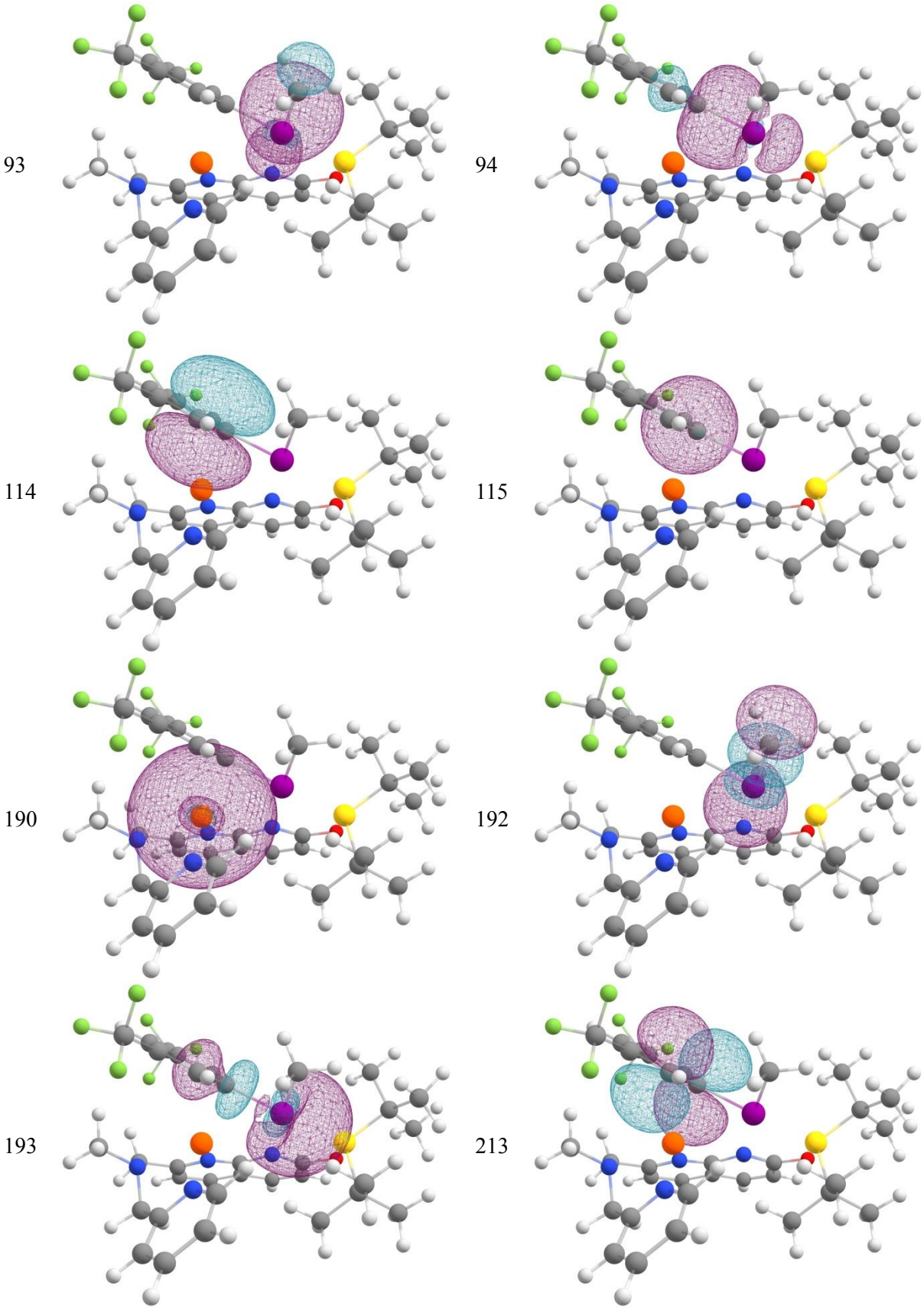

Figure 157. Orbital Plots for Complex **6**.

Complex 7:

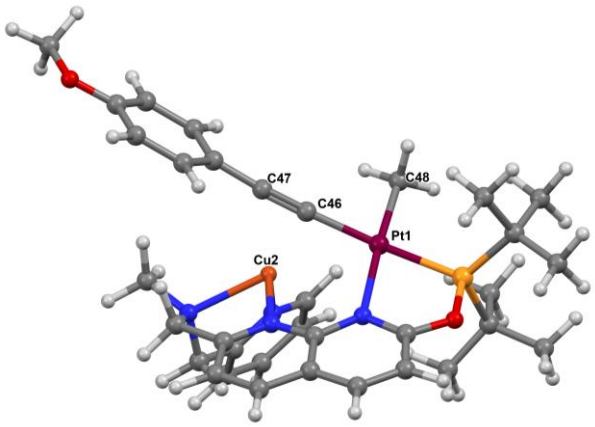

Figure S158. Atom numbering scheme for complex **7** used in the analysis below.

Interaction of the Pt-(C≡C) and Pt-Me fragments with the Cu(2) center: Complex **7** exhibits strong donation of electrons from Pt(1)-C(46) fragment to an empty *s*-type orbital on the Cu(2)-center [$E^{(2)}$ = 56.69 kcal/mol]. Additionally, a moderate [$E^{(2)}$ = 56.69 kcal/mol] donation of electrons from the *p*-type orbitals of the π-bond of the C(46)-C(47) fragment to the Cu(2)-center, and corresponding back-donation from a *d*-type orbital on the Cu(2) to the antibonding (π*) orbital of the C(46)-C(47) fragment [$E^{(2)}$ = 16.14 kcal/mol] were found. The back-donation from Cu(2) to Pt(1)-C(46) was found to be extremely weak [$E^{(2)}$ = 1.32 kcal/mol].
In addition to the interactions between the Pt-(C≡C) fragment and the Cu(2) center, a relatively weaker [$E^{(2)}$ = 12.84 kcal/mol] donation of electrons from the Pt-CH_3 fragment to the Cu(2) center, i.e. from the Pt(1)-C(48) fragment to an empty s-type orbital on Cu was found.
Interactions between Cu and the Pt: A modest interaction [$E^{(2)}$ = 13.38 kcal/mol] involving donation of electrons from predominantly Pt *d*-type to *s*-type orbitals on Cu was found.

Table S17. Key interactions in complex **7**.

Donor			**Acceptor**			$E^{(2)}$ **kcal/mol**
#	**Orbital**	**NAO (%contribution)**	**#**	**Orbital**	**NAO (%contribution)**	
73	BD(1)Pt1-C46	Pt(28.20%) s(55.74%) p(0.17%) d 44.09%) C(71.80%) s(49.68%) p(50.31%) d(0.01%)	172	LV(1)Cu2	Cu s(98.03%) p(0.09%) d(1.89%)	56.69
131	BD(3)C46-C47	C46(48.79%) s(0.42%) p(99.38%) d(0.20%) C47(51.21%) s(2.03%) p(97.88%) d(0.10%)	172	LV(1)Cu2	Cu s(98.03%) p(0.09%) d(1.89%)	29.67
62	LP(5)Cu2	Cu s(0.08%) p(0.04%) d(99.88%)	232	BD*(3)C46-C47	C(51.21%) s(0.42%) p(99.38%) d(0.20%) C(48.79%) s(2.03%) p(97.88%) d(0.10%)	16.14
60	LP(3)Cu2	Cu s(1.08%) p(0.02%) d(98.90%)	174	BD*(1)Pt1-C46	Pt(71.80%) s(55.74%) p(0.17%) d(44.09%) C(28.20%) s(49.68%) p(50.31%) d(0.01%)	1.32
74	BD(1)Pt1-C48	Pt(42.87%) s(39.61%) p(0.21%) d(60.18%) C(57.13%) s(20.68%) p(79.26%) d(0.06%)	172	LV(1)Cu2	Cu s(98.03%) p(0.09%) d(1.89%)	12.84
55	LP(2)Pt1	Pt s(2.93%) p(0.01%) d(97.06%)	172	LV(1)Cu2	Cu s(98.03%) p(0.09%) d(1.89%)	13.38

Table S18. Natural Binding Indices (NBI) in complex **7**.

	Pt(1)	**Cu(2)**	**C(46)**	**C(47)**	**C(48)**
Pt(1)	-	0.1949	0.6922	0.2232	0.8492
Cu(2)	0.1949	-	0.4174	0.3346	0.0703

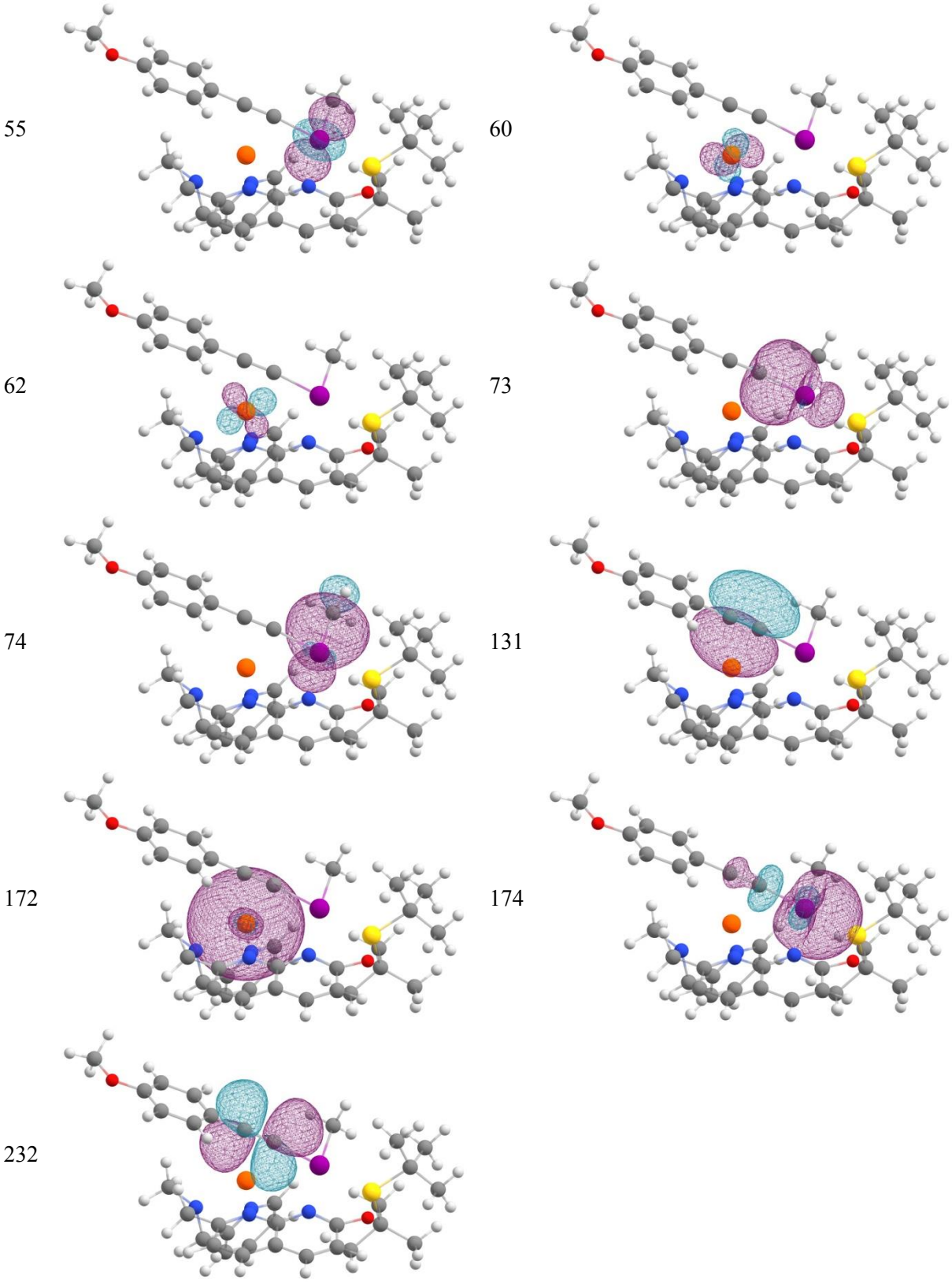

Figure S159. Orbital plots for complex **7**.

(3) Computational investigation of reaction profile

For computational efficiency, a truncated ligand motif with a PMe_2-terminus (instead of the P^tBu_2-terminus employed in the experimental work) was considered alongwith propyne (instead of 4-ethynylanisole). All geometries (for propyne, complexes **3'**, **A**, **A'**, **B**, **B'** and **C** and associated transition states, i.e. $\mathbf{TS_{AB}}$, $\mathbf{TS_{AB'}}$, $\mathbf{TS_{AC}}$) were fully optimized in the gas-phase using the RPBE1PBE[13] functional using def2tzvp[22] basis set for all elements which includes effective core potentials (ECPs) for Cu and Pt.

The PBE0 (pbe1pbe in Gaussian terminology) functional has been demonstrated to be adequate for modeling reaction free energies.[23] In yet another computational benchmarking article,[24] Chen et al. note mean unsigned errors (MUDs) of < 2 kcal/mol for PBE0. Noting that most benchmarking papers involve reactions of monometallic complexes, and in calculations with the fairly large basis sets (i.e., close to convergence limit), basis set effects are typically small,[25] we chose the def2tzvp basis sets which have been warranted in DFT calculations of both Cu[26] and Pt[27] complexes.

NBO charge analyses were performed using the NBO6[20] package as implemented in Gaussian 16. Molecular coordinates and associated free energies are being provided in a multi-XYZ file named 'Reaction_Profile.xyz' and animations for TSs are being provided as a ZIP-archive named 'Reaction_Profile_Animations.zip' containing GIF files.

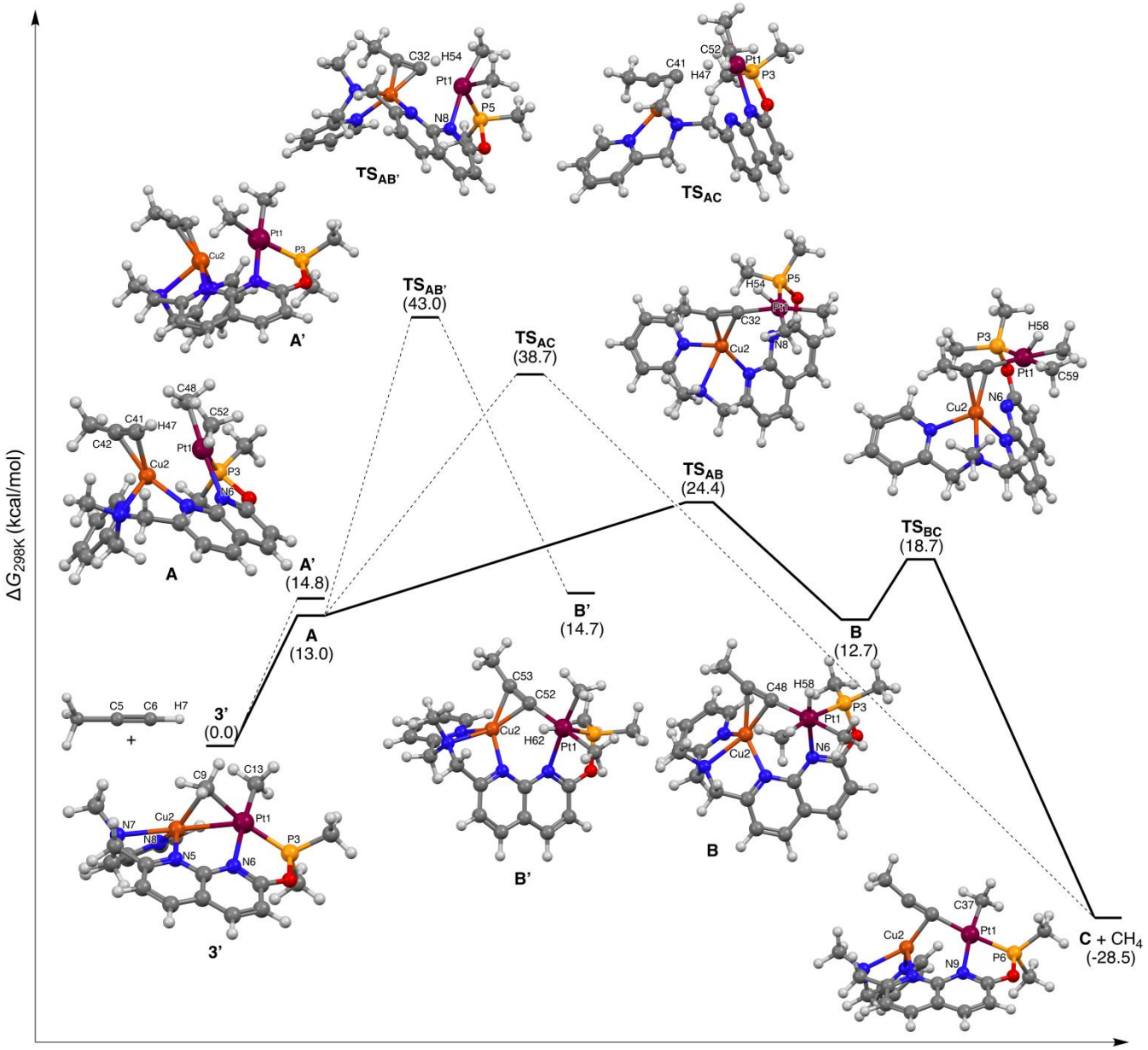

Figure S160. Full energy profile calculated for alkyne activation and DFT-optimized structures for intermediates and transition states.

Discussion:

Complex **3'** features a square planar Pt^{II}-center with the Pt-CH_3 fragments *trans* to the PMe_2 (P3) and pyridine (N6) donors. Consistent with the strong *trans* influence of the Pt-bound CH_3 fragment, the Pt1-N6 distance is elongated (2.21 Å). The Cu^{I}-center is coordinated by three N donors (N5, N7 and N8) on one side, and flanked on the other side by the Pt(1)-C(9)H_3 fragment exhibiting the same Pt-CH_3-Cu interaction observed in the X-ray structure of **3**. Consequently, the Pt(1)-Cu(2) distance is 2.64 Å. The Pt(1)-C(9) distance is considerably longer (2.14 Å), as opposed to the Pt(1)-C(13) distance (2.04 Å).

π-Coordination of propyne to the Cu^{I}-center to form **A** by displacement of the Pt-CH_3-Cu interaction in **3'** is endergonic by 13.0 kcal/mol. As a consequence of this displacement, the Pt-CH_3 bond length (Pt1-C48: 2.08 Å) of the fragment previously involved in the Pt-CH_3-Cu interaction is now only slightly longer than that of the other Pt-CH_3 fragment (Pt1-C52: 2.04 Å) *trans* to the pyridine (N6) fragment. The coordinated propyne is almost periplanar with the square plane of the Pt^{II}-center, with the terminal C-H of the propyne pointing towards the naphthyridine fragment. Owing to the π-interaction, the C(41)-C(42) distance (1.22 Å) in the coordinated propyne is slightly elongated than that of free propyne (1.20 Å). Interestingly, significant departure of the C42-C41-H47 angle (164.4°) from the C5-C6-H7 angle of 180° in free propyne is observed. NBO calculations reveal that there is enhancement in the polarization of the terminal C-H fragment of the coordinated propyne (C41: -0.369; H47: +0.273) when compared to those of free propyne (C6: -0.265; H7:+0.239). Another isomer (**A'**), the formation of which is slightly more endergonic (14.8 kcal/mol) than **A**, was located. This isomer features the terminal C-H of the coordinated propyne pointing away from the naphthyridine fragment, but is otherwise unremarkable when compared to **A**.

Noting the enhancement in the polarization of the terminal C-H fragment of the coordinated propyne in **A**, we considered the possibility of its oxidative addition to the Pt^{II}-center. The transition state $\mathbf{TS_{AB'}}$, leading to the $Pt^{IV}(CH_3)_2(H)$ complex, **B'** was found to have an associated barrier of 43 kcal/mol. The Pt^{II}-center is pseudo 5-coordinate with the naphthyridine-N(8) donor exhibiting de-coordination (N8-Pt1: 2.26 Å, as opposed to the N6-Pt1 distance of 2.18 Å in **A**), consistent with literature precedents[28] on the oxidative addition/reductive elimination transformations between Pt^{II} and Pt^{IV} centers. We ascribed the high barrier of this transition state to the coordination geometry around the Pt^{II}-center: in this structure, the C-H fragment (C32-H54) undergoing oxidative addition places the Pt-H(54) fragment undergoing formation *trans* to the highly *trans*-influencing Pt-bound P(5)Me_2-fragment.

Although the formation of **B'** from **A** is virtually thermo-neutral, since the kinetic barrier for its formation is inaccessible under reaction conditions, we discarded its relevancy towards further reactivity such as reductive elimination of methane (*vide infra*).

Another transition state ($\mathbf{TS_{AB}}$) leading to $Pt^{IV}(CH_3)_2(H)$ complex **B** was located, where the C-H fragment of the coordinated propyne (C32-H54) undergoes oxidative addition to the Pt^{II}-center. In contrast to $\mathbf{TS_{AB'}}$, the lower barrier of 24.4. kcal/mol associated with $\mathbf{TS_{AB}}$ can be ascribed to the geometry of the C-H fragment undergoing oxidative addition (C32-H54) resulting in the incumbent Pt-H forming *trans* to a formally vacant coordination site generated by dissociation of the naphthyridine-N(8) donor from the Pt-center (N8-Pt1: 3.04 Å). The stabilization of $\mathbf{TS_{AB}}$ can also be attributed, in part, to the propynilide fragment having undergone σ-coordination to the Pt-center (C32-Pt1: 2.03 Å, comparable to that in the resultant complex, **B**, C32-Pt1: 2.05 Å). The formed complex **B** is similar to **B'** in that the propynilide fragment is π-coordinated to the Cu^{I}-center and σ-coordinated to the pseudo-octahedral Pt^{IV}-center, but differs in that the naphthyridine fragment is coordinated trans to the Pt-H fragment resulting in an elongated N6-Pt1 bond length of 2.32 Å. As a consequence of this elongation, complex **B** is pre-disposed to undergo facile C-H reductive elimination via $\mathbf{TS_{BC}}$ with an associated barrier of 18.7 kcal/mol, leading to the evolution of methane and the highly exergonic formation of **C** (41.2 kcal/mol relative to **B**). In $\mathbf{TS_{BC}}$, the napththyridine-N(6) donor, once again, has virtually undergone dissociation from the Pt-center (N6-Pt1: 2.77 Å). The C(59)-H(58) bond is being formed trans to the P(3) fragment with a C(59)-Pt(1)-H(58) angle of 51.2° is consistent with an early transition state. Following reductive elimination, reinstatement of the square-planar Pt^{II}-center occurs by re-coordination of the napthyridine N(9) donor trans to the residual Pt^{II}-CH_3 fragment. The overall reaction is exergonic by 28.5 kcal/mol.

Based on literature precedence,[29] we also considered an alternate pathway for the protonolysis of the Pt^{II}-CH_3 fragment of **A** to form **C** in a concerted manner. The transition state located ($\mathbf{TS_{AC}}$) was found to be have a very high associated barrier of 38.7 kcal/mol and was its consideration was discarded in the mechanism being proposed.

References

1. O. Rivada-Wheelaghan, S. L. Aristizábal, J. López-Serrano, R. R. Fayzullin and J. R. Khusnutdinova, *Angew. Chem. Int. Ed.*, 2017, **56**, 16267-16271.
2. A. Lüning, M. Neugebauer, V. Lingen, A. Krest, K. Stirnat, G. B. Deacon, P. R. Drago, I. Ott, J. Schur, I. Pantenburg, G. Meyer and A. Klein, *Eur. J. Inorg. Chem.*, 2015, **2015**, 226-239.
3. T. G. Appleton, J. R. Hall and M. A. Williams, *J. Organomet. Chem.*, 1986, **303**, 139-149.
4. G. Sheldrick, *Acta Crystallogr., Sect. A*, 2015, **71**, 3-8.
5. G. Sheldrick, *Acta Crystallogr., Sect. C*, 2015, **71**, 3-8.
6. L. J. Farrugia, *J. Appl. Crystallogr.*, 2012, **45**, 849-854.
7. A. Spek, *Acta Crystallogr., Sect. C*, 2015, **71**, 9-18.
8. Gaussian 16, Revision B.01, M. J. Frisch, G. W. Trucks, H. B. Schlegel, G. E. Scuseria, M. A. Robb, J. R. Cheeseman, G. Scalmani, V. Barone, G. A. Petersson, H. Nakatsuji, X. Li, M. Caricato, A. V. Marenich, J. Bloino, B. G. Janesko, R. Gomperts, B. Mennucci, H. P. Hratchian, J. V. Ortiz, A. F. Izmaylov, J. L. Sonnenberg, D. Williams-Young, F. Ding, F. Lipparini, F. Egidi, J. Goings, B. Peng, A. Petrone, T. Henderson, D. Ranasinghe, V. G. Zakrzewski, J. Gao, N. Rega, G. Zheng, W. Liang, M. Hada, M. Ehara, K. Toyota, R. Fukuda, J. Hasegawa, M. Ishida, T. Nakajima, Y. Honda, O. Kitao, H. Nakai, T. Vreven, K. Throssell, J. A. Montgomery, Jr., J. E. Peralta, F. Ogliaro, M. J. Bearpark, J. J. Heyd, E. N. Brothers, K. N. Kudin, V. N. Staroverov, T. A. Keith, R. Kobayashi, J. Normand, K. Raghavachari, A. P. Rendell, J. C. Burant, S. S. Iyengar, J. Tomasi, M. Cossi, J. M. Millam, M. Klene, C. Adamo, R. Cammi, J. W. Ochterski, R. L. Martin, K. Morokuma, O. Farkas, J. B. Foresman, and D. J. Fox, Gaussian, Inc., Wallingford CT, 2016.
9. J.-D. Chai and M. Head-Gordon, *PCCP*, 2008, **10**, 6615-6620.
10. D. Andrae, U. Haeussermann, M. Dolg, H. Stoll and H. Preuss, *Theor. Chim. Acta*, 1990, **77**, 123-141.
11. (*a*) P. C. Hariharan and J. A. Pople, *Mol. Phys.*, 1974, **27**, 209-214; (*b*) P. C. Hariharan and J. A. Pople, *Theor. Chim. Acta*, 1973, **28**, 213-222; (*c*) W. J. Hehre, R. Ditchfield and J. A. Pople, *J. Chem. Phys.*, 1972, **56**, 2257-2261; (*d*) M. M. Francl, W. J. Pietro, W. J. Hehre, J. S. Binkley, M. S. Gordon, D. J. DeFrees and J. A. Pople, *J. Chem. Phys.*, 1982, **77**, 3654-3665.
12. AIMAll (Version 19.10.12), Todd A. Keith, TK Gristmill Software, Overland Park KS, USA, 2019 (aim.tkgristmill.com).
13. J. P. Perdew, K. Burke and M. Ernzerhof, *Phys. Rev. Lett.*, 1996, **77**, 3865-3868.
14. (*a*) R. F. W. Bader, *Chem. Rev.*, 1991, **91**, 893-928; (*b*) R. F. W. Bader, *Atoms in Molecules: A Quantum Theory*, Clarendon Press, 1994.
15. C. Lepetit, P. Fau, K. Fajerwerg, M. L. Kahn and B. Silvi, *Coord. Chem. Rev.*, 2017, **345**, 150-181.
16. R. Bianchi, G. Gervasio and D. Marabello, *Inorg. Chem.*, 2000, **39**, 2360-2366.
17. P. R. Varadwaj, A. Varadwaj and H. M. Marques, *J. Phys. Chem. A*, 2011, **115**, 5592-5601.
18. (*a*) P. R. Varadwaj, I. Cukrowski and H. M. Marques, *J. Phys. Chem. A*, 2008, **112**, 10657-10666; (*b*) P. Macchi, D. M. Proserpio and A. Sironi, *J. Am. Chem. Soc.*, 1998, **120**, 13429-13435; (*c*) G. Gervasio, R. Bianchi and D. Marabello, *Chem. Phys. Lett.*, 2004, **387**, 481-484.
19. (*a*) E. Espinosa, I. Alkorta, J. Elguero and E. Molins, *J. Chem. Phys.*, 2002, **117**, 5529-5542; (*b*) D. Cremer and E. Kraka, *Croat. Chem. Acta*, 1985, **57**, 1259-1281; (*c*) R. F. W. Bader and H. Essen, *J. Chem. Phys.*, 1984, **80**, 1943-1960.
20. NBO 6.0. E. D. Glendening, J. K. Badenhoop, A. E. Reed, J. E. Carpenter, J. A. Bohmann, C. M. Morales, C. R. Landis, and F. Weinhold (Theoretical Chemistry Institute, University of Wisconsin, Madison, WI, 2013); http://nbo6.chem.wisc.edu/.
21. Chemcraft - graphical software for visualization of quantum chemistry computations. https://www.chemcraftprog.com.
22. F. Weigend and R. Ahlrichs, *PCCP*, 2005, **7**, 3297-3305.
23. K. H. Hopmann, *Organometallics*, 2016, **35**, 3795-3807.
24. Y. Sun, L. Hu and H. Chen, *J. Chem. Theory Comput.*, 2015, **11**, 1428-1438.
25. C. Latouche, D. Skouteris, F. Palazzetti and V. Barone, *J. Chem. Theory Comput.*, 2015, **11**, 3281-3289.
26. A. Jesser, M. Rohrmüller, W. G. Schmidt and S. Herres-Pawlis, *J. Comput. Chem.*, 2014, **35**, 1-17.
27. J. Vícha, M. Patzschke and R. Marek, *PCCP*, 2013, **15**, 7740-7754.
28. (*a*) D. M. Crumpton and K. I. Goldberg, *J. Am. Chem. Soc.*, 2000, **122**, 962-963; (*b*)A. T. Luedtke and K. I. Goldberg, *Inorg. Chem.*, 2007, **46**, 8496-8498; (*c*) K. I. Goldberg, J. Y. Yan and E. L. Winter, *J. Am. Chem. Soc.*, 1994, **116**, 1573-1574; (*d*) K. I. Goldberg, J. Yan and E. M. Breitung, *J. Am. Chem. Soc.*, 1995, **117**, 6889-6896.
29. J. E. Bercaw, G. S. Chen, J. A. Labinger and B.-L. Lin, *Organometallics*, 2010, **29**, 4354-4359.